Winter 12-15-2018

Towards Engineering Advanced Nanomaterials: Elucidating Fundamental Particle Behavior in Water and Critical Sorption Dynamics

Changwoo Kim
Washington University in St. Louis

Follow this and additional works at: https://openscholarship.wustl.edu/eng_etds

Part of the Environmental Sciences Commons, and the Nanoscience and Nanotechnology Commons

WASHINGTON UNIVERSITY IN ST. LOUIS

Department of Energy, Environmental & Chemical Engineering

Dissertation Examination Committee:
John D. Fortner, Chair
Damena Agonafer
Marcus B. Foston
Daniel E. Giammar
Young-Shin Jun

Towards Engineering Advanced Nanomaterials: Elucidating Fundamental Particle Behavior in
Water and Critical Sorption Dynamics
by
Changwoo Kim

A dissertation presented to
The Graduate School
of Washington University in
partial fulfillment of the
requirements for the degree
of Doctor of Philosophy

December 2018
St. Louis, Missouri

Table of Contents

List of Figures

List of Tables

<u>Acknowledgments</u>

I would like to thank Dr. John D. Fortner, my PhD. advisor, for his guidance, advice, and support over the past five years. He always encourages me throughout my graduate student career. I deeply appreciate his guidance and support during my Ph. D. program. I would like to thank Dr. Daniel Giammar, Dr. Young-Shin Jun, Dr. Marcus B. Foston, and Dr. Damena Agonafer for their time and support as committee members. I would also like to thank all my past and current group members: Dr. Jiewei Wu, Dr. Yi Jiang, Dr. Wenlu Li, Dr. Yao Nie, Dr. Kelsey Haddad, Dr. Hui Qiu, Siyuan An, Qingqing Zeng, Wining Ou, Anushree Ghosh, Junseok Lee, Neha Sharma, Kit Tan Kwan, Trey Oldham, Carl Hinton, Daniel Schmucker, Nick Matteucci, Samantha Cobb. I would really like to thank to Dr. Seung Soo Lee. He always encourages me and pushes me to pursue a broad range of scientific careers. I would like to thank to all of my research collaborators for their great efforts on my Ph. D. researches. I would also like to thank all of my friends at Washington University.

I would specifically like to thank my mother and father for their love, support and help. Also, I would like to thank my three older sisters for their support and love. I would specifically like to thank my wife for understanding and encouraging me. She is my constant source of constant source of encouragement. I would like to thank to my two sons and daughter for being the strongest driving force of my life. I would like to thank to parents-in-law for their love and support.

Changwoo Kim

Washington University in St. Louis

December 2018

ABSTRACT OF THE DISSERTATION

Towards Engineering Advanced Nanomaterials: Elucidating Fundamental Particle Behavior in

Water and Critical Sorption Dynamics

by

Changwoo Kim

Washington University in St. Louis, 2018

Professor John D. Fortner, Chair

As advanced nanomaterials, inorganic-organic nano composites have received great interest as potential platform (nano) structures for sensor, catalyst, sorbent, and environmental applications. Here, my Ph.D. research has focused on the design, synthesis, and characterization of advanced water-stable engineered metal-oxide nanoparticles functionalized by organic frames for environmental applications. For the environmental applications, I have evaluated particle-optimized sorption processes for the remediation and separation of arsenic, chromium, and uranium under environmentally relevant conditions. More specifically, I have explored the critical role of organic coating on sorption mechanisms and performances using engineered iron oxide -based, manganese oxide -based, and manganese ferrite -based (core) nanoparticles with varying size, composition, surface coating and functional groups. With the application for environmental remediation of organic functionalized metal oxide nanoparticles, implication of advanced materials is another essential subject for environmental nano impact. As environmental implications, I fundamentally described material transport behavior(s), including aggregation and deposition in terms of surface organic matrix; I quantitatively explored the role of organic coating on collision and attachment of inorganic-organic nano composites for the environmental fate and transport of new nano platforms. Further, I evaluated highly stable

organic coated superparamagnetic nanoparticles as potential draw solute for osmotic pressure driven membrane system to exploit paramagnetism of the particles. These works suggest better understanding of environmental application and implication for inorganic-organic nano composites.

Chapter 1. Introduction

1.1 Introduction

Advances in nanotechnology have recently contributed to science and engineering fields including material science, biotechnology, environmental engineering, among other disciplines. Nanotechnology is generally focused on materials and processes that are defined by one of the dimensions typically being 1 - 100 nm.[1] For perspective about just how small this is; if a fullerene ($C_{60,}$ MW 720) was the size of soccer ball, the actual soccer ball would be around size of the earth (Figure 1.1).[2] Interestingly, mankind already has been using nanotechnology for over some time. Four thousand years ago, ancient Egyptian used lead-sulphide nanoparticles (5 nm) for cosmetic purposes (hair dying).[3] Ancient Romans made gold and silver nanocomposites to decorate the glass cup (e.g. Lycurgus Cup).[4] In the middle ages, various sized gold nanoparticles were applied to stained glass, as gold nanoparticles have unique size dependent color characteristics/properties.[4] The modern concept of nanotechnology was first introduced by R. Feynman in 1959[5] in a talk that titled, "There is plenty of room at the bottom" at the annual meeting of the American Physical Society. This being said, practically speaking, nanotechnology research really began in earnest at the end of 20th century. In 1985, C_{60} (Bucky ball), a nano sized carbon material, was experimentally identified by Curl, Kroto, and Smalley, for which they were awarded the Nobel Prize in chemistry in 1996.[6] Nanosized materials have attracted significant attention due to unique materials properties which can vary considerably compared to bulk materials. The first private nanotech company (Zyvex) was founded in 1997, and the first nano-centric governmental effort (U.S. National Nanotechnology Initiative) was established in 2000.
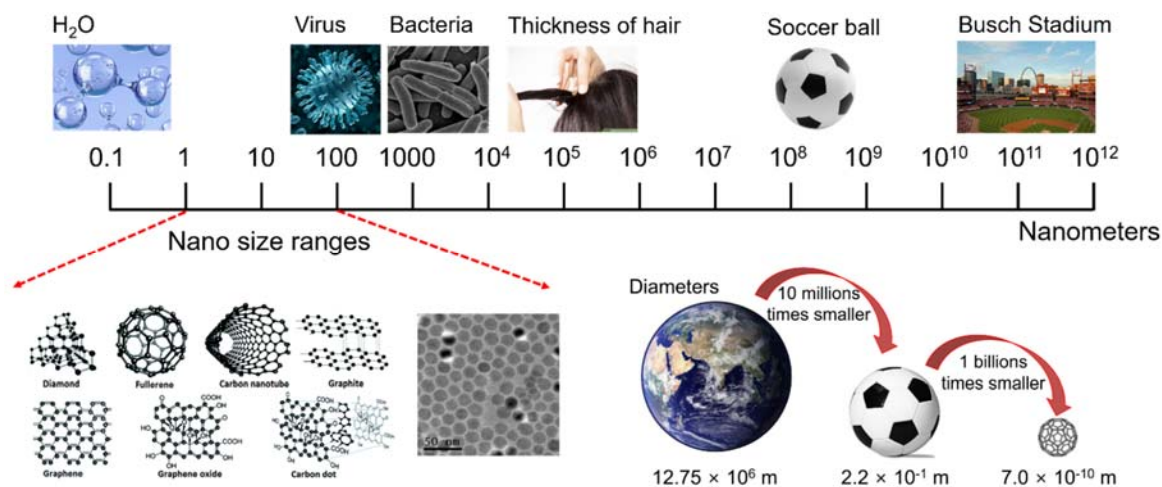
Figure 1.1 Length scales when considering the size of nanomaterials. Shown on the left, within the nanoscale size range, are classic carbon nano materials (diamond, fullerene, carbon nanotube, graphite, graphene, graphene oxide, and carbon dot)[7] and iron oxide nanocrystals. On the bottom right, the size of the earth, soccer ball, and fullerene (C_{60}) are compared for reference.[2]

Unique properties found at the nanoscale have led to a large number of material applications in a wide range of commercial and industrial products such as catalysts, construction materials, electronic devices, and cosmetics, among others.[8-10] It is estimated that by the year 2020, related industries will reach to a market value of approximately $3 trillion.[11] Among the usage of engineered nanomaterials, metal- and metal-oxide nanoparticles currently comprise a significant fraction of all produced and applied engineered nanoparticles.[12] For example, nanoscale silver and nanoscale titanium are widely used in treated paints for car, outdoor, and indoor facilities.[13-14] As a color additives, food industries have widely used titanium dioxide nanoparticles.[15] Nano sized titanium dioxide and zinc oxide currently are also routinely used in skin cosmetics and sunscreens as ultraviolet (UV) filters.[13]

Along with unique material property advantages, the impacts of nanomaterials on environment and human health must also be evaluated for technological sustainability. In 2007, Science Policy Council of U.S. Environmental Protection Agency published a "Nanotechnology

White Paper" to address potential risks from environmental exposure to nanomaterials.[16] The

White Paper provided information regarding the potential risk of nanomaterials including human

health (toxicity), fate, and transport research. Since, concerns regarding the possible unwanted

release of nanoparticles into the environment during their production, usage, or disposal have

been topics of considerable attention.[17-19] Upon release to the environment, nanomaterials have

the potential to be transported into/through the environment, including surface and

groundwater(s), and eventually enter a food web. While a number of studies have examined

nanoparticles transport in porous media using well-controlled sand columns,[20-23] recently,

research has taken the next step in complexity analyses and focused on the role(s) of natural

organic matter (NOM) on fate and transport of nanoparticles.[24] NOM is expected to play a

critical role in the stabilization of nanoparticles and corresponding stability dynamics will guide

environmental implications as they relate to fate, transport, and exposure. Research to date has

demonstrated that NOM can broadly stabilize nanoparticles in water, reducing aggregation under

a range of typically unstable conditions.[25-28]

To take advantage of novel material properties in water, colloidal stability of

nanomaterials is also a critical issue for engineered applications. When unaltered, the surface

energy of nano size material is typically high and thus the systems are unstable – nanoparticles

aggregates when the total free energy of the nano system is reduced as the surface area

decreases.[1, 29] Further, the stabilization of surface energy of nanoparticles is crucial for the

control of their size during synthesis. Recently, organic functionalized (typically at the surface)

metal and metal oxide nano materials have been recognized as promising next generation

material in, tumor targeting, sensor, sorption, and catalyst due to their extreme stability

properties and specific surface affinities.[30-32] As another example, inorganic (metal- and metal

3

oxide-) based sorbents with rigid core structures and controllable geometries can be broadly surface passivated with a number of organic coating strategies for selective contaminant affinity and aqueous stability, among other desired properties.[33-35] An organic surface coating provides electrostatic double layer (EDL) repulsion as well as extended Derjaguin, Landau, Verwey, and Overbeek (XDLVO) repulsive interactions, such as osmotic and elastic-steric repulsion.[36-39] Despite being a critical aspect of next generation, engineered nanomaterials,[36-39] the role of soft, organic coatings remains unclear a fundamental colloidal stability, aggregation, and deposition (transport) perspective.

In this Ph.D. thesis, research is focused on the design, synthesis, and characterization of engineered metal-oxide nanoparticles which are surface functionalized by a library of organic coating types and strategies for environmental applications and to understand potential implications of such materials. Towards this, research here is organized into two interrelated topic areas: 1) Defining the critical role of organic surface coatings with regard to the sorption and separation of As(V), Cr(VI), and U(VI) by metal-(Mn, Fe) oxide nanocrystals (NCs) core materials; 2) Fundamentally describing the role of organic coating(s) for inorganic-organic nano platforms in terms of aggregation and deposition to better understand their behavior in water considering both implications and applications.

Chapter 2: Literature Review

2.1. Synthesis of Metal Oxide Nanocrystals

To control the surface chemistry of nanocrystals in liquids, organic surfactants, including long chain organic acids, are often applied as capping agents. Organic surfactants are bound to the surface of nanoparticles by attractive forces, including as hydrophobicity, electrostatics, van der Waals attraction, and chemisorption.[40] Grafted surfactants provide electrostatic (double layer) repulsion and steric repulsion stabilizing surface based processes including additional growth and aggregation.[37-39] Synthesized nanocrystals can be dispersed in both polar solvents (i.e. water) or non-polar solvents (i.e. hexane, toluene, or chloroform) depending on the surface chemistry. In non-polar solvents, organic surfactants cover the surface of nanocrystals, typically with hydrophobic terminal groups facing outwards (into the liquid phase).[40] For polar solvents, organic surfactants with hydrophilic functionality can be employed.[40] For synthesis in polar solvents, especially for water, van der Waals attraction between nanocrystals is significant and rapid, even with capping agents present, making highly monodisperse particles difficult to reproducibly prepare and control.[41] Therefore, for monodiperse metal oxide nanocrystals, including single crystal synthesis, non-polar organic solvents are often preferred for core particle synthesis, with organic surfactant used as capping / stabilizing agents.

2.1.1. Metal Oxide Nanocrystal Growth Mechanism

Organic-based methods using metal-organic precursor(s) and organic surfactants at high temperatures have been developed, by our lab and others, for nanocrystal synthesis routes that allow for tunable shape and size along with very narrow size distributions. Growth of the metal oxide nanocrystals (via metal-organic decomposition and particle nucleation) is affected by various reaction conditions such as reaction time, temperature, concentration and ratio of metal

5

precursors, and organic surfactants.[42-45] Typically, the size of nanocrystal increases with reaction time and concentration of metal precursors.[42] Further, the shape of nanocrystal can be controlled through the co-surfactant and organic addictive.[46] Additionally, an increase in the ratio of surfactants to metal precursors promotes nanocrystal growth.[45]

Classic metal oxide nanocrystal formation can be thought of through two steps; first nucleation and then particle growth according to LaMer and Dignae (LaMer model).[43] Fig. 2.1 presents a generalized illustration of time dependent monomer concentration and nucleation/growth of nanocrystals. Before nucleation, metal precursors and surfactants form monomers (reactive feeding sources), which reaches a critical concentration (part 1). As monomer concentration continues to increase (past the critical concentration), nucleation begins (Part II). In this part, metal precursor and surfactant are still forming monomers. As the reaction proceeds, monomer concentration reaches a maximum concentration then decreases back to the critical concentration level. Under the critical concentration, particle growth occurs. During this stage, molecularly dissolved monomer diffuse to/at the nuclei. growing to nanocrystal until the monomer concentration reaches an equilibrium concentration.[43-44] During this stage, monomer depletion can promote Ostwald ripening, whereby larger nanocrystals become larger and smaller nanocrystals shrink.[43, 47] Since growth of synthesized nanocrystals is time dependent, reaction time is crucial and often empirically informed. After the reaction is complete, nanocrystals are stabilized hydrophobic interface of the surface based surfactants (facing outwards), as mentioned above.
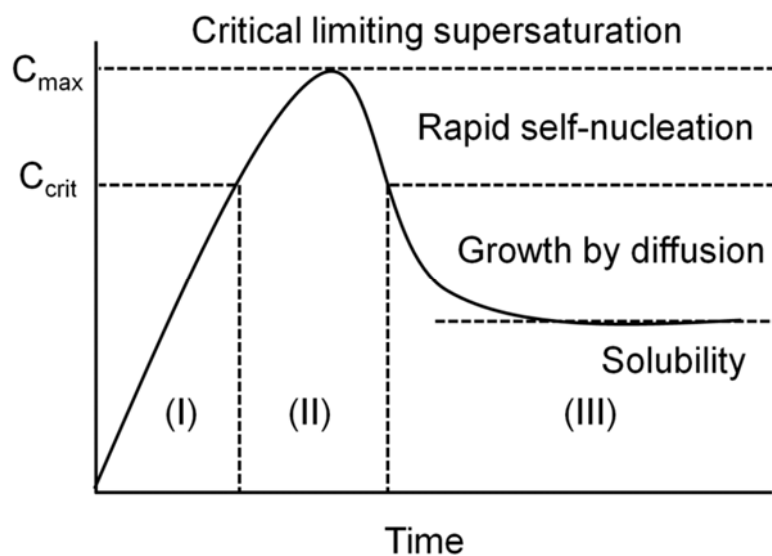
Figure 2.1 The LaMer mechanism for nanocrystal nucleation and growth[43]

2.1.2. Iron Oxide Nanocrystal Synthesis

The iron oxide nanocrystals can be synthesized through several types of methods including thermal decomposition,[42, 48] coprecipitation,[49] and microemulsion.[50] For monodisperse nanocrystals, thermal decomposition methods with organic surfactants in nonpolar solvent is widely employed.[51] This method is was first developed by Rockenberger et al. using organometallic compounds FeCup$_3$ (iron N-nitrosophenylhydroxylamine) as an iron precursor.[52] Various organometallic compounds have been demonstrated as suitable iron precursors including iron pentacarbonyl,[53] iron acetylacetonate,[54] and iron chelated complexes, among others.[55] Yu et al. developed a method for highly monodisperse iron oxide nanocrystals using iron oxy-hydrate as an iron precursor with oleic acid as an organic surfactant.[42] Park et al. separated monomer formation step, and nanocrystal nucleation and growth step using iron salts and sodium oleate.[48]

2.1.3. Manganese Oxide Nanocrystal Synthesis

Similar to iron oxides described above, monodisperse manganese oxide nanocrystals can be precisely synthesized via thermal decomposition methods using a variety of manganese

7

precursors, such as $Mn_2(CO)_8$,[56] Mn(II) acetylacetonate,[57] Mn(II) acetate,[58] and Mn(II) formate[59] with oleate acid as a surfactant. Ghosh et al. used fatty acids as a stabilizing organic agent with Mn(II) cupferronate.[60] Recently, Schladt et al. separated the monomer (Mn-oleate) formation step using the mixture of Mn(II) chloride and sodium oleate, forming Mn-oleate at (relatively) low temperature (58^oC);[61] by decomposition of Mn-oleate (monomer) at high temperature (320^oC), which resulted in exceptionally narrow size distributions of manganese oxide nanocrystals.

2.1.4. Manganese Ferrite Nanocrystal Synthesis

Manganese ferrite nanocrystals have Mn ions in the tetrahedral or octahedral sites of the magnetite nanocrystals, which has (inverse)spinel structure.[45] The replacement of iron in magnetite can be also accomplished with transition metal ions such as Co, Zn, Ni, Cr, and Al.[62] Further, multiple types of substations can be accomplished results in binary, ternary, or quaternary (and beyond) metal oxide nanocrystals.[63] In our research group, Lee et al. demonstrated that the composition of manganese ferrite is controlled by molar ratio of initial precursors.[45] Here, iron rich or manganese rich manganese ferrite nanocrystals were demonstrated to be precisely synthesized by changing the ratio of Fe-oleate : Mn-oleate.

2.1.5. Core@shell Manganese Ferrite Nanocrystal Synthesis

Core@shell structured nanocrystals can be synthesized through a modified metal oleate method.[64] Here, the concentration of core nanocrystals should be above the critical concentration and concentration of metal oleate for the shell structure should be below the nucleation concentration. The chemical composition of shell structure is determined by the initial ratio of metal monomer.

2.2. Organic Surface Functionalization

For aqueous studies, nanocrystals synthesized in organic solvents must be phase transferred, which involves surface modification.[65] In addition, this step allows for desired functionalization for engineering applications.[66-67] Here, we summarize approaches for organic-based surface modifications, which are relevant to research within this thesis.

2.2.1 Ligand Exchange

Ligand exchange methods replace the hydrophobic (original) surfactant layer in non-polar solvents with hydrophilic surfactants, facilitating transfer to polar solvents (water phase).[40] For example, Uyeda et al. exchanged phosphine-based hydrophobic ligands of the CdSe/ZnS quantum dots with poly(ethylene glycols) functionalized with thioctic acid.[68] Benoit et al. demonstrated that citrate stabilized gold nano colloids can be ligand exchanged with thiol-functionalized methylpoly(ethylene glycol).[69] With thermogravimetric and total organic carbon analysis, grafting density was found to increase with increasing the diameter of nanoparticles when length of polymer or surfactant is equal or less than the radius of the particles.[69]

2.2.2 Ligand Encapsulation

In addition to ligand exchange, ligand encapsulation methods also provide a tunable strategy for particle transfer into polar solvents (here as water).[40] The premise of the method is a bilayer structure coating on the surface of nanocrystal. To do this, a second layer of amphiphilic surfactant which has hydrophobic carbon chain with hydrophilic functionality head group is used (facing outwards) to render particles hydrophilic. This structure is similar to a cell membrane in concept. For example, Prakash et al. developed an oleic acid - oleic acid surface bilayer for the stabilization of nanoscale magnetite.[51] Lee et al. synthesized oleylamine coated cerium oxide nanocrystals, with a bilayered structure, using poly(acrylic acid), oleic acid, and

polymaleicanhydride-alt-1-octadecene.[70] To date, the ideal size and yield of bilayer ligand density is obtained under optimized ligands concentrations which have been empirically derived. One limitation for this method is for surfactants with relatively low critical micelle concentration (CMC)s, whereby micelles preferentially form, leading to the surfactant release from the surface of nanocrystal(s) and thus loss of colloidal solubility.[51]

2.3. Environmental Applications: Sorption and Separation

For sorption technologies, nanomaterials provide extremely large surface areas and novel reactivity for a number of aqueous contaminants.[71-72] Further, organic-inorganic hybrid nano composites, such as organic coated nanomaterials, have gained attention as potential next generation nanoscale sorbents as they can be molecularly tuned with multi-functionality.[33-35] For example, magnetic separation and pollutant removal can achieved via magnetic inorganic materials which can be surface modified to further enhance sorption capacities and colloidal stabilities.[37, 66, 73] With regard to the organically surface modification, a range of materials have been proposed, including, clays, oil palm, charcoal, and zeolite to increase the sorption affinity for target contaminants.[74-77] Celis et al. and Lagadic et al. demonstrated that organic ligands with thiol functional groups coated on clays are effective for heavy metal adsorption.[76-77] Nomanbhay et al. coated oil palm-based charcoal using chitosan to remove Cr(VI) from industrial wastewaters.[75] Kumar et al. prepared hexadecyltrimethylammonium bromide and tetramethylammonium bromide coated zeolites to increase adsorption capacities, kinetics, and selectivity for arsenic and chromium.[74]

The detection and remediation of heavy metals and metalloids have received interest due to the regulatory requirements (i.e. human health concerns) at relatively low concentrations.[78-92] Towards this, multifunctional organic-inorganic nano composite materials have been recently

demonstrated and show considerable potential. Organic-inorganic nano sorbent, have been demonstrated for a number of inorganic cores including silica as the surface can be easily (organically) functionalized. Brown et al.,[93] Yoshitake et al.,[94] and Lu et al.[95] functionalized thiol, amino, and amine group on the surface of silica nanoparticle, respectively. The organically encapsulated silica nanoparticles showed excellent adsorption performance for heavy metals (Hg(II), Cd(II)) and metalloid (As(V)).[93-95] Magnetic nanoparticles were used inorganic nano-platforms for a number of organic coating materials, including decanoic acid,[92] sodium dodecyle sulphate,[91] cetylpyridinium bromide,[90] 3-mercaptopropionic acid,[89] 3-mercaptopropyl trimethoxysilane,[88] 3-(2-aminoethylamino) propyltrimethoxysilane,[87] Dithizone,[86] Schiff base,[85] zincon,[84] Bismuthiol,[83] 3-(trimethoxysilyl)-1-propantiol, 2-amino-5-mercapto-1,3,4-thiadiazole,[82] Polyethylenimine,[81] and 1,5-diphenylcarbazide.[80] Further, researchers have demonstrated effective magnetic separation with these and other materials.[81, 96-98] Takafuji et al. embedded poly(1-vinylimidazole) with a trimethoxysilyl terminal group on the nanoscale maghemite particles to remove the Cu(II), Ni(II), and Co(II),[98] which demonstrated selective adsorption performance for divalent metal ions. Specific affinity for heavy metal contaminants (Pb, Cu, Hg, Ag, Cd, Co, and Ti) was explored by Warner et al. using a series of organically coated magnetite nanocrystals.[96] Pang et al. showed that polyethylenimine grafted magnetic porous adsorbent have a preferential sorption performance for Cu(II), Zn(II), and Cd(II).[81] Wang et al. modified the surface of magnetite using rhodamine hydrazide and verified the excellent Hg (II) selectivity over other metal ions.[97] Organic coating(s) also increases the colloidal stability and thus maintains material the surface area in water.[45, 99-101] Yavuz et al. and Mayo et al. showed surface area dependent arsenite and arsenate sorption using colloidal stable oleic acid bilayer magnetite nanocrystals.[100] Yantasee et al. demonstrated that dimercaptosuccinic acid

surface coatings on iron oxide nanocrystals increased affinity for arsenic.[99] Feng et al. presented that surfactant (ascorbic acid) on iron oxide nanocrystal not only improved dispersity of the nanocrystal in water but also prevented dissolution of iron oxide in arsenic sorption experiments.[101] Lee et al. showed that oleyl phosphate (OP) coatings have extremely high affinity for uranyl ions.[45]

2.4 Aggregation and Deposition of Nanoparticles

In natural waters, nanoparticles have the potential to be transported, while the surface of nanoparticles may be affected by natural organic matter (NOM) among other aqueous constituents.[17] Further, such interactions and coatings are inevitable irrespective of the composition and origin of nanoparticles. For this, aggregation potential typically decreases in the presence of NOM, while reactivity, toxicity, persistence (dissolution), and fate/transport (mobility) can also be affected.[102-106] With NOM surface modification/attachment, aggregation behaviors of nanoparticles vary and have been described by extended Derjaguin, Landau, Verwey, and Overbeek (XDLVO) interactions including osmotic and elastic-steric repulsion forces.[11, 28-30 107-110] Johnson et al. demonstrated that stability of nano zero valent iron (nZVI) significantly increased in the presence of NOM as NOM adsorbed on the surface of nZVI reducing the attachment coefficient.[108] Pelley and Tufenkji showed that Suwannee River humic acid (SRHA) encapsulated latex NPs, lowering attachment efficiency due to steric stabilization.[107] Hyung et al. demonstrated that multi-welled carbon nanotubes were colloidally stable in the presence of NOM.[110]

Organic coatings also play an important role in the deposition of nanoparticles. Franchi and O'Melia demonstrated that humic acid reduced deposition of latex colloids and enhanced re-entrainment of deposited particles at secondary minima, which are (more) susceptible to flow

dynamics.[111]   Phenrat et al. developed an attachment efficiency model equation for organic matter encapsulated nanoparticles; the model equates increasing attachment efficiencies with increasing flow velocity,[112] which was different than previous model frameworks (in the absence of NOM) developed by Elimelech,[113] and Bai and Tien.[114-115]

2.4.1. Particle Interaction Energies

Interaction energies for classic particle aggregation was developed by Derjaguin, Landau, Verwey, and Overbeek (DLVO), whereby two kinds of energies are considered; van der Waals (vdW) attraction and electrical double layer (EDL) repulsion,[116] which are taken together as a summation of interactions. Since, additional energies having also be considered for soft materials as part of extend DLVO (XDLVO) energy consideration. With organic coatings, the role of XDLVO energy of nanoparticles can be significant.[36]

van der Waals Interaction

The vdW interactions originate from the dispersion forces between atoms (here constituting particles).[117]   Dispersion interactions is divided by three different types; Debye interactions, Keesom interactions, and London interactions.[118]   The vdW interaction is not always attractive. For example, carbon-water-Teflon system and carbon-butanol-Teflon systems actually have net vdW repulsion.[119]   However, most of vdW interactions in aqueous phase is attraction. There are two different approaches for describing vdW attractive forces. One is Hamaker's microscopic approach and the other is Lifshitz's macroscopic approach. The Hamaker approach is based on the pair wise summation of inter molecular interactions.[120] Hamaker expressed vdW intraction by summing the all of interactions of molecules in one particle with all of the molecules in the other particle. This approach can thus express vdW interaction as a simple equation, which is composed of Hamaker constant with appropriate geometries in the equation. The dispersion

force is electromagnetic which requires a finite time to travel in the medium. This results in decrease of vdW interaction that is referred retardation. Hamaker's approach is needed to correct the retardation.[121] Gregory made simple empirical factor for ideal spherical particles.[122] However, this simple correlation factor is inaccurate for long separation distances. vdW interaction, however, is negligible at long separation distance. Lifshitz expressed the vdW interaction based on the quantum electrodynamics which implicitly accounts for retardation effects.[123] Since Lifshitz's macroscopic approach is mathematically limited (complicated), Hamaker's approach is widely used for practical purposes.[119]

Electric Double Layer Interactions
EDL interactions originate from overlap of geometrically opposed electrical double layers.[124] The magnitude of EDL interaction is depended on thickness of diffuse layer (Debye screening length), which is reciprocal of the Debye-Hückel parameter.[125] Debye-Hückel parameter increases with increasing ionic strength and valence of ions, and vice versa. Thus, EDL interactions are effectively reduced as the ionic strength and valence of ions increase.[126]

Various expressions for EDL interaction energies have been developed based on several assumptions. Gouy-Chapman developed EDL model based on the four assumptions 1) infinite, flat and impenetrable interface 2) ions are point charges (no volume) 3) the surface charge and potential are uniformly smeared out over the surface 4) the properties of medium is constant.[127] These assumptions give charge density and potential relationship (Poission equation). The distribution of anions and cations is derived and expressed on the assumption of zero gradient of the electrochemical potential (Boltzmann equation).[128] The combined Poission-Boltzmann equation can be simplified by a Taylor series expansion when electrolyte solution considered with symmetrical electrolytes (Z-Z).[129]

The Stern-Grahame model applies finite size of ions of the solution to overcome the draw backs of Gouy-Chapman model.[130-131] The main refinements of Stern-Grahame models affect short range potentials (ca. within 0.3 nm from the surface).[119] In the Stern-Grahame model, electrostatic double layer consists of Stern and diffuse (Gouy) layers. The Stern layer is divided by the inner Helmholtz layer (inner sphere complex) and outer Helmholtz layer (outer sphere complex). The difference of inner and outer Helmholtz layer is hydration of adsorbed ions – un-hydrated ions occupy the Inner Helmholtz layer.[130-131] In addition, the Stern-Grahame model incorporates variation of dielectric permittivities. The permittivity of medium can significantly decrease at a charged surface due to (high) field strengths. The values of relative permittivity of water at diffuse layer, outer and inner Helmholtz layer are 78, 32 and 6, respectively.

The surface potential is not usually directly measurable and changes via overlapping EDL. Thus, boundary condition of both Gouy-Chapman and Stern-Grahame model approaches are limited.[132-133] To overcome this limitation, three different approximations have been developed. First assumption is the constant potential assumption (CPA).[134] In this assumption, surface potential remains constant but surface charge changes when EDL is overlapped. Second assumption is the constant surface charge assumption (CCA),[135] whereby the surface charge remains constant but surface potential is changed (dynamic). These two assumptions are extreme cases that lead overestimation (CCA) and underestimation (CPA). To overcome drawbacks of CCA and CPA, linear superposition approximations (LSA) were developed.[136] These approximations are useful compromises between CCA and CPA by calculation total potential as sum of each potential of surfaces. The LSA shows intermediate value between CCA and CPA at short separation (< 3 nm).[119]

Born Repulsion

15

Born repulsion is originated from the strong repulsive force between atoms due to interpenetration of their electron shells.[137] Lennard-Jones m-n potential is widely used to consider the born repulsion.[138] In water phase, born repulsion is not typically considered due to the hydration of surface and inherently low momentum scenarios.[119]

Hydration Effects

The hydration effects originate from the hydration of ions and surface(s) of materials. The hydration effect is typically a repulsive force. For approaching materials, release of water molecules is necessary, meaning that additional energy is required.[139] Generally, the range of hydration effect on is 3 - 4 nm. The hydration effect is significant at high ionic strength conditions.[119]

Hydrophobic (Lewis acid-base) Attraction

Truly hydrophobic surfaces having no polar, ionic group, or hydrogen binding sites which effectively lower favorable interactions with water molecules.[140] In contrast with other extended DLVO interaction, hydrophobic attraction is a long range interaction (up to 80 nm) and decays exponentially at a separation rage from 20 to 60 nm.[119] Hydrophobic materials, such as C_{60} or carbon nanotube (CNT), have a strong hydrophobic interaction, resulting in aggregation.

Magnetic Attraction

Under ambient conditions, relevant magnetic properties are typically found for transition metals and metal oxides.[141] For example, zero-valent iron and magnetite materials have long range magnetic attraction that induces rapid aggregation.[142-143] However, research regarding magnetic attraction with regard to aggregation at the nanoscale is unclear. Only a few experimental observations have been reported considering magnetic attraction (in the case of zero-valent iron).[144]

Elastic-Steric Repulsion

The elastic-steric repulsion is originated from the 'soft' surface coatings, typically organic.[39, 145] When organic coated particles interact, organic coating layer can actually overlap (interpenetrate) each other and compresses the organic layer.[146] The elastic-steric repulsion is a kind of physical hindrance, effecting only below the range of organic coating layer length.[39, 145]

Osmotic repulsion

The concept of osmotic pressure differences between bulk solution and interfacial layers was first reported by Langmuir.[147] With organic coating, the surface of organic coated particle has low osmotic pressure compared to the osmotic pressure of the bulk solution. The osmotic pressure difference leads to transport of water molecules from low to high osmotic pressure points, resulting in osmotic pressure repulsion.[148] The range of osmotic repulsion is typically considered as ca. two times of the length of organic coating layer.[39, 145]

2.4.2. Aggregation of Nanoparticles

Interaction Energy for Aggregation

To describe the interaction energy for particle aggregation, sphere-sphere geometrical factor was developed by Derjaguin.[149] Derjaguin assumes that radius of approaching particle is large enough with separation distance. Using the Chord theorem, plate-plate interaction can be changed to sphere-sphere interaction with simple geometric factor.[150]

Collision Theory for Aggregation

Particle collision theory is based on the Smoluchowski's (1917) approach with two assumptions.[151] One is that aggregation is a second order reaction and the other is only two colliding species aggregation (i.e. three or higher body collisions are neglect). There are three different collision mechanisms: (1) Brownian diffusion (perikinetic aggregation), (2) fluid motion (orthokinetic aggregation), and (3) differential settling. Nanoparticles are randomly

move via Brownian motion, resulting in perikinetic aggregation behavior. Also, nanoparticles aggregate under stirring condition by fluid motion (high sheer force) leading to orthokinetic aggregation. Differential sedimentation happens when settling velocity of nanoparticles is different relative to each other.[152]

Attachment Efficiency for Aggregation
Every event approach does not result in successful particle-particle attachment when there is an effective energy barrier between nanoparticles. Thus, attachment efficiency concept is applied. The stability ratio (W) is used can be determined by dividing fast aggregation rate constant (100% favorable) with the observed aggregation rate constant. The reciprocal of stability ratio is attachment efficiency (Equation 2.1).[153]

$$W = \frac{k_{11,fast}}{k_{11,slow}} = \frac{1}{\alpha} \qquad \text{(Equation 2.1)}$$

Where, k_{11fast} and k_{11slow} are fast and slow aggregation rate constants for very early stage of aggregation, respectively. Generally, stability of nanoparticles is reduced with increasing ionic strength, finally reaching the critical coagulation concentration (CCC) which the minimum ionic strength for reaching an attachment efficiency of one. Above the CCC (referred to as diffusion (transport) limited zone), attachment efficiency is nearly constant regardless of ionic strength. On the other hand, below the CCC (called the reaction limited zone), attachment efficiency is a function of ionic strength.[154]

2.4.3. Deposition of Nanoparticles

Interaction Energy for Deposition
For deposition processes, sphere-sphere interactions can be reconsidered as plate-sphere interactions by defining the radius of one of colloidal particle is infinite.[119]

18

Colloidal Filtration Theory

Colloid filtration theory, expanded from collision theory (above), is widely used for describing transport of particles in saturated porous media (i.e. model groundwater flow) was originally developed by Yao et al. (Equation 2.2).[155]

$$\frac{C_e}{C_0} = \exp(-\frac{3}{2}\frac{(1-\theta)}{d_c}\eta_0\alpha L) \qquad \text{(Equation 2.2)}$$

Where, d_c is the diameter of the sand, θ is the porosity of the sand, L is the length of column, ε is the porosity of the sand, C_e and C_0 are the effluent and influent concentrations of particles, respectively. And η_0 is the single collector efficiency, which represents ratio of the rate particles strike a collector to the rate particles flow toward the collector. This relationship was derived based on the assumption that porous media is an assemblage of isolated spheres. Further, Yao et al. developed the single collector efficiency by considering main three different transport term; diffusion, interception, and sedimentation. However, single collector efficiency developed by Yao et al. has been observed to have discrepancies with regard to experimental data. To overcome this difference, Rajagopalan and Tien adapted pore space geometry, called Happel's sphere-in-cell model (Happel, 1958), in the diffusion term.[156-157] They modified the single collector efficiency by considering an additional dimensionless term, which is related to the London-van der Walls attraction forces of particles.[157] Tufenkji and Elimelech further modified and improved the Rajagopalan and Tien equation by considering van der Waals number characterizing ratio of van der Waals interaction energy to the thermal energy of particle.[158]

Attachment Efficiency for Deposition

Attachment (collision) efficiency for deposition of nanoparticles is defined as the ratio of the actual deposition rate to the deposition rate under favorable condition (absence of the energy barrier).[159] Prediction models for attachment efficiency has been explored by a number of

19

groups, including Elimelech's.[160] He considers electrostatic double layer (EDL) repulsion, (i.e.,

Debye parameter, electrical surface potential) and van der Waals attraction (i.e., Hamaker

constant). Attachment efficiency of this model is constant regardless of fluid velocity.

Hydrodynamic interactions can affect the release of attached nanoparticles and the torque applied

to the particles, which includes lift and drag forces. In case of the nanoparticle, the lifting force

is negligible comparing to the drag force. Thus torque applied to the nanoparticle is governed by

drag force.[102] Bai and Tien also proposed a predictive framework for attachment efficiency.[114-115] They considered the effects of hydrodynamic interaction via London number. In the Bain ad

Tien prediction, attachment efficiency decreases as a function of fluid velocity due to release of

detached nanoparticle via hydrodynamic interactions. Recently, Phenrat et al. developed

attachment efficiency equation when particles were coated with organic matter or polymer.[112]

Phenrat et al. added dimensionless layer-electrokinetic parameter, considering effect of organic

matter. This empirical model presents increasing attachment efficiency with increasing flow

velocities.

2.5 Forward Osmosis
2.5.1. History of Draw Solutes
Development of ideal draw solutes is a significant issue for feasible application of forward

osmosis (FO) systems for water treatment. Ideal draw solutions should be highly soluble, non

toxic, and non reactive with the separating membrane.[161] Cost effectiveness is also primary

factor for selecting an ideal draw solute as well. In addition, a draw solute properties should

limit of reverse diffusion, which promotes not only loss of draw solute but also significant water

flux decline due to the concentration polarization.[162]

Historically, four different types of draw solute have been developed and applied as a potential draw solution.[163] The first draw solute type is a gas (with volatile compounds), such as ammonia and carbon dioxide,[164] sulfur dioxide,[165] mixture of sulfur dioxide and aliphatic alcohols,[166] ammonium bicarbonate,[167] and mixtures of carbon dioxide and tertiary amines.[168] The gas and volatile compounds can be removed and regenerated by heating and/or air stripping, but these systems are expensive to install and operation cost is inefficient.[163] In addition, reverse diffusion is inevitable due to the small molecular weight of gas and volatile compounds.[169] The second draw solute type is inorganic salts dissolved in water. Sodium chloride (NaCl) is widely used as a draw solute because of its high solubility and osmotic pressure.[170-172] However, sodium chloride (NaCl) has been used for only purpose of specific research such as evaluation of FO membrane performance,[170] and comparing the fouling[171] and rejection[172] behaviors between reverse osmosis (RO) and FO system. For the possible inorganic draw solute, precipitable salt (aluminum sulfate) was suggested by Frank (1972).[173] The salt removal by precipitation requires several complex processes. Early 2010, divalent ion salts, such as $CaCl_2$, $MaCl_2$, $MgSO_4$, and Na_2SO_4 were proposed.[174] For these it was proposed that divalent cation salts have enough osmotic pressure and solubility. Additionally, divalent cation salts can be reusable via using ultrafiltration (UF) and/or nanofiltration (NF). Comparing to the monovalent cation, reverse diffusion of divalent cation in FO system is low, however small amount of divalent cation leads to significant fouling at the membrane surface.[175]

The third draw solute type is organic solutes, such as ethylenediaminetetraacetic acid (EDTA) sodium salts,[176] poly (aspartic acid sodium salt) (PAspNa),[177] and dendrimers.[178] Due to their large molecular sizes, reverse diffusion is limited and recovery of organic solute can be achieved by UF and/or NF. Also, as a part of organic draw solute, non toxic, green draw solutes

21

(i.e. glucose, sucrose, or fructose) was proposed,[179-181] and commercially applied in U.S army[182] and National Aeronautics and Space Administration (NASA).[183] The last draw solute type is nanoparticle suspensions. A major advantage for NP suspensions is that the reverse diffusion of nano sized materials is negligible due to their size.[163] Several nanomaterials have been developed and suggested such as hydrophilic nanoparticles[184] and citrate-coated carbon quantum dots.[185] The nano draw solute could be separated and regenerated by UF or membrane distillation (MD).

As an alternative method for draw solute recovery system (and fouling management), magnetic separation has been recently gained attraction.[163] Among the magnetic nanoparticles (MNPs), iron oxide nanocrystals (IONCs),, are promising due to its environmentally input abundance,[186] cost, and relatively low toxicity property.[187] Consequently, iron oxide nanoparticles have been suggested and applied as a draw solute; however, while magnetic separation was achieved, severe aggregation leads to significant flux decline. To overcome aggregation of IONCs, organic coated IONCs have been proposed. An organic surface coating provides osmotic and elastic-steric repulsion as well as electrostatic double layer (EDL) repulsion.[36-39] Triethylene glycol,[188-189] polyacrylic acid,[40] poly sodium acrylate,[190] poly(N-isopropylacrylamide),[191] polyglycerol,[192] dextran,[193] citrate,[194] and poly(ethylene glycol)diacid[195] were used as coating agents. Comparing to the non-coated IONCs, organic functionalized IONCs showed higher colloidal stability; however, eventual aggregation and IONCs adsorption on membrane surface still decreased the water flux.

Chapter 3: Engineered Superparamagnetic Nanomaterials for Arsenic (V) and Chromium (VI) Sorption and Separation: Quantifying the Role of Organic Surface Coatings

3.1. Overview

Inorganic-organic nanoscale materials have recently received significant interest as tunable, next generation, sorbents for the separation of metal and metalloid contaminants, including arsenic (As) and chromium (Cr), among others. In this work, we have designed and synthesized IONCs coated with specific functionalized organic materials with the goal of variable explicit evaluation. Specifically, single domain, superparamagnetic, monodisperse IONCs were synthesized and transferred into water via surface functionalization by ligand exchange and encapsulation methods. As synthesized, hybrid materials showed high performance for both As(V) and Cr(VI) sorption when nanocrystals are coated with positively charged organic surface coatings such as, polyethyleneimine (PEI) and cetyltrimethylammonium bromide (CTAB). IONC cores coated with negatively charged organic coating materials (polyethyleneglycol (PEG), oleic acid (OA), sodium dodecyl sulfate (SDS)) and silica (SiO_2) demonstrated significantly lower sorption capacities. When silica coated IONCs ($Fe_3O_4@SiO_2$, core-shell materials) were surface coated with PEI, sorption capacities for As(V) and Cr(VI) of $Fe_3O_4@SiO_2@PEI$ are comparable to $Fe_3O_4@PEI$, underscoring the importance of surface coating functionality. To complement these

studies, real-time sorption behavior of As(V) and Cr(VI) with PEI was explored by quartz crystal microbalance with dissipation (QCM-D).

3.2. Introduction

U.S. drinking water regulations require treated water to meet metals/metalloid standards, including arsenic and chromium. To meet these standards, a number of techniques are applied, such as membrane filtration, ion exchange, sorption, and photocatalytic reduction.[197-201] In line with rapid expansion and application of material science and nanoscale engineering over the last few decades, water treatment technologies have experienced significant advancements.[71-72] With regard to nanoscale materials specifically designed for the sorption, and thus removal, of dissolved inorganic contaminants, a number of materials have been proposed and demonstrated, including engineered carbon-, mineral-, metal-, metal oxide-, and polymeric-based structures.[72, 202-206] For metal oxide-based technologies, iron oxides have been the most heavily evaluated for the treatment of metals and metalloids, including arsenic and chromium due to magnetic properties for separation and high affinity for sorption.[207-210] Generally, inorganic (metal- and metal oxide-) based sorbents have rigid core structures with controllable geometries and surface-based organic coatings with tunable functional groups for selective contaminant affinity and aqueous stability, among other desired properties.[33-35] Surface coated materials provide large (extended) surface areas as well as improved colloidal stability of the nanocrystals (NCs) in water. To date, the majority of previous reports have demonstrated negatively charged surfactant coated inorganic composite materials.[96, 99-101] As an example, Yavuz et al. showed surface area dependent arsenite and arsenate sorption using colloidal stable oleic acid bilayer IONCs.[100] Feng et al. reported that surface coating agents (e.g. ascorbic acid) not only improved stability of the nanocrystal(NC) in water but also hindered dissolution of the iron oxide nanocrystal (IONC)

core during As(III) and As(V) sorption.[101] Yantasee et al. demonstrated that dimercaptosuccinic acid surface coatings on IONCs increased affinities for metals and metalloids (Hg (II), Ag (I), Pb (II), Cd (II), and As (III)).[99] Warner et al. reported excellent heavy metal sorption performance with a series of ligand-based surface functionalization of IONCs.[96] Despite these reports, the role of organic surfactant is still largely unclear from a mechanistic perspective; there is currently a direct need for a systematic approach in terms of surface structure/species, charge, grafting density, and solution pH, allowing for the deconvolution and ultimate optimization of key material properties.

In this work, we describe the critical role of organic surface coatings with regard to the sorption of As(V) and Cr(VI) by iron oxide nanocrystals (IONCs) core materials. For this we quantitatively explored the role's core particle size, ligand density, and modified surface chemistries. Positively charged, amine-based, surface coated IONCs (IONCs coated with polyethyleneimine (Fe_3O_4@PEI) and cetyltrimethylammonium bromide (Fe_3O_4@CTAB)) demonstrate high sorption capacities compared with negatively charged and control surfaces (with no organic surface coating). As(V) and Cr(VI) sorption properties for the PEI coated nanocrystal system were further explored using silica coated iron oxide (Fe_3O_4@SiO_2) materials to delineate the role(s) of PEI vs. core surface processes. Finally, fast and irreversible As(V) and Cr(VI) sorption behaviors (kinetics and extent) for PEI coatings were explored using a novel quartz crystal microbalance-based technique.

3.3. Results and discussion

3.3.1. Synthesis and Surface Functionalization of Iron Oxide Nanocrystals

Monodisperse IONCs were synthesized via iron carboxylate decomposition in the presence of oleic acid at 320 °C.[42, 211] The size and shape of IONCs, as measured by TEM, were precisely

controlled through the ratio of iron precursor (FeOOH) to oleic acid (OA), concentration of the

mixture of FeOOH and OA; and/or reaction time (Figure 3.1, Figure 3.S1 in the supporting

information) - resulting in a library of spherical particles with diameters from 8 to 25 nm.[212] Size

distributions are presented in Figure 3.S2 in the supporting information. Resulting NCs were

highly stable without visible precipitation in hexane for over one year. As shown in Figure 3.2

(a), the crystalline structure of synthesized IONCs matches magnetite (Fe_3O_4) (JCPDS Card #

190629), which is consistent with previous reports by our group and others.[100, 213]
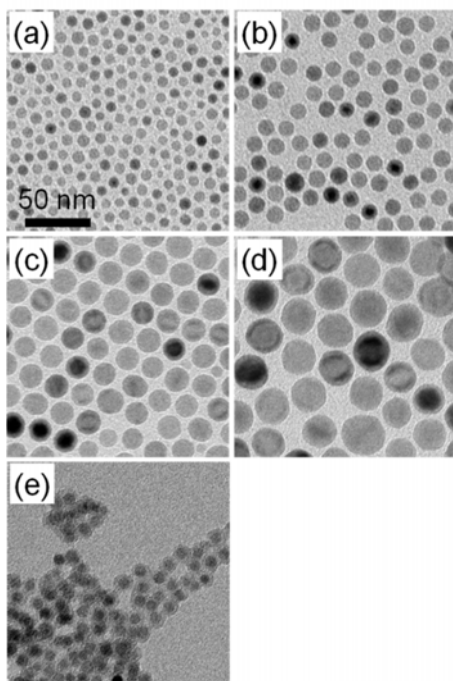
Figure 3.1 TEM images of monodisperse iron oxide (Fe_3O_4) NCs. Average diameter of Fe_3O_4
NCs was measured using Image-Pro 6.0 with over a thousand crystals counted; (a) 7.9 ± 0.9 nm,
(b) 12.3 ± 1.0 nm, (c) 18.7 ± 1.0 nm, (d) 24.8 ± 1.4 nm. (e) Silica coated 7.9 nm IONCs.

Synthesized iron oxides were phase transferred from organic solvent into water through

both ligand encapsulation and exchange methods.[65, 213] Simple addition of hydrophilic

polymer(s), such as polyethylenimine (PEI) and polyethylene glycol (PEG) to the IONC in

hexane replaces the surface associated hydrophobic organic acid (here as oleic acid), resulting in

a single layered structure on the surface of the NC (termed ligand exchange). For ligand addition methods, the hydrophobic tail of the secondary ligand interacts with the first layer's hydrophobic tail (here as oleic acid), to effectively form a bilayer coating.[45] Bilayer structures were systematically varied with varied outer layers (hydrophilic region facing outward) including, oleic acid (OA), cetyltrimethylammonium bromide (CTAB), and sodium dodecyl sulfate (SDS).[40, 51] For both ligand encapsulation and exchange methods, IONCs, synthesized in an organic solvent were successfully phase transferred from organic solvent to water with >70% phase transfer efficiency.

Phase transferred NCs were characterized by dynamic light scatter (DLS) to measure hydrodynamic diameter (D_H) and surface zeta potential. As shown in Figure 3.2 (b), D_H of the bilayer structure of IONC (coated with CTAB, OA, and SDS) is smaller than that of monolayer IONCs (coated with PEG and PEI); D_H for CTAB, OA, SDS, PEG (MW = 2000) and PEI (MW = 25000) coated IONC were 26.2, 24.7, 24.4, 34.5 and 45.3 nm, respectively. Additionally, D_H of NCs increased as a function of IONC size (when the NC was treated with the same surface stabilizer); D_H of 8, 12, 19 and 25 nm IONC coated with CTAB was 22.7, 26.2, 31.4 and 33.8 nm, respectively. Surface charge of the phase transferred IONC was observed via zeta potential measurement, shown in Figure 3.2 (c). CTAB, OA, SDS, PEG and PEI coated IONC had zeta potentials of 26.7, -29.6, -31.2, -5.6 and 39.1 mV, respectively. The (inorganic) core size of IONC did not significantly affect the surface charge when IONC was coated with the same surface stabilizer (CTAB); zeta potential values were 28.7, 26.7, 29.0 and 30.1 mV for the 8, 12, 19 and 25 nm IONC coated with CTAB (Figure 3.2 (c)).

Figure 3.2 (d) shows the number of organic molecules per nanocrystal (NC) as measured by total organic carbon (TOC). For 12 nm IONCs, surfactant loadings for CTAB, OA, SDS,

PEG and PEI were ca. 4,600, 7,100, 6,900, 3,100 and 200 molecules per NC, respectively. As expected, larger molecular weight surface stabilizers, such as PEG and PEI, have higher associated mass (normalized to particle surface area) than ligands encapsulation materials, such as OA, SDS, and CTAB (Table 3.S1). Interestingly, surfactant loading increased with the size of IONC, when stabilized with the same surface coating (CTAB); surfactant loadings on 8, 12, 19 and 25 nm IONC were ca. 800, 4,600, 26,400 and 102,600 molecules per NC, respectively. We hypothesize that as the core NC size is increased a more dense surfactant (CTBA) layer is allowed based on relaxed steric hindrance (relatively less core curvature), as observed by others.[214-215] Additionally, van der Waals attraction energy is proportional to size of NCs, thus larger particles may require thicker organic loading.[69, 119]
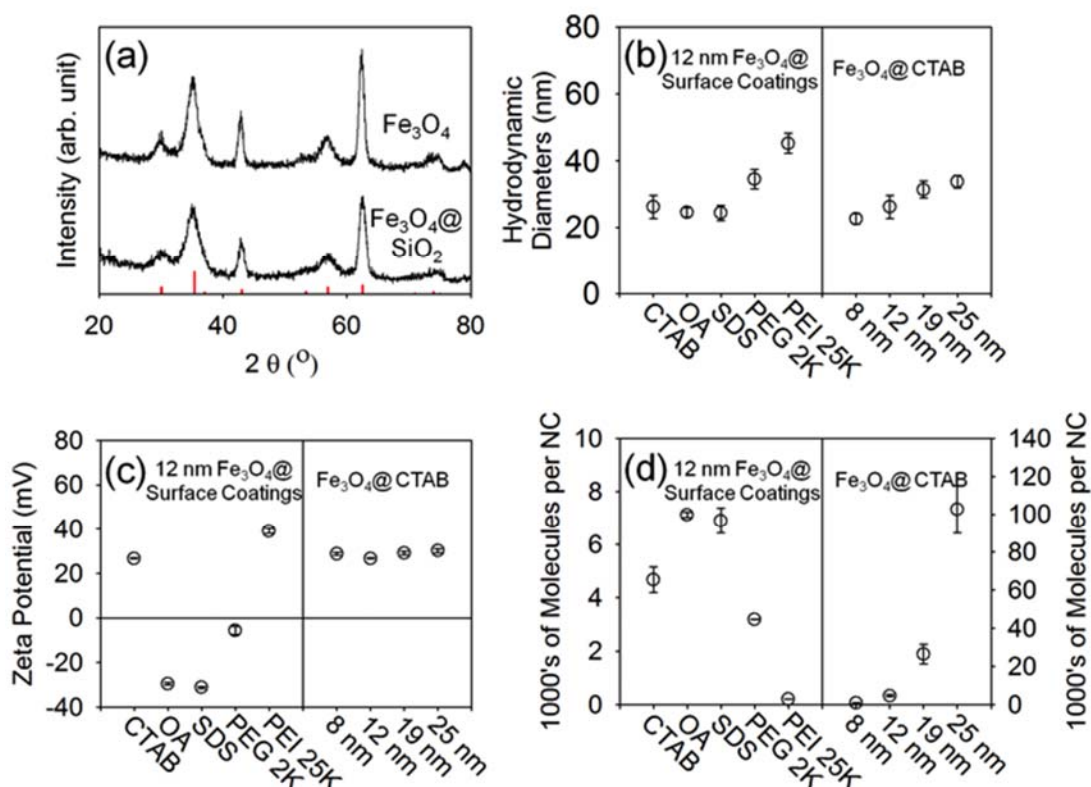
Figure 3.2 Characterization of the engineered iron oxide (Fe_3O_4) coated with various surface stabilizers. (a) X-ray diffraction (XRD) data of Fe_3O_4 NCs and silica coated Fe_3O_4 NCs

(Fe$_3$O$_4$@SiO$_2$). Diffraction patterns were well matched with magnetite (Fe$_3$O$_4$) crystalline structure (JCPDS Card # 190629) and broad XRD patterns (20° to 30°) of silica coated magnetite NCs indicate that the silica shell was amorphous. (b-d) Water disperse magnetite NCs were characterized. 12 nm magnetite NCs were functionalized with series of surfactant (cetyl trimethylammonium bromide (CTAB), oleic acid (OA), sodium dodecyl sulfate (SDS), polyethylene glycol (PEG) and polyethylenimine (PEI)) and four different sized, Fe$_3$O$_4$ NCs were stabilized with CTAB; (b) hydrodynamic diameters at pH 7, (c) zeta potential at pH 7, (d) number of organic molecules loaded on the NC surface.

3.3.2. Discerning the Roles of Surface Functional Group and Size of Iron Oxide Nanocrystals as Sorbents

Pentavalent arsenic (As(V)) and hexavalent chromium (Cr(VI)) largely exist as anions over a wide range of pH (above pH 2.2),[216] and are thus expected to preferentially associate with oppositely charged (positively) surfaces. Functional group dependent As(V) and Cr(VI) sorption was evaluated at pH 7 using IONC stabilized with various surface stabilizers including, OA with a negatively charged carboxyl ending, SDS with a negatively charged, sulfate terminal group, PEG with hydroxyl functional groups within the polymer chain, CTAB with a positively charged methyl ammonium terminal group, and PEI with amine functional groups (primary, secondary and tertiary amines). Dominant species for As(V) and Cr(VI) at pH7 are H$_2$AsO$_4^-$, HAsO$_4^{2-}$ and CrO$_4^{2-}$, respectively.[216-217] As shown in Figure 3.3, net positively charged IONC stabilized by PEI and CTAB (Fe$_3$O$_4$@PEI and Fe$_3$O$_4$@CTAB) showed significantly enhanced sorption performance compared to negatively charged nanocrystals coated with OA, SDS, and PEG. The maximum sorption capacity towards As(V) and Cr(VI) was 98 ± 9.0 mg As g^{-1} NC^{-1} and 154 ± 8.9 mg Cr g^{-1} NC^{-1} for Fe$_3$O$_4$@PEI, and 44 ± 2.8 mg As g^{-1} NC^{-1} and 103 ± 4.6 mg Cr g^{-1} NC^{-1} for Fe$_3$O$_4$@CTAB. In contrast, negatively charged NCs had considerably lower sorption affinity for both As(V) and Cr(VI) - sorption capacity values for OA, SDS and PEG coated NCs (Fe$_3$O$_4$@OA, Fe$_3$O$_4$@SDS, and Fe$_3$O$_4$@PEG) were below 14 mg As g^{-1} NC^{-1} and 30 mg Cr g^{-1} NC^{-1}. The colloidal stability did not significantly affect the sorption performance as all of the

NCs maintained their initial hydrodynamic diameters except for Fe_3O_4@OA (Figure 3.S3 in the supporting information). Similar to others, we speculate that amine groups at the surface for PEI and CTAB coatings are key binding sites for anionic As(V) and Cr(VI).[218-219] Interestingly, there was little difference in sorption efficiency between Fe_3O_4@PEI and Fe_3O_4@CTAB despite the fact that Fe_3O_4@PEI has over 25 times more amine groups than Fe_3O_4@CTAB, implicating the role of steric hindrance, which is likely related to the internally branched structure of PEI, for these sorption processes (Fe_3O_4@PEI had an average of ca. 118,500 amine groups per NC while Fe_3O_4@CTAB averaged ca. 4,500 amine groups per NC).[220]
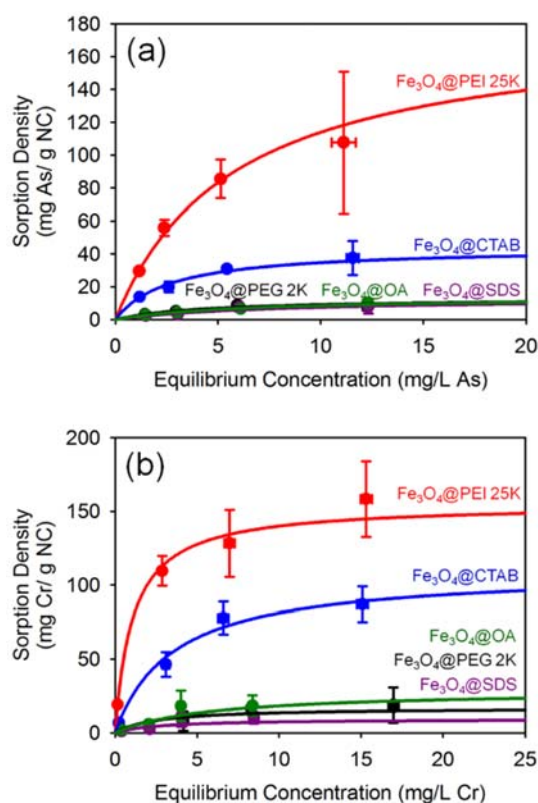
Figure 3.3 Arsenic (a) and chromium (b) sorption isotherm on 12 nm Fe_3O_4 NCs coated with positively charged surface stabilizer (PEI (red) and CTAB (blue)) as well as negatively charged organic coating (OA (green), SDS (purple) and PEG (black)). Dot plots with error bars and line plots present experiment measurement values with standard deviations and Langmuir isotherm fittings, respectively.

Nanocrystal size was also considered as a key material variable for sorption performance. Here, four different sizes of IONC (8, 12, 19 and 25 nm), coated with CTAB, were evaluated for As(V) and Cr(VI) sorption at pH 7. Considering the standard deviations of the maximum sorption densities, sorption performance similar for all sizes evaluated (Figure 3.4). The maximum sorption density for 8, 12, 19 and 25 nm IONC was 56 ± 3.3, 44 ± 2.8, 45 ± 2.8 and 43 ± 1.9 mg g^{-1} NC^{-1}, respectively for As(V) and 96 ± 7.0, 103 ± 4.6, 97 ± 7.7 and 90 ± 2.2 mg g^{-1} NC^{-1}, respectively for Cr(VI). This is likely due to an effective tradeoff due to higher mass loading of CTAB per surface area for larger particles. In other words, the surface area advantage of smaller particles is negated due to lower sorption densities of functional ligands. The number of CTAB molecules of 25 nm Fe_3O_4@CTAB per NC was >100 times more than that of 8 nm Fe_3O_4@CTAB per NC (Table 3.S1 in the supporting information). Interestingly, the sorption capacity per number of amine groups actually decreased when size of NCs was increased, indicating an eventual maximum sorbate density per surface area, where additional amine functional groups are not sterically available.[21] Sorption capacities per surface area and per number of amine group as a function of size of NCs were presented in Figure 3.S4 and Table 3.S2 in the supporting information.
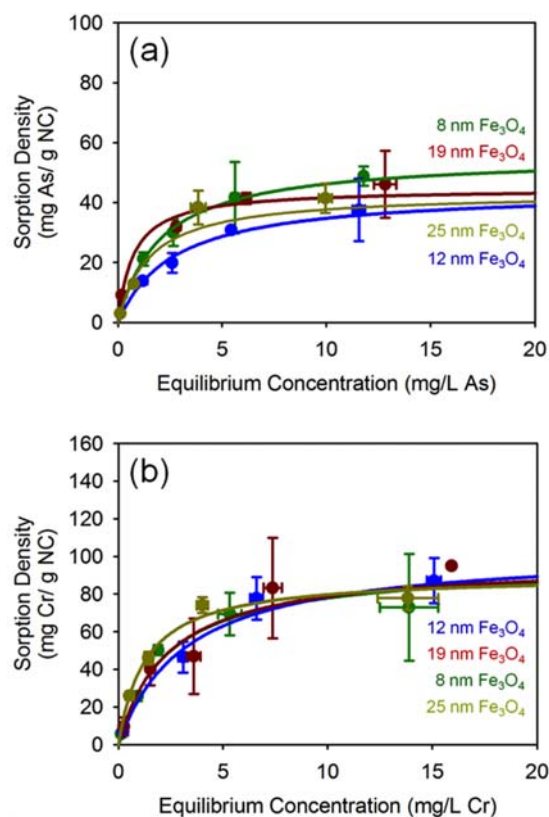
Figure 3.4 Arsenic (a) and chromium (b) sorption isotherm on four different sized (8 nm (green), 12 nm (blue), 19 nm (red) and 25 nm (yellow)) Fe_3O_4 NCs coated with the same surface stabilizer (CTAB)

3.3.3. Delineating the Role of Surface Coating(s) vs. Particle Surface

As(V) and Cr(VI) sorption performances were evaluated using silica coated iron oxide with ($Fe_3O_4@SiO_2@PEI$) and without ($Fe_3O_4@SiO_2$) PEI. $Fe_3O_4@SiO_2$ NCs were designed to evaluate the role of organic surface coating (PEI) by inhibiting sorption and reduction of contaminants on/at the surface of magnetite NCs. Resulting $Fe_3O_4@SiO_2$ NCs were observed to be monodisperse in water at pH 7. Figure 3.1 (e) shows silica coatings on the surface of Fe_3O_4 with uniform coating thickness of ca. 2 nm for 8 nm IONC cores. As shown in Figure 3.2 (a), an amorphous phase silica coating on IONC was observed with a broad XRD response from 20° to 30°.[222] Additionally, $Fe_3O_4@SiO_2$ was also functionalized with PEI encapsulation by favorable (electrostatic) interaction between hydroxyl groups of silica and amine groups of PEI.

32
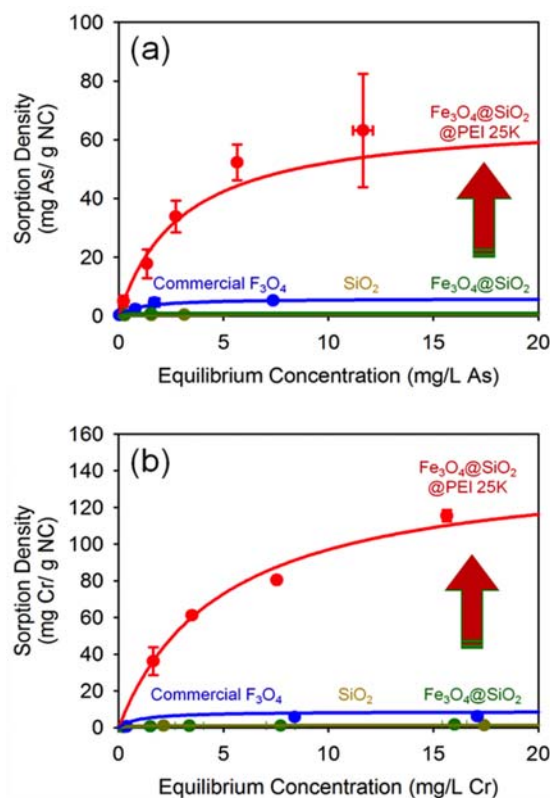
Figure 3.5 Arsenic (a) and chromium (b) sorption isotherm on PEI and silica coated 8 nm Fe_3O_4 NCs ($Fe_3O_4@SiO_2@PEI$ 25K, red), silica coated 8nm Fe_3O_4 NCs ($Fe_3O_4@SiO_2$, green), commercial iron oxide NCs (commercial Fe_3O_4, blue) and 22 nm silica NCs (SiO_2, yellow).

The role of surface coating on sorption for As(V) and Cr(VI) was evaluated using $Fe_3O_4@SiO_2$ and $Fe_3O_4@SiO_2@PEI$ via batch sorption isotherms (pH 7). As shown in Figure 3.5, sorption capacity of 8 nm $Fe_3O_4@SiO_2$ for As(V) and Cr(VI) was relatively low (1.0 ± 0.1 mg As g^{-1} NC^{-1} and 1.4 ± 0.4 mg Cr g^{-1} NC^{-1}) due to surface passivation of IONC by silica coating (maximum sorption capacity of nanocrystalline SiO_2 (d = 22 nm) for As(V) and Cr(VI) was 0.4 ± 0.1 mg As g^{-1} NC^{-1} and 1.2 ± 0.2 mg Cr g^{-1} NC^{-1}). SiO_2 coating on IONC also prevented the surface redox reactions at the surface of the IONC as shown by XPS analysis (Figure 3.S5 in the supporting information). Fe(II) composition of 8 nm $Fe_3O_4@SiO_2$ was consistent before and after As(V) and Cr(VI) sorption; the ratio of Fe (II) before sorption and after As(V) and Cr(VI) sorption was 13.7, 13.0 and 12.8%, respectively. In contrast, the sorption

33

capacity of 8 nm $Fe_3O_4@SiO_2@PEI$ is dramatically enhanced to 68 ± 4.3 mg As g^{-1} NC^{-1} and 143 ± 2.1 mg Cr g^{-1} NC^{-1}, although IONC was covered with a silica coating. This implicates positively charged polyethylenimine (PEI) coatings as primary sorption sites (via amine groups) for anion sorbates.

The role of pH was explored for As(V) and Cr(VI) sorption with 12 nm $Fe_3O_4@PEI$ at pH 5.6, 7.0, 8.5, and 11.5. For these, 12 nm $Fe_3O_4@PEI$ particles were chosen based on high sorption capacities (Figure 3.3). pH affects not only sorbate speciation (As(V) and Cr(VI)) but also particle surface charge. As(V) has three acid dissociation constants (pk$_a$: 2.2, 7.0 and 11.5);[216] As(V) becomes a monovalent anion ($H_2AsO_4^-$) or a divalent anion ($HAsO_4^{2-}$) in near pH 7. Cr(VI) is also a weak acid;[217] the monovalent anion ($HCrO_4^-$) is the dominant chemical form in weak acid and chromate becomes a divalent anion (CrO_4^{2-}) above pH 6.5.

As shown in Figure 3.S6 in the supporting information, zeta potential and hydrodynamic diameters of 12 nm $Fe_3O_4@PEI$ were measured over a wide range of pH (from 3.8 to 12.2). Zeta potential decreases with increasing pH to 11.5, which was close to point of zero charge (PZC) of 12 nm $Fe_3O_4@PEI$. NCs maintained their initial size at the PZC point due to steric repulsion of PEI coatings. As shown in Figure 3.6, the highest sorption was found at pH 5.6 for As(V) (154 ± 2.0 mg g^{-1} NC^{-1}) and at 7.0 for Cr(VI) (154 ± 8.9 mg g^{-1} NC^{-1}). The lowest sorption capacity of 19 ± 2.7 mg As g^{-1} NC^{-1} and 25 ± 3.3 mg Cr g^{-1} NC^{-1} was observed at pH 11.5. The maximum sorption capacity increased with decreasing solution pH; only Cr(VI) sorption at pH 7 (154 ± 8.9 mg g^{-1} NC^{-1}) was slightly higher than at pH 5.6 (147 ± 14.3 mg g^{-1} NC^{-1}).
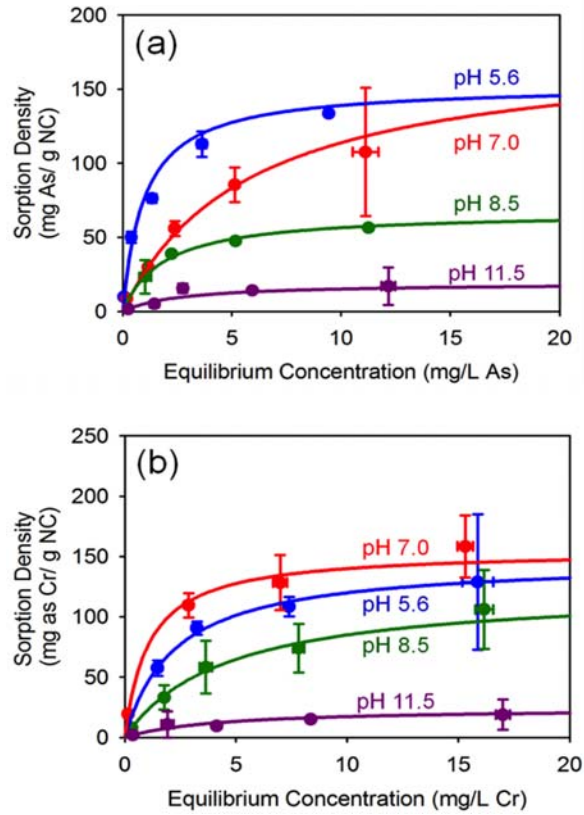
Figure 3.6 pH dependent As(V) and Cr(VI) sorption. Arsenic (a) and chromium (b) sorption isotherm on 12 nm iron oxide NCs coated with PEI (12 nm Fe_3O_4@PEI 25K) were investigated as a function of pH (5.6 (blue), 7.0 (red), 8.5 (green) and 11.5 (purple)).

3.3.4. Real Time Analysis of Arsenate and Chromate Sorption on PEI

To quantify real time As(V) and Cr(VI) interfacial processes, sorption and desorption phenomenon were investigated using quartz crystal microbalance with dissipation monitoring (QCM-D). For these studies, real time frequency shifts, as a result of deposition (i.e. resonance dampening) has a linear relationship with the deposited total mass according to the Sauerbrey relationship[223] (Equation (3.1)).

$$\Delta m = -\frac{C\Delta F_n}{n} \qquad \text{(Equation 3.1)}$$

Here, m is the total deposited mass on the sensor surface, C is the quartz sensor constant, F_n is the shift in resonance frequency and n is the resonance number (1, 3, 5, 7, 11 and 13).

As shown in Figure 3.S7 in the supporting information, PEI coated sensors were prepared using a surface grafting method, as described by others.[224] Upon introducing the PEI solution, the frequency shifted from 0 to ca. -63 Hz (after 1 to 3 min), which includes the PEI deposited mass as well as the viscosity difference between DI water (background) and the PEI solution. Sensors were saturated with PEI (solution) for 20 min and then subsequently washed with DI water (pH 7) to rinse and eliminate any weakly (loosely) associated PEI. Figure 3.S8 in the supporting information shows real time frequency and dissipation (n=3, 5 and 7) shifts of PEI on sensor surfaces at pH 7.0 and 11.5; the pH was changed every 20 min for six times. As pH increased from 7.0 to 11.5, the frequency increased (decreasing dissipation) and then decreased (increasing dissipation) with decreasing pH from 11.5 to 7.0. Such behavior indicates that PEI polymer coatings lose mass at pH 11.5, which is a result of water molecules adsorbing to the positively charged PEI polymer. Whereas, at pH 11.5 (point of zero charge), associated water molecules are released from the PEI via charge neutralization and thus the observed mass decrease (Figure 3.S9 in the supporting information).[225-226] Expanding this technique, we next explored real time As(V) and Cr(VI) sorption behaviors on PEI coated sensor surfaces.
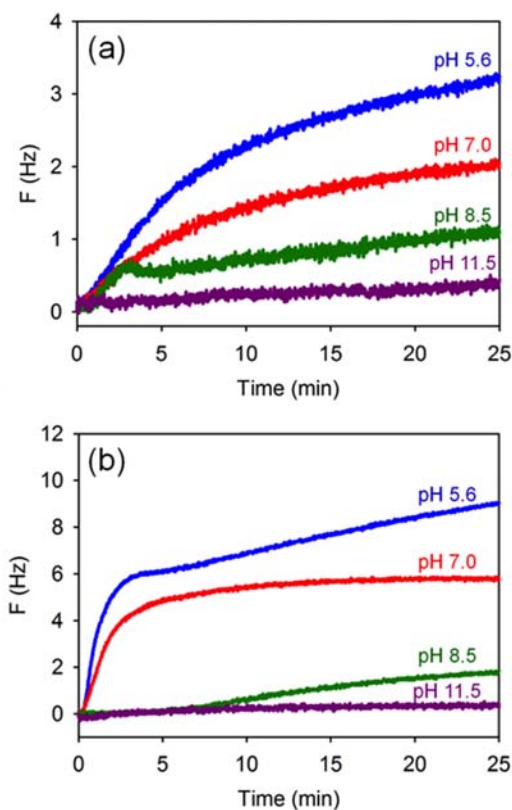
Figure 3.7 The pH dependent (pH 5.6 (blue), 7.0 (red), 8.5 (green) and 11.5 (purple)) frequency shift (overtone is 3) on PEI coated Q-sensors with 1 mM of arsenate (a) and chromate (b). Surface associated water molecules are released from the PEI (increasing frequency) via sorption of anion contaminants (As(V) and Cr(VI)) on PEI.

To understand As(V) and Cr(VI) sorption behavior on a PEI coated surface, time dependent frequency shift (release of water molecules) was monitored at four different pH conditions. Before evaluating As(V) and Cr(VI) solution, PEI grafted sensors were stabilized over 20 min using DI water at desired pH. Figure 3.7 presents real time frequency shifts of PEI coated sensors exposed to 1 mM arsenate or 1 mM chromate under various pH conditions (pH 5.6, 7.0, 8.5 and 11.5). As the pH decreased, As(V) or Cr(VI) sorption increased (frequency increased). PEI coated sensors have quick responses after reaction with As(V) or Cr(VI) solution. These results corresponded well with the 12 nm Fe_3O_4@PEI batch sorption isotherm and kinetic experiments for both As(V) and Cr(VI) (Figure 3.S10 in the supporting information).

PEI coated nanocrystals reached equilibrium within 2 hrs (including the separation time); sorption densities were 117 ± 2.2 mg g^{-1} NC^{-1} for As(V) and 120 ± 3.4 mg g^{-1} NC^{-1} for Cr(VI).

To explore the potential of recycling/reuse of PEI coated NCs, desorption tests were also conducted using PEI coated sensors via surfactant charge neutralization at pH 11.5 (PZC of PEI). As shown in Figure 3.S11 in the supporting information, the frequency of arsenate adsorbed Q-sensor maintained their initial frequency during pH 11.5 solution flow (i.e. no mass desorption). For chromate, 26.1% of frequency was recovered at pH 7 but the frequency was consistent at pH values of 5.6, 8.5 and 11.5.   These observations indicate that both As(V) and Cr(VI) adsorbed on functionality group of PEI are quite strong near PZC conditions. We speculate that there is no repulsive energy between neutralized amine functional groups and anion contaminants. Desorption may require even more basic conditions above pH 11.5 to create significant repulsive energy interactions.

3.4. Experimental

Materials

Iron oxy hydroxide (FeOOH), commercial magnetite nano power (<50 nm 98%), oleic acid (OA, technical grade, 90%), 1-octadecene (ODE, technical grade, 90%), cetyltrimethylammonium bromide (CTAB, 95%), sodium dodecyl sulfate (SDS, 99%), poly (ethylene glycol) (PEG, Mw = 2000) and branched polyethyleneimine (PEI, Mw = 25000), Igepal CO-520 ((C_2H_4O)n · $C_{15}H_{24}O$, n ≈ 5), tetraethoxy orthosilcate (TEOS), cyclohexane (99%), ethanol (99.9%), acetone (99.5%), hexane (98.5%) sodium arsenate ($Na_2HAsO_47H_2O$), potassium chromate ($K_2Cr_2O_7$) were purchased from Sigma-Aldrich. Silica nanocrystals (d =22 nm) were obtained from NanoComposix.

Synthesis of Magnetite

Iron oxide nanocrystals (IONCs) were synthesized by iron precursor decomposition at high temperature (over 320 °C)[42, 211]. IONCs were synthesized in a 50 ml of three-neck flask equipped with condenser, magnetic stirrer, and heating mantle under argon gas purging. 1 to 4 mmol of FeO(OH) with oleic acid (from 6 to 12 mmol) were used in the 1-octadecene (5 g) as a solvent for synthesis of NCs. As shown in Figure 3.S1, the size of the engineered NC was controlled by the concentration of the mixture of FeOOH and OA (the mole ratio of FeOOH/OA was fixed to 1/3) in 1-octadecene (5 g); the synthesized iron oxide became lager (nm average diameter) as the concentration of the mixture of FeOOH/OA increased (from 1/3 to 4/12). The resulting NCs were purified using ethanol (20 ml) and acetone (25 ml) with 8000 rpm centrifuging for 15 min; the purification process was repeated over six times. The purified NCs were dissolved and stored in hexane because oleic acid stabilized NCs by forming a monolayer via the hydrophilic head group (carboxyl group) facing the surface of the NCs.[51, 227]

The Organic Functionalization of Nanocrystals

Synthesized IONCs were surface functionalized and phase transferred from hexane to water by ligand exchange or encapsulation methods[40, 51]. Oleic acid (OA), cetyltrimethylammonium bromide (CTAB), sodium dodecyl sulfate (SDS), polyethylene glycol (PEG) and branched polyethyleneimine (PEI) were used as phase transfer agents. Particular amounts of surface stabilizer (0.05 to 10 mmol) were mixed with 0.5 mL IONCs in hexane (particular concentration was 6.8×10^{17} particles) and vigorously stirred in 8 mL dionized (DI) water (>18.2 MΩ-cm resistivity, Milli-Q, Millipore Corp). The mixture of phase transfer agents and NCs was then probe-sonicated (Qsonica, Q-700, Taperd microtip) for 5 to 10 min at 80% amplitude with full cycle. The as-phase transferred NC (in water) was put in the fume hood over 24 hrs to evaporate excess hexane and purified using stirred cell with ultra filtration membrane (cellulose, 100K

Dalton, Millipore) at 10 psi under inert gas (Ar) condition. Lastly, the resulting solution was further filtrated by syringe filter (0.22 μm, WHATMAN-PTFE) and the concentration of NC solution was measured using inductively coupled plasma optical emission spectroscopy (ICP-OES).

Silica coated IONCs were synthesized based on the previous report[228-229]. For details, 8 nm synthesized NCs (40 mg) were dispersed in cyclohexane (15 ml) containing Igepal CO-520 (2 ml) with vigorous stirring at room temperature for 5 min. To this mixed solution, NH_4OH (29%, 0.4 ml) and tetraethoxy orthosilcate (TEOS, 0.1 ml) were rapidly injected and kept for 12 hrs with vigorous mixing. The resulting NCs were isolated by centrifugation at 8,000 rpm for 20 min after six times purification with ethanol and DI-water.

Sorption Isotherms
The surface functionalized (and phase transferred) NCs were used as sorbents targeting As(V) or Cr(VI) over a range of 0.30 to 12.59 mgL^{-1} as As(V) and 0.42 to 17.47 mgL^{-1} as Cr(VI) at different pH (5.6, 7.0, 8.5 and 11.5). pH of the solution was adjusted using HNO_3 and NaOH solution before batch sorption experiments and during the sorption test (after 4 and 8 hrs). After 24 hrs sorption isotherm, NCs were separated using ultracentrifuge (Sorvall WX Ultra 80, Thermo Scientific) at 50,000 rpm for 2 hrs and the remaining concentrations of arsenic and chromium in the supernatant were measured using Inductively Coupled Plasma Mass Spectroscopy (ICP-MS, Perkin Elmer ELAN DRC II). The calculated sorption isotherm was plotted by Langmuir isotherm (Equation (3.2)), that was best fitted with measurements.

$$q_e = \frac{q_{max} k C_e}{(1 + k C_e)} \qquad \text{(Equation 3.2)}$$

Where q_e is the sorption density of the system (mg as sorbed arsenic or chromium g^{-1} as NC), q_{max} maximum sorption density, k_L Langmuir sorption constant, and C_e the equilibrium concentration of arsenic and chromium.

Transmission Electron Microscope (TEM)
The diameter of synthesized IONCs was measured using transmission electron microscope (TEM, Tecnai G2 Spirit, FEI). TEM images were further analyzed by Image Pro Plus 6.0 (Media Cybernetics, USA); size and size distribution were obtain by counting over a thousand of NCs.[230]

Hydrodynamic Diameter and Zeta Potential
The hydrodynamic diameter and zeta potential of aqueous phase IONCs were determined by dynamic light scattering method (Malvern, Zetasizer Nano ZS, ZEN3600) at 22 °C.

X-Ray Diffraction (XRD)
XRD patterns (from 20º to 80º of 2θ) of synthesized NCs were measured using a powder diffractometer (Bruker d8 Advance X-ray Diffractometer) with Cu Kα radiation (1.54 Å).

Total Organic Carbon (TOC)
TOC (Shimadzu Scientific Instrument) was used to measure the mass of organic surface stabilizers coated on NCs.

X-ray Photoelectron Spectroscope (XPS)
XPS spectrometer PHI 5000 VersaProbe II Scanning ESCA Microprobe (Physical Electronics) was used with monochromatic Aluminum 38.6 W X-ray source and 200.0 μm X-ray spot size with a pass energy of 26.00 eV at 45.0°.

Quartz Crystal Microbalance with Dissipation (QCM-D)
QCM-D (Q-sense E4, Biolin Scientific) was used with a quartz sensor (5MHz silica coated QCM-D crystal, QSX-202, Q-sense) at 22.00 ± 0.02 °C under 100 μlmin^{-1} of flow rate (ISM935, ISMATEC).

3.5. Conclusions

As synthesized IONCs were functionalized and phase transferred to water by tailored surface modification. Net positively charged surface stabilizers, such as PEI and CTAB, grafted on the surface of IONC, demonstrate superior anion (here as arsenate and chromate) sorption. Moreover, surface associated PEI polymer acts as an independent sorbent for arsenate and chromate. Fast sorption onto PEI was observed via real-time monitoring, and sorbates were not completely desorbed (irreversible) by simple pH adjustment. Taken together, these detailed observations provide a better understanding of As(V) and Cr(VI) sorption on the organically surface stabilized nanocrystal system depending on the surface functional group, grafting density, and the surface coating structure.

3.6. Supporting Information
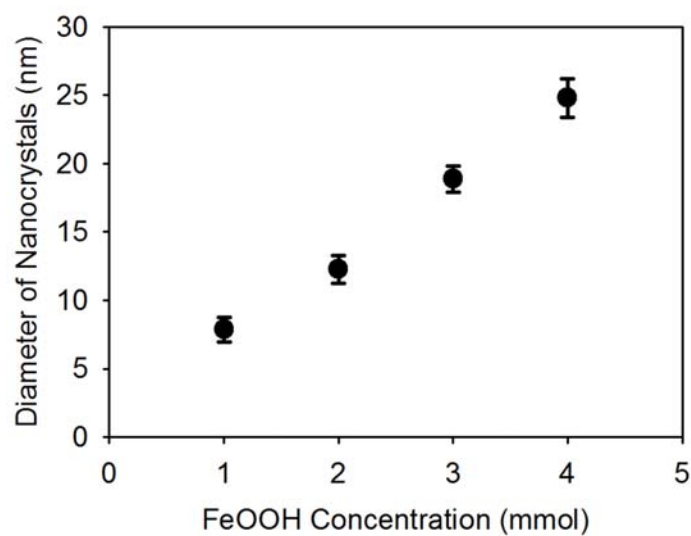
Figure 3.S1 The diameter of synthesized Fe_3O_4 NCs as a function of oxyhydroxide (FeOOH) concentration in 5 g of 1-octadecene as a solvent with the ratio of FeOOH/OA fixed to 1/3.
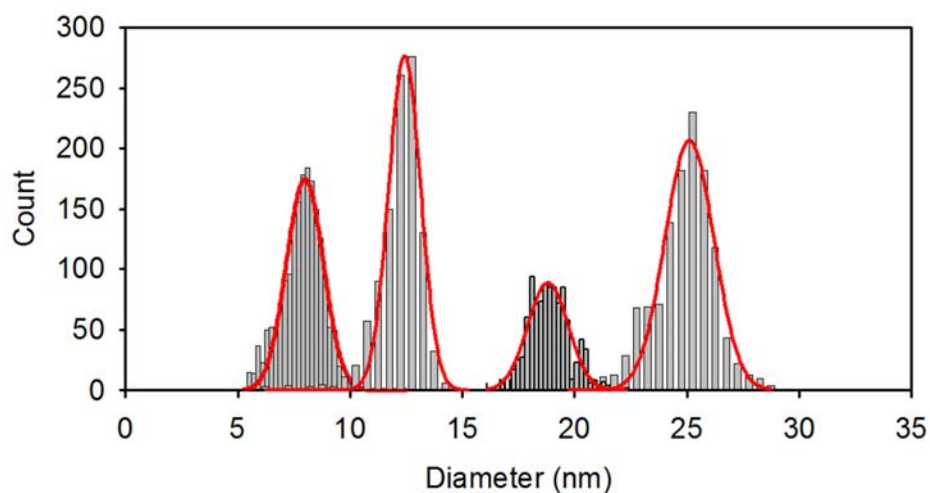
Figure 3.S2 Histograms of the size distribution of synthesized Fe$_3$O$_4$ NCs. The average diameter and their standard deviations were 7.9 ± 0.9, 12.3 ± 1.0, 18.7 ± 1.0, and 24.8 ± 1.4 nm. Size and size distribution was analyzed using Image Pro Plus 6.0 with over a thousand NCs counted.
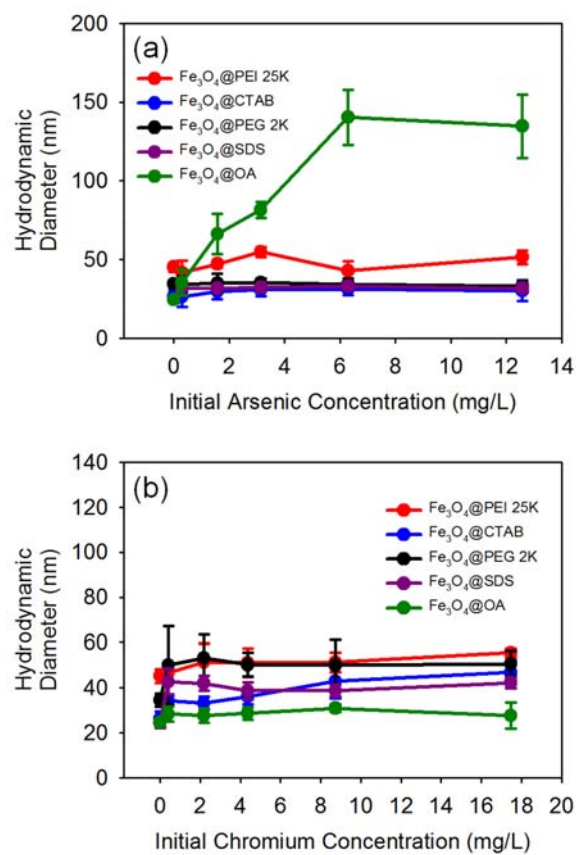
Figure 3.S3 Hydrodynamic diameter of functionalized (PEI (red), CTAB (blue), PEG (black), SDS (purple) and OA (green)) Fe₃O₄ NCs after (a) As(V) and (b) Cr(VI) sorption.
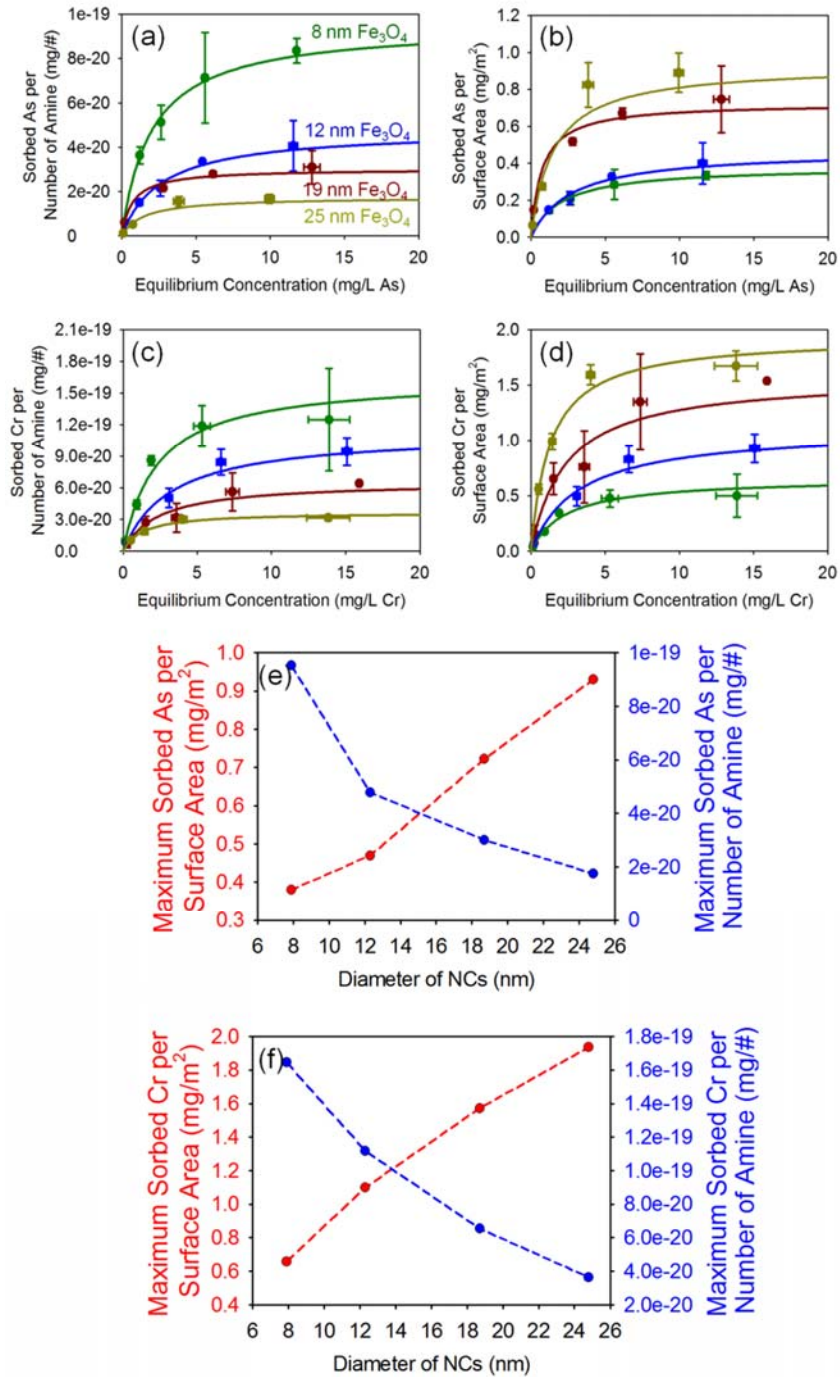
Figure 3.S4 (a-d) Normalized sorption isotherm by number of amine or by surface area of NC as a function of size of NCs (e) Maximum sorbed As per surface area and per number of amine

group as a function of size of NCs. (f) Maximum sorbed Cr per surface area and per number of amine group as a function of size of NCs.
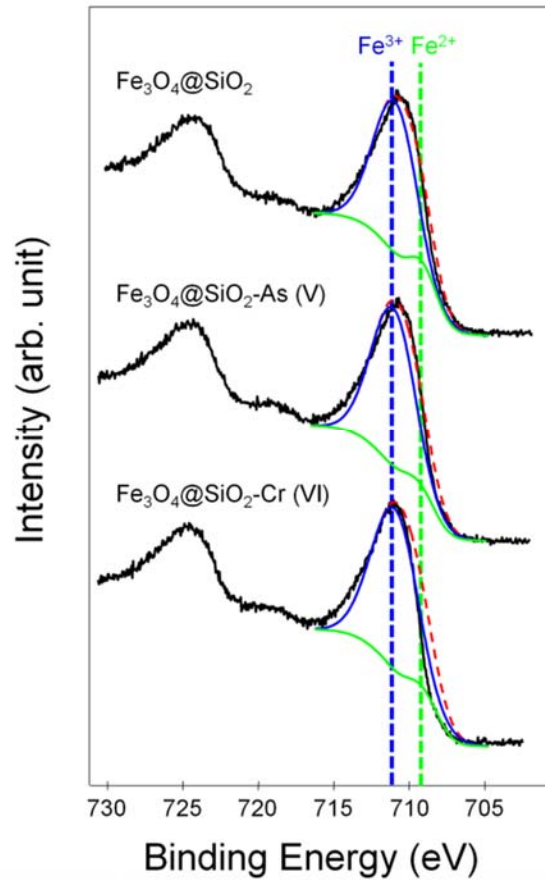
Figure 3.S5 The oxidation states of iron (Fe) of silica coated 8nm iron oxide NCs (Fe$_3$O$_4$@SiO$_2$) before sorption and after As(V) and Cr(VI) sorption were explored using XPS by measuring 2P iron.
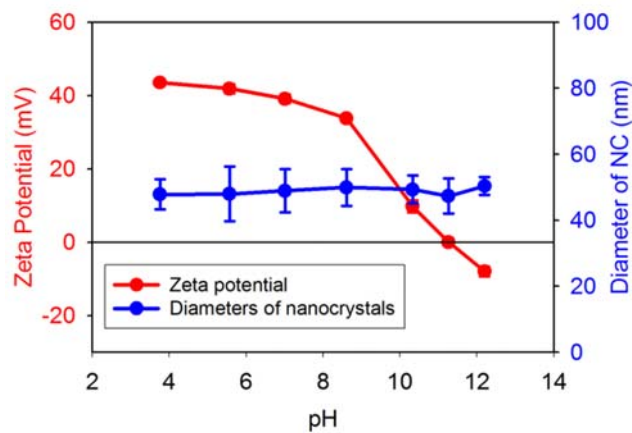
Figure 3.S6 Hydrodynamic diameter (blue) and zeta potential (red) of PEI coated 12 nm Fe_3O_4 NCs as a function of pH.
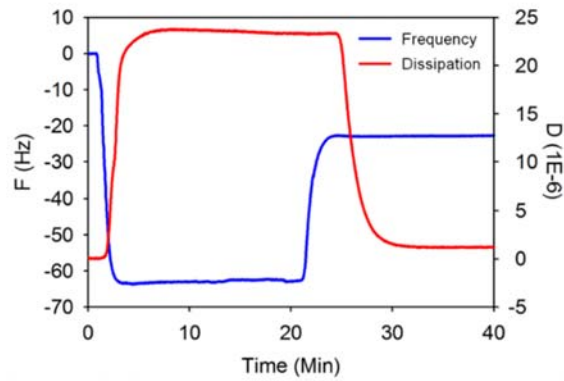
Figure 3.S7 Time dependent frequency (blue) and dissipation (red) responses for PEI coating on Q-sensor with overtone (n = 3). DI stabilized Q-sensor was coated by PEI solution (1 min to 3 min) and further stabilized for 20 min, and then PEI coated Q-sensor was restabilized with DI water at pH7 (22 min to 40 min).
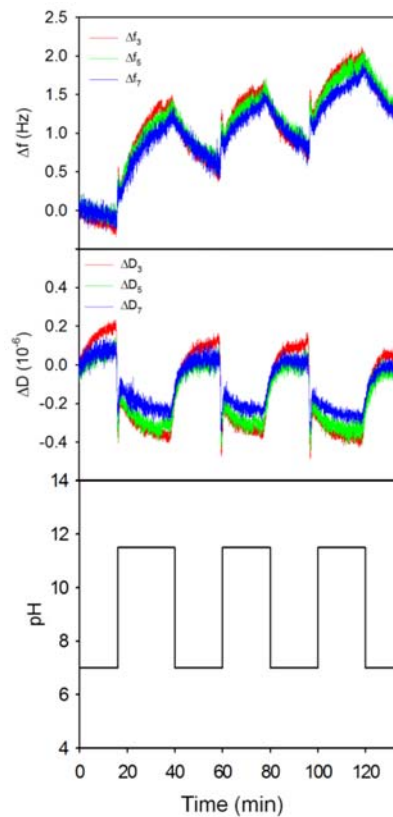
Figure 3.S8 Frequency and dissipation shifts of PEI coated sensors as a function of pH between 7 and 11.5 with the overtone n = 3 (red), 5 (green) and 7 (blue). Low frequency (high dissipation)

at pH 7 indicates that water molecules adsorbed with the charged functional groups of PEI and adsorbed water molecules are released via the charge neutralization of PEI functional groups at pH 11.5 (point of zero charge).
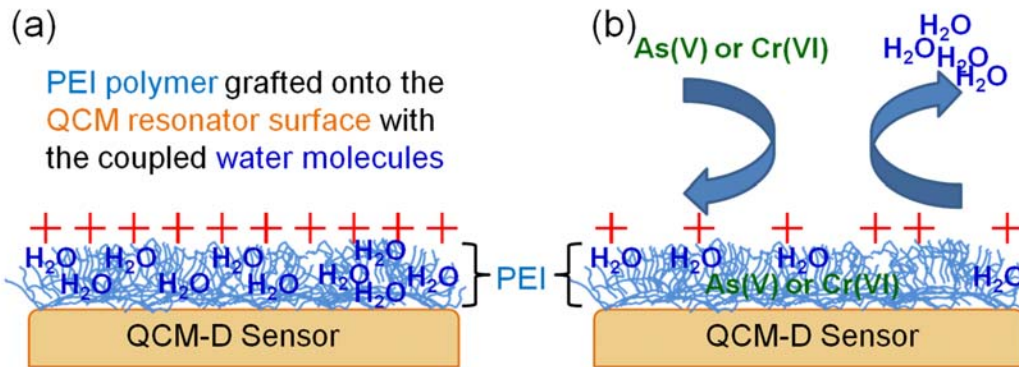
Figure 3.S9 Conceptual depiction of arsenate and chromate binding on PEI grafted sensor. (a) Water molecules adsorbed with positively charged functional groups of PEI grafted sensor. (b) The positively charged PEI functional group is neutralized via anion contaminants (As(V) and Cr(VI)) sorption and then adsorbed water molecules are released from the sensor surface. As(V) and Cr(VI) speciation are dependent on solution pH.
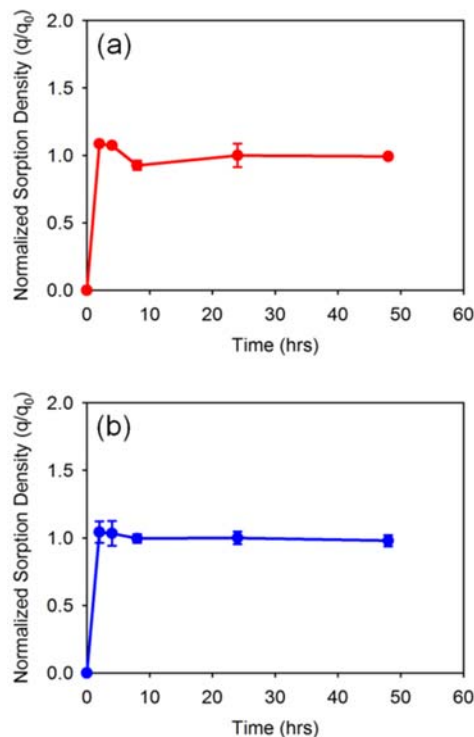
Figure 3.S10 Time dependent normalized sorption density for 1 mM (a) arsenate (red) and (b) chromate (blue) using PEI coated 12 nm Fe_3O_4 NCs at pH7.
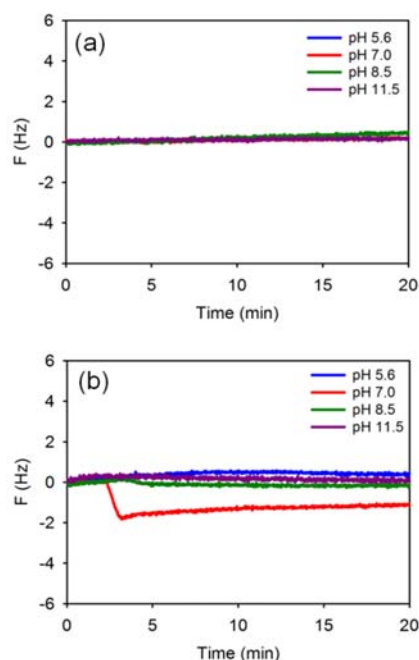
Figure 3.S11 The frequency responses (overtone is 3) of (a) arsenate and (b) chromate adsorbed PEI coated Q-sensor after applying a pH 11.5 solution.

Table 3.S1 Organic loading of surface of NC

Nanocrystals	Molecular Weight of Coating Material	Total Organic Carbon (ppm of carbon)[α]	Number of carbon per nanocrystal	Number of amine groups per carbon[β, γ]	Number of amine group per nanocrystal	Number of molecules per nanocrystal
8 nm Fe$_3$O$_4$@CATB		21.7 ± 4.5	21,172	0.037[α]	784	784
12 nm Fe$_3$O$_4$@CATB		34.3 ± 3.5	126,198	0.037	4,674	4,674
19 nm Fe$_3$O$_4$@CATB	364.45	55.2 ± 10.8	713,203	0.037	26,415	26,415
25 nm Fe$_3$O$_4$@CATB		92.0 ± 11.3	2,771,424	0.037	102,645	102,645
12 nm Fe$_3$O$_4$@PEI	25000	64.5 ± 0.5	236,989	0.5[β]	118,495	204

α. Total organic carbon (TOC) for organic coated iron oxide NCs (50 ppm Fe)
β. Number of amine groups per carbon of CTAB functionalized NCs was calculated based on an assumption of full CTAB surfactant encapsulation.
γ. Number of amine groups per carbon of 12 nm Fe$_3$O$_4$@PEI was obtained by considering repeat unit of multi branched PEI structure (Mw = 25000).

Table 3.S2 Maximum sorption capacity per surface area of NC and per number of amine

Nanocrystals	Maximum As sorption capacity per surface area of NC (mg/m^2)	Maximum As sorption capacity per number of amine	Maximum Cr sorption capacity per surface area of NC (mg/m^2)	Maximum Cr sorption capacity per number of amine
8 nm Fe$_3$O$_4$@CATB	0.38	9.51×10^{-20}	0.66	1.65×10^{-19}
12 nm Fe$_3$O$_4$@CATB	0.47	4.78×10^{-20}	1.10	1.12×10^{-19}
19 nm Fe$_3$O$_4$@CATB	0.72	3.00×10^{-20}	1.57	6.54×10^{-20}
25 nm Fe$_3$O$_4$@CATB	0.93	1.75×10^{-20}	1.94	3.64×10^{-20}

Chapter 4: Surface Optimized Core-Shell Nanocomposites (Fe$_3$O$_4$@Mn$_x$Fe$_y$O$_4$) for Ultra-High Uranium Sorption and Low-Field Separation in Water

4.1. Overview

Multifunctional manganese ferrite coated superparamagnetic magnetite (core-shell) nanocrystals, surface stabilized by (organic) a phosphate functionalized bilayer, have been simultaneously optimized for ultra-high uranium sorption capacity, colloidal stability under elevated ionic strengths, and susceptibility to low magentic fields, which are critical for subsequent separation processes.

4.2. Introduction

Superparamagnetic metal oxide nanocrystals (iron based materials such as, iron oxides, ferrites, etc.) have attracted significant interest for environmental applications due to their high potential in sorption, separation, sensing, and catalytic processes for a variety of aqueous pollutants including heavy metals and metalloids such as arsenic (As(III and V)), chromium (Cr(VI), and uranium (U(VI)).[196, 231-236] A number of such materials have been developed by various wet chemical methods.[237-241] For example, Yavuz et al. demonstrated arsenic (As(III and V)) adsorption properties and magnetic separation of monodisperse iron oxide nanocrystals synthesized via a precise organic route.[239] Crane et al. reported the removal of U(VI) in water using iron oxide nanocrystals synthesized by coprecipitation method.[237] Dui et al. have demonstrated As(V) and Cr(VI) adsorption properties using MnFe$_2$O$_4$ hollow nanospheres

ranging from 180 to 380 nm synthesized by a hydrothermal process.[238] Cai et al. have described a phosphorylated graphene oxide–chitosan composite for selective U(VI) removal.[240] Chen et al. reported amidoxime amended metal-organic framework for U(CI) extraction from seawater.[241]

Recently, our group has developed and demonstrated monodisperse manganese oxide (MO) and manganese ferrite (MF) nanocrystals with varying composition ratios of manganese to iron for ultra-high capacity uranium (VI) sorption and separation properties while considering colloidal stability, pH, and ionic strengths.[45] In these studies, iron-rich manganese ferrite ($MnFe_2O_4$) nanocrystals show better U(VI) sorption performance than manganese-rich manganese ferrite (Mn_2FeO_4) nanocrystals (q_{max} for $MnFe_2O_4$@OA and Mn_2FeO_4@OA at pH 7.0 was 667and 270 milligram of U per gram of nanocrystal (mg U / g NC), respectively). Higher concentration of Fe(II) (and Mn(II)) on the surface of $MnFe_2O_4$ leads to higher U(VI) sorption (than Mn_2FeO_4 materials) due to enhanced redox reactions between U(VI) and Fe(II) and Mn(II).[45]

Considering excellent uranium sorption by iron-rich manganese ferrite materials and the superparamagnetic properties of single domain iron oxides (IO), typically as magnetite, we propose that by combining these properties into one particle-based material – as a single domain magnetite core coated with a thin manganese ferrite – an optimized material for uranium sorption and separation may be achieved. Core@shell type biferrimagnetic nanocrystals have been synthesized as reported by López-Ortega and Krycka et al.[242] For these, iron oxide @ manganese ferrite (or manganese oxide) nanocrystals were synthesized under non-hydrolytic route by decomposing manganese (II) acetylacetonate (as a manganese precursor) with 1,2-hexadecandiol, oleylamine, and oleic acid in the presence of preformed iron oxide nanocrystals (as seed materials) at 200 °C.[242-243] Resulting core@shell nanocrystals were shown to be

manganese-rich $Mn_xFe_{3-x}O_4$ (in the range between Mn_3O_4 and Mn_2FeO_4) as the shell phase(s) on the surface of 11 nm iron oxide nanocrystals. However, based on our previous findings, iron-rich manganese ferrite surfaces are significantly better than manganese-rich ferrites with regard to U(VI) sorption capacities.

In this work, we have synthesized iron oxide nanocrystals coated with manganese ferrite (IO@MF) shells with varying composition ratios of manganese to iron (Figure 4.1). These nanocrystals were phase transferred into water via bilayer surface coatings, which consist of oleic acid (OA) inner layer and an oleylphosphate (OP), which has an outward facing phosphate head group. Uranium sorption was then explored and directly compared with analogous IO and MF particles with the same bilayer surface coatings.

4.3. Results and discussion

Monodisperse, iron-rich manganese ferrite coated iron oxide nanocrystals (Fe-rich IO@MF) were precisely synthesized by decomposition of Mn-OA, as an Mn precursor, in the presence of preformed IO nanocrystal seeds in 1-octadecene at 320 °C for 1h. Control of Shell composition (i.e. Mn:Fe ratio) was achieved by precisely varying the molar ratio of Fe and Mn in the reaction (Figure 4.S1).[242-243] Specific synthetic processes are described in the SI. Average diameters of the resulting core@shell type nanocrystals increased slightly from 10.2 nm to 11.0 nm as a Mn-OA precursor decomposed onto the surface of seed materials (IO nanocrystal, d = 10.2 ± 0.9 nm) as shown in Figure 4.S2.

Characterization of IO@MF materials is shown in Figure 4.S3 and 4.S4. Fe-rich manganese ferrite shell composition was observed with a molar ratio of Mn to Fe of 0.28 with no core alteration. Under these conditions, there was no evidence of forming individual (free) manganese oxide nanocrystals in the reaction as shown in GIF (Gatan Image Filter) images of

the synthesized nanocrystals (Figure 4.1 and Figure 4.S5). Furthermore, the composition ratio of

Mn/Fe of the synthesized nanocrystal sample was identical with the ratio of Mn/Fe of the starting

chemicals (the ratio of Mn-OA/Fe-OA). As shown in Figure 4.S6, XRD diffraction patterns of

IO@MF nanocrystals with varied composition of Mn/Fe in an IO@MF nanocrystal from 0.28 to

0.73 are well matched to the diffraction patterns of magnetite (core, Fe_3O_4; red vertical lines;

JCPDS cards #19-0629); however, MnO (200) phase was found from IO@MF with high ratio of

Mn/Fe concentration over 2.1. A high ratio of Mn precursor to Fe seed material over 2.08

mol/mol led to the formation of manganese oxide layer(s) on the surface of IO seed materials.
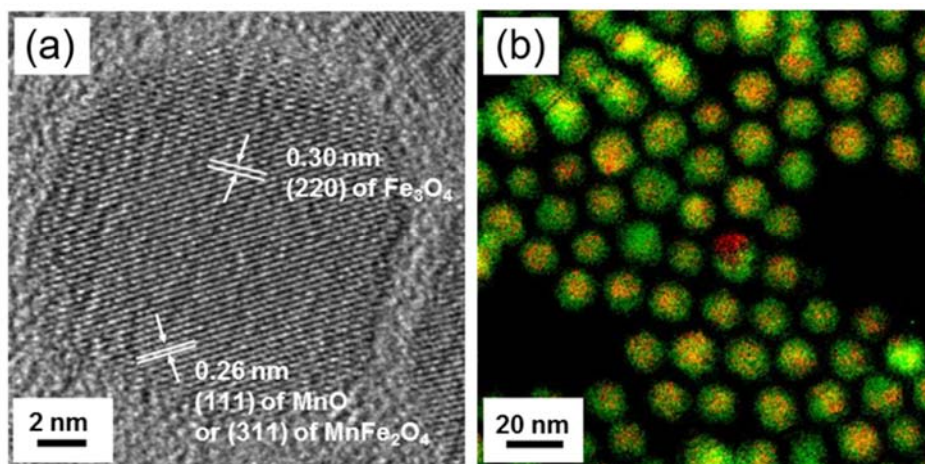
Figure 4.1 TEM images of the IO@MF nanocrystals. (A) HR TEM image of IO@MF nanocrystals. The lattice fringes of 0.30 nm (center) and 0.26 nm (side) correspond to (220) of Fe_3O_4 and (311) of $MnFe_2O_4$ (or (111) of MnO), respectively. (B) Gatan Image filter (GIF) image of IO@MF nanocrystals. The overlay map shows the distribution of iron (red) and manganese (green) in the particles.

The magnetic properties of engineered IO@MF nanocrystals were characterized by

SQUID analysis (Figure 4.2). IO@MF, IO (Fe_3O_4), $MnFe_2O_4$, and Mn_2FeO_4 nanocrystals

synthesized under organic reactions at 320°C showed superparamagnetic behavior with

hysteresis loops exhibiting nearly zero remanence and coercivity at 300K; 11 nm manganese

oxide nanocrystals, which is known as core@shell type materials of $MnO@Mn_3O_4$

52

(antiferromagnetic core and ferrimagnetic shell) from the previous research, revealed a displacement of hysteresis loop along the magnetic field axis, exchange bias (H_E), with -274.6 Oe at 2K (Table 4.S1).[45, 244] While being superparamagnetic, IO@MF nanocrystal samples were also similar to inverted soft/hard ferrimagnetic core@shell structures, exhibiting a higher exchange bias with -20.65 Oe of H_E at 2K (Table 4.S1).[242-243]
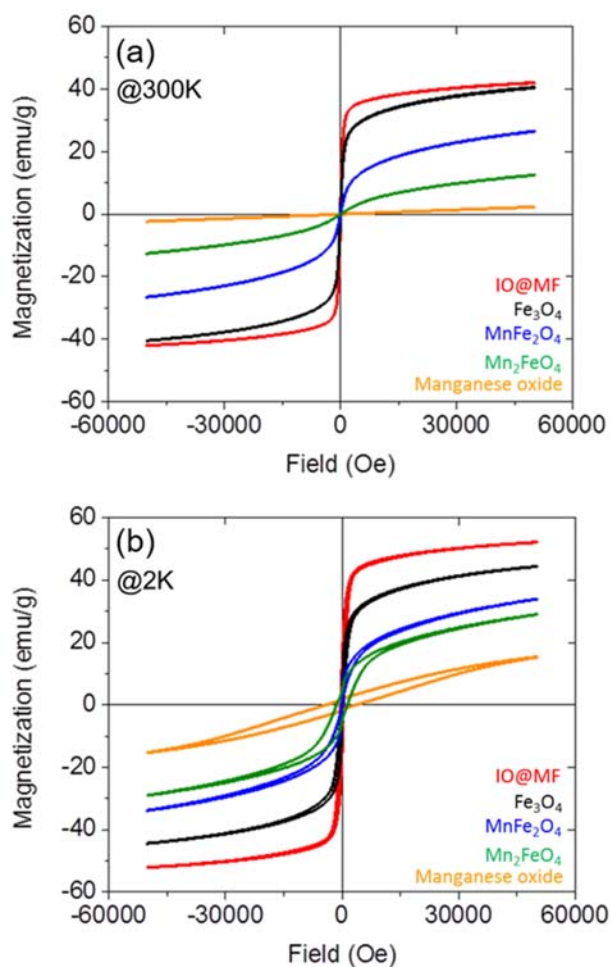
Figure 4.2 Magnetic properties of the nanoparticles synthesized under organic route. (A) Hysteresis curves of IO@MF ([Mn]/[Fe] = 0.28, red), Fe_3O_4 (black), $MnFe_2O_4$ (blue), Mn_2FeO_4 (green), manganese oxide (orange) measured at 300 K. (B) Hysteresis curves of IO@MF ([Mn]/[Fe] = 0.28, red), Fe_3O_4 (black), $MnFe_2O_4$ (blue), Mn_2FeO_4 (green), manganese oxide (orange) measured at 2K.

For aqueous application, we employed a surface-based organic bilayer technique to facilitate aqueous transfer and stability (Supplemental Information†).[45, 245] Oleylphosphate (OP) was used as a phase transfer agent (also as a surface stabilizer), which coordinates with the first surface layer (oleic acid) on the as-synthesized IO@MF nanocrystal surface via hydrophobic-hydrophobic interaction.[45, 245] The resulting hydrodynamic diameter (D_H) and surface charge for the phase transferred IO@MF@OP nanocrystals were 20.9 ± 3.0 nm with -50.4 ± 1.4 mV. These IO@MF@OP nanocrystals were also colloidally stable in water under relatively high ionic strengths. Critical coagulation concentration (CCC) values of sodium (Na) and calcium (Ca) for the particles were 892.5 mM of Na^+ and 15.9 mM of Ca^{2+} for IO@MF@OP (Figure 4.S7).
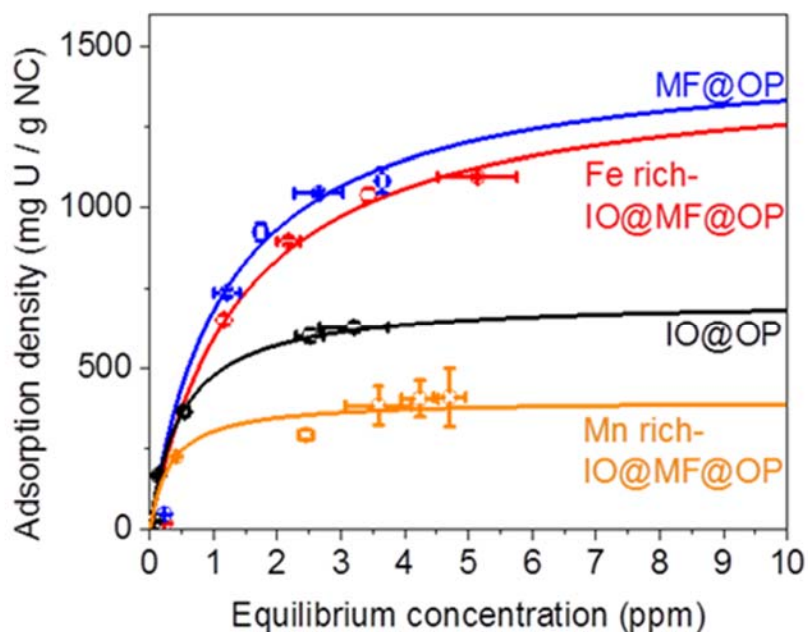
Figure 4.3. Uranium sorption isotherm of four different types of the nanocrystal samples (MF ([Mn]/[Fe] = 0.30, blue), iron-rich IO@MF ([Mn]/[Fe] = 0.28, red), IO (black), and Mn-rich IO@MF@OP ([Mn]/[Fe] = 2.07, orange)) coated with oleylphosphate (OP) at pH 7.0 for 24 h. The curves were plotted and modeled as Langmuir isotherms.
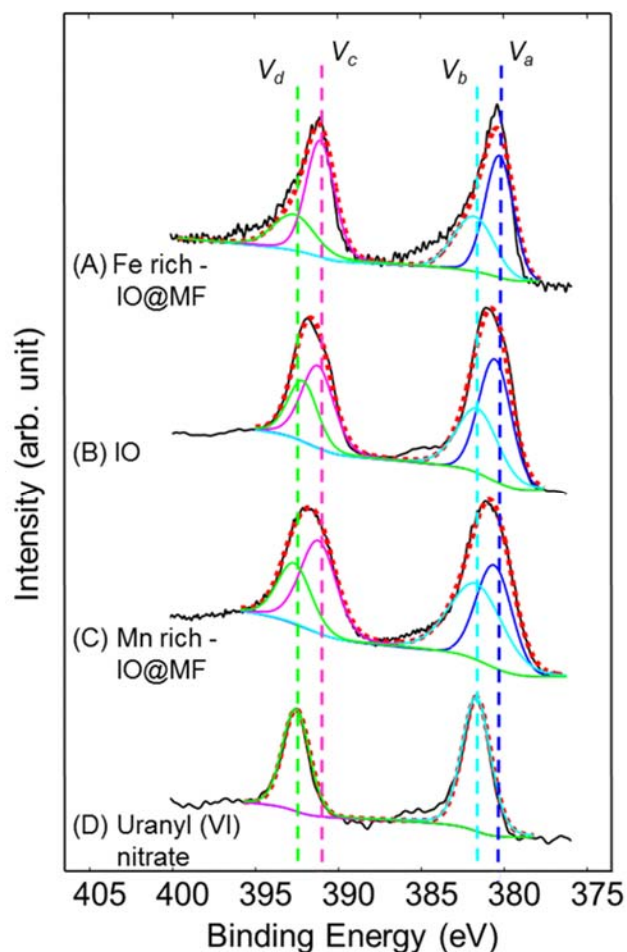
Figure 4.4 XPS spectra of the uranium (U) 4f spectra for the sample after uranium sorption. The black lines are the raw data and the red dash lines are the fitted curves based on curve fitting using V_a (blue), V_b (sky blue), V_c(pink), and V_d(green). The ratio of U(IV) to U(VI) was calculated by $(V_a+V_b)/(V_c+V_d)$ in the XPS spectra of U4f from the sample after the uranium sorption measurement and compared with uranyl (VI) nitrate.

Surface stabilized IO@MF@OP nanocrystals were evaluated as sorbent materials for uranyl (VI) cations (UO_2^{2+} and hydroxo complexes such as, $(UO_2)_m(OH)_n^{2m-n}$, depending on pH) over varied water chemistries.[246] It should be noted that IO@MF@OP nanocrystals maintained their monodisperse status for U concentration up to 20 ppm (Figure 4.S8); D_H for IO@MF@OP slightly increased from 20 to ca. 35 nm at pH 5.6 and pH 7.0 as U concentration was increased to 40 ppm. Figure 4.3 shows nanocrystal composition dependent U sorption capacity

55

measurements. Each was modeled as a Langmuir isotherm.[247] Maximum sorption capacity (q_{max}) for IO@MF with an iron rich ferrite shell is similar to values for MF nanocrystals with the same bilayer coatings. q_{max} for IO@MF@OP ([Mn]/[Fe] = 0.28) and manganese ferrites (MF: $Mn_{0.6}Fe_{2.4}O_4$, [Mn]/[Fe] = 0.30) at pH 7.0 was 1438 and 1492 mg of U per g of nanocrystal (mg U / g NC), respectively.[45] U(VI) sorption capacity of IO@MF@OP ([Mn]/[Fe] = 0.28) at pH 5.6 was near the capacity at pH 7.0 (Figure 4.S9). For these, all isotherm modeling data is presented in Table 4.S2. These value are among some of the highest values reported for uranium sorbents.[45, 248]

While iron rich MF coatings can improve U sorption capacities of IO nanocrystals by a factor of two, higher Mn shell content ([Mn]/[Fe] = 2.07), which resulted in Mn-rich MF coatings (with manganese oxide phase shown in via XRD Figure 4.S6), display a marked decrease of U sorption capacity. Figure 4.3 shows U sorption capacities of IO@MF@OP as a function of Mn to Fe ratios in the shell composition from 0.28 to 2.07 with

q_{max} of IO@MF@OP nanocrystals decreasing from 1438 to 400 mg U / g NC, respectively. We hypothesize that the decrease of q_{max} for Mn-rich IO@MF nanocrystal ([Mn]/[Fe] in a nanocrystal was 2.07) is due to the formation of pure manganese oxide phases (and/or manganese-rich ferrite such as, Mn_2FeO_4) on the iron oxide core.[45, 242] It has been previously reported that Mn precursor decomposition with high concentration in the presence of IO seeds (when [Mn] / [Fe] of the starting materials was over 2.1) does form thick layered Mn_2FeO_4, MnO, or Mn_3O_4 on the surface of IO nanocrystals (Figure 4.S6).[45, 242-243] Such (thick) Mn-rich phase layers on IO nanocrystal may prevent high U sorption properties as less reduced Fe (Fe(II)) is available, which is critical for U reduction from U(VI) to U(IV), on the surface of IO-based materials.[45, 249]

For materials exhibiting the highest U sorption capacity ([Mn]/[Fe] in a nanocrystal was 0.28), the relatively highest percentage of U reduction was also observed. Figure 4.4 shows U reduction as a function of nanocrystal surface composition. The highest U reduction (from U(VI) to U(IV)) was found from Fe-rich IO@MF with U(IV) of 65 %; the U reduction percentage of IO and Mn-rich IO@MF was 58 and 52 %, respectively (Table 4.S3). As mentioned above, we hypothesize that Fe(II) on the surface of the nanocrystal samples play a significant role in U reduction (Figure 4.S9 and Table 4.S4). Fe(II) concentration of Fe-rich IO@MF decreased from 75 % to 25 % upon U reduction; Mn(II) of Fe-rich IO@MF was also observed to decrease from 28 % to 14 % with U reduction experiment (Figure 4.S10, Figure 4.S11, Table 4.S4, and Table 4.S5).

4.4. Experimental

Chemicals.

Manganese (II) chloride tetrahydrate ($MnCl_2 \cdot 4H_2O$, 99.99 %), Ferric hydroxide oxide (FeOOH, catalyst grade, 30-50 mesh), oleic acid (OA, 90 %), 1-octadecene (90 %) were purchased from Sigma-Aldrich. Sodium oleate (97 %) and oleylphosphate (OP) were purchased from TCI America. Uranyl nitrate hexahydrate ($UO_2(NO_3)_2 \cdot 6H_2O$) was purchased from Antec, Inc. All nanocrystals were synthesized under nitrogen condition (N_2, 99.999%).

Synthesis of Manganese Oleate.

Manganese oleate was synthesized by the method reported by An et al.[250] Manganese chloride tetrahydrate (15.8 g, 80 mmol) reacted with oleic acid (45.2 g, 160 mmol) in 20 g of ethanol, 10 g of water, and 30 g of hexane at 60 °C for 4 h. The resulting pink colloid was washed by using water and ethanol. The purified manganese oleate was extracted by hexane.

Synthesis of Iron Oxide Nanocrystals.

Iron oxide nanocrystals were synthesized by decomposition of iron oleate in 1-octadecene at 320 °C as reported by Park et al.[48] For 10 nm iron oxide nanocrystals, 21.8 μmol of iron oleate was decomposed in the presence of 0.5 mmol of oleic acid in 1-octadecene at 320 °C for 1h. The resulting black colloidal iron oxides were purified using ethanol, acetone, and hexane.[48] The purified iron oxide nanocrystals were stored in hexane.

Synthesis of Nanocrystalline Manganese Iron Oxide Coated Iron Oxides (IO@MF).
IO@MF nanocrystals were synthesized by decomposition of manganese oleates (Mn-OA) in the presence of iron oxide (IO) nanocrystals as seed materials as at 320 °C. For details, 10 ml of IO nanocrystals in hexane solution ([Fe] = 5,096 mg/L) and 0.5 ml of manganese oleate ([Mn] = 12,150 mg/L) was mixed with 1 mmol of oleic acid in 4 g of 1-octadecene at room temperature. The mixture was heated at 60 °C for 0.5h and kept at 120 °C for 1h to evaporate hexane and water. The reaction was then treated at 320 °C for 1h to decompose manganese oleate on the surface of iron oxide nanocrystals (seeds). A schematic of IO@Mn$_x$Fe$_y$O$_4$ nanocrystal synthesis is presented in Figure 4.S12. The synthesized black colloids were purified using ethanol (and/or acetone), and precipitated by centrifugation at 7000 rpm for 15 min. The resulting black precipitates were then dissolved in hexane and the purified IO@MF was separated from hexane solution containing colloidally unstable nanocomposites. The purified and colloidally stable nanocrystalline IO@MF was well dispersed in various nonpolar solvents such as, hexane, THF, and toluene. The concentration ratio of manganese to iron in IO@MF nanocrystals was 0.28, measured by ICP-OES.

Phase Transfer of IO@MF Nanocrystals
The as-synthesized IO@MF nanocrystals were transferred to aqueous solution by ligand encapsulation methods using probe sonication.[245] Briefly, 0.05 mmol of oleylphosphate as a surface stabilizer was stirred with 5 mg of nanocrystal in hexane solution ([Fe] = 1,500 mg/ml

and [Mn] = 870 mg/L, measured by ICP-OES) and 10 ml of ultra-pure water (MILLIPORE, 18.2 MΩcm). Aqueous and organic phases were mixed by application of a probe-sonicator (UP 50H, DR.HIELSCHER) for 10 min at 80 % amplitude and full cycle.[245] The resulting solution was further stirred for 1 day under vacuum to evaporate hexane and to obtain a clean black solution. To remove excess free surface stabilizer molecules left in the suspension, the phase transferred IO@MF nanocrystals were further purified using ultracentrifugation (Sorvall WX Ultra 80, Thermo scientific) at 50,000 rpm for 2 h, and membrane filtration (Ultrafiltration cellulose membranes, 100 KDa MWCO) using a stirred cell (Amicon), followed by syringe filtration (pore size of 0.22 μm, WHATMAN-NYL).

Dynamic Light Scattering

The hydrodynamic diameters and surface charge of IO@MF nanocrystals stabilized by bilayered surface coating materials (oleic acid linked oleylphosphate (OA-OP)) were measured at pH 7.2 and 25 °C, using a Malvern Nano ZS system by Malvern Instruments equipped with a HeNe 633 nm laser (Malvern Zetasizer Nanoseries, Malvern, UK). The average hydrodynamic diameters were obtained by the mean size of the first peak of the number distribution and the standard deviation was determined from triplicate measurements.

Transmission electron microscope (TEM)

The diameters of the as-synthesized nanocrystals were measured through transmission electron microscope (TEM). TEM specimens were prepared using carbon support film on 300 mesh copper grids (electron Microscopy Sciences). The TEM micrographs were taken by a Tecnai G2 Spirit Twin microscope (FEI, Hillsboro, OR) operated at 120 kV. HR-TEM analysis was performed using a JEOL 2100F microscope (JEOL. Tokyo, Japan) operated at 200 kV. The size and size distribution data were obtained by counting over 1000 nanocrystals using Image-Pro Plus 5.0.[251]

X-ray diffraction (XRD)

X-ray powder diffraction (XRD) patterns were obtained using a Rigaku D/Max/A. 2θ range was from 10 to 80 degree with a Cu Kα radiation (1.54 Å) and the X-ray was generated at 40 kV and 40 mA.

Inductively coupled plasma optical emission spectroscopy (ICP-OES)

The particle concentrations were measured by an inductively coupled plasma optical emission spectroscopy (ICP-OES, Perkin Elmer Optima 7300DV) instrument equipped with autosampler.

Inductively coupled plasma mass spectroscopy (ICP-MS)

The uranium concentrations remained after uranium sorption measurement using manganese oxide nanocrystals were measured by an inductively coupled plasma mass spectroscopy (ICP-MS, Perkin Elmer ELAN DRC II) instrument equipped with autosampler.

Uranium sorption measurement

IO@MF coated with oleylphosphate (IO@MF@OP; [Fe] = 45.4 mg/L, [Mn] = 11.1 mg/L; 2.34×10^{13} nanocrystals calculated by the number of IO nanocrystal obtained by by iron concentration) was used from uranium sorption experiment at uranium concentrations ranging from 0.1 to 40 mg/L of uranium (VI)) at pH 5.6, pH 7.0, and pH 8.5. After the sorption experiment for 24 h, the nanocrystals were separated using ultracentrifugation at 50,000 rpm for 2 h and the remaining concentrations of uranium (VI) in the supernatant solution were analyzed by ICP-MS.[45] These measurements were conducted in triplicates. The measured uranium sorption density values (mass of sorbed uranium per mass of manganese) as a function of equilibrium concentration of uranium (mg/L) were best fitted with the plot drawn by the Langmuir isotherm equation:

$$q_e = \frac{q_{max} k \mathrm{C}_e}{(1 + k \mathrm{C}_e)} \qquad \text{(Equation 4.1)}$$

where q_e is the amount of adsorbed uranium at equilibrium concentration (mg/g), k is the sorption constant, q_{max} is the maximum sorption density (mg/g; mass of the sorbed uranium per mass of manganese), and C_e is the equilibrium concentration of uranium.

4.5. Conclusions

Surface tunable, superparamagnetic IO@MF nanocrystals coated with phosphate group functionalized bilayer surface coatings are demonstrated to be highly effective for uranium sorption/separation in water. The highest U sorption capacity of IO@MF nanocrystals (q_{max} was 1438mg U / g NC) was found to occur for surface stable IO nanocrystals with an iron-rich MF shell structure ([Mn]/[Fe] of an IO@MF nanocrystal = 0.28) with significant redox reactions at the particle interface. Such capacity is among the highest reported to date. Taken together, these findings underpin broad, platform potential for these and similar materials for next generation water treatment, including actinide separation and sensing technologies.

4.6. Supporting Information
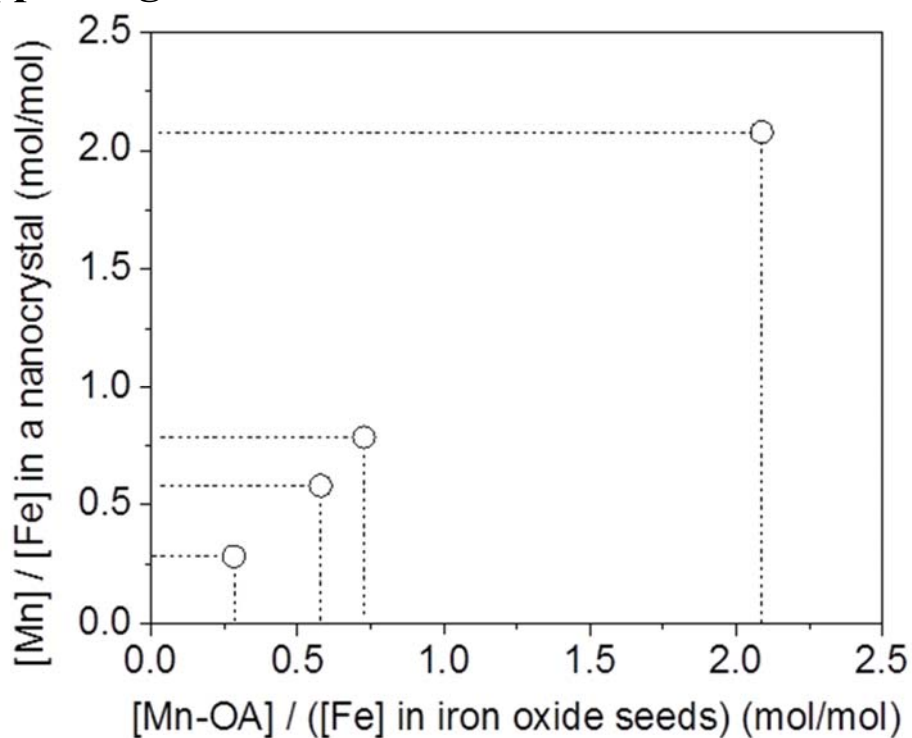
Figure 4.S1 Composition control of IO@MF nanocrystals. The molar concentration of Mn in IO@MF nanocrystal increases with elevated ratio of Mn precursor (Mn-oleate, Mn-Ol) to Fe seed materials (10 nm iron oxide nanocrystals, IO).
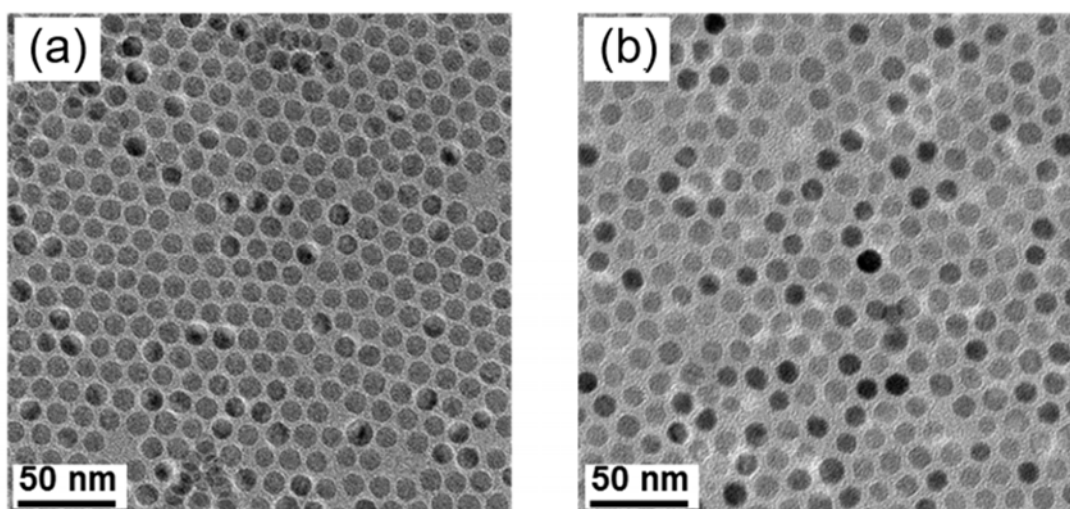
Figure 4.S2 TEM images of iron oxide (IO) nanocrystals as seed materials (A) and manganese ferrite coated iron oxide (IO@MF) nanocrystals (B). The average diameters of IO and IO@MF nanocrystals are 10.2 ± 0.9 nm and 11.0 ± 1.0 nm, respectively.
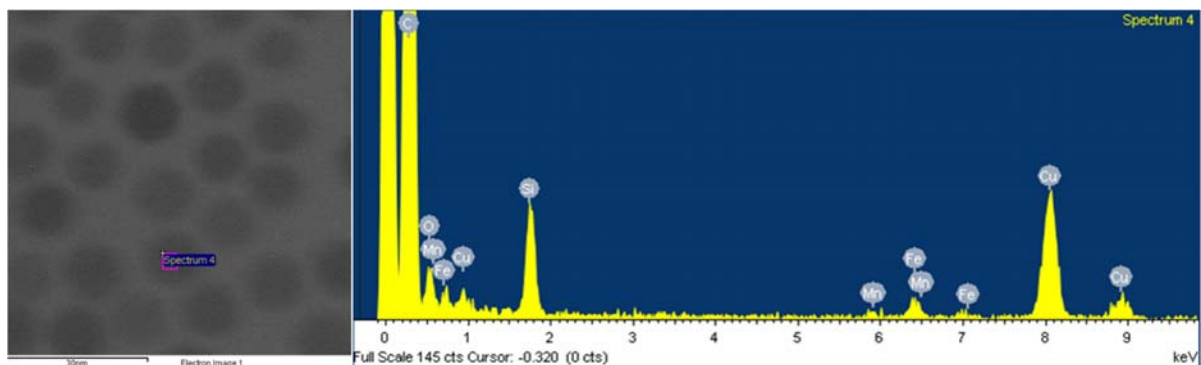
Figure 4.S3 EDS information of the center of IO@MF nanoparticle. The atomic ratio of manganese to iron is 14.3 to 85.7.
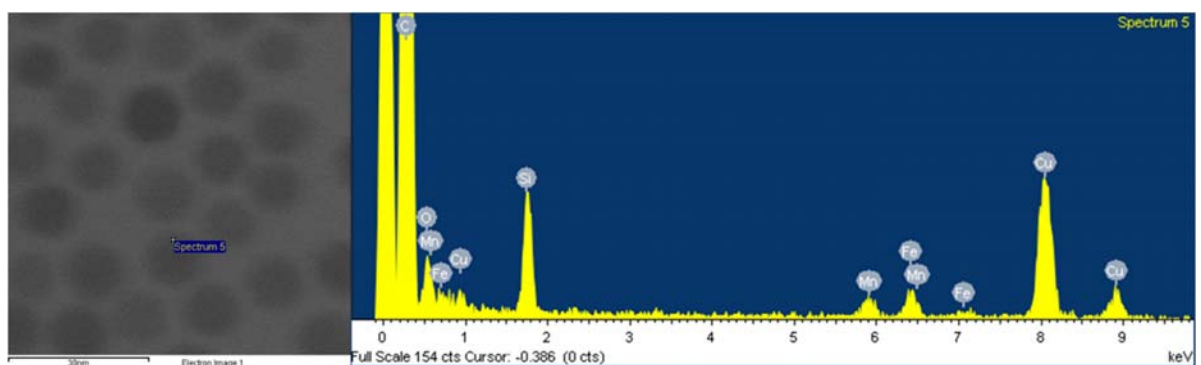
Figure 4.S4 EDS information of the side of IO@MF nanoparticle. The atomic ratio of manganese to iron is 22.2 to 77.8.
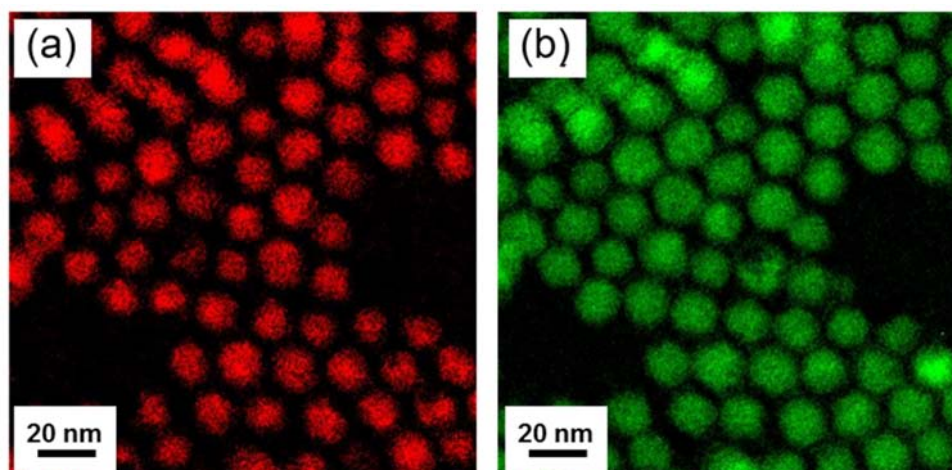
Figure 4.S5 EFTEM micrograph at iron (A, red) and manganese (B, green) L_3 edges in the particles.
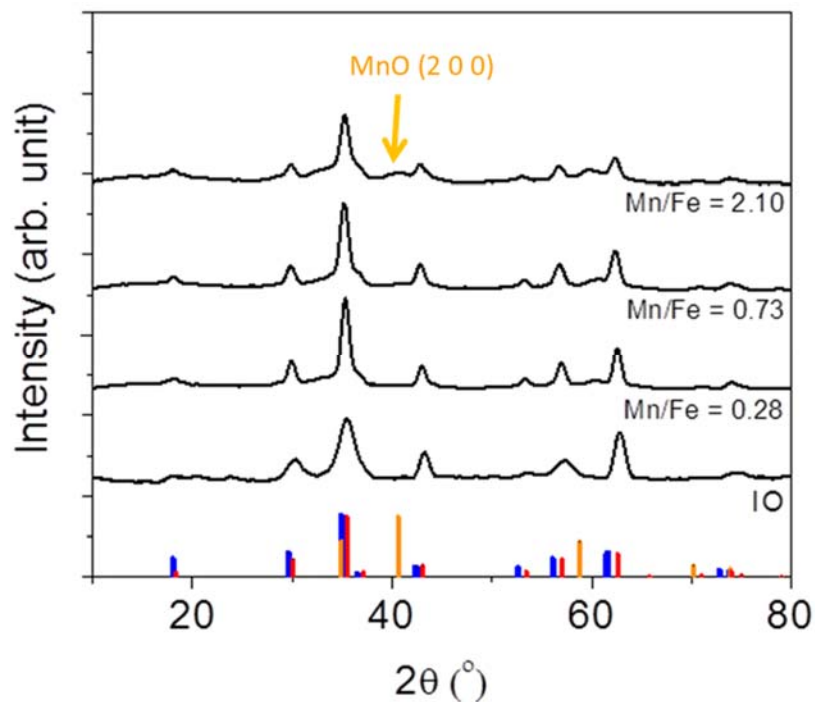
Figure 4.S6 XRD of manganese ferrite coated iron oxide (IO@MF) nanocrystals depending on the composition ratio of manganese to iron (from 0 to 2.10). The vertical lines at the bottom of the chart indicate the reference peaks of iron oxide (red, JCPDS # 19-0629), manganese ferrite (blue, JCPDS # 38-0430), and manganese oxide (orange, JCPDS # 07-0230).
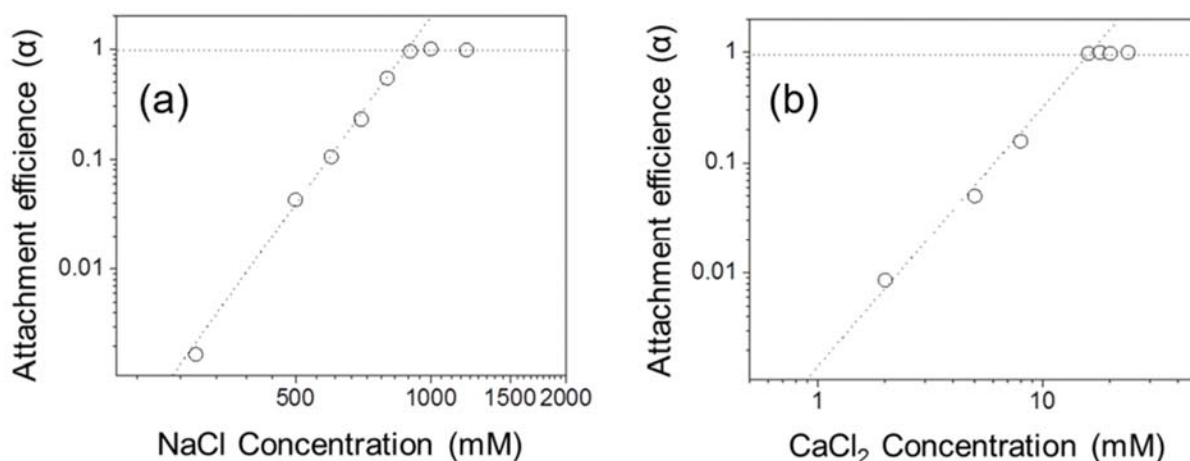
Figure 4.S7 Attachment efficiencies of oleyl phosphate (OP) coated IO@MF nanocrystals as a function of $NaCl_2$ (A) and $CaCl_2$ (B) concentrations at pH 7.0. The nanocrystal concentration employed was 3.0×10^{12} nanocrystals/L. The critical coagulation concentrations (CCC) are 892.5 mM of NaCl and 15.9 mM of $CaCl_2$ for IO@MF@OP nanocrystals.
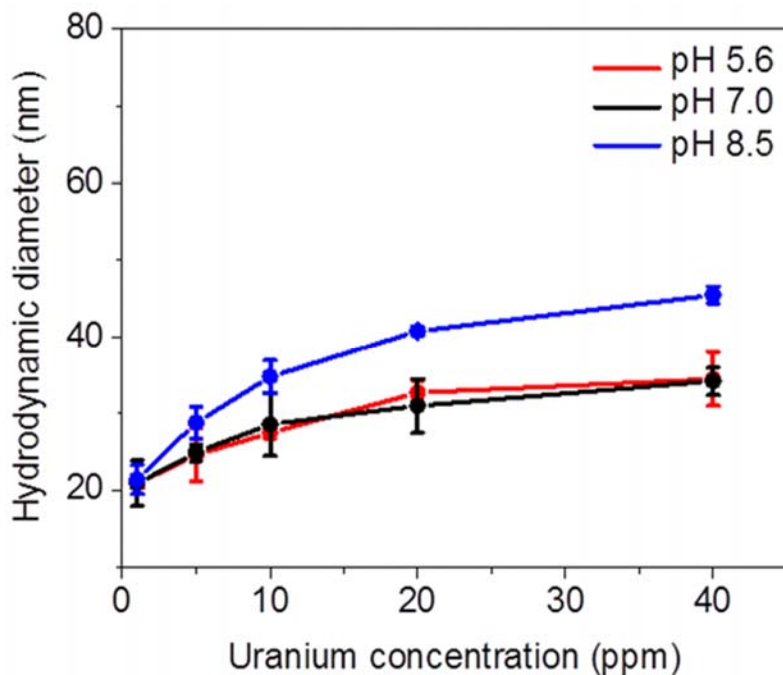
Figure 4.S8 The hydrodynamic diameters of IO@MF@OP nanocrystals at elevated uranium concentrations in water (from 0 to 40 ppm of uranium) at pH 5.6 (red), 7.0 (black), and 8.5 (blue).
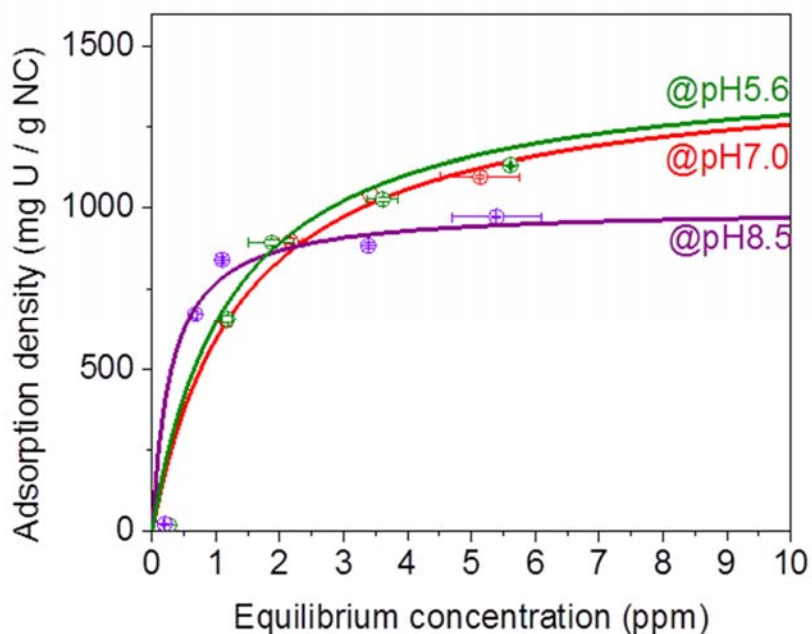
Figure 4.S9 Uranium sorption isotherms of iron-rich IO@MF ([Mn]/[Fe] = 0.28) coated with oleylphosphate (OP) at pH 5.6, 7.0, and 8.5 (equilibrated for 24 h). All sorption curves are modeled as Langmuir isotherms.
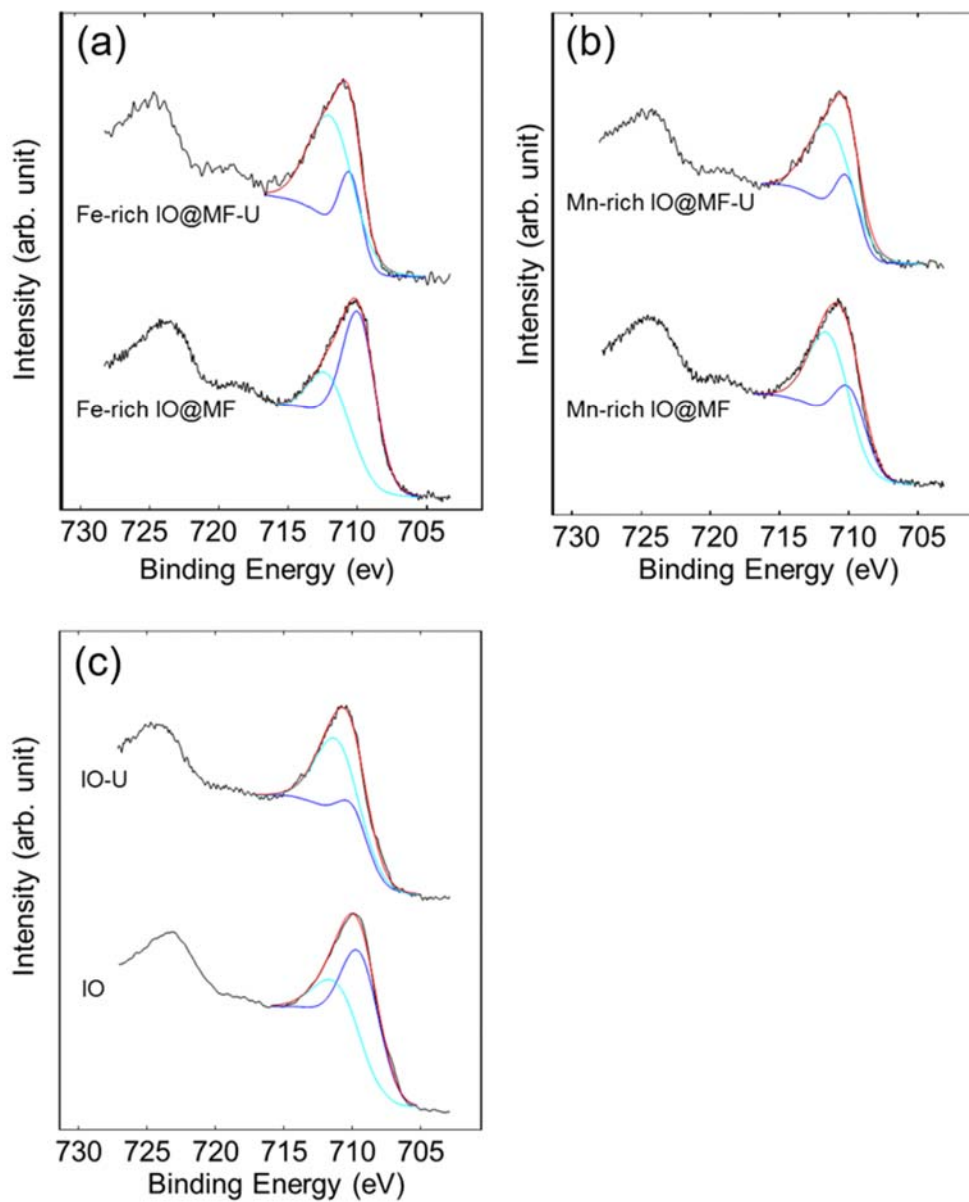
Figure 4.S10 XPS spectra of the iron (Fe) 2P spectra for the sample (Fe rich IO@MF (A), Mn-rich IO@MF (B), and IO (C)) before and after uranium (U) sorption. The black lines are the raw data and the red lines are the fitted curves based on curve fitting using V_α (blue) and V_β (sky blue). The ratio of Fe(II) to Fe(III) was calculated by $(V_\alpha)/(V_\beta)$ in the XPS spectra of Fe $2P_{3/2}$ from the sample before and after the U sorption measurement.
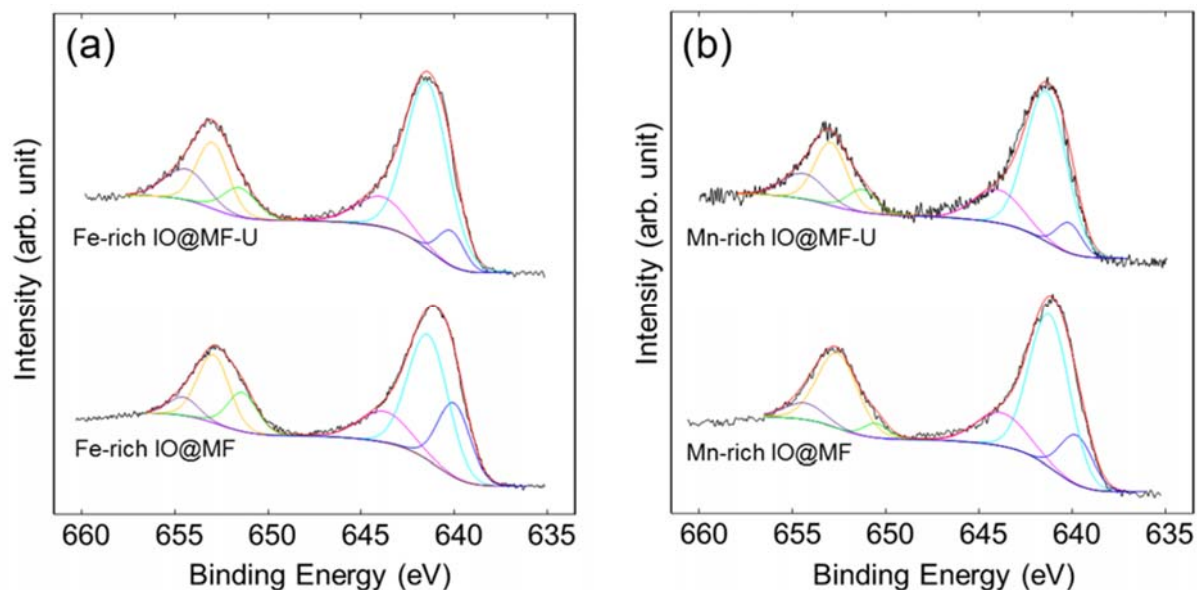
Figure 4.S11 XPS spectra of the manganese (Mn) 2P spectra for the sample (Fe rich IO@MF (A) and Mn-rich IO@MF (B)) before and after uranium (U) sorption. The black lines are the raw data and the red lines are the fitted curves based on curve fitting using V_1 (blue), V_2 (sky blue), V_3 (pink), V_4 (green), V_5 (orange), and V_6 (purple). The ratio of Mn(II)/Mn(III)/Mn(IV) was calculated by $(V_1+V_4)/(V_2+V_5)/(V_3+V_6)$ in the XPS spectra of Mn 2P from the sample before and after the U sorption measurement.
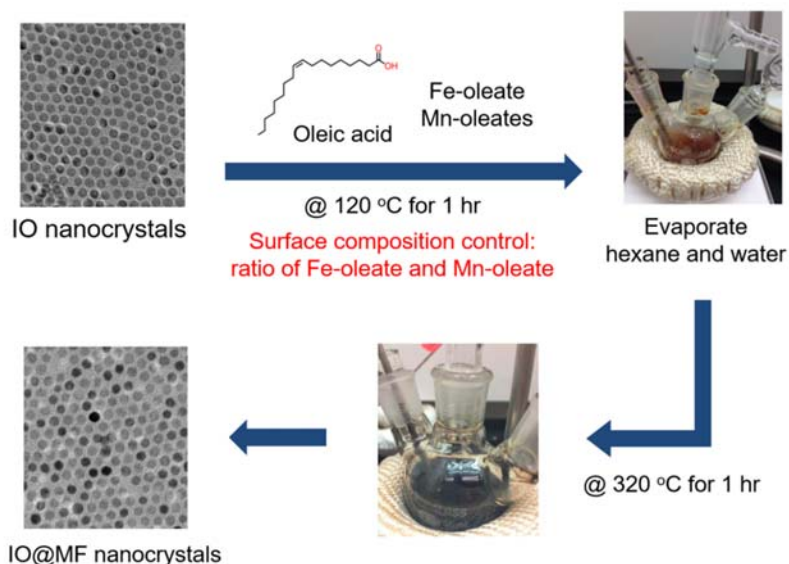
Figure 4.S12 Schematic of IO@MnxFeyO4 (core@shell structured) nanocrystal synthesis

Table 4.S1 The information of average coercivity ($H_C = (H_{RC} + H_{LC}) / 2$) and exchange bias ($H_E = (H_{RC} - H_{LC}) / 2$) values of a series of magnetic nanoparticles measured by hysteresis loops.

| | @300K | | | | @2K | | | |
| | H_C (Oe) | | | | H_C (Oe) | | | |
	H_{LC}	H_{RC}	H_C	H_E	H_{LC}	H_{RC}	H_C	H_E
Iron oxide@Mn_xO_y	15.40	14.35	14.88	-0.53	351.12	309.83	330.48	-20.65
Fe_3O_4	11.83	11.37	11.60	-0.23	233.86	226.08	229.97	-3.89
$MnFe_2O_4$	11.53	11.67	11.60	-0.07	113.50	102.51	108.0	-5.50
Mn_2FeO_4	10.18	10.34	10.26	-0.08	1418.76	1311.21	1364.99	-53.78
Manganese oxide	13.68	12.49	13.08	-0.60	4096.11	3546.91	3821.51	-274.60

Table 4.S2 The information of the sorption isotherm of oleylphosphate stabilized IO@MF, MF, and IO nanocrystals at pH 5.6, 7.0, and 8.5.

		IO@MF@OP			MF@OP			IO@OP		
Langmuir	pH	5.6	7.0	8.5	5.6	7.0	8.5	5.6	7.0	8.5
	q_{max} (mg U/g NC)	1428.6	1428.6	1000.0	1666.7	1428.6	1111.1	833.3	714.3	625.0
	K_L (L/mg)	0.8	0.7	3.3	0.5	0.9	1.3	0.7	2.0	2.7
	R^2	0.985	0.990	0.953	0.984	0.989	0.976	0.924	0.991	0.937
Freundlich	K_F (L/g)	532.2	522.1	597.3	429.2	585.2	496.0	275.2	398.4	398.4
	n	2.05	1.94	0.30	1.58	1.80	2.15	1.05	4.01	4.01
	R^2	0.856	0.884	0.689	0.884	0.905	0.838	0.847	0.974	0.847

Table4.S3 XPS binding energies and the area under the curve of individual peaks of the uranium (U) 4f spectrum for the sample after uranium sorption. The concentration of each of oxidation state of U(IV) and U(VI) is V_a+V_c and V_b+V_d, respectively.

Samples	V_a	V_b	V_c	V_d	U(IV)/U(VI)
Fe-rich IO@MF	32.15 (380.28 eV)	19.92 (381.80 eV)	32.93 (391.07 eV)	15.00 (392.65 eV)	65.08/34.92
IO	33.50 (380.55 eV)	25.04 (381.60 eV)	24.78 (391.23 eV)	16.68 (392.13 eV)	58.28/41.72
Mn-rich IO@MF	26.10 (380.58 eV)	32.09 (381.65 eV)	25.98 (391.17 eV)	15.84 (392.62 eV)	52.08/47.92
Uranyl (VI) nitrate	0 (380.57 eV)	58.60 (381.71 eV)	0 (391.23 eV)	41.40 (392.55 eV)	0

Table 4.S4 XPS binding energies and the area under the curve of individual peaks of the iron (Fe) 2P spectrum for the sample before and after uranium sorption. The concentration of each of oxidation state of Fe(II) and Fe(III) is V_α and V_β, respectively.

Samples	V_α	V_β	Fe(II)/Fe(III)
Fe-rich IO@MF	74.74 (709.46 eV)	25.26 (711.78 eV)	74.74/25.26
Fe-rich IO@MF-U	25.41 (710.07 eV)	74.59 (711.39 eV)	25.41/74.59
IO	68.43 (709.32 eV)	31.57 (710.98 eV)	68.43/31.57
IO-U	30.51 (709.87 eV)	69.49 (710.82 eV)	30.51/69.49
Mn-rich IO@MF	37.32 (709.81 eV)	62.68 (711.32 eV)	37.32/62.68
Mn-rich IO@MF-U	27.07 (710.09 eV)	72.93 (711.20 eV)	27.07/72.93

Table 4.S5 XPS binding energies and the area under the curve of individual peaks of the manganese (Mn) 2P spectrum for the sample before and after uranium sorption. The concentration of each of oxidation state of Mn(II), Mn(III), and Mn(IV) is V_1+V_4, V_2+V_5, and V_3+V_6, respectively.

Samples	V_1	V_2	V_3	V_4	V_5	V_6	Mn(II)/Mn(III)/Mn(IV)
Fe-rich IO@MF	18.31 (640.02 eV)	38.07 (641.42 eV)	12.40 (643.76 eV)	9.35 (651.38 eV)	17.50 (652.94 eV)	4.37 (654.57 eV)	27.66/55.57/16.77
Fe-rich IO@MF-U	6.35 (640.21 eV)	50.63 (641.51 eV)	10.82 (643.99 eV)	7.15 (651.56 eV)	15.36 (653.03 eV)	9.69 (654.46 eV)	13.5/65.99/20.51
Mn-rich IO@MF	11.55 (637.77 eV)	44.84 (641.22 eV)	12.81 (643.76 eV)	2.69 (650.55 eV)	23.22 (652.61 eV)	4.89 (654.33 eV)	14.24/68.06/17.70
Mn-rich IO@MF-U	6.33 (640.18 eV)	49.33 (641.41 eV)	13.21 (643.99 eV)	5.86 (651.28 eV)	16.33 (652.97 eV)	8.94 (654.45 eV)	12.19/65.66/22.15

Chapter 5: Surface Functionalized Ferrites for Single- and Multi-Sorption of Arsenic (V), Chromium (VI), and Uranium (VI)

*To be submitted in peer review journal

5.1. Overview

Surface functionalized ferrite nanocrystals (NCs) were evaluated for single- and multisorbate scenarios considering arsenic (V), chromium (VI), and uranium (VI) in varied water chemistries (deionized (DI), ground and sea water). Multi sorbate systems were further examined for competitive and/or cooperative effects. Synthesized manganese ferrite ($MnFe_2O_4$), were compared with iron oxide (Fe_3O_4), and manganese oxide (Mn_xO_y) nanocrystal cores. The positively charged cetyltrimethylammonium bromide (CTAB) and negatively charged oleyl phosphate (OP) were used as organic coating agents. $MnFe_2O_4$ NCs showed better sorption performance and colloidal stability than Fe_3O_4 and Mn_xO_y when NCs were functionalized with the same surfactant coating. For these, the maximum sorption densities for As(V), Cr(VI), and U(VI) were 2.62, 3.43, and 4.27 mmol g^{-1}, respectively. Number of organic molecules loading on the surface of $MnFe_2O_4$ NCs was outstanding and high organic grafting density provides a large number of sorption sites (functional group) for target sorbate and high repulsive energy (osmotic and elastic-steric interaction) for enhanced stability. In the As(V) and Cr(VI) multi-sorbate system, nano-sorbents showed higher As(V) sorption preference over Cr(VI). This As(V) sorption preference was further verified using quartz crystal microbalance (QCM) via a CTAB mimic polymer (Poly(diallyldimethylammonium chloride)). In the As(V) and U(VI) multi-sorbate system, removal rates were significantly enhanced with CTAB functionalized $MnFe_2O_4$

70

(MnFe$_2$O$_4$@CTAB) because increased local As(V) concentration at the surface of NCs promoted uranyl arsenate precipitation.

5.2. Introduction

Treatment of heavy metals and metalloids has received significant interest due to regulatory requirements and related toxicity concerns.[78-79] Hazardous heavy metals and metalloids, are globally distributed and often occur as mixed (or multi-contaminate) systems.[252-254] For example, As(V) and Cr(VI) simultaneously occur in the case of chromated copper arsenate (CCA), which is been widely used as an antimicrobial treatment (e.g. utility poles, fence, and playground equipment, etc.) to prevent fungal and bacterial decay.[255-256] While CCA has been prohibited in U.S. due to its toxicity, CCA treated equipment and furniture are still used.[257] Additionally, uranium ore, which can contain 1.2 to 10 weight percent of arsenic as uranyl and arsenate readily form mineral precipitates (uranyl arsenate), leading to simultaneous contamination scenerios.[258]

For sorption/separation technologies, nanomaterials provide an large surface area and reactivity for target contaminants.[71-72, 259] Organic-inorganic hybrid nano composites such as organic coated nanomaterial have been regarded as next generation nano sorbents as they offer a controllable rigid inorganic body (often magnetic) and a flexible organic coating with the tunable functional groups.[33-35] For example, the affinity for heavy metal contaminants (Pb, Cu, Hg, Ag, Cd, Co, and Ti) is described by Warner et al. for a series of organic coated magnetite NCs.[96] Our previous research also demonstrated that surface-based surfactants having a positively charged functional groups (e.g. cetyltrimethylammonium bromide (CTAB) and polyethylenimine (PEI)) have excellent sorption performance for As(V) and Cr(VI).[260] In addition, phosphate functional groups, such as oleyl phosphate (OP)[45] and monododecyl phosphate (SDP)[249] have shown the highest U(VI) affinity since uranyl ions were thermodynamically favored by phosphate.[261]

While many of the aforementioned materials show excellent sorption properties for sinlge sobates, few have been evaluated for multi-sorbate loading and separation. Here, we evaluate and compare single and multi sorbate systems with a focus on competitive and/or cooperative effects for a range of water chemistries. For inorganic core particles, same sized manganese ferrite ($MnFe_2O_4$), iron oxide (Fe_3O_4), and manganese oxide (Mn_xO_y) NCs are compared. Synthesized NCs were further organic functionalized using CTAB and OP via ligand encapsulation method. Results demonstrate that $MnFe_2O_4$ NCs shows better sorption performance toward As(V), Cr(VI), and U(VI) than Fe_3O_4 and Mn_xO_y when NCs were coated with same functional surface coating. This result is due to enhanced ligand density of CTAB and OP loading on the surface of $MnFe_2O_4$ NCs. In the case of two sorbates, Cr(VI) sorption capacity declined significantly in presence of As(V) due to competition for adsorption sites (here as the amine functional group of CTAB). The As(V) sorption preference (in a dual As(V) and Cr(VI) multi sorbate system) was further evaluated using Quartz crystal microbalance with dissipation monitoring (QCM-D) by loading Poly(diallyldimethylammonium chloride) on the surface of the Q-sensor. In As(V) and U(VI) multi sorbate systems, positively charged CTAB functionalized $MnFe_2O_4$ NCs ($MnFe_2O_4$@CTAB) showed outstanding removal performance as adsorbed As(V) on the surface of NCs enhanced further sorption and precipitation of U(VI).

5.3. Results and discussion

5.3.1. Synthesis and Characterization of Metal Oxide Nanocrystals

Three different composite metal oxide (manganese ferrite, iron oxide, and manganese oxide) nanocrystals (NCs) were precisely synthesized by decomposition of both Fe-oleate or/and Mn-oleate as precursors in the presence of excess oleic acid at high temperature (320°C).[45, 262] As synthesized NCs were monodisperse in a non-polar solvent (hexane).[45, 65] Figure 5.1 shows the

TEM images for the synthesized NCs and their sizes and distributions. Manganese ferrites, iron oxide, and manganese oxide NCs were 10.0 ± 0.7, 9.3 ± 0.9, and 10.6 ± 1.6 nm, respectively. As reported by our previous study and others,[45, 65, 263] crystalline structures of the synthesized manganese iron oxide and iron oxide NCs matches with the crystalline structure of $MnFe_2O_4$ (JCPDS Card # 380430) and Fe_3O_4 (JCPDS Card # 190629), respectively. Manganese oxide NCs matches with MnO (JCPDS Card # 070230) and Mn_3O_4 (JCPDS Card # 240734), which has been previously reported as a MnO core with Mn_3O_4 shell structure (Figure 5.S1 (a)).[65, 262]
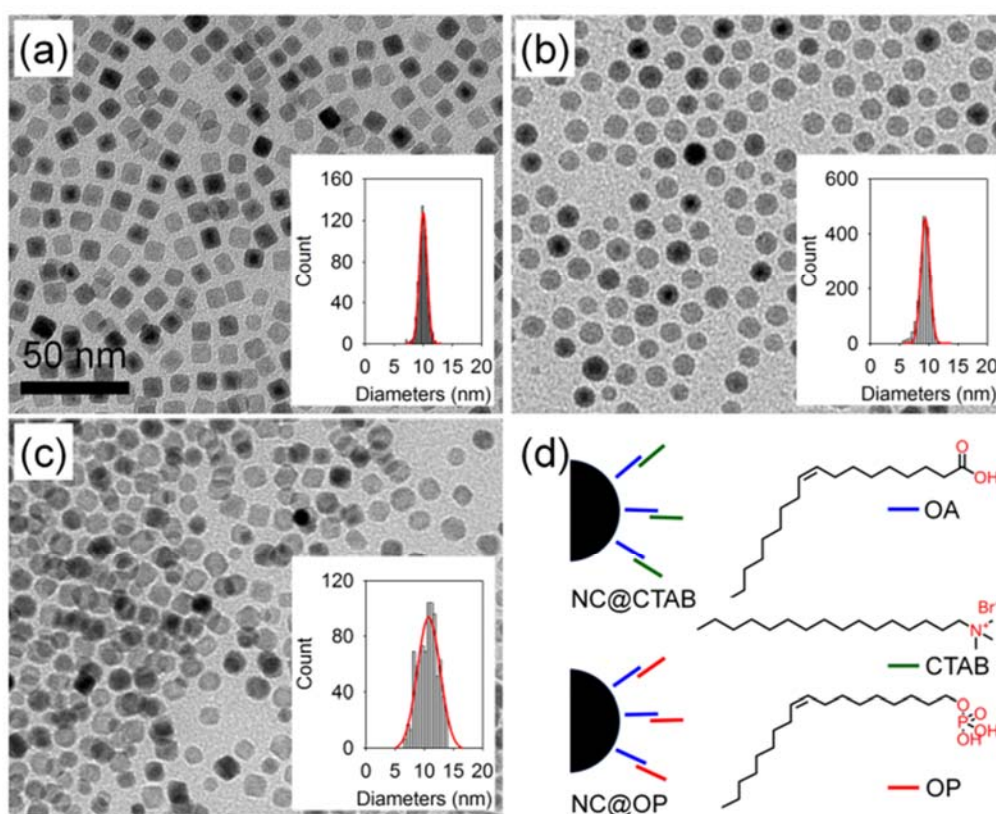
Figure 5.1 TEM images of monodisperse metal oxide NCs (a) manganese ferrites, (b) iron oxide, and (c) manganese oxide. The inset Figure presents the histograms of the size distribution of NCs. The average diameter and its standard deviation were 10.0 ± 0.7, 12.3 ± 1.0, 9.3 ± 0.9, and 10.6 ± 1.6 nm, respectively.

Synthesized metal oxide NCs were phase transferred from organic solvent into water through ligand encapsulation method using cetyltrimethylammonium bromide (CTAB) and oleyl phosphate (OP), as discussed previously in this thesis.[45, 260] Positively charged CTAB is an favorable coating material for As(V) and Cr(VI), while OP having negative phosphate functional group, has been demonstrated to be favorable for U(VI) in our previous studies.[45, 260] Phase transferred NCs were characterized by dynamic light scatter (DLS) at pH 7 to measure hydrodynamic diameter (D_H) and zeta potential (ζ). As shown in Figure 5.S1 (b), D_H were 22.7, 24.1, and 23.4 nm for CTAB functionalized manganese ferrite ($MnFe_2O_4$@CTAB), magnetite (Fe_3O_4@CTAB), and manganese oxide (Mn_xO_y@CTAB) NCs, respectively. D_H of OP coated manganese ferrite ($MnFe_2O_4$@OP), magnetite (Fe_3O_4@OP), and manganese oxide (Mn_xO_y@OP) NCs were 22.3, 25.2, and 21.9 nm, respectively. ζ values of the NCs were 23.7, 23.4, and 25.6 mV, respectively for $MnFe_2O_4$@CTAB, Fe_3O_4@CTAB, and Mn_xO_y@CTAB, and -27.7, -27.3, and -26.3 mV, respectively for $MnFe_2O_4$@OP, Fe_3O_4@OP, and Mn_xO_y@OP (Figure 5.S1 (c)).

Surfactant loadings on $MnFe_2O_4$@CTAB, Fe_3O_4@CTAB, and Mn_xO_y@CTAB were ca. 16,000, 5,000, and 3,000 molecules per NC, respectively (Figure 5.S1 (d)). The numbers of OP per NC were 19,000, 7,000, and 4,000 for $MnFe_2O_4$@OP, Fe_3O_4@OP, and Mn_xO_y@OP, respectively. Surfactant loading was varied depending on core metal oxide composition. Interestingly, surfactant loading by both CTAB and OP was highest for $MnFe_2O_4$ followed by Fe_3O_4 and Mn_xO_y. The surface stabilizers, such as CTAB and OP, also reduce the thermodynamic energy of NCs to prevent particle aggregation.[264]

5.3.2. As(V), Cr(VI), and U(VI) Single Sorbate System

As expected, high colloidal stability has an advantage for sorption performance through the maintenance of available surface area. Before evaluating the sorption performance of the

synthesized NCs, their colloidal stabilities were investigated by measuring the critical coagulation concentration (CCC). As shown in Figure 5.S2 (a), CCC values for Mn_xO_y@CTAB were 259 mM in NaCl and 133 mM in $CaCl_2$. The counter ion of Mn_xO_y@CTAB is the anion Cl^-, thus divalent cation Ca^{2+} does not significantly affect their colloidal stability. $MnFe_2O_4$@CTAB and Fe_3O_4@CTAB were colloidally stable under high mono- or di-valent cation concentrations; NCs maintained their initial diameter in up to 1 M of NaCl and in up to 1M of $CaCl_2$. As presented in Figure 5.S2 (b), (c), and (d), CCC values for OP coated NCs were 449.6, 694.5, and 1129.5 mM in NaCl and 6.9, 7.1, and 9.9 mM in $CaCl_2$ for Mn_xO_y, Fe_3O_4, and $MnFe_2O_4$ NCs, respectively. The highest number of organic molecules loaded $MnFe_2O_4$ showed the best colloidal stability. We speculate that the grafting density plays critical role in colloidal stability by providing effective repulsive energies, such as elastic-steric and osmotic repulsion.[36-39]
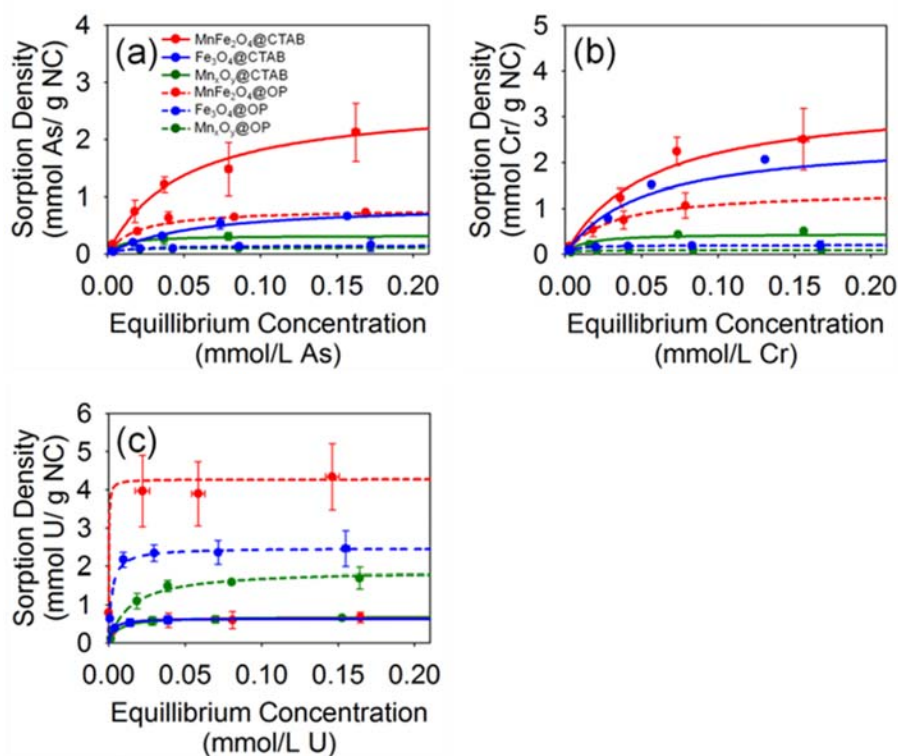
Figure 5.2 As(V) (a), Cr(VI) (b), and U(VI) sorption isotherm on metal oxide ($MnFe_2O_4$ (red), Fe_3O_4 (blue), and MnxOy (green)) NCs coated with the positively charged surface stabilizer (CTAB (solid line)) or the negatively charged organic coating (OP (dotted line)). Dot plots with error bars and line plots present experiment measurement values with standard deviations and Langmuir isotherm fittings, respectively.

The sorption performances of synthesized metal oxide NCs were first explored in single sorbate system. As expected, positively (oppositely) charged CTAB functionalized NCs ($MnFe_2O_4$@CTAB, Fe_3O_4@CTAB, and Mn_xO_y@CTAB) showed better As(V) and Cr(VI) sorption performance than negatively charged OP coated NCs ($MnFe_2O_4$@OP, Fe_3O_4@OP, and Mn_xO_y@OP) (Figure 5.2 (a) and (b)). The maximum sorption density (q_{max}) of CTAB stabilized NCs for As(V) was 2.62 ± 0.15, 0.86 ± 0.02, and 0.31 ± 0.03 mmol g^{-1} for $MnFe_2O_4$, Fe_3O_4, and Mn_xO_y, respectively and q_{max} of OP functionalized NCs towards As(V) was 0.97 ± 0.03, 0.14 ± 0.02, and 0.06 ± 0.01 mmol g^{-1} for $MnFe_2O_4$, Fe_3O_4, and Mn_xO_y, respectively. The q_{max} of CTAB stabilized NCs for Cr(VI) was 3.43 ± 0.19, 2.53 ± 0.01, and 0.45 ± 0.02 mmol g^{-1} for $MnFe_2O_4$, Fe_3O_4, and Mn_xO_y, respectively and q_{max} of OP functionalized NCs towards Cr(VI) was 1.39 ± 0.09, 0.20 ± 0.03, and 0.09 ± 0.01 mmol g^{-1} for $MnFe_2O_4$, Fe_3O_4, and Mn_xO_y, respectively. We speculate that positively charged quaternary amine group of CTAB is the key binding sites for both As(V) and Cr(VI) as they exist in an anionic form above pH ca. 2.2.[260] For U(VI) removal, negatively charged OP functionalized NCs showed outstanding sorption performance (Figure 5.2 (c)). The phosphate functional group of OP is the dominant sorption site for the uranyl cation.[45] The q_{max} towards U(VI) for OP coated NCs was 4.27 ± 0.38, 2.47 ± 0.13, and 1.91 ± 0.08 mmol g^{-1} NCs for $MnFe_2O_4$, Fe_3O_4, and Mn_xO_y, respectively and q_{max} towards U(VI) for CTAB functionalized NCs was 0.65 ± 0.08, 0.64 ± 0.05, and 0.69 ± 0.04 mmol g^{-1} NCs for $MnFe_2O_4$, Fe_3O_4, and Mn_xO_y, respectively.

In our previous research, $MnFe_2O_4$ showed the highest U(VI) sorption and separation among the expanded series of particle core compositions ($MnFe_2O_4$, Fe_3O_4, and Mn_xO_y) evaluated.[45] In that reports, we also verified that $MnFe_2O_4$ NCs had enhanced (surface) redox potentials compared to the Fe_3O_4, and Mn_xO_y NCs.[45] Here, we found out $MnFe_2O_4$ NCs showed the highest surfactant loading comparatively, which is key for sorption sites and stability. The sorption performance for synthesized NCs was also compared with commercial $MnFe_2O_4$, Fe_3O_4, and MnO NCs, which demonstrated lower q_{max} than all as synthesized NCs regardless of the composition of the NCs and contaminants (Figure 5.S3). The q_{max} of commercial NPs was below 0.14 ± 0.01 mmol g^{-1} for As(V), 0.04 ± 0.00 mmol g^{-1} NCs for Cr(VI) and 0.04 ± 0.00 mmol g^{-1} NCs for U(VI). Two reasons to account for the differences including 1) the commercial NCs were severely aggregated in water phase compared to the synthesized NCs (Figure 5.S4) and 2) The presence of organic stabilizer with specific functional groups (CTAB and OP) increased sorption capacity of synthesized NCs as compared to the commercial NCs – i.e. increased favorable surface sites.
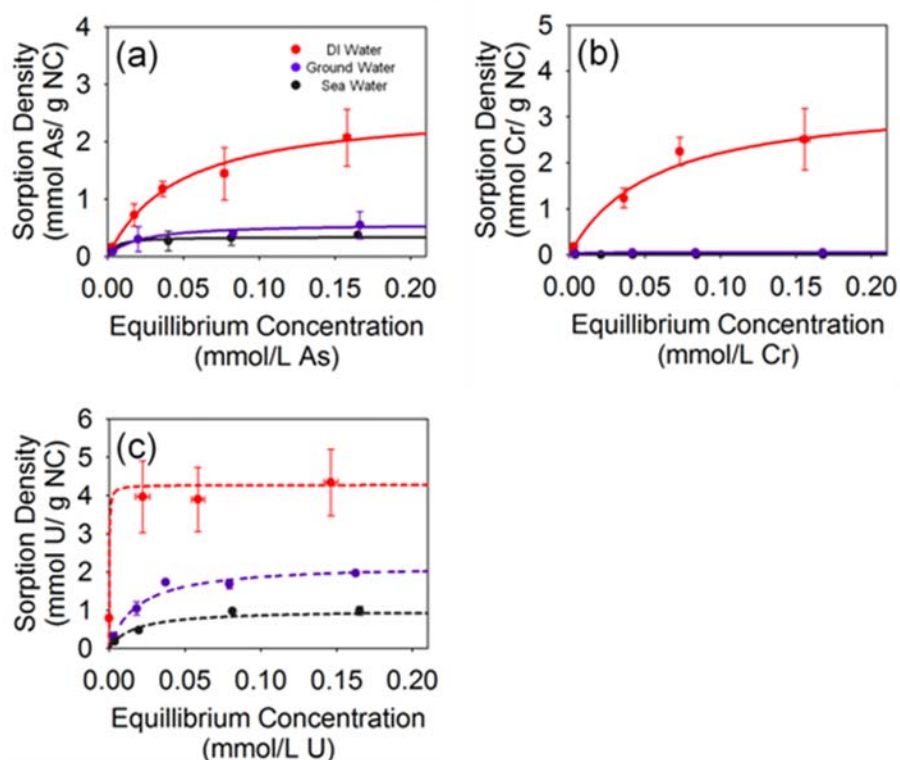
Figure 5.3 As(V) (a) and Cr(VI) (b) sorption isotherm on manganese ferrite (MnFe$_2$O$_4$) NCs coated with CTAB (solid line) and U(VI) (C) sorption isotherm on MnFe$_2$O$_4$ with OP (dotted line) in DI water (red), synthesized ground water (purple), and sea water (black).

5.3.3. Effects Water Chemistry on Single Sorbate Systems

To understand how environmentally relevant ionic conditions affects these processes, we explored the sorption behaviors in DI water, synthesized groundwater, and synthesized seawater using MnFe$_2$O$_4$@CTAB for As(V) and Cr(VI) and MnFe$_2$O$_4$@OP for U(VI). The composition of the synthesized ground water and seawater are presented in Table 5.S1.[265-266] As presented in Figure 5.3, sorption capacities for As(V) and U(VI) decreased in groundwater and sea water conditions. The q$_{max}$ towards As(V) was 2.62 ± 0.15, 0.57 ± 0.08, and, 0.34 ± 0.05 mmol g^{-1} for DI, ground water, and, sea water, respectively and q$_{max}$ towards U(VI) was 4.27 ± 0.38, 2.21 ± 0.05, and, 1.00 ± 0.03 mmol g^{-1} for DI, ground water, and, sea water, respectively. The Cr(VI) sorption density for MnFe$_2$O$_4$@CTAB was dramatically reduced in the ground and sea water

conditions. The q_{max} towards Cr(VI) was 3.43 ± 0.19, 0.05 ± 0.01, and, 0.00 ± 0.00 mmol g^{-1} for DI, ground water, and sea water, respectively. The surface area of $MnFe_2O_4$ did not play critical role in ionic conditions dependent sorption performance because NCs maintained their initial size after sorption isotherm test except for the case of U(VI) sorption in synthesized seawater (Figure 5.S5).

To further explore the reason(s) why sorption affinities were decreased in the ground and sea water conditions, sorption densities were explored using each divalent cation and divalent anion of the synthesized ground and seawater (Mg^{2+}, Ca^{2+}, and SO_4^{2-}). In addition, effects of total ionic strength of groundwater and seawater were evaluated using monovalent ions (NaCl). As shown in Figure 5.S6 (a), total ionic strength is not a significant factor in As(V) sorption performance. Normalized sorption densities for total ionic strength of groundwater (C7) and seawater (C4) were 0.84 and 0.98, respectively. For the Cr(VI) sorption, both total ionic strength of groundwater and seawater critically blocked the Cr(VI) sorption (Figure 5.S6 (b)). Normalized sorption densities were 0.30 (C7) and 0.00 (C4). The divalent cations (Mg^{2+} and Ca^{2+}) have a significant effect on Cr(VI) sorption density; normalized sorption density was 0.0 (C1), 0.15 (C2), and 0.64 (C5). The ionic strength influence the double layer thickness of $MnFe_2O_4$@CTAB,[267] affecting binding for both As(V) and Cr(VI). In the presence of sulfate ions (SO_4^{2-}), As(V) sorption performance for $MnFe_2O_4$@CTAB was significantly hindered; normalized sorption densities were 0.18 (C3) and 0.26 (C6). Also, small amount of sulfate ions significantly influence the Cr(VI) sorption affinities; normalized sorption densities was 0.00 (C3) and 0.02 (C6). Taken togethers, we conclude that the divalent anions, including sulfate, act as competing ions for both As(V) and Cr(VI). Contrary to the As(V) and Cr(VI), sulfate ions did not have a significant effect on the U(VI) sorption performance on $MnFe_2O_4$@OP (Figure 5.S6

79

(c)). Normalized sorption density was above 0.8 in presence of sulfate ions. However, divalent cations, such as Mg^{2+} and Ca^{2+}, suppressed sorption U(IV) affinity; normalized sorption density was 0.27 (C1), 0.26 (C2), and 0.67 (C5). Also, with increasing ionic strength, normalized U(VI) sorption density decreased to 0.53 in ground water and 0.20 in sea water due to charge screening of $MnFe_2O_4@OP$.[45]

5.3.4. Multi Sorbate Systems

Multi sorbate systems were explored to evaluate the competitive and/or cooperative effects when two or more contaminants are involved in sorption processes simultaneously. Manganese ferrite ($MnFe_2O_4$) NCs, which showed outstanding sorption performance in single sorbate systems, were used for the multi contaminant sorption study. To investigate every possible multi sorbate system scenerio, four different systems As(V) and Cr(VI); As(V) and U(VI); Cr(VI) and U(VI); and As(V), Cr(VI), U(VI) were evaluated with comparison of single sorbate systems. Among these, As(V) and Cr(VI) showed significant competitive effects. In the As(V) and U(VI) systems, we could not present the As(V) and U(VI) sorption isotherms as As(V) and U(VI) readily formed uranyl arsenate precipitates.[258] Therefore, we focus our discussion on As(V) and Cr(VI); As(V) and U(VI) systems. And other multi sorbate systems (Cr(VI) and U(VI); As(V), Cr(VI), and U(VI)) are presented in Supplementary Information (Figure 5.S7 and S8).

5.3.5. As(V) and Cr(VI) Multi Sorbate System

Figure 5.4 (a) and (b) present the Cr(VI) sorption isotherm for multi (As(V) and Cr(VI)) and single sorbate systems on $MnFe_2O_4@OP$ and $MnFe_2O_4@CTAB$. Cr(VI) sorption on $MnFe_2O_4@OP$ was strongly hindered in the presence of As(V). The q_{max} for Cr(VI) was 1.39 ± 0.09 mmol g^{-1} for the single Cr(VI) system and the q_{max} for multi sorbate systems was below 0.23 ± 0.04 mmol g^{-1}. With $MnFe_2O_4@CTAB$, Cr(VI) sorption performance was significantly

decreased in the presence of As (V). The q_{max} for Cr(VI) was 3.43 ± 0.19 mmol g^{-1} for single

system and 1.62 ± 0.08 mmol g^{-1} in the presence of As(V). Regardless of surfactant coating of

the NCs, Cr(VI) sorption capacity was greatly reduced in the presence of As(V) due to the

competition for sorption sites.[268] Within the standard deviation of the q_{max} values, NCs had no

influence on As(V) sorption performance in the presence of Cr(VI); resulting in 2.72 ± 0.22 and

2.62 ± 0.15 mmol g^{-1} for $MnFe_2O_4$@CTAB with and without Cr(VI), respectively and $0.96 \pm$

0.05 and 0.97 ± 0.03 mmol g^{-1} for $MnFe_2O_4$@OP with and without Cr(VI), respectively (Figure

5.4 (c)).

To further quantify the sorption preference between As(V) and Cr(VI), real time sorption

behaviors were investigated using quartz crystal microbalance with dissipation (QCM-D) by

monitoring. Real time frequency shifts obtained by QCM-D can be correlated with a variation of

deposited total mass based on Sauerbrey relationship (Equation 5.1).[223]

$$\Delta m = -\frac{C \Delta F_n}{n} \qquad \text{(Equation 5.1)}$$

Here, m is the total deposited mass on the Q-sensor, C is the quartz sensor constant, F_n is the

shift in resonance frequency, and n is the resonance number (1, 3, 5, 7, 11 and 13). Dissipation

obtained by QCM-D presented viscoelastic properties of the adsorbed layer on the Q-sensor.

The dissipation during the oscillation of Q-sensor is described below (Equation 5.2).[225, 269]

$$D = \frac{E_d}{2\pi E_s} \qquad \text{(Equation 5.2)}$$

Where, D is the energy dissipation, E_d is the energy dissipated during one oscillation, and E_s is

the energy stored in the oscillation system. To mimic the quaternary amine group (functionality

head group of CTAB), we loaded the quaternary amine polymer Poly(diallyldimethylammonium

chloride) (PDDA) on the surface of the silica Q-sensor by "grafting to" method;[224] PDDA was

anchored from the PDDA solution (2.0 wt.% in H_2O) to the Q-sensor surface. After grafting

PDDA, we re-stabilized the PDDA coated Q-sensors using DI water (pH 7) to rinse and eliminate weakly anchored PDDA and close the viscosity gap (Figure 5.S9). For these, one must also consider potential changes in the polymer configuration, and thus the Sauerbrey relationship is not fully valid[225, 270] because PDDA is linear polymer. However, we can confirm whether the PDDA polymer interacts with As(V) and Cr(VI) or not by monitoring real time frequency and dissipation shifts.
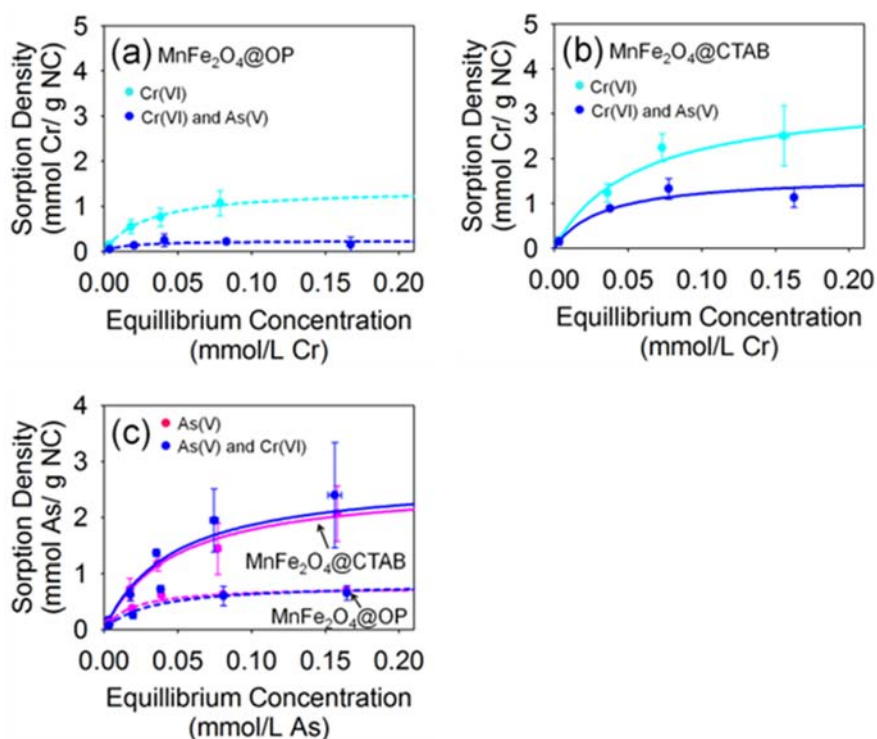
Figure 5.4 Single and multi sorption isotherm on MnFe$_2$O$_4$ NCs coated with CTAB (solid line) or OP (dotted line); single sorbate systems (As(V) (pink) and Cr(VI) (cyan)) and multi sorbate systems (As(V) and Cr(VI) (blue)).

To explore the As(V) and Cr(VI) sorption preference, we flowed each of an As(V) or Cr(VI) solution (1 mM) at pH 7 ove the PDDA coated sensor. As shown in Figure 5.5, frequency and dissipation of PDDA coated Q-sensor significantly decreased after applying 1 mM As(V) solution. In the Cr(VI) solution, a similar dissipation decrease was observed with small

frequency decrease. After signal stabilization, we switched the influent solution from As(V) to Cr(VI) and Cr(VI) to As(V), respectively. As(V) bound to PDDA coated Q-sensor had no significant frequency and dissipation change upon the addition of 1 mM Cr(VI) solution. In the case of Cr(VI) sorbed onto PDDA frequency and dissipation shift where obvious when As(VI) solution was applied, indicating surface exchange. This observation provides strong evidence for an As(V) sorption preference on amine functionality head group over Cr(VI).
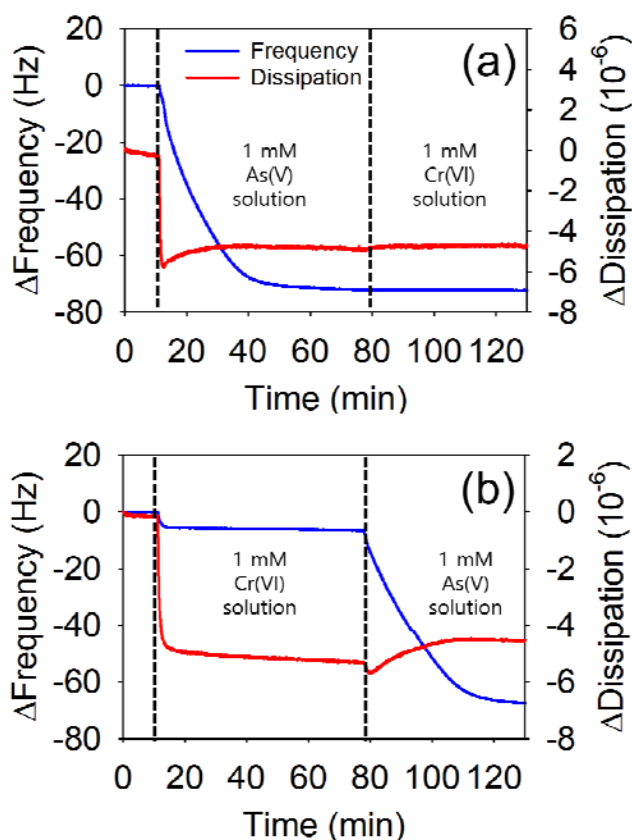
Figure 5.5 Time dependent frequency and dissipation shift (overtone n = 3) of the PDDA coated Q-sensor. At 10 min, 1 mM As(V) solution (a) or 1 mM Cr(VI) solution (b) were applied to the Q-sensor. Then at 77 min, after frequency and dissipation signals were stabilized, 1 mM Cr(VI) solution (a) and 1mM As(V) solution (b) were flowed to the Q-sensors.

5.3.6. As(V) and U(VI) Multi Sorbate System

As mentioned, As(V) and U(VI) multi sorbate systems were not explored via sorption isotherms, due to the formation of uranyl arsenate precipitates.[258] However, specific evaluation of uranyl

arsenate precipitates are interesting due better understanding of remediation of uranium mine waters.[271] To explore removal performance for the NCs in the presence of both As(V) and U(VI), we applied MnFe$_2$O$_4$ NCs (100 ppm) at pH 7 with same initial As(V) and U(VI) (concentration) ratios for low and high initial concentrations (0.004 and 0.021 mM). As shown in Figure 5.6, without NCs (blank), 11.9% of As(V) and 13.5% of U(VI) were removed in low initial concentration and 85.4% of As(V) and 84.8% of U(VI) were removed in high initial concentration due to the uranyl arsenate mineral precipitation.

In the presence of MnFe$_2$O$_4$@CTAB, As(V) and U(VI) removal rates increased in both low and high concentrations. 80.6% of As(V) was removed and 99.1% of U(VI) was removed for low initial concentration. At high concentration, 97.6% of As(V) was removed and 99.8% of U(VI) was removed. The functionality head group (amine) of MnFe$_2$O$_4$@CTAB had a strong affinity for As(V), resulting in enrichment of local As(V) concentration at the surface of the NCs. We speculate that this increased local As(V) concentration promotes additional U(VI) sorption and precipitation as adsorbed As(V) become thermodynamically stable with U(VI) along with potential surface-based concentration polarization.[45, 272] With negatively charged MnFe$_2$O$_4$@OP, U(VI) removal also increased; 93.6% removal in low concentration and 96.6% removal in high concentration. However, MnFe$_2$O$_4$@OP had no significant influence on As(V) removal; 7.8% removal in low concentration and 15.3% removal in high concentration. We hypothesize that adsorbed U(VI) on the phosphate functional group is likely to be thermodynamically stable with the phosphate functional group, resulting in no additional As(V) sorption and precipitation.

To further investigate these observations, precipitates were analyzed by XRD. Figure 5.S10 presents XRD patterns of the precipitate samples; precipitates were prepared under 1 mM uranyl and arsenate with or without the NCs (500 ppm) at pH 7 for 24 hr. Additionally, uranyl

phosphate precipitate was prepared to compare the U(VI) precipitate with MnFe$_2$O$_4$@OP because OP has phosphate functional head group. After preparing the precipitates, NC samples were extracted by external magnetic force or filtered. Then the samples were washed several times (over 3 times) to exclude the solution precipitates. XRD patterns for uranyl arsenate mineral precipitates matched with trögerite (UO$_2$HAsO$_4$·4(H$_2$O)) with a 1:1 ratio of U(VI) and As(V). XRD for uranyl phosphates corresponded with hydrogen uranyl phosphate (UO$_2$HPO$_4$·4(H$_2$O)) at a one to one ratio. For MnFe$_2$O$_4$@CTAB, uranyl arsenate precipitates were observed on the surface of NCs, suggesting adsorbed arsenate could promote uranyl arsenate precipitates. In the precipitates with MnFe$_2$O$_4$@OP, however, there was no crystalline peak, indicating that precipitates are amorphous or just simply MnFe$_2$O$_4$@OP with strong uranyl binding.
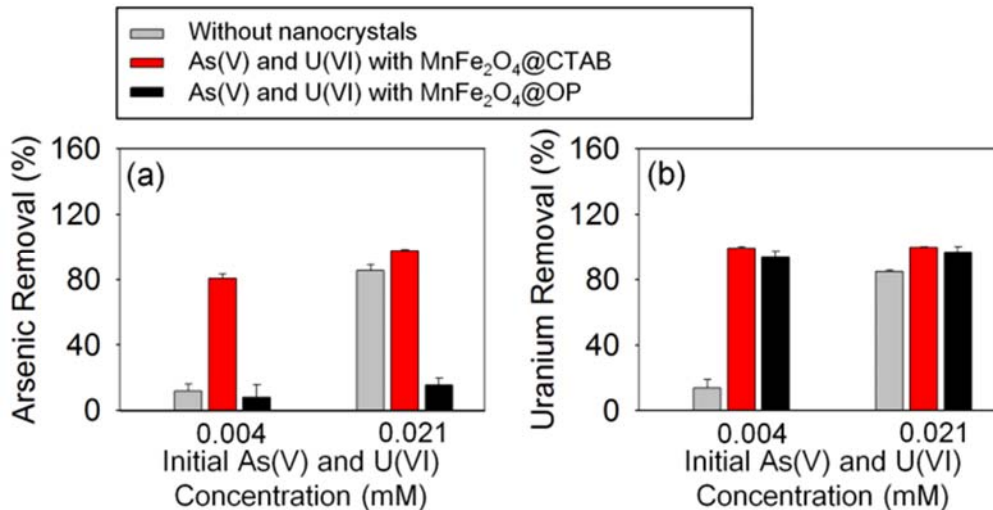
Figure 5.6 As(V) (a) and U(VI) (b) removal with or without MnFe$_2$O$_4$@CTAB and MnFe$_2$O$_4$@OP.

5.4. Experimental

Chemicals.

Chemical material including iron (III) chloride hexahydrate ($FeCl_3 \cdot 6H_2O$, 97%), manganese (II) chloride tetrahydrate ($MnCl_2 \cdot 4H_2O$, 99.99%), oleic acid (OA, technical grade, 90%), 1-octadecene (ODE, technical grade, 90%), cetyltrimethylammonium bromide (CTAB, 95%), ethanol (99.9%), acetone (99.5%), hexane (98.5%), sodium arsenate ($Na_2HAsO_47H_2O$), potassium chromate ($K_2Cr_2O_7$), and Poly(diallyldimethylammonium chloride) were purchased from Sigma-Aldrich. Oleyl phosphate (OP) and sodium oleate (97%) were obtained from TCI America. Uranyl nitrate hexahydrate ($UO_2(NO_3)_2 \cdot 6H_2O$) was purchased from Antec, Inc. Manganese (II) oxide (MnO, 60 mesh, CAS Number 1344-43-0), iron (II, III) oxide (Fe_3O_4, < 50 nm, CAS Number 1317-61-9), and manganese iron oxide ($MnFe_2O_4$, 50 nm, CAS Number 12063-10-4) nano powder were obtained from Sigma-Aldrich; TEM images of commercial nano materials were presented in Figure 5.S11.

Synthesis of Iron Oleate and Manganese Oleate.
Iron oleate (Fe-oleate) and manganese oleate (Mn-oleate) were synthesized by the method reported by An et al.[244] Fe-oleate was synthesized by heating the mixture of iron (III) chloride hexahydrate (40 mmol) and oleic acid (120 mmol) in ethanol (100 g), water (50 g), and hexane (80 g) for 4 hrs at 58 °C. The mixture of manganese chloride tetrahydrate (40 mmol) and oleic acid (80 mmol) in ethanol (100 g), water (50 g), and hexane (80 g) were heated 4 hrs at 58 °C for Mn-oleate synthesis. The resulting metal-oleate (Fe-oleate or Mn-oleate) suspensions were purified over six times using water and ethanol (1:1 volume ratio) and then the purified metal-oleate was extracted using hexane.

Synthesis of Manganese Ferrite, Iron Oxide, and Manganese Oxide Nanocrystals.
Manganese ferrite, iron oxide, and manganese oxide nanocrystals (NCs) were synthesized by the method reported by our previous reasearch.[45] Iron oxide NCs were synthesized by decomposition of Fe-oleate (0.31 mmol) with oleic acid (0.21 mmol) in 1-octadecene (5 g) at

320 °C for 1 hr. Manganese oxide NCs were synthesized by Mn-oleate decomposition at 320 °C; Mn-oleate (0.3 mmol) with oleic acid (0.15 mmol) was used for synthesizing NCs in 1-octadecene (5 g) as a solvent. Manganese ferrite NCs were synthesized by decomposition of the mixture of metal-oleate as precursors (Mn-oleate (0.27 mmol) and Fe-oleate (0.54 mmol)) with oleic acid (2 mmol) in 1-octadecene (5 g) at 320 °C for 1 hr. All NCs were synthesized under argon purging (99.999%). The resulting NCs were washed with ethanol (20 ml) and acetone (25 ml); the purify process was repeated over six times. The purified NCs were stored in the non polar solvent hexane.

Surface Functionalization and Phase Transfer.
Synthesized NCs were organically surface functionalized and phase transferred from the organic solvent (hexane) to water phase by ligand encapsulation method.[40, 51] Cetyltrimethylammonium bromide (CTAB) and oleyl phosphate (OP) were used as phase transfer agents. Particular amounts of surface stabilizer (1 to 10 mmol) were mixed with 0.5 mL nanocrystal (NC) in hexane (particle number of 3.8×10^{17}) and vigorously stirred in 8 mL dionized (DI) water (>18.2 MΩ-cm resistivity, Milli-Q, Millipore Corp). The mixture of phase transfer agents and NCs was probe-sonicated (Qsonica, Q-700, Taperd microtip) for 5 to 10 min at 80% amplitude with full cycle. The phase transferred NC (in water) was put in the fume hood for over 24 hrs to evaporate excess hexane and then purified using stirred cell with an ultra-filtration membrane (cellulose, 100K Dalton, Millipore) at 10 psi using argon gas. Lastly, the resulting solution was further filtrated by syringe filter (0.22 μm, WHATMAN-PTFE) and the concentration of the NC solution was measured using inductively coupled plasma optical emission spectroscopy (ICP-OES, Perkin Elmer Optima 7300 DV).

Sorption Isotherms.

The synthesized metal oxide NCs were used as sorbents for arsenic (V), chromium (VI), and uranium (VI) over ranges of 0.021 to 0.168 mM at pH 7.0. In the multi sorption systems, all initial contaminant concentrations were the same molar concentration. pH of the solution was adjusted using HNO_3 and NaOH solution before batch sorption experiments and during the sorption test (after 4 and 8 hrs). After 24 hrs, to measuring the sorption isotherm, NCs were separated using ultracentrifuge (Sorvall WX Ultra 80, Thermo scientific) at 50,000 rpm for 2 hrs and supernatants were measured using Inductively Coupled Plasma Mass Spectroscopy (ICP-MS, Perkin Elmer ELAN DRC II). The calculated sorption isotherm was plotted by Langmuir isotherm (Equation 5.3), that was best fitted with measurements.

$$q_e = \frac{q_{max} k_L C_e}{(1 + k_L \cdot C_e)} \qquad \text{(Equation 5.3)}$$

Where q_e is the sorption density of the system (mmol as sorbed contaminants per g as NC), q_{max} maximum sorption density, k_L Langmuir sorption constant, and C_e the equilibrium concentration of contaminants.

Critical Coagulation Concentrations (CCC).
The critical coagulation concentration (CCC) of NCs was measured in varied concentrations of NaCl or $CaCl_2$ using the dynamic light scattering (DLS) method at pH 7.0. The attachment efficiency (α) of NCs was calculated by dividing the measured aggregation rate constant (k_{11}) into the fast aggregation rate constant ($k_{11,fast}$). Here, CCC is at a minimum concentration when the α becomes one (Equation 5.4).

$$\alpha = \frac{k_{11}}{k_{11,fast}} \qquad \text{(Equation 5.4)}$$

Transmission Electron Microscope (TEM).

The diameter of synthesized NCs was measured using a transmission electron microscope (TEM, Tecnai G2 Spirit, FEI). TEM images were analyzed by Image Pro Plus 6.0 (Media Cybernetics, USA); size and size distribution were obtain by counting over a thousand of NCs.[230]

Hydrodynamic Diameter and Zeta Potential.
The hydrodynamic diameters and zeta potential of NCs were determined by dynamic light scattering method (Malvern, Zetasizer Nano ZS, ZEN3600) at 22 °C.

X-Ray Diffraction (XRD).
XRD patterns (from 20º to 80º of 2θ) of synthesized NCs were measured using a powder diffractometer (Bruker d8 Advance X-ray Diffractometer) with Cu Kα radiation (1.54 Å).

Total Organic Carbon (TOC).
A total organic carbon analyzer (TOC, Shimadzu Scientific Instrument) was used to measure the number of organic molecules coated on NC.

Quartz Crystal Microbalance with Dissipation (QCM-D).
Quartz crystal microbalance with dissipation (QCM-D, Q-sense E4, Biolin Scientific) was used with a quartz sensor (5MHz silica coated QCM-D crystal, QSX-202, Q-sense) at 22.00 ± 0.02 °C under 100 μl min^{-1} of flow rate (ISM935, ISMATEC) to verify the sorption preference.

5.5. Conclusions

The composition dependent manganese iron oxide NCs were synthesized and surface functionalized with CTAB and OP to explore their sorption performance on single and multi sorbate systems considering As(V), Cr(VI), and U(VI). Outstanding As(V), Cr(VI), and U(VI) sorption performances and colloidal stability were observed for $MnFe_2O_4$ NCs in a single sorbate system due to high organic grafting densities of CTAB or OP on the NC, which provide a large number of effective sorption sites for sorbate and osmotic and elastic-steric repulsion for colloidal stability. For the As(V) and Cr(VI) multi sorbate system, As(V) has higher sorption

preference over Cr(VI) for all cases explored. In the As(V) and U(VI) multi sorbate system, both As(V) and U(VI) removal was significantly enhanced with positively charged MnFe$_2$O$_4$@CTAB due to increased As(V) local concentration at the surface of the NC which promoted the uranyl arsenate precipitation.

5.6. Supporting Information
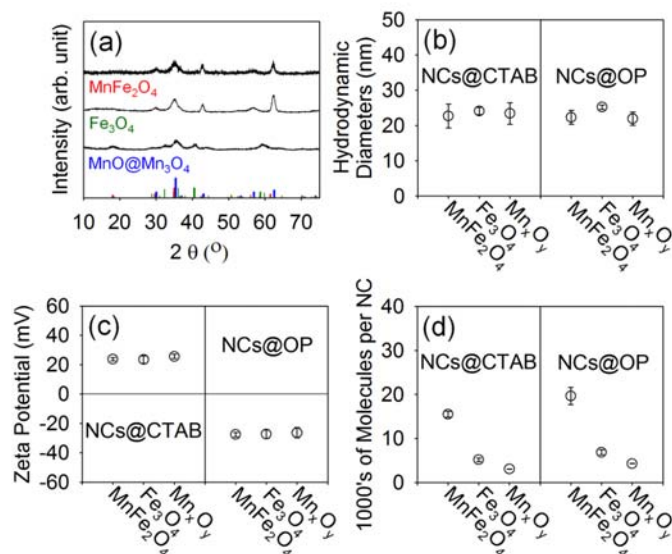
Figure 5.S1 (a) XRD of manganese iron oxide, iron oxide, and manganese oxide NCs. Diffraction patterns matched with MnFe2O4 (JCPDS Card # 380430), Fe3O4 (JCPDS Card # 190629), and MnO core (JCPDS Card # 070230) with Mn3O4 shell structure (JCPDS Card # 240734). Water disperse synthesized NCs coated with cetyltrimethylammonium bromide (CTAB) and oleyl phosphate (OP) were characterized; (b) hydrodynamic diameters at pH 7, (c) zeta potential at pH 7, (d) number of organic molecules loaded on the NC surface.
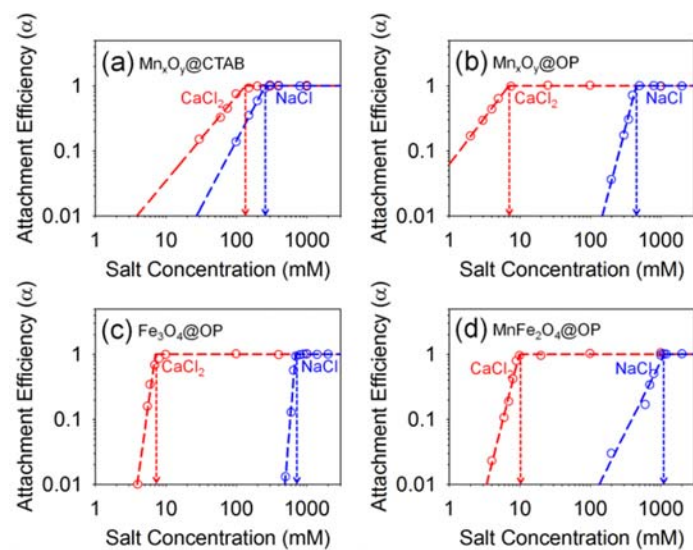
Figure 5.S2 Critical coagulation concentration (CCC) of water dispersed metal oxide NCs was determined by measuring attachment efficiency as a function of salt concentration (NaCl (blue) and CaCl$_2$ (red)); (a) MnxOy@CTAB, (b) MnxOy@OP, (c) Fe$_3$O$_4$@OP, and (d) MnFe$_2$O$_4$@OP.
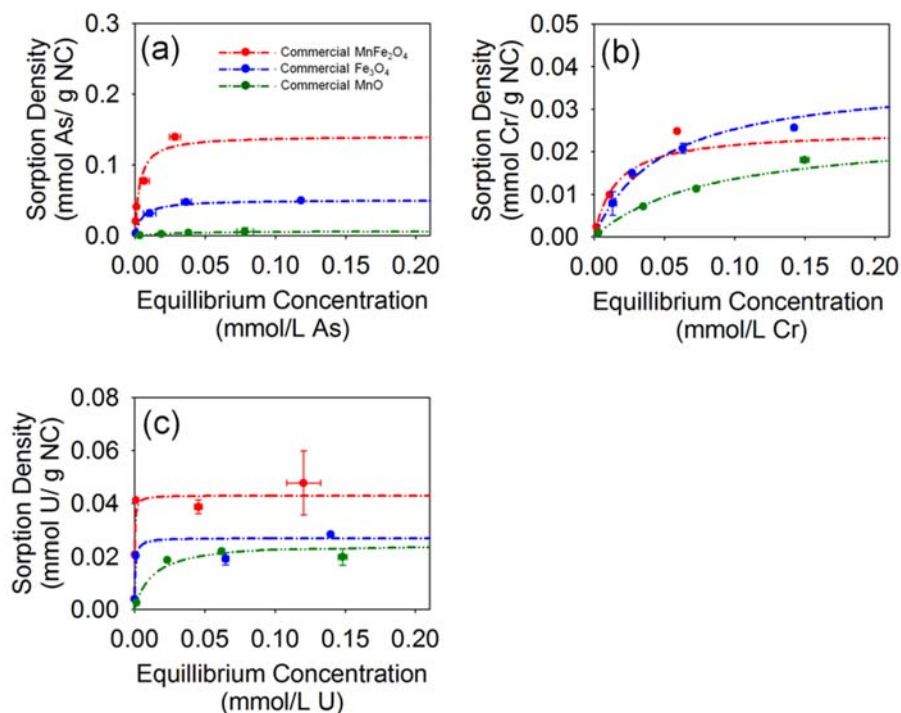
Figure 5.S3 As(V) (a), Cr(VI) (b), and U(VI) (c) sorption isotherm on commercial metal oxide (MnFe$_2$O$_4$ (red), Fe$_3$O$_4$ (blue), and MnO (green)) NCs.
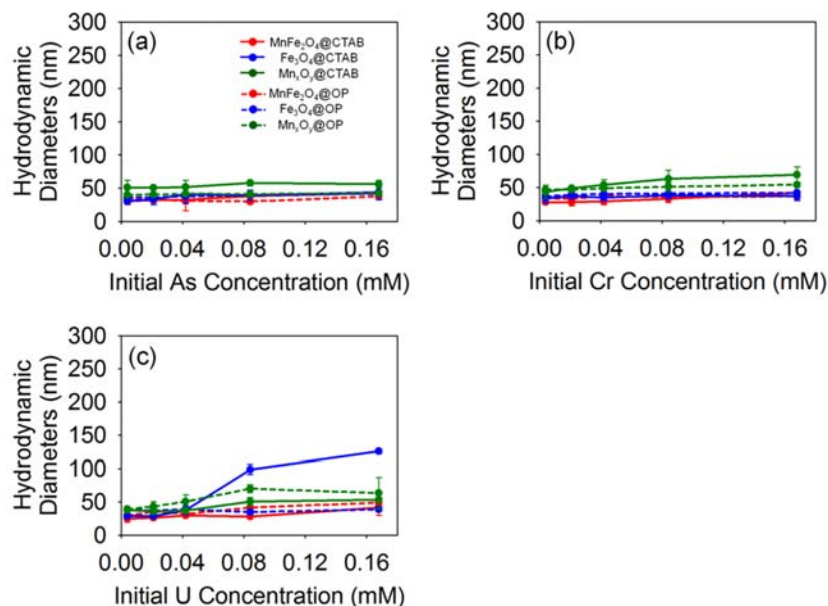
Figure 5.S4 Hydrodynamic diameter of CTAB (solid line) and OP (dotted line) functionalized metal oxide ($MnFe_2O_4$ (red), Fe_3O_4 (blue), and Mn_xO_y (red)) NCs after (a) As(V), (b) Cr(VI), and (c) U(VI) sorption experiments.
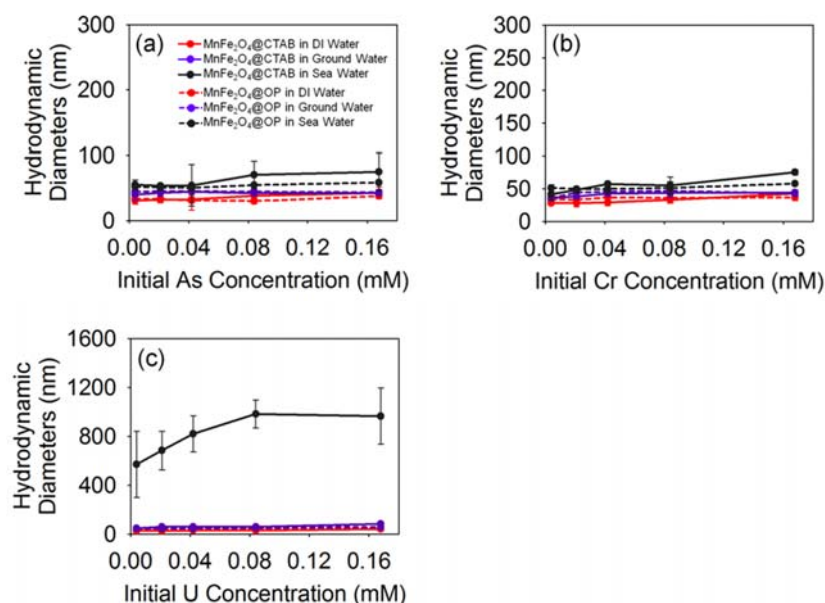
Figure 5.S5 Hydrodynamic diameter of CTAB (solid line) and OP (dotted line) functionalized $MnFe_2O_4$ NCs after (a) As(V), (b) Cr(VI), and (c) U(VI) sorption experiments in DI water (red), ground water (purple), and sea water (black); $MnFe_2O_4@OP$ not shown because it precipitate after uranyl sorption in sea water conditions.
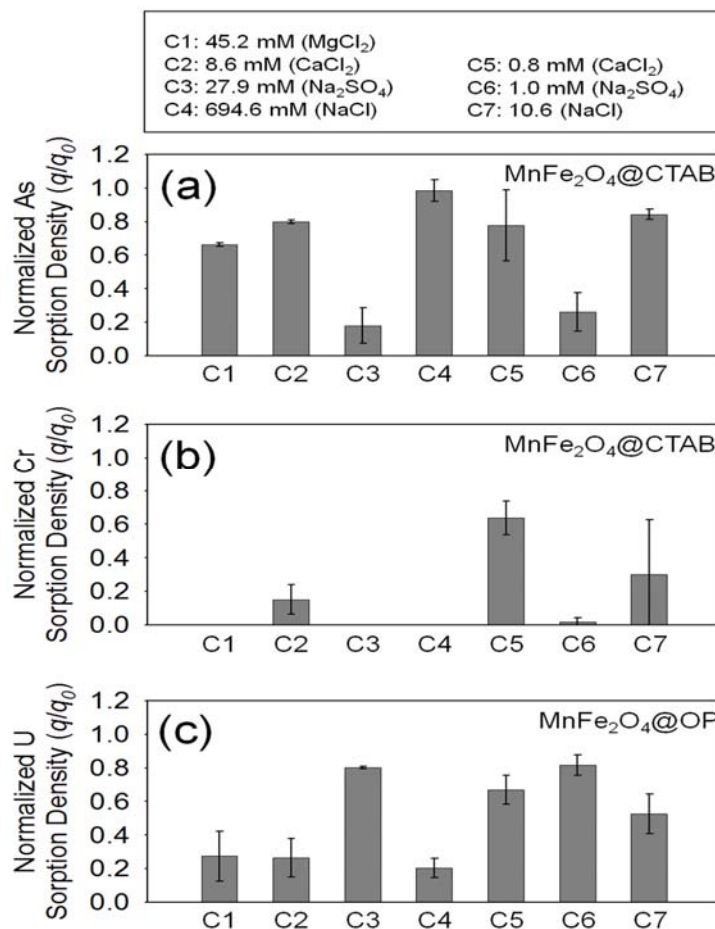
Figure 5.S6 Normalized As(V) (a), Cr(VI) (b), and U(VI) (c) sorption density on $MnFe_2O_4@OP$ or $MnFe_2O_4@CTAB$ with a series of ions and concentrations; sea water condition: C1, C2, C3, and C4. The NaCl concentration is adjusted to the total ionic strength of sea water. Ground water condition: C5, C6, andC7. The NaCl concentration is adjusted to the total ionic strength of ground water. Error bars present standard deviations
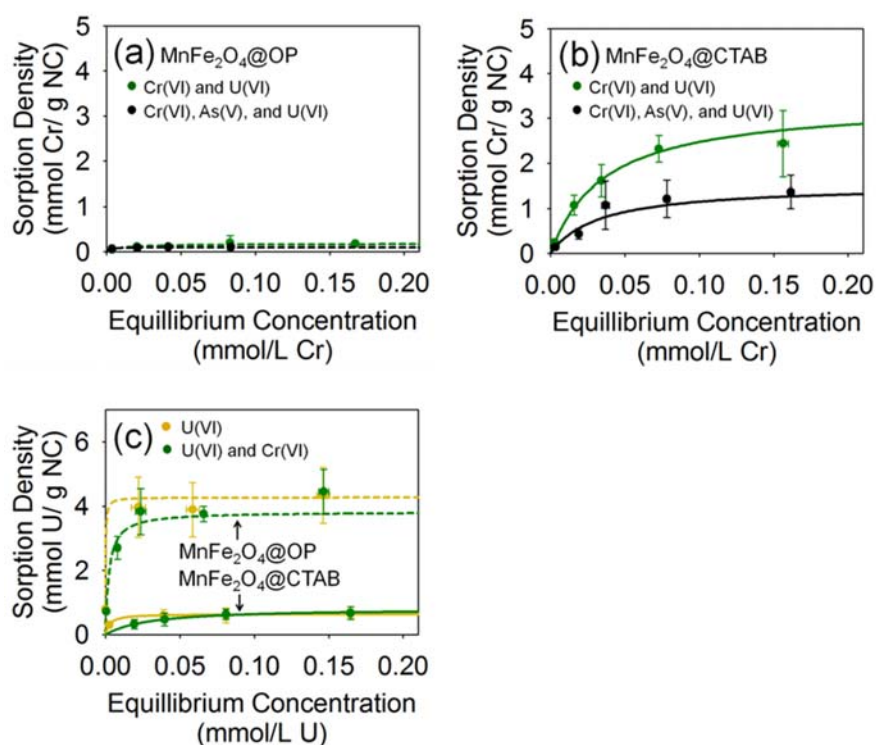
Figure 5.S7 Single and multi sorption isotherm on MnFe$_2$O$_4$ NCs coated with CTAB (solid line) or OP (dotted line); single sorbate systems (U(VI) (yellow)) and multi sorbate systems (Cr(VI) and U(VI) (green); and As(V), Cr(VI), and U(VI) (black)).
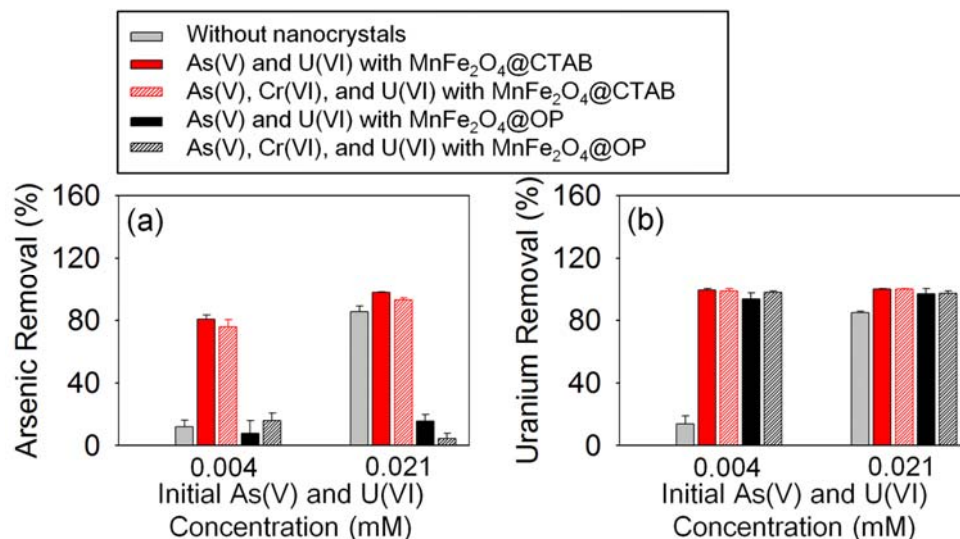
Figure 5.S8 As(V) (a) and U(VI) (b) removal with or without MnFe$_2$O$_4$@CTAB and MnFe$_2$O$_4$@OP.
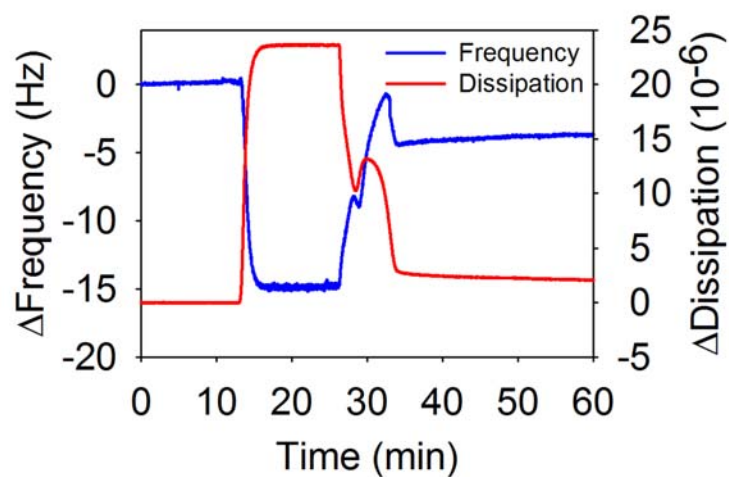
Figure 5.S9 Time dependent frequency (blue) and dissipation (red) shifts for Q-sensor with overtone (n = 3). The DI stabilized Q-sensor was coated by PDDA solution (after 12 min) and further stabilized for 15 min. Then the PDDA coated Q-sensor was restabilized with DI water at pH 7 (for 27 min to 60 min).
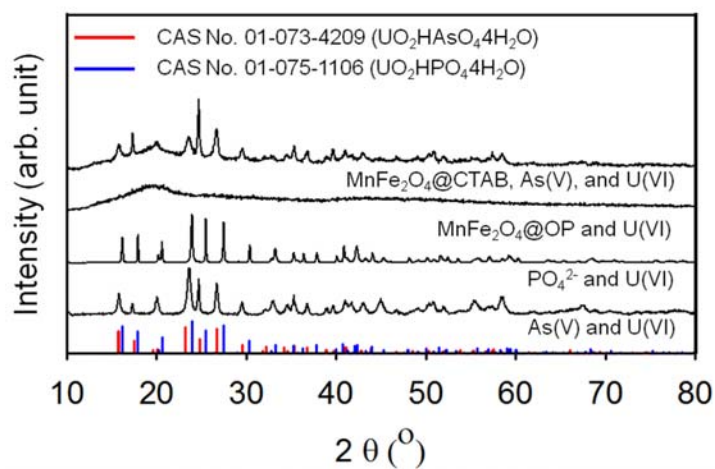
Figure 5.S10 XRD patterns of precipitates
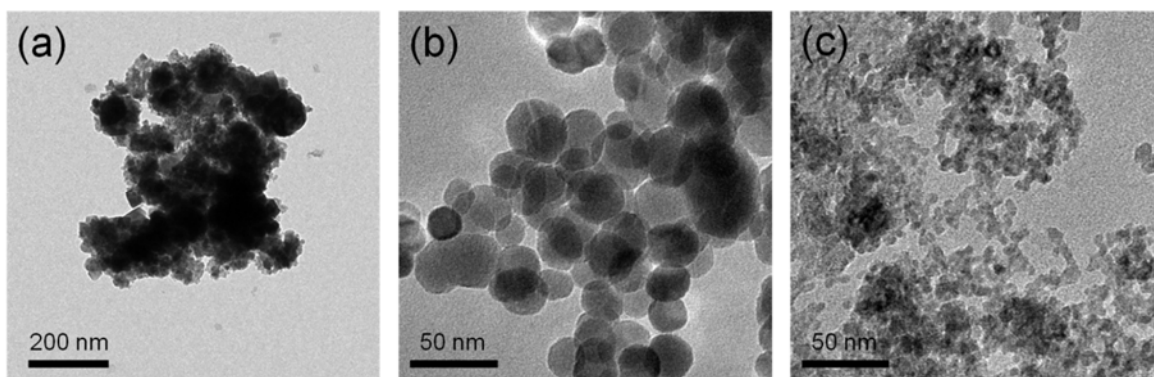
Figure 5.S11 TEM images of commercial NCs. (a) manganese ferrite ($MnFe_2O_4$), (b) iron oxide (Fe_3O_4), and (c) manganese oxide (MnO)

Table 5.S1 Composition of synthesized ground water and sea water

Ion	Ground water mM	Sea water mM
Cl^-	6.6	564.1
Na^+	7	488.9
K^+	-	8.7
Mg^{2+}	-	45.2
Ca^{2+}	0.8	8.6
SO_4^{2-}	1.0	27.9
Br^-	-	0.6

Chapter6: Exploring Fundamental Behavior of Organic Coated Silica Nanoparticles via QCM-D

*To be submitted in peer review journal

6.1. Overview

Here we investigate the influence of organic coatings on the deposition of silica nanoparticles (NPs) with respect to their diameter, flow velocity, and attachment efficiency using a quartz crystal microbalance with dissipation monitoring (QCM-D). For favorable conditions, organic coating decrease deposition rate. Unexpectedly, the attachment efficiency (under the unfavorable condition) of organic coated NPs increased with increasing flow velocity (up to 2.65 $\times$ 10^{-5} m/s for 20 nm NPs and 1.32 $\times$ 10^{-5} m/s for 200 nm NPs), although hydrodynamic torque also increased with increasing flow velocity. To better understand these observations, we deconvolute deposition mechanisms (diffusion and sedimentation) and determined relative effects (diffusion velocity, intermediate distance, and travel time) for partitioning from the liquid phase (bulk solution) to the solid phase (the surface of Q-sensor). For these, the diffusion velocity (from liquid to solid) of NPs increased with increasing flow velocity, leading to increase NP's kinetic energy for deposition. With organic coatings, a flow velocity increase reduces the secondary minimum deposition of NPs, and thus enhances their primary minimum deposition. NPs deposited at the primary minimum are resistant to hydrodynamic torque forces, resulting in an attachment efficiency increase with increasing flow velocities.

6.2. Introduction

Organic surface coatings significantly influence not only the aggregation of NPs but also deposition of NP as described and discussed in the introduction and literature review in previous chapters.[111-112, 273] Regarding NP deposition, different mechanisms, such as diffusion, sedimentation, and interception occur simultaneously,[158] which makes specific elucidation difficult. Towards this, a quartz crystal microbalance with dissipation (QCM-D) monitoring can be a powerful tool to elucidate the deposition mechanism of nanoparticles in terms of organic coating, due to its a nanogram sensitivity and configuration flexibility.[274] QCM-D, which is based on the (inverse) piezoelectric effect, measures the frequency and dissipation of Q-sensor in real time.[275] Deposited mass has a linear relationship with negative frequency shift (via Sauerbrey relation) based on the assumption of deposition via (near) homogeneous films.[225] In the case of NPs deposition, NPs forms laterally heterogeneous films composed of discrete NPs.[275] The Sauerbrey equation is still valid for the NPs deposition when dissipation is relatively low (and NPs have solid core structures).[275]

In this work, we observe increasing attachment efficiency between SiO_2 NPs (surface functionalized, 20 - 200 nm) and QCM sensors with increasing flow velocities, while remaining in the range of typical ground water flow velocities (6.11×10^{-6} to 1.32×10^{-5} m/s). This is an interesting discrepancy, as it does not match with previous theoretical conclusions. To better understand this observation, for the first time, we directly calculated the diffusion velocity, intermediate distance, and travel time of NPs (assumption free). The diffusion velocity of NPs from the bulk (liquid phase) to the collector (solid phase) increased as flow velocity was increased. With organic coatings, a flow velocity increase can reduce the secondary minimum deposition of NPs, and enhance their primary minimum deposition via increasing their kinetic

energy. This enhancement results in increasing attachment efficiency with increasing flow velocity.

6.3. Results and discussion

6.3.1. Size-Dependent and velocity-Dependent Deposition (Favorable Conditions)

The size of NPs governs their deposition, as diffusion and sedimentation are significantly affected by the diameter of NPs.[158] Here, the effects of organic coating on size dependent (20, 50, 100, and 200 nm) under favorable deposition conditions were evaluated in 1mM of NaCl at pH 7.2, with a 1.06×10^{-4} m/s flow rate. Highly monodisperse silica NPs, with or without organic coating ((3-aminopropyl) triethoxysilane, APTES), were used as model NPs. Detailed characterization information, including, TEM image, size histogram, TEM diameter, hydrodynamic diameter (number mean and volume mean), mass of NP, mass of coating, and zeta potential, can be found in the supporting information (Figure 6.S1, Table 6.S1, and 6.S2).
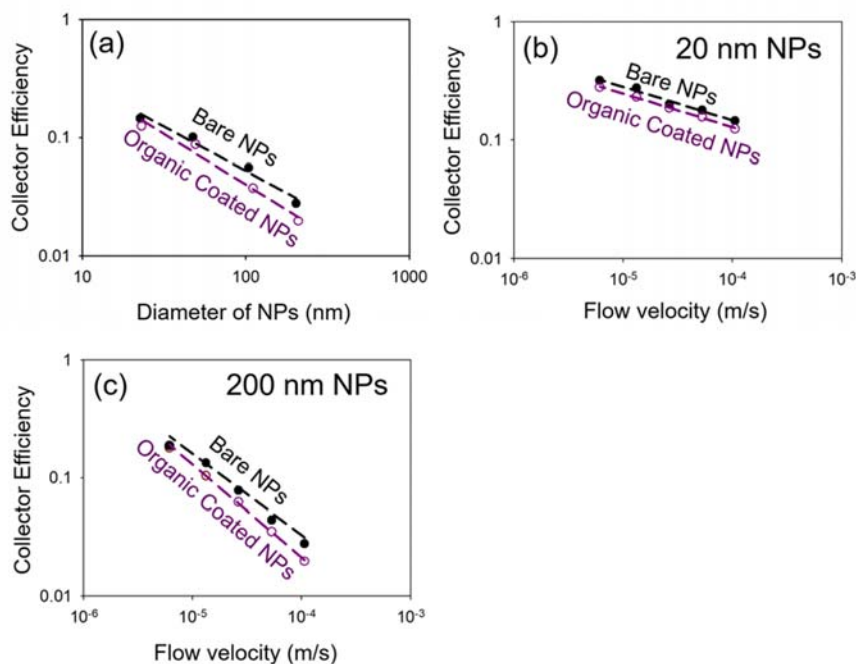
Figure 6.1 (a) Collector efficiency as a function of diameter of NPs. (b) Collector efficiency of 20 nm NPs as a function of flow velocity. (c) Collector efficiency of 200 nm NPs as a function of flow velocity. The black dashed linear regression line is for bare NPs and the purple dashed linear regression line is for organic coated NPs.

Figure 6.1 (a) presents collector efficiency for bare and organic coated silica NPs as measured by QCM-D. For this system, the collector efficiency is the ratio of total NPs (mass) flux in QCM-D chamber (reactor) compared with total NPs deposited rate on Q-sensor. Also, favorable deposition implies that every collision between NPs and Q-sensor leads to permanent deposition. The collector efficiencies are 0.145, 0.100, 0.056, and 0.028 for 20, 50, 100, and 200 nm bare NPs, respectively and 0.125, 0.087, 0.037, and 0.020 for 20, 50, 100, and 200 nm organic coated NPs, respectively (Figure 6.1 (a)). As NP size increased, the collector efficiency decreased, regardless of surface coating. As previously reported, while the settling velocity of NPs increases with (increasing) size, Brownian diffusion of NPs is inversely proportional to their diameter.[158] Over the explored range of 20 - 200 nm, deposition of NPs is more significantly affected by a diffusion decrease than a sedimentation increase.[119, 158] Collector efficiency of organic coated NPs was slightly lower than that of bare NPs, which is more pronounced for larger NPs. In this case, lower collector efficiency means a reduction of collision not a decrease of attachment efficiency as all NPs were deposited under favorable conditions. Collision is affected by not only external factors (flow velocity, fluid viscosity, and temperature), but also characteristics of NPs (size, density, van der Waals (vdW) interaction).[158] Here, every experiment condition (external factors) is identical, and core size and density differences between bare and organic coated NPs are negligible. Thus, we speculate that the organic surface coating is likely to reduce pairwise intermolecular interaction (vdW interaction). On the basis of Hamaker's approach, total interaction is calculated by simply summing the vdW interactions of

100

each molecule in one particle with all of the molecules in the substrate, which is the Q-sensor in this case.[276] The separation distance is governing factor for vdW interaction. The small portion of the surface coating (as mass ratio) likely contributes to the relatively large interaction energy difference[277] because the separation distance of coating is always closer than core particles. Also, the influence of interaction energy induced by coating may be size-dependent; the contribution (separation distance) of the surface of the material increases with a decreased radius of curvature (increasing size) of NPs.

Flow velocity is also considered as a key variable for evaluating the role of a surface coatings on the deposition as NPs can be resuspended via flow dynamics under the unfavorable condition.[111] Before exploring the flow velocity effects under the unfavorable deposition, we investigated favorable deposition as a function of flow velocity in 1mM of NaCl at pH 7.2. Two different size (20 and 200 nm) NPs, with or without organic coating, were used in five different flow velocity conditions (6.11×10^{-6}, 1.32×10^{-5}, 2.65×10^{-5}, 5.29×10^{-5}, and 1.06×10^{-4} m/s). As shown in Figure 6.1 (b), the collector efficiency for 20 nm NPs decreased with increasing flow velocity, regardless of surface coating, because the total number of collisions decreased with increased flow velocity.[119, 158] The collector efficiencies were 0.32, 0.28, 0.20, 0.18, and 0.14 for 20 nm bare NPs in 6.11×10^{-6}, 1.32×10^{-5}, 2.65×10^{-5}, 5.29×10^{-5}, and 1.06×10^{-4} m/s flows, respectively. For organic coated 20 nm NPs, they were 0.28, 0.23, 0.19, 0.16, and 0.12 in 6.11×10^{-6}, 1.32×10^{-5}, 2.65×10^{-5}, 5.29×10^{-5}, and 1.06×10^{-4} m/s flows, respectively. Figure 6.1 (c) presents the collector efficiency of 200 nm NPs as a function of flow velocity. The collector efficiencies of bare NPs were 0.187, 0.133, 0.078, 0.044, and 0.028 with increasing flow velocity, and the collector efficiencies of organic coated NPs were 0.180, 0.104, 0.062, 0.035, and 0.020 with increasing flow velocity. Similarly to the 20 nm NPs case, the collector

efficiencies of both bare and organic coated 200 NPs decreased with increasing flow velocity due to the diffusion decreases the number of NP collisions with collector.[119, 158]   With organic coating, both 20 nm and 200 nm NPs had slightly lower collector efficiency than bare NPs.

6.3.2. Attachment Efficiencies for Unfavorable Conditions

To further investigate the role of surface coatings, we explored the deposition of NPs as a function of flow velocity under unfavorable conditions, using 20 and 200 nm NPs at pH 7.2. To obtain proper attachment efficiency, the mass change resulting from deposition of NPs should be large enough to provide clearly detectable frequency signal. Through initial screening, we found that 0.2 M NaCl for 20 nm NPs, 0.1 M for 200 nm bare NPs, and 0.25 M NaCl for 200 nm organic coated NPs provide a sufficient frequency signal without aggregation of NPs. Though the zeta potential of NPs decreased in the presence of high salts, the NPs maintained their initial diameters (Figure 6.S2). The zeta potentials of 20 and 200 nm bare NPs and 20 and 200 nm organic coated NPs were -7.0 and -10.1 mV, and 6.8 and 14.8 mV, respectively. As presented in Figure 6.2, the attachment efficiency of bare NPs was either constant or decreased with increasing flow velocity, regardless of size. These results match well with previous attachment efficiency model equations developed by Elimelech[113] and Bai and Tien.[114-115]   However, the attachment efficiency of organic coated NPs increased with increasing flow velocity for certain flow ranges (up to 2.65×10^{-5} m/s for 20 nm NPs, and 1.32×10^{-5} m/s for 200 nm NPs), though the torque applied NPs increased with increasing the flow velocity (Figure 6.S3) and then dropped. Recent studies reported increasing attachment efficiency of NPs with increasing flow velocities when NPs are coated with organic materials.[102, 112]   Kim et al. suggested that the roughness of collector (porous media) may contribute to the unexpected attachment efficiency behavior in the presence of dissolved organic matter.[278]   Additionally, a change in aggregate

density could lead to unexpected attachment efficiency as aggregates density changes would result in under- or over-estimation of the number of collision in terms of flow velocity.[113, 119] However, the roughness of the collector and aggregation of NPs were negligible in this study as we used ideal collectors (Q-sensor) with highly monodisperse NPs. The unexpected attachment efficiency increase may result from enhanced interaction energy between organic coated NPs and the collector. According to the classical Derjaguin-Landau-Verwey-Overbeek (DLVO) theory, secondary minimum plays significant role in deposition of large colloid (e.g., 1000 nm).[119, 279] With an organic coating, the different interaction energy sources include elastic-steric and osmotic repulsion components. These short range energies are important under high ionic strength conditions[280] as they can result in considerable secondary energy barriers[111, 281] for particles of this size range. In the presence of potential secondary minima, detailed deposition information, such as the diffusion velocity, intermediate distance, and travel time of NPs are required for fundamental understanding. For this, by operating the QCM-D upside down, we can obtain these parameters.
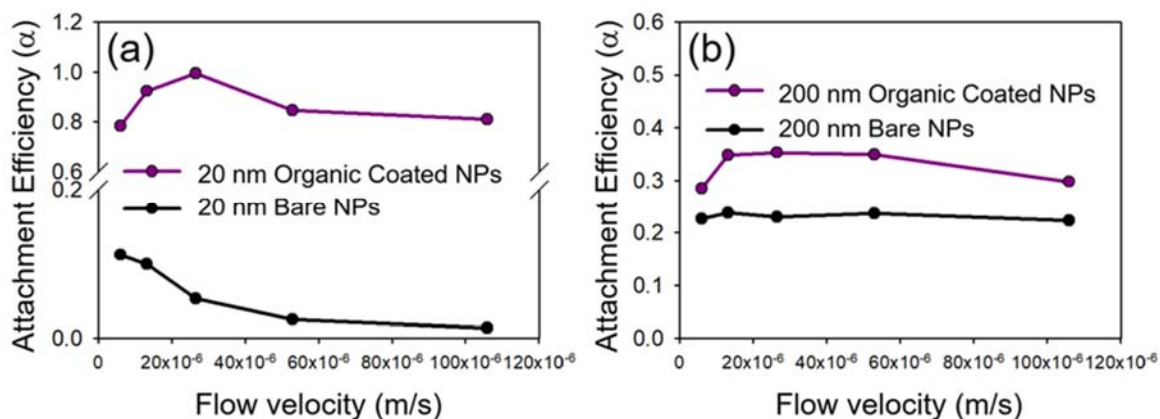
Figure 6.2 (a) Attachment efficiency of 20 nm bare (black) and organic coated (purple) NPs as a function of the flow velocity under unfavorable conditions. (b) Attachment efficiency of 200 nm bare (black) and organic coated (purple) NPs as a function of flow velocity.
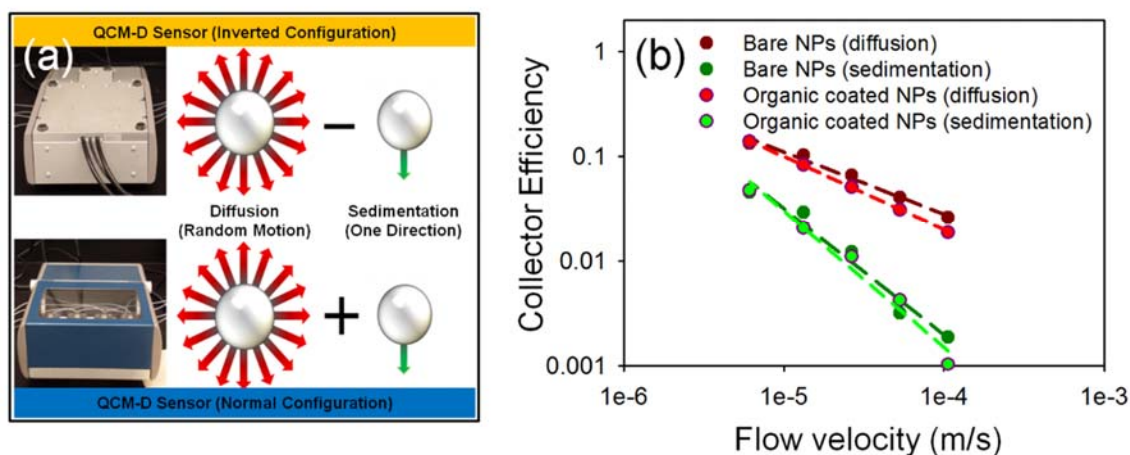
Figure 6.3 (a) Sketch of the motion of NPs by diffusion and sedimentation in normal and inverted configurations of QCM-D operation. (b) Collector efficiency resulting from diffusion and sedimentation for 200 nm bare and organic coated NPs as a function of flow velocity.

6.3.3. Inverted QCM-D Approach

Because sedimentation is readily measurable, 200 nm NPs were used for these studies. To separate the different deposition mechanisms (diffusion vs. sedimentation), the QCM-D was operated in both normal and inverted (upside down) configurations at five flow velocities (6.11×10^{-6}, 1.32×10^{-5}, 2.65×10^{-5}, 5.29×10^{-5}, and 1.06×10^{-4} m/s). Every deposition test was conducted in 1mM NaCl at pH 7.2. The possible velocity vectors of diffusion (Brownian motion) and sedimentation for NPs are presented in Figure 6.3 (a). In normal QCM-D operation mode, gravity works in the deposition direction, but in inverted operation, it acts opposite to the direction of deposition. The driving forces for NPs deposition in the normal QCM-D configuration are diffusion and sedimentation (diffusion + sedimentation), but gravity hinders the deposition of NPs in the inverted QCM-D configuration (diffusion - sedimentation). The separated collector efficiencies of 200 nm bare and organic coated NPs are presented in Figure 6.3 (b); here diffusion is the governing deposition mechanism. The collector efficiency (by diffusion) of organic coated NPs decreased slightly more than bare NPs as flow velocity was

increased. Cho et al. calculated the diffusion velocity (V_d) of NPs by assuming a constant intermediate (travel) distance (1 mm).[282] However, in our work, for the first time, the diffusion velocity, intermediate distance, and travel time of NPs were explored on the basis of the two deposition mechanisms (diffusion and sedimentation). Diffusion works in all directions by Brownian random motion of NPs, and sedimentation proceeds in only one direction, driven by gravity (Figure 6.3 (a)). As shown in Figure 6.4 (a), the sum of the Y-axes of every diffusion velocity vector is $V_d \cdot sin\,\theta$ (0 - 360°), and the settling velocity (V_g) acts only downward (-90°).

Hence, the total of the velocity vectors (Y-axis) of NPs in the normal QCM-D configuration is $V_d \cdot sin\,\theta + V_g.$ In inverted mode, it is $V_d \cdot sin\,\theta - V_g$. The settling velocity (V_g) can be obtained by Stoke's equation (Equation 6.1):[283]

$$V_g = \frac{g(\rho_p - \rho_w)d^2}{18\mu} \qquad \text{(Equation 6.1)}$$

Here, g is the acceleration caused by gravity, ρ_p is the density of NP, ρ_w is the density of water, d is the diameter of the NP, and μ is the viscosity of the solution. The diffusion velocity (V_d) can be calculated because the ratio of the collector efficiency of the normal configuration to the collector efficiency of the inverted configuration is proportional to the ratio of the positive area to the negative area of $V_d \cdot sin\,\theta + V_g$ from 0 to 360 degree (Figure 6.4 (a)). Based on the calculated diffusion velocity, the intermediate distance and travel time can be obtained using Equations 6.2 and 6.3, which derived from the Stokes-Einstein relationship:[284]

$$D = \frac{k_B T}{3\pi\mu d} \qquad \text{(Equation 6.2)}$$

where D is the diffusion coefficient of the silica NP, k_B is the Boltzmann constant, and T is the absolute temperature.

$$V_d = \frac{x}{t} = \frac{2D}{x} \qquad \text{(Equation 6.3)}$$

Here, x is the intermediate distance (travel distance). As presented in Figure 6.4 (b), the diffusion velocity of both bare and organic coated NPs increases with increasing flow velocity. Conversely, the travel distance and time for both NPs decreases with increasing flow velocity (Figure 6.4 (c) and Figure 6.S4). Travel distance implies the thickness of diffusion boundary layer, which decreases with increasing flow velocity.[285] NP concentration near the collector approaches the bulk concentration when flow velocity is increased. A NP concentration gradient increase results in increased diffusion velocity. The kinetic energy of NPs is directly related to their velocity: $0.5 \cdot m_{NP} \cdot V$. Here, m_{NP} is the mass of the NP and V is the velocity of the NP. High kinetic energy increases the ratio of NPs deposition on the primary minimum to their deposition on the secondary minimum. With an increased number of NPs deposited on the primary minimum, detachment by hydrodynamic force becomes lower,[286-287] resulting in increasing attachment efficiency with increasing flow velocity.
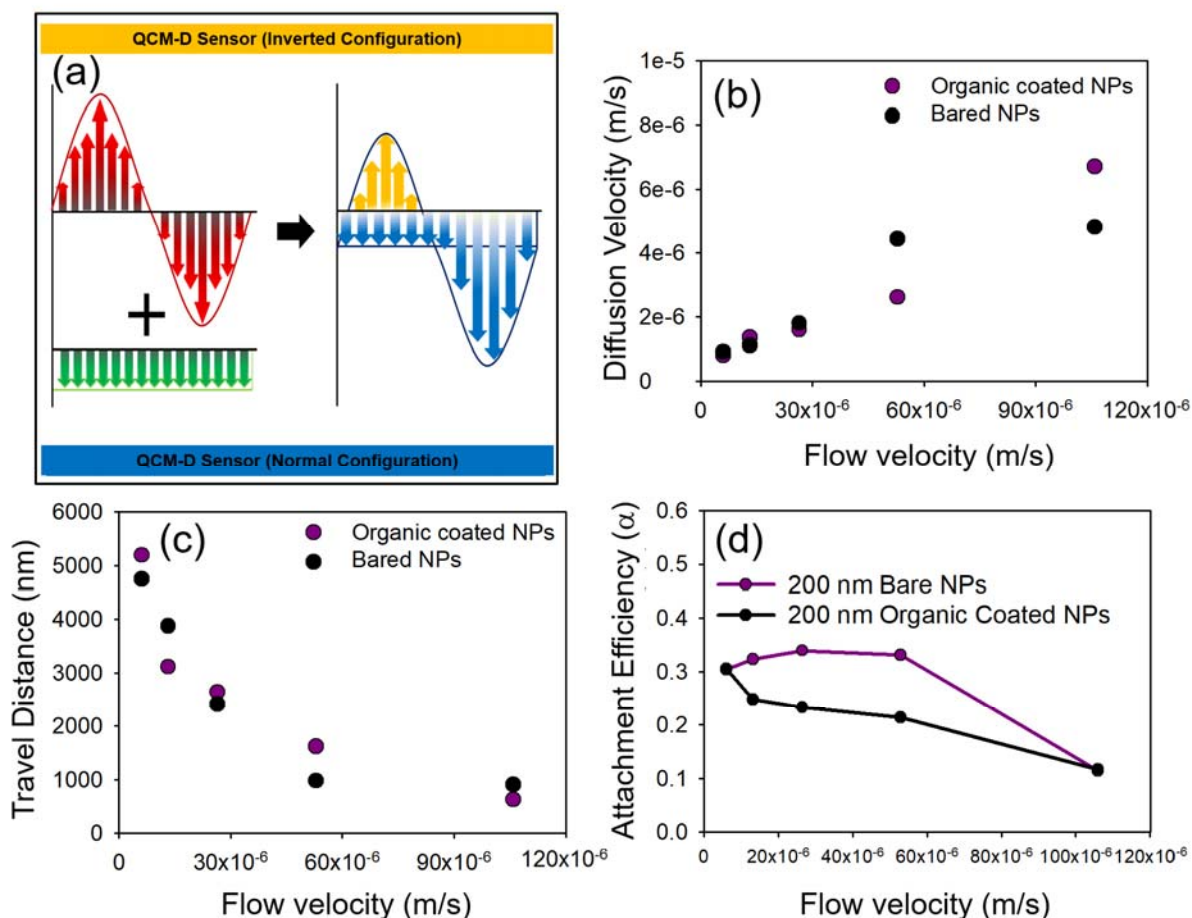
Figure 6.4 (a) Sketch of the sums of the Y-axes of motion from diffusion and sedimentation. (b) Diffusion velocity (c) travel distance for 200 nm bare (black) and organic coated (purple) NPs as a function of flow velocity. (d) Attachment efficiency of 200 nm bare (black) and organic coated (purple) NPs as a function of flow velocity under inverted QCM-D operation.

In addition, we observe that sedimentation significantly affects attachment efficiency at high flow velocity conditions even though diffusion is dominant. As shown in Figure 6.2 (b) and Figure 6.4 (d), the attachment efficiencies of the normal and inverted configurations were similar, except for the highest flow velocity condition (1.06×10^{-4} m/s). The deposition mechanism of 200 nm NPs at the highest velocity condition was mainly diffusion. Sedimentation was small (but not negligible) compared to diffusion (Figure 6.3 (b)); the sedimentation percentages were 7.27 and 5.55 % for bare and organic coated NPs. Hence, we

hypothesize that under high flow velocities, NPs are more readily deposited on the upper surface of the porous media than the under surface. Based on this observation, diameter and density, which are governing factors for sedimentation, could be important when injecting a solution containing NPs for sensing and subsurface environmental remediation. For biomedical applications such as tumor targeting, diameter and density could also be important, as blood flow velocity is much higher (3.0×10^{-4} - 4.0×10^{-1} m/s)[288-289] than typical ground water velocities.

6.4. Experimental

Nanoparticles (NPs).
Bare (hydroxylated) and organic coated ((3-aminopropyl) triethoxysilane ($C_9H_{23}NO_3Si$), APTES) 20, 50, 100, and 200 nm silica NPs were purchased from nanoComposix. The average size and distribution of NPs were measured using transmission electron microscopy (TEM, Tecnai G2 Spirit, FEI) images with Image Pro Plus 6.0 (Media Cybernetics, USA) by counting over 1000 NPs.[230] The hydrodynamic diameter (D_H) and zeta-potential of the NPs were measured by dynamic light scattering (Malvern, Zetasizer Nano ZS, ZEN3600) at pH 7.2 and 22 °C. The number concentration of NPs was measured using inductively coupled plasma optical emission spectroscopy (ICP-OES, Perkin Elmer Optima 7300DV), and organic loading mass was measured using a total organic carbon analyzer (TOC, Shimadzu Scientific Instrument).

Quartz Crystal Microbalance with Dissipation (QCM-D).
The deposition of NPs was monitored using QCM-D (Q-sense E4, Biolin Scientific) with a Q-sensor (5 MHz silica-coated QCM-D crystal, QSX-202, Q-sense). The flow velocity was controlled by a peristaltic pump (ISM935, ISMATEC).

Measuring the Collector Efficiency.
The deposition experiments were conducted in duplicate with four different mass flux conditions, by applying oppositely charged NPs to the quartz Q-sensor (Figure 6.S5-S7). For the

positively charged Q-sensor coating agent, poly-L-lysine (PLL, Sigma Aldrich) was used.[16]

From the QCM-D deposition results, we calculated the collector efficiency (Equation 6.4).[290]

$$\text{Collector efficiency} = \frac{C \cdot \Delta F_n}{n \cdot \Delta t} \times \frac{1}{mass\ flux} = \frac{deposited\ mass}{mass_{in}} \qquad \text{(Equation 6.4)}$$

Here, C is the mass sensitivity constant (17.7 ng/cm^2 for a 5 MHz AT-cut quartz Q sensor), F_n is

the resonance frequency, n is the resonance number (1, 3, 5, 7, 11, 13), and m is the mass of NPs

deposited. We monitored every n and selected the third n due to its stability.

Measuring the Attachment Efficiency.
The attachment efficiency of NPs on quartz Q-sensors was evaluated by dividing the time-

dependent frequency shift of the unfavorable condition to that of the favorable condition

(Equation 6.5).[290] Every test was conducted in duplicate with four different mass flux conditions

(Figure 6.S8-S9). .

$$\alpha = \frac{(\Delta F_3/\Delta t)_{\text{Unfavorable}}}{(\Delta F_3/\Delta t)_{\text{Favorable}}} \qquad \text{(Equation 6.5)}$$

Protocol for poly-L-lysine (PLL) coating.
To make positively charged Q-sensor, we coated Q-sensor using PLL. First, we rinsed the quartz

sensors in 10 mM HEPES buffer (4-(2-hydroxyethyl)-1-piperazineethanesulfonic acid) and 100

mM NaCl for 10 min. Then we coated the quartz sensors using 0.1 g/L of PLL in 10 mM

HEPES buffer and 100 mM NaCl solution. After the signal stabilized, we rinsed the quartz

sensor again for 10 min using 10 mM HEPES buffer in100 mM NaCl solution (Figure 6.S10).[16]

6.5. Conclusions

In this chapter, we measured the diffusion velocity (bulk solution to Q-sensor) of NPs by

deconvolution of diffusion velocity vector on the basis of a new and novel QCM-D technique.

The diffusion velocity of NPs increased as a function of flow velocity. The organic coated NPs

deposited more on the primary minimum due to the increased kinetic energy (diffusion velocity) when flow velocity was increased, which leads to increased attachment.

6.6. Supporting Information

Figure 6.S1 presents TEM images and size histograms of bare and organic coated silica NPs; the sizes were measured for over 1000 NPs, counted using Image Pro Plus 6.0. Hydrodynamic diameter (D_H) of NPs was further analyzed using dynamic light scattering (DLS). The size information (TEM diameter, D_H (number mean and volume mean)) is summarized in Table S1 for bare silica NPs and in Table S2 for organic coated NPs. As shown, the TEM diameter and number mean D_H had highly similar values, suggesting that the silica NPs used in this study were highly monodisperse. The zeta potentials of the NPs were measured by DLS in 1 mM of NaCl at pH 7.2. The zeta potentials were -9.26, -17.6, -33.1, and -41.0 mV for 20, 50, 100, and 200 nm bare silica NPs, respectively, and 9.05, 20.2, 22.4, and 39.6 mV for 20, 50, 100, and 200 nm organic coated silica NPs, respectively.
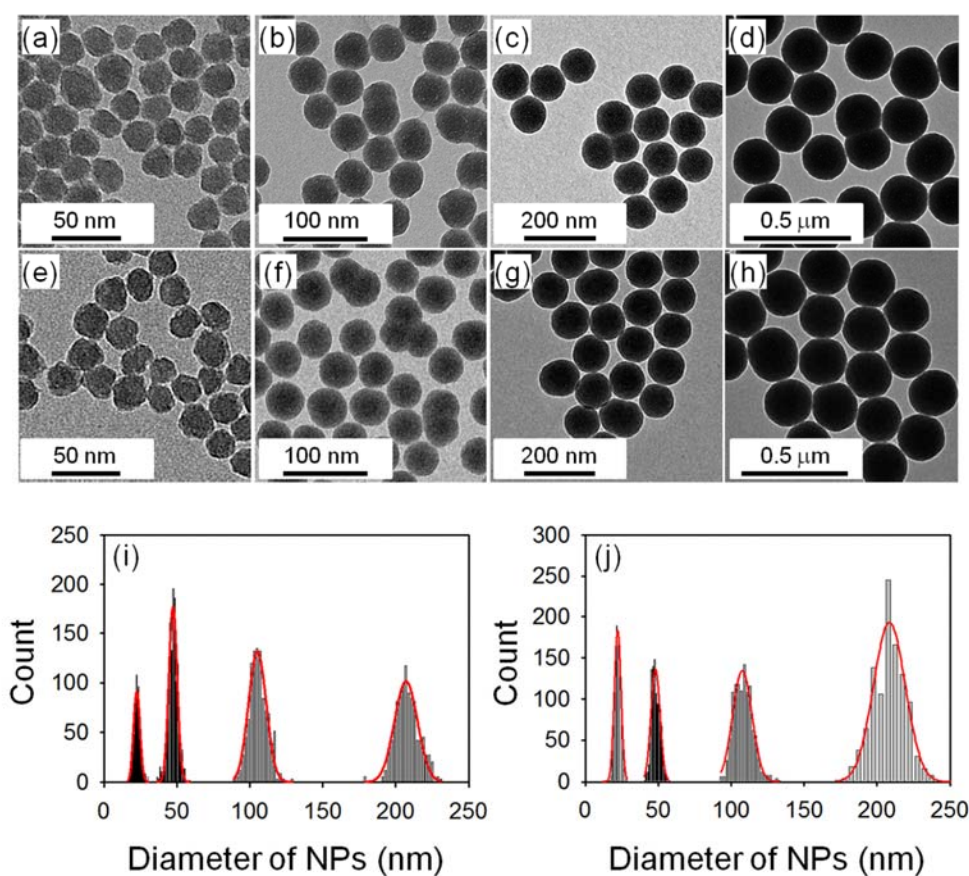
Figure 6.S1 TEM images of bare silica NPs (a) 20 nm, (b) 50 nm, (c) 100 nm, and (d) 200 nm, and organic coated silica NPs (e) 20 nm, (f) 50 nm, (g) 100 nm, and (h) 200 nm. Histograms for (i) bare and (j) organic coated silica NPs.
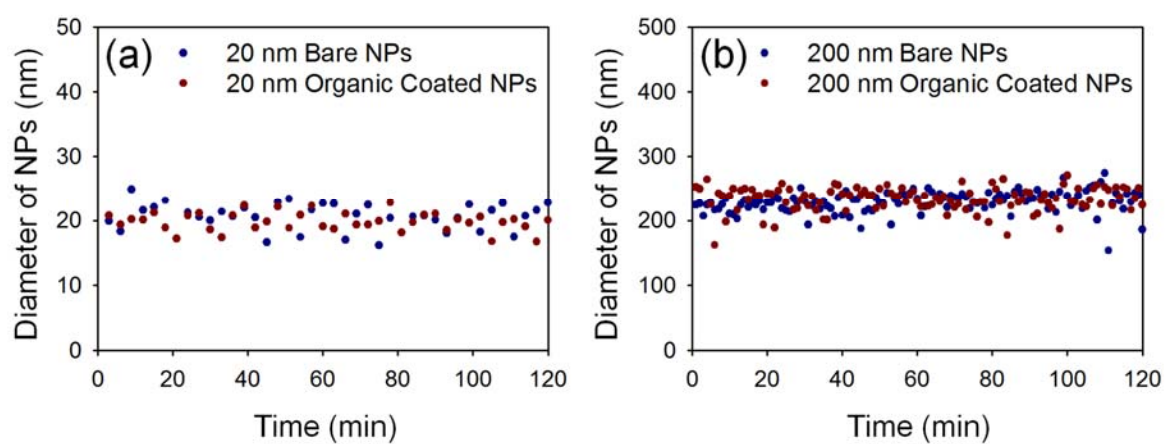
Figure 6.S2 The time-dependent diameters of (a) 20 nm bare NPs at 0.2 M NaCl and 20 nm organic coated NPs at 0.2 M NaCl. (b) The time-dependent diameters of 200 nm bare NPs at 0.25 M NaCl and 200 nm organic coated NPs at 0.1 M NaCl. Solution pH was 7.2.

Measuring the Torque Applied to Deposited Nanoparticles. Two hydrodynamic forces act on a deposited NP; one is the drag force (F_D, Equation 6.6) and the other is the lifting force (F_L, Equation 6.7).[287, 291]

$$F_D = (1.7005)6\pi\mu Vr_p \qquad \text{(Equation 6.6)}$$

Here, V is the fluid velocity and r_p is the radius of deposited NP.

$$F_L = 81.2r_p{}^2\mu\omega^{0.5}V/v^{0.5} \qquad \text{(Equation 6.7)}$$

Here, ω is the velocity gradient at the collector surface, and v is the kinematic viscosity of the fluid. The torque applied to a deposited NP was determined by the larger of drag and lift forces. In our experimental conditions, drag was the governing force in calculating the torque applied to a deposited NP (Equation 6.8).[291]

$$T_{applied} = 1.399r_p F_D \qquad \text{(Equation 6.8)}$$
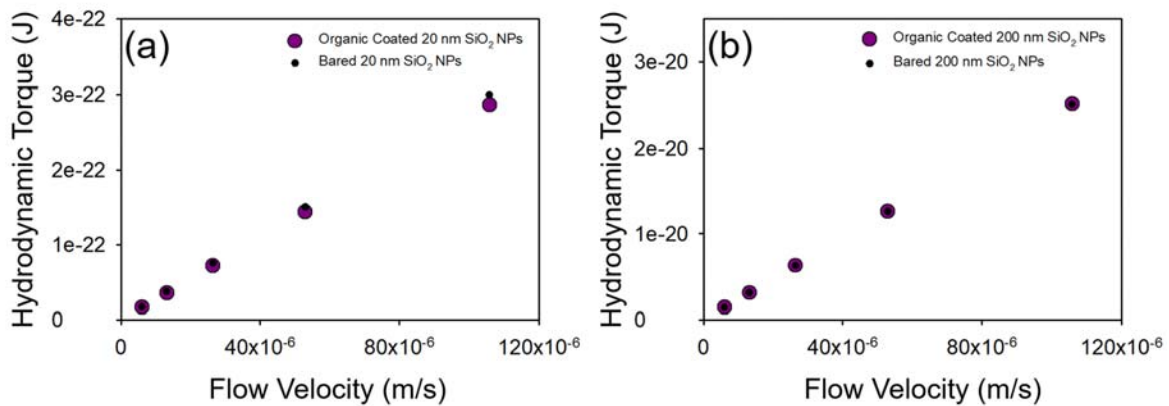
Figure 6.S3 (a) The torque applied to 20 nm bare (black) and organic coated (purple) NPs as a function of flow velocity. (b) The torque applied to 200 nm bare (black) and organic coated (purple) NPs as a function of flow velocity.
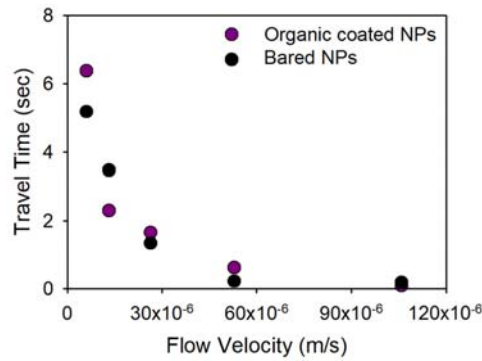
Figure 6.S4 Travel time for 200 nm bare (black) and organic coated (purple) NPs as a function of flow velocity.
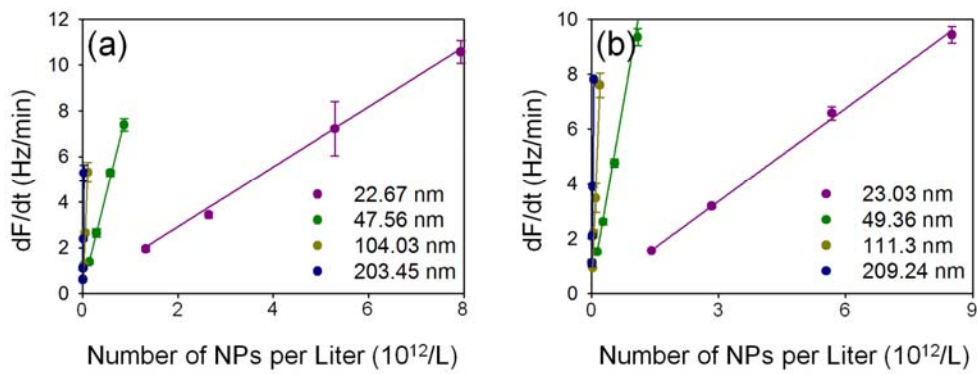
Figure 6.S5 Frequency shift (dF/dt) as a function of the number of NPs under favorable condition. (a) 20, 50, 100, and 200 nm bare NPs, (b) 20, 50, 100, and 200 nm organic coated NPs.
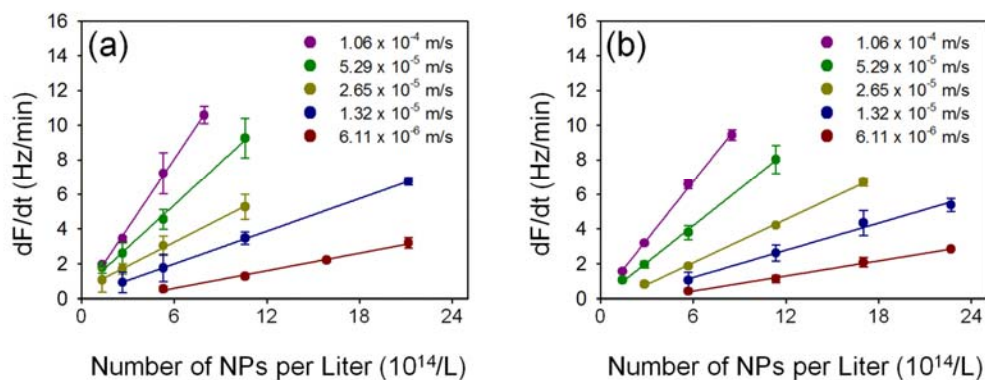
Figure 6.S6 Frequency shift (dF/dt) as a function of the number of 20 nm (a) bare, (b) organic coated NPs under favorable condition at various flow velocities (1.06×10^{-4} m/s (purple), 5.29×10^{-5} m/s (green), 2.65×10^{-5} m/s (yellow), 1.32×10^{-5} m/s (blue), and 6.11×10^{-6} m/s (red)).

113
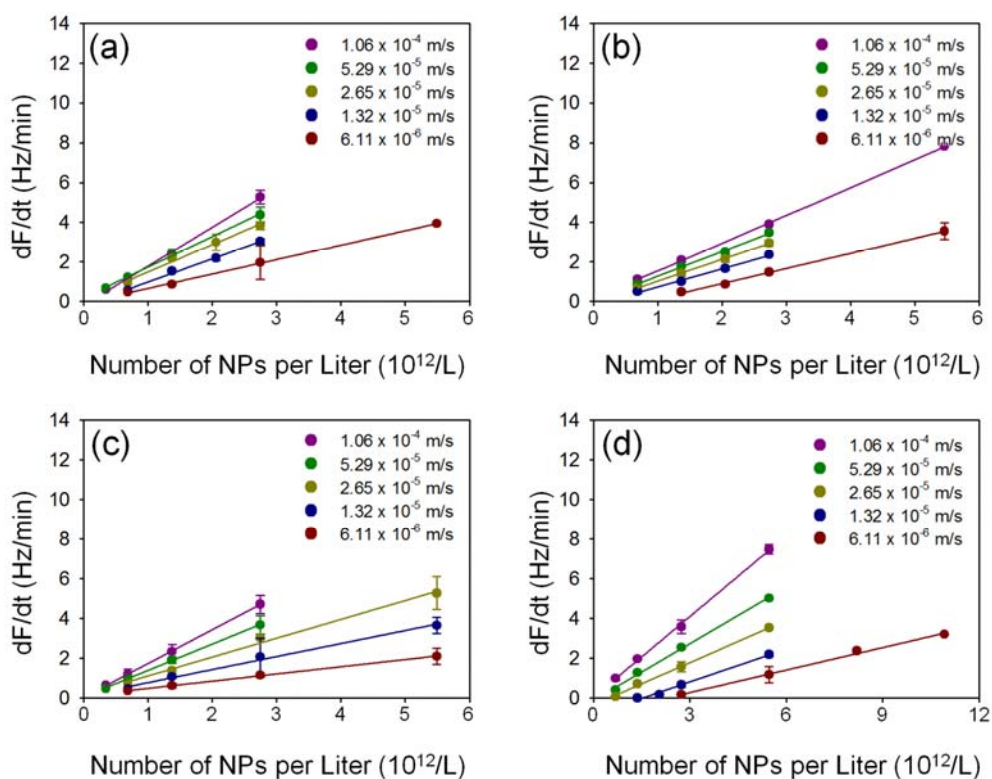
Figure 6.S7 Frequency shift (dF/dt) as a function of the number of NPs under favorable deposition conditions at different flow velocities (1.06 × 10^{-4} m/s (purple), 5.29 × 10^{-5} m/s (green), 2.65 × 10^{-5} m/s (yellow), 1.32 × 10^{-5} m/s (blue), and 6.11 × 10^{-6} m/s (red)). 200 nm (a) bare and (b) organic coated NPs with normal QCM-D operation. 200 nm (c) bare, (d) organic coated 200 m NPs with inverted QCM-D operation under favorable conditions.
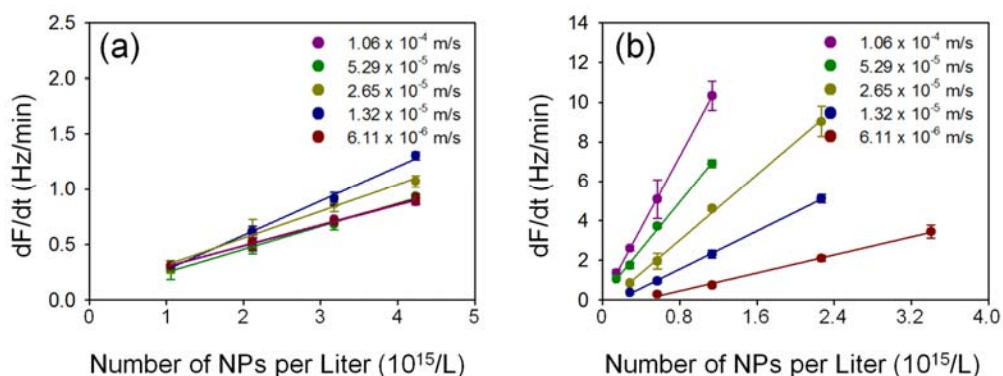
Figure 6.S8 Frequency shift (dF/dt) as a function of the number of 20 nm NPs under unfavorable deposition conditions at different flow velocities (1.06 × 10^{-4} m/s (purple), 5.29 × 10^{-5} m/s

(green), 2.65×10^{-5} m/s (yellow), 1.32×10^{-5} m/s (blue), and 6.11×10^{-6} m/s (red)). (a) 20 nm bare NPs in 0.2 M NaCl and (b) 20 nm organic coated NPs in 0.2 M NaCl.
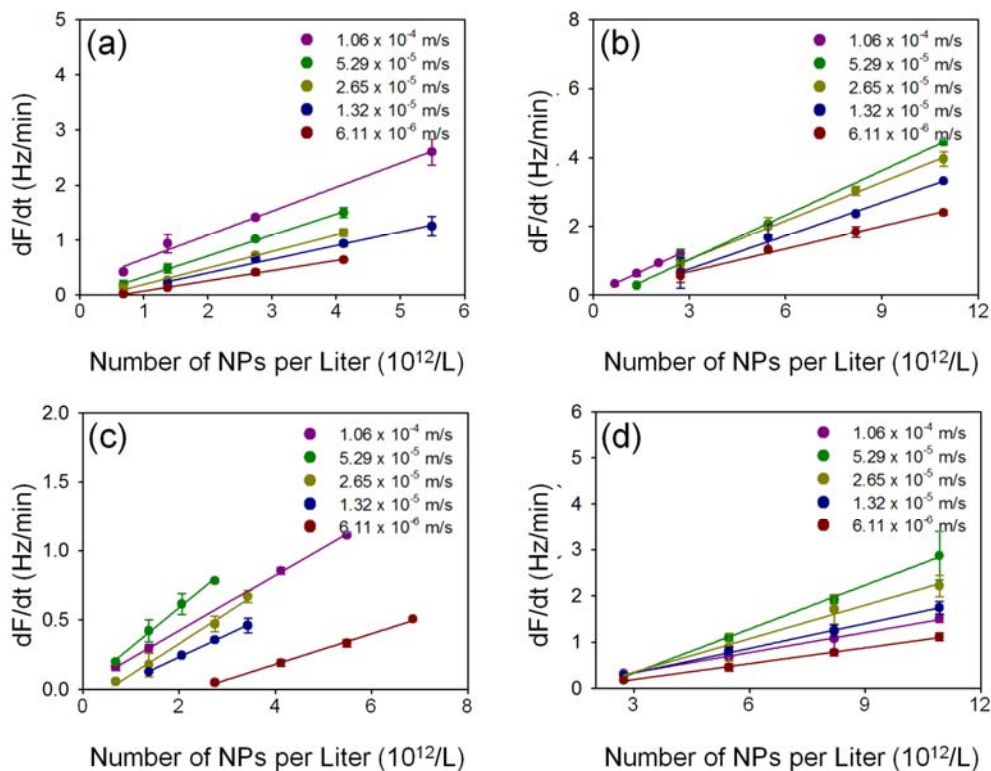
Figure 6.S9 Frequency shift (dF/dt) as a function of the number of NPs under unfavorable deposition conditions at different flow velocities (1.06×10^{-4} m/s (purple), 5.29×10^{-5} m/s (green), 2.65×10^{-5} m/s (yellow), 1.32×10^{-5} m/s (blue), and 6.11×10^{-6} m/s (red)). (a) 200 nm bare NPs in 0.25 M NaCl and (b) 200 nm organic coated NPs in 0.1 M NaCl with normal QCM-D operation. (c) 200 nm bare NPs in 0.25M NaCl and (d) 200 nm organic coated NPs in 0.1 M NaCl with inverted operation.
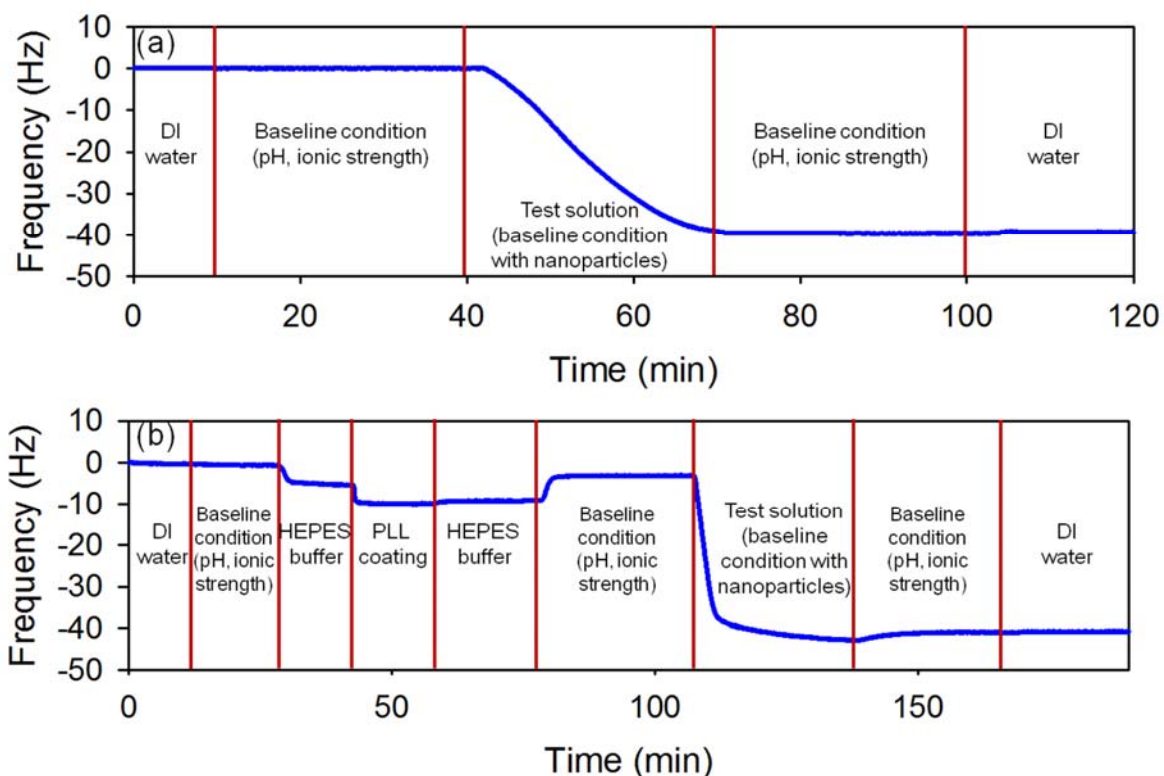
Figure 6.S10 Real time frequency responses of Q-sensor for NPs deposition; (a) The NPs deposited on the negative quartz sensor. A linear slope represents their deposition (40 < t min). (b) The NPs deposited on the positive quartz sensor. The profile (25 min to 70min) represents Poly-L-lysine coating process on the surface of quartz sensors. Deposition shows after 105 min (a linear slope).

Table 6.S1 The detailed information of bare silica NPs (20, 50, 100, and 200 nm)

Bare NPs	TEM diameter	Hydrodynamic diameter (number mean)	Hydrodynamic diameter (volume mean)	Mass of NP	Zeta potential at pH 7.2 (1 mM NaCl)	Zeta potential at pH 7.2 (high salt condition)
20 nm	22.67 ± 2.40 nm	22.7 ± 1.5 nm	26.0 ± 1.9 nm	1.62E-17 g	-9.26 ± 1.95 mV	-7.0 ± 2.1 mV (0.2 M NaCl)
50 nm	47.38 ± 3.30 nm	47.6 ± 1.5 nm	52.4 ± 0.4 nm	1.48E-16 g	-17.6 ± 0.65 mV	-
100 nm	105.86 ± 6.22 nm	104.0 ± 2.4 nm	104.7 ± 0.7 nm	1.65E-15 g	-33.1 ± 0.30 mV	-
200 nm	207.91 ± 8.13 nm	203.5 ± 5.0 nm	224.5 ± 5.9 nm	1.25E-14 g	-41.0 ± 0.22 mV	-10.1 ± 1.0 mV (0.25 M NaCl)

Table 6.S2 The detailed information of organic coated silica NPs (20, 50, 100, and 200 nm)

Organic coated NPs	TEM diameter	Hydrodynamic diameter (number mean)	Hydrodynamic diameter (volume mean)	Mass of NP	Mass of surface coating	Zeta potential at pH 7.2 (1 m M NaCl)	Zeta potential at pH 7.2 (high salt condition)
20 nm	22.2 ± 2.2 nm	23.0 ± 2.3 nm	30.0 ± 2.2 nm	1.51E-17 g	8.22E-19 g	9.05 ± 1.12 mV	6.8 ± 0.1 mV (0.2 M NaCl)
50 nm	48.4 ± 2.9 nm	49.4 ± 0.5 nm	55.1 ± 0.9 nm	1.57E-16 g	9.53E-18 g	20.18 ± 0.60 mV	-
100 nm	108.3 ± 6.5 nm	111.3 ± 1.1 nm	123.7 ± 2.2 nm	1.76E-15 g	5.62E-17 g	22.42 ± 0.47 mV	-
200 nm	208.2 ± 11.8 nm	209.2 ± 1.8 nm	234.6 ± 3.1 nm	1.25E-14 g	5.11E-16 g	39.56 ± 0.34 mV	14.8 ± 1.4 mV (0.1 M NaCl)

Chapter 7: Nanoparticle Stability in Water: Understanding Critical Dynamics of Organic Coatings and Relative Aggregation Density

*To be submitted in peer review journal

7.1. Overview

Inorganic-organic nano composites have received interest as a potential platform (nano) structure for sensor, catalyst, sorbent, and environmental applications. Here we describe the critical role of organic surface coatings with regard to the colloidal stability of engineered manganese oxide nanoparticles (Mn_xO_y NPs) core materials (chosen due to antiferromagnetic properties at room temperature). To systematically evaluate the role of surface coating on colloidal stability, we prepared libraries of monodisperse Mn_xO_y NPs with a series of surface coatings including those with different structures. Quantitatively, we specified the role of surface organic coating by comparing critical coagulation concentration (CCC) with experiment and expectation (Schulze-Hardy rule). We observed that the effective density of nanoclusters can exceed NPs' primary (bulk) density depending on empty space of organic coating regime(s). Interestingly, poly(maleic anhydride-alt-1-octadecene) coated NPs were more colloidally stable at the point of zero charge (PZC) than at pH 7, though the NPs lost its surface charge potential. Critical coagulation concentrations (CCC) was 334 mM in NaCl and 1.5 mM in $CaCl_2$ at pH 7, compared to CCC values of 807 mM in NaCl and 210 mM in $CaCl_2$ at PZC. We determined that polymer configuration changes significantly effects colloidal stability. The shrinkage of polymer chains (at PZC) dramatically increases bulk colloidal stability of organic coated NPs, which was confirmed with a quartz crystal microbalance-based technique to evaluate polymer dynamics.

Overall, we systematically demonstrate and quantify organic coating variables, including structure, grafting density, and configuration influence on colloidal stability of organic coated NPs.

7.2. Introduction

In water, nanoscale particles aggregate when the free energy of the system is reduced by decreasing the surface area.[1, 29] Particle aggregation decreases reactivity and affects not only toxicity and persistence, but also fate and transport.[102-106] For charge-stabilized nanomaterials, the stability ratio, as a function of ionic strength (reciprocal of attachment efficiency) provides fundamental insight into particle stability regimes.[65, 211, 213] Practically, this is measured by critical coagulation concentrations (CCC), which are directly calculated via stability ratios, are widely used as a practical index for evaluating of stability of nanomaterials in water.[292-294] According to classical Derjaguin–Landau–Verwey–Overbeek (DLVO) theory, electrostatic double layer (EDL) repulsion is reduced as a function of counter ion concentration and type through the effective decrease of Debye screening length (surface charge screening).[36, 295]

There are a number of approaches for evaluating the CCC (colloidal stability) of nano materials on the basis of classical DLVO interactions.[119, 153, 296-298] For most, CCC relationships are described in terms of counter valence ion concentration and/or type, as described by the Schulze-Hardy rule, which is derived from linear superposition of Gouy-Chapman and unretarded Hamaker expressions (i.e. classical DLVO theory).[119, 153] Such DLVO expressions, including the Schulze-Hardy rule, have theoretical limitations when asymmetric ions are incorporated. Because the Taylor series expansion of the Poisson-Boltzmann equation (involved in the description of EDL) is simplified only when dissolved ions are symmetric electrolytes.[299-301] Without such simplification, complex numerical computational procedures are required.

Despite this limitation, the Schulze-Hardy rule is widely accepted when describing monovalent and asymmetric divalent counter ion dynamics.[302-303] Interestingly, when (nano)materials are coated or encapsulated by organic substances, such as artificial surfactants, organic matter, the Schulze-Hardy rule is no longer valid.[302] Because the Schulze-Hardy rule considers only classical DLVO interactions, extended DLVO (XDLVO) interactions have been explored to better describe the behavior of particles with organic coatings in water.

Organic-inorganic nanoscale composites have gained considerable interest as next generation materials for catalysts, sorbents, and sensors, among other environmental applications, due to unique, tunable physico-chemical properties in addition to high colloidal stability upon surface passivation.[35, 304] Organic surface coatings can provide EDL repulsion as well as XDLVO interactions, such as osmotic and elastic-steric repulsion for inorganic bodies.[36-39] XDLVO interactions relating to colloidal stability remains an area of ongoing research.[36-39] Specifically, the quantifying the role of organic coatings remains a challenge from a colloidal stability and (net) aggregation density perspective.

In this work, we explore the role of organic coated nanoparticles with regard to structure (bilayer- linear polymeric- multi branched polymeric-) and conformation change (shrink and stretch of polymer chains). We have designed and synthesized monodisperse manganese oxide nanoparticles (NPs) with varied organic surface coatings (polymer- and organic acid-based) and an inorganic shell (silica), for comparison. We observed that the presence of the unsaturated carbon (i.e. double bond) in organic surfactant plays significant role in colloidal stability of bilayer structured NPs. For polymer functionalized NPs, colloidal stability is highly influenced by coating structure and configuration. Additionally, the relative amount of empty space (density) of organic coating regime strongly correlates with relative aggregation density. The

collapse (shrinking) of polymers grafted on the surface of NPs dramatically increases elastic-steric repulsion, which significantly affects colloidal stability.

7.3. Results and discussion

7.3.1. Synthesis and Characterizations

Manganese oxide (MnO and Mn_3O_4) NPs were designed as model core NPs due to antiferromagnetic properties at room temperature.[305] Highly monodisperse manganese oxide (M_xO_y) NPs were precisely synthesized via Mn-oleate (precursor) decomposition in the presence of oleic acid at 320 C°.[48, 262] As measured by TEM, the sizes and size distributions of resulting synthesized M_xO_y NPs were 13.8 ± 1.4, 18.4 ± 1.5, and 24.6 ± 1.3 nm, respectively (Figure 7.1 and Figure 7.S1); size was controlled by Mn-oleate concentration (Figure 7.S2). As shown in Figure 7.2 (a), X-ray diffraction (XRD) patterns were matched with MnO (JCPDS Card # 07-0230) and Mn_3O_4 (JCPDS Card # 24-0734), which matches the well-known MnO-Mn_3O_4 core shell structure (Figure 7.2 (a)).[65, 262]
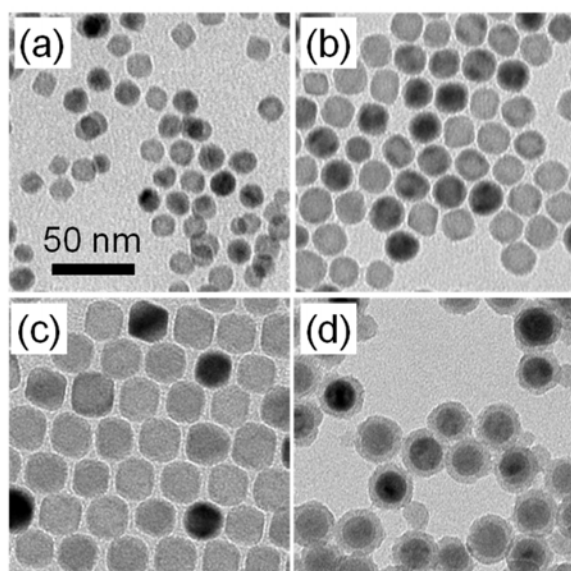
Figure 7.1 TEM images of monodisperse Mn_xO_y (from a to c) and (d) silica encapsulated 18.4 nm Mn_xO_y NPs; Average diameter of NPs was measured by counting over 1000 NPs using Image-Pro 6.0; (a) 13.8 ± 1.4 nm, (b) 18.4 ± 1.5 nm, (c) 24.6 ± 1.3 nm.

Synthesized Mn_xO_y NPs were surface functionalized by both ligand encapsulation and exchange methods for phase-transfer from organic solvent into water.[65, 213] Mn_xO_y NPs with surface bilayers were synthesized by first surface stabilizing the particles in NP phase upon formation, with oleic acid (aligned with hydrophobic tail facing outwards, into the organic phase. Particles were then phase transferred via a second organic acid outer layer (s) such as oleic acid (OA) and stearic acid (SA) with the functional head group faces outward, effectively rendering the particle surface hydrophilic and thus stable. As shown in Figure 7.S3 (a), optimized bilayer structure (arrangement/concentration) was achieved by adjusting ligand(s) concentrations. Above or below the optimal organic acid concentrations resulted in poor dispersion and/or low stability. For example 35.4 μmol of OA was the optimized concentration for phase transfer of a particular concentration (0.16 g/L) of Mn_xO_y NPs. Above the critical micelle concentration (CMC), organic acid (OA and SA) forms micelles in the water phase, leading to the removal of the surfactant from the surface of NPs and decrease the stability of NPs.[51] Below optimal concentrations, colloidal stability decreases due to the insufficient surface stabilization.

Polymer stabilized Mn_xO_y NPs were prepared using negatively charged poly(maleic anhydride-alt-1-octadecene) (PMAO), positively charged linear polyethylenimine (PEI), for which multi-branched PEI was used. As presented in Figure 7.S3 (b), above the certain polymer concentration, particle transfer is optimized; 0.32 μmol of multi branched PEI was the minimum needed to transfer and surface stabilize Mn_xO_y NPs (0.16 g/L or 1.8×10^{17} particles/L). As a control (no organic coating), silica coated 18 nm Mn_xO_y NPs were synthesized via a sol-gel method using tetraethyl orthosilicate (TEOS) as the silica source.[228-229] For these, silica shell thickness was controlled by TEOS concentration[228-229], resulting in shells of ca. 3 nm.
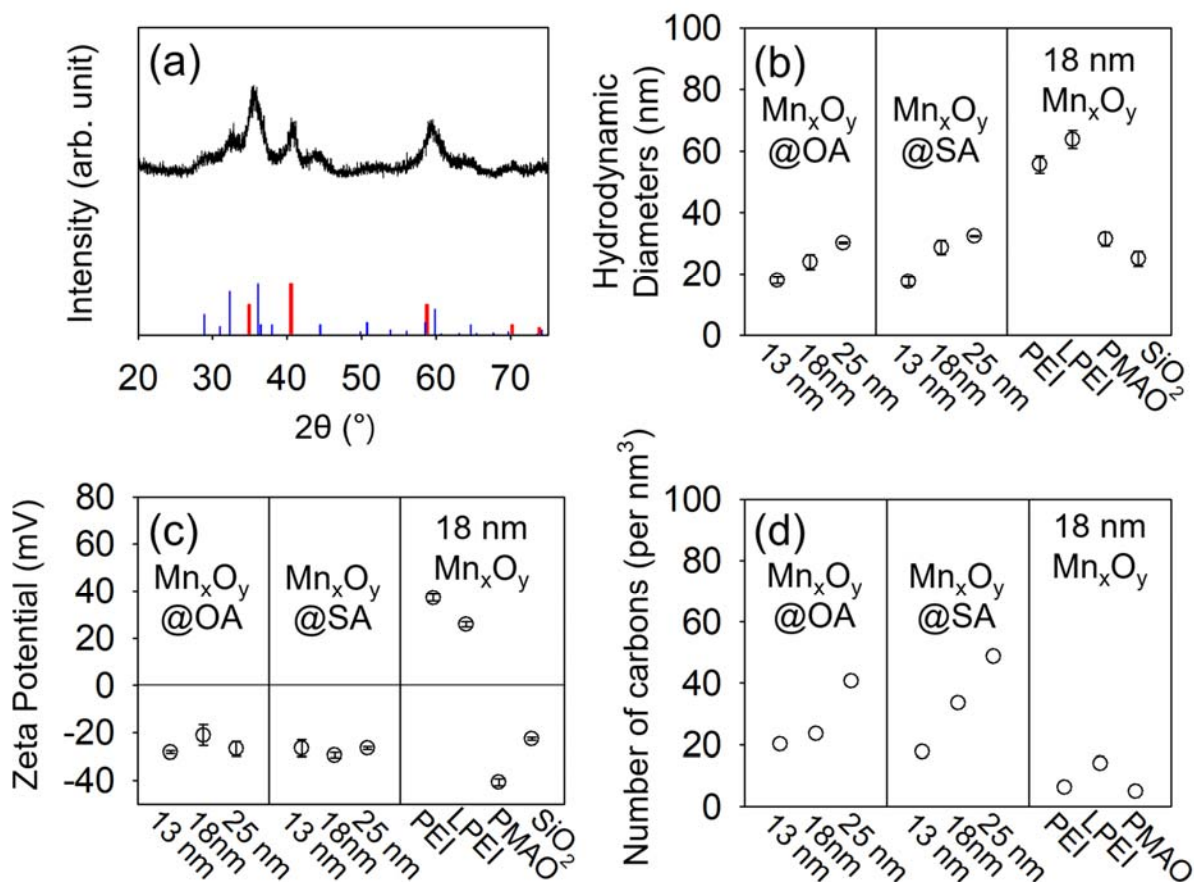
Figure 7.2 Characterization of the Mn_xO_y NPs coated with various surface stabilizers. (a) XRD data of manganese oxide (Mn_xO_y) NPs; diffraction patterns were matched well with MnO (JCPDS Card # 07-0230) and Mn_3O_4 (JCPDS Card # 24-0734) crystalline structures. (b to d) Three different size Mn_xO_y NPs (13, 18, and 25 nm as diameters) were stabilized with oleic acid (OA) and stearic acid (SA). 18 nm Mn_xO_y NPs were functionalized with series of surfactants (poly(maleic anhydride-alt-1-octadecene) (PMAO), linear polyethylenimine (LPEI), multi branched polyethylenimine (PEI), and silica ($SiO2$)). (b) Surface functionalized Mn_xO_y NPs were characterized by measuring hydrodynamic diameter at pH 7.0, (c) zeta potential at pH 7.0, and (d) number of carbons per cubic nm.

Phase transferred NPs were characterized by dynamic light scattering (DLS, Malvern, Zetasizer Nano ZS, ZEN3600) to measure hydrodynamic diameters (D_H) and zeta potential (ζ). As shown in Figure 7.2 (b), D_H of the bilayer structure NPs increased with increasing diameters of Mn_xO_y NPs. D_H of 14, 18 and, 25 nm OA (bilayer) coated Mn_xO_y NPs (Mn_xO_y@OA) were

123

18.0, 23.9, and 30.2 nm, respectively. And D_H of 14, 18 and, 25 nm SA coated Mn_xO_y NPs (Mn_xO_y@SA) were 17.5, 28.7, and 32.4 nm, respectively. D_H of polymer coated Mn_xO_y NPs was 55.7 nm for multi branched PEI coated NPs (Mn_xO_y@PEI), 63.9 nm for linear PEI stabilized NPs (Mn_xO_y@LPEI), and 31.5 nm for PMAO stabilized NPs (Mn_xO_y@PMAO). Additionally, silica encapsulated manganese oxide NPs (Mn_xO_y@SiO_2) had a D_H of 25.1 nm. As shown in Figure 7.2 (c), similar ζ was measured for NPs surface coated with the same coatings: ζ of 14, 18, and 25 nm Mn_xO_y@OA was -28.2, -21.0, and -26.8 mV, respectively and -26.4, -29.4, and -26.4 mV for 14, 18, and 25 nm Mn_xO_y@SA, respectively. ζ of 18 nm Mn_xO_y@PEI, Mn_xO_y@LPEI, Mn_xO_y@PMAO, and Mn_xO_y@SiO_2 was 37.2, 25.9, -40.8, and -22.6 mV, respectively.

As shown in Figure 7.2 (d), the number of carbon molecules (surface associated) per cubic nm was measured by total organic carbon (TOC, Shimadzu Scientific Instrument). When NPs encapsulated with the same organic stabilizer, organic surfactant loading increased with the size of NPs. Surfactant loadings on 14, 18, and 25 nm Mn_xO_y@OA were 20.2, 23.5, and 40.7 carbons per cubic nm, respectively. Numbers of carbons on 14, 18, and 25 nm Mn_xO_y@SA were 17.8, 33.5, and 48.7 per cubic nm, respectively. To achieve similar degrees of colloidal stability, larger NPs require dense organic loading because van der Waals attraction energy is proportional to size of NPs.[69, 119] In addition, larger NPs are likely to allow for more dense surfactant loading due to the relaxed steric hindrance (i.e. relatively less core curvature).[214-215] As expected, larger molecular weight, polymeric, coatings, such as PEI and PMAO, have heavier organic loading on the surface of NPs than ligands encapsulation agents, such as OA and SA (Table S1). For 18 nm Mn_xO_y NPs, organic loadings for PEI, LPEI, and PMAO were 6.3, 5.0, and 14.0 carbons per cubic nm, respectively.
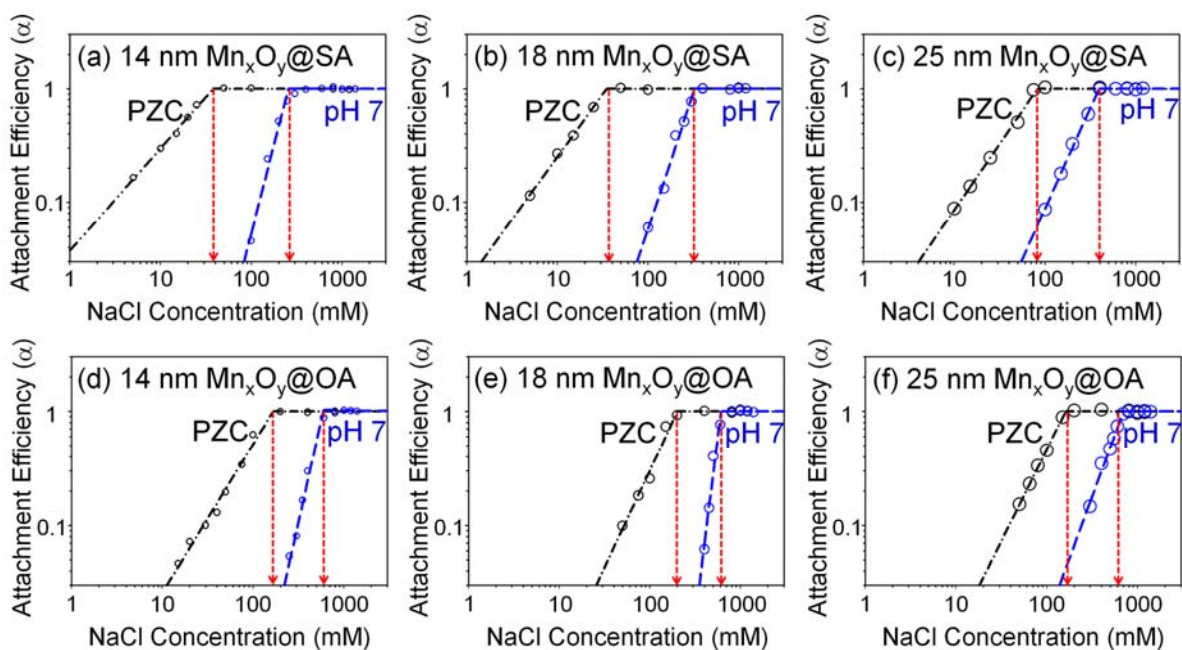
Figure 7.3 Attachment efficiency of bilayer structured Mn_xO_y NPs as a function of NaCl concentration at pH 7.0 (blue) and at pH 4.0 (PZC, balck); stearic acid (SA) stabilized (a) 14 nm MnxOy NPs (14 nm Mn_xO_y@SA), (b) 18 nm Mn_xO_y@SA, (c) 25 nm Mn_xO_y@SA, oleic acid (OA) coated (d) 14 nm Mn_xO_y NPs (14 nm Mn_xO_y@OA), (e) 18 nm Mn_xO_y@OA, and (f) 25 nm MnxOy@OA.

7.3.2. Role of Bilayer Structure on Colloidal Stability

Bilayer coatings were evaluated for three different sized particles (14, 18 and 25 nm) with oleic acid (OA) and steric acid (SA) outer coatings. Both SA and OA have 18 carbon chains with identical functional head groups (carboxyl). While SA is made of (sp3) C18 linear carbon chain, OA has an unsaturated *cis*-C18 organic acid with a double bond between C9-C10.[45] As shown in Figure 7.3, CCC values for both Mn_xO_y@SA and Mn_xO_y@OA were measured using NaCl at pH 7.0. CCC values for 14, 18 and 25 nm Mn_xO_y were 256, 326 and 392 mM for Mn_xO_y@SA, respectively and 596, 609 and 702 mM for Mn_xO_y@OA, respectively. Here, larger NPs are more actually more stable than smaller NPs, despite van der Walls (vdW) attractions increasing as a function of size (Figure 7.S4). This is likely due to the fact that, larger particles have

significantly higher grafting density (grafting density ratio of 25 nm to 14 nm is 2.0 and 2.7 for OA and OA, respectively).

Interestingly, Mn_xO_y@OA shows better colloidal stability than Mn_xO_y@SA over all size ranges tested. To explore this finding, CCC values for both Mn_xO_y@OA and Mn_xO_y@SA were additionally measured at a pH near the point of zero charge (PZC) to minimize electrostatic double layer (EDL) repulsion. As pH was lowered, ζ of Mn_xO_y@SA and Mn_xO_y@OA decreased via protonation of carboxyl group (Figure 7.S5). At PZC (pH 3.5), Mn_xO_y@SA and Mn_xO_y@OA readily aggregated. We selected the pH of solution at pH 4 (near the PZC) to prevent unwanted aggregation. At pH4, ζ for 14, 18 and 25 nm Mn_xO_y@SA was -5.0, -4.2, and -4.5 mV, respectively, and ζ for 14, 18 and 25 nm Mn_xO_y@OA was -6.5, -5.5, and -4.7 mV, respectively. CCC values at pH 4 were 38, 35 and 83 mM for Mn_xO_y@SA, respectively and 167, 202, and 162 mM for Mn_xO_y@OA, in order of increasing the size (Figure 7.3). Mn_xO_y@OA containing *cis* double bond has better colloidal stability than Mn_xO_y@SA. In previous reports, our group demonstrated that the restricted vibration and rotation of unsaturated carbon chains (OA) compared to the saturated carbon chains (SA) likely lower net entropy (effects), leading to higher elastic-steric repulsive energies.[45]

7.3.3. Surface Coating Dependent Colloidal Stability

The effects of surface coating types on colloidal stability were evaluated using 18 nm M_xO_y NPs with three types of surface coatings: inorganic (silica) coated NPs (M_xO_y@SiO$_2$), bilayer structured NPs (M_xO_y@SA and M_xO_y@OA), and poly(maleic anhydride-alt-1-octadecene (PMAO, Mw=40000) coated M_xO_y NPs (M_xO_y@PMAO). Without organic coating(s) (negative control), M_xO_y@SiO$_2$ has no osmotic or elastic-steric repulsion. As shown in Figure 7.4, the CCC values were measured using NaCl or CaCl$_2$ at pH 7.0. CCC values in NaCl were 415 mM

for $M_xO_y@SiO_2$, 609 mM for $M_xO_y@OA$, 326 mM for $M_xO_y@SA$, and 334 mM for $M_xO_y@PMAO$. Unexpectedly, $M_xO_y@SiO_2$ demonstrates a relatively high CCC value without organic surface stabilization. Here, we hypothesize that silica coating effective decreases vdW interactions. Hamaker constant (A_{121}) for the silica (SiO_2) has been reported over a range from 0.63×10^{-20} to 0.85×10^{-20} J,[10, 306-307] which is significantly lower than Hamaker constant (A_{121}) for manganese oxides (7.84×10^{-20} J).[308] In addition, polymer coated $M_xO_y@PMAO$ has smaller CCC (334 mM) than bilayered $M_xO_y@OA$ (609 mM). Grafting density also plays important role in steric repulsion.[36] Despite the fact that the organic loading mass for $M_xO_y@PMAO$ was higher than $M_xO_y@OA$, grafting density of $M_xO_y@OA$ was 1.7 times higher than that of $M_xO_y@PMAO$ (Table S1).
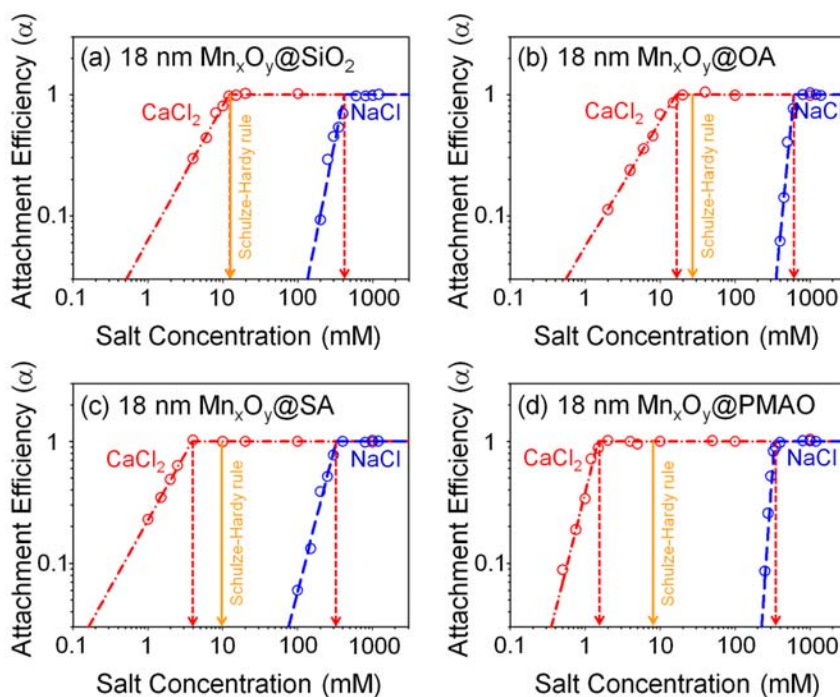
Figure 7.4 Attachment efficiency of surface functionalized 18 nm Mn_xO_y NPs ((a) $Mn_xO_y@SiO_2$, (b) $Mn_xO_y@OA$, (c) $Mn_xO_y@SA$, and (d) poly(maleic anhydride-alt-1-octadecene) coated Mn_xO_y ($Mn_xO_y@PMAO$)) as a function of salt concentration (NaCl (blue) and $CaCl_2$ (red)) and Schulze-Hardy rule expectation (yellow line).

The Schulze-Hardy rule relates the valence of counter ion(s) to colloidal stability via classical DLVO approach (XDLVO interactions are not considered). To elucidate effects of XDLVO integrations on colloidal stability, we compared experimentally measured CCC values in CaCl$_2$ and CCC calculated (modeled) by the Schulze-Hardy rule.[17, 20] As shown in Figure 7.4, CCC values in CaCl$_2$ for M$_x$O$_y$@SiO$_2$, M$_x$O$_y$@OA, M$_x$O$_y$@SA, and M$_x$O$_y$@PMAO were 12.0, 16.3, 3.8, and 1.5 mM (measurement), respectively and 12.6, 24.6, 9.9, and 7.9 mM (Schulze-Hardy rule), respectively. While M$_x$O$_y$@SiO$_2$ corresponded well with Schulze-Hardy, organic coated NPs significantly deviated from Schulze-Hardy calculations, as expected. The percentage differences between them for M$_x$O$_y$@SiO$_2$, M$_x$O$_y$@OA, M$_x$O$_y$@SA, and M$_x$O$_y$@PMAO were 4, 50, 155, 430 %, respectively. Polymer stabilized M$_x$O$_y$@PMAO had the highest discrepancy between experimental measurements and Schulze-Hardy calculations. These differences are likely to be from XDLVO interactions in addition to (PMAO) configuration changes. To further explore the configuration change of PMAO, we used Quartz Crystal Microbalance with Dissipation monitoring (QCM-D). Frequency shift has linear relationship with variation of deposited total mass (Sauerbrey Equation).[223]

$$m = -\frac{C \Delta F_n}{n} \qquad \text{(Equation 7.1)}$$

Here, m is the total deposited mass on the Q-sensor, C is the quartz sensors constant, F_n is the shift in resonance frequency and n is the resonance number (n =3). Dissipation shift presents viscoelastic properties of the adsorbed layer on the sensor. The dissipation during the oscillation of Q-sensor is described as below (Equation 7.2).[225, 269]

$$D = -\frac{E_d}{2\pi E_s} \qquad \text{(Equation 7.2)}$$

Where, D is the energy dissipation, E_d is the energy dissipated during one oscillation, and E_s is the energy stored in the oscillation system. Figure 7.5 presents the frequency and dissipation shift of the PAMO grafted sensor as a function of salt concentration (NaCl or CaCl₂). With increasing NaCl concentration (up to 2 M NaCl), frequency shift was decreased and dissipation shift was increased. This indicates that counter ions (in this case as Na^+) can cause swelling-type interactions with PMAO.[225, 309] For M_xO_y@PMAO particle systems, as the ionic strength is increased, the organic coatings effectively decreases in density and thus additional overlapping with coatings on other particles can occur. In contrast with monovalent counter ions (Na^+), PMAO dynamics behave differently in the presence of divalent counter ion (Ca^{2+}). From 1 to 20 mM (CaCl₂), frequency shift decreased with slightly increasing dissipation shift, indicative of PMAO swelling;[225, 309] however, higher CaCl₂ concentration (20 mM to 1 M) led to the effective collapse of the PMAO also releasing water molecules (adsorbed in PMAO) due to neutralization of functional groups(maleic anhydride)[225, 310] Further, above 1 M (CaCl₂), the frequency was re-decreased (increasing dissipation). indicating that re-expansion (re-hydration) of the PAMO; the adsorbed Ca^{2+} ions is likely to form a strong counterion-counterion correlation by developing opposite charges at functional groups of PMAO.[311]
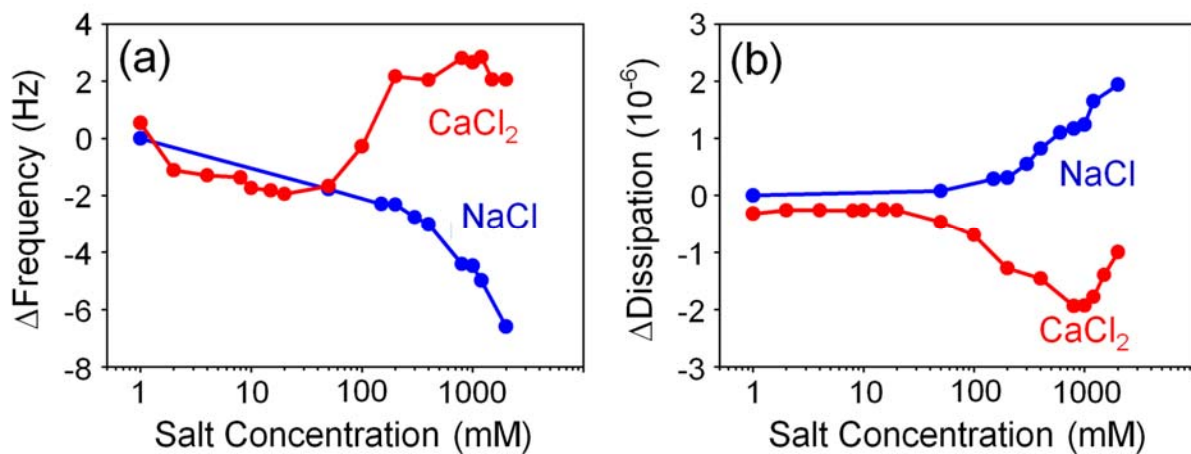
Figure 7.5 (a) Frequency shift and (b) dissipation shift of poly(maleic anhydride-alt-1-octadecene) (Mw = 40000, PMAO) as a function of salt concentration (NaCl (blue) and $CaCl_2$ (red)).

7.3.4. Surface Coating Dependent Aggregation Density

Particles aggregate, the importance of aggregation (cluster) density is crucial for transport behavior(s), including sedimentation.[158] To date, cluster density of particle aggregates, as a function of organic surface coating(s) not been quantified. Aggregation behavior of organic coated NPs is different from NPs aggregation without surfactant or NOM due to the XDLVO interactions. Specifically, elastic-steric repulsion originates from interaction (collision), interpenetration (surface layer overlapping) and final compression of the adsorbed organic coating layer.[146] Further, upon aggregation, overlap of the organic coating regime(s) is likely for organic coated NPs. For critical coagulation concentrations (CCC) experiments, normalized density as a function of attachment efficiency can be quantified by considering two types of number concentrations. Here the number of nanoclusters was measured based upon DLS (intensity mean) using the photon count rate as an indicator of the number concentration via Rayleigh scattering relationship (Equation 7.3).[312]

$$I = I_0 \frac{\pi^4 (1+cos^2\theta)}{8R^2\lambda^4} \left(\frac{m^2-1}{m^2+2}\right) d^6 N \qquad \text{(Equation 7.3)}$$

Where, I is the scattered light intensity, I_0 is the incident light intensity, θ is the scattering angle, λ is the wavelength of incident light, R is the distance of observation point and particles detected. m is the ratio of the refractive index of particles to the medium, d is the diameters of nanoclusters and N is the number concentration of nanoclusters. Equation 7.3 is reduced by applying the method coefficient term (α) (Equation 7.4), which is constant regardless of experimental conditions.

130

$$I = I_0 \alpha \left(\frac{m^2-1}{m^2+2}\right) d^6 N \qquad\qquad \text{(Equation 7.4)}$$

Number of aggregates can be measured with information of initial number concentration (Equation 7.5).[313-314]

$$\frac{P_1}{P_2} = \frac{d_1{}^6 N_1}{d_2{}^6 N_2} \qquad\qquad \text{(Equation 7.5)}$$

Normalized aggregate (relative) density can then be obtained by dividing the two different number concentrations for two different times with spherical shape assumption, typically starting with t = 0. It should be noted that there are limitations to this approach as average aggregate diameters need to be below the wavelength of incident light (Rayleigh scattering criteria). As shown in Figure 7.S6, the number of nanoparticles has a linear relationship with photon count rate over a wide range of sizes from 23 to 208 nm of silica NPs. This indicates that such density evaluations can be made for clusters under ca. 200 nm, as the incident laser wavelength is 633 nm and thus we only evaluate and describe aggregate density for nanoclusters up to ca. 200 nm.
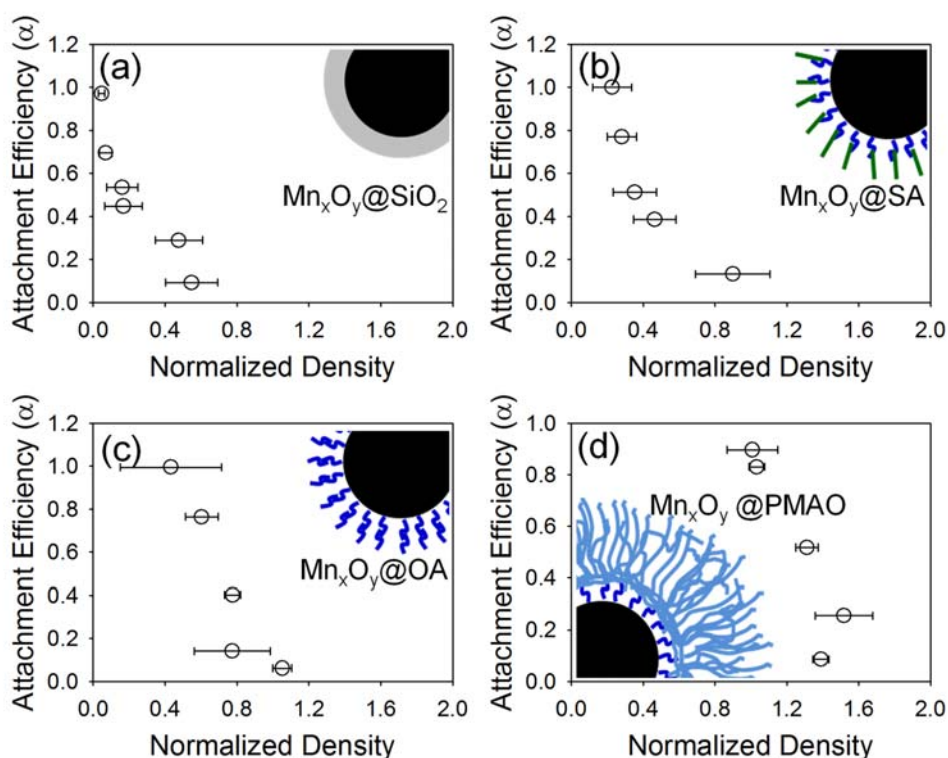
Figure 7.6 Normalized density of surface coated 18 nm Mn_xO_y NPs ((a) $Mn_xO_y@SiO_2$, (b) $Mn_xO_y@SA$, (c) $Mn_xO_y@OA$, and (d) $Mn_xO_y@PMAO$) as a function of attachment efficiency (attachment efficiency was controlled using NaCl).

Figure 7.6 shows relative aggregate density as a function of attachment efficiency (ionic strength as NaCl). Interestingly, density of the nanoclusters is highly dependent on coating type. $M_xO_y@SiO_2$ nanoclusters have < 0.6 normalized densities at low attachment efficiencies ($\alpha < 0.2$) as shown in Figure 7.6 (a). In contrast, normalized density of bilayer structured NPs ($M_xO_y@SA$ and $M_xO_y@OA$) maintained their primary density under low attachment efficiency conditions ($\alpha < 0.1$) (Figure 7.6 (b) and (c)). Perhaps even more interesting, $M_xO_y@PMAO$ has *above* 1 relative density over a wide range of attachment efficiency conditions due to $M_xO_y@PMAO$ surface coating overlap (Table S1). In addition, as increasing the attachment efficiency, normalized density decreases regardless of surface coating types. Under low attachment efficiency conditions (low salt concentration), NPs have a chance to penetrate into nanoclusters

before permanent sticking, leading dense aggregates. However, NPs permanently attach to the nanoclusters at less contact at high attachment efficiency condition (high salt concentration).[119, 315]
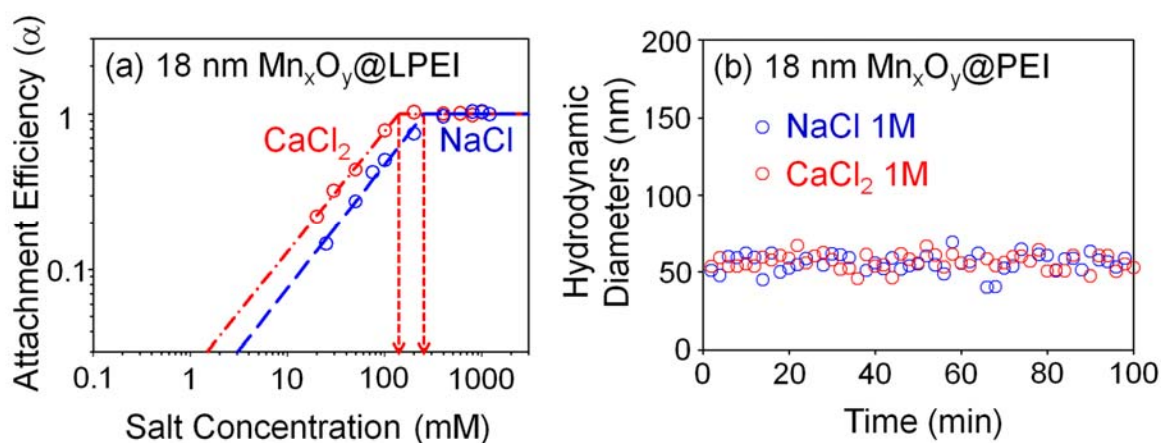
Figure 7.7 (a) Attachment efficiency of 18 nm linear polyethyleneimine (LPEI) coated Mn_xO_y (18 nm Mn_xO_y@LPEI) as a function of salt concentration (NaCl (blue) and $CaCl_2$ (red)); (b) Time dependent hydrodynamic diameters of multi branched polyethyleneimine (PEI) coated 18 nm Mn_xO_y (18 nm Mn_xO_y@PEI).

7.3.5. Effects of Polymer Structure and Configuration Change on Colloidal Stability

To elucidate the effects of polymer structure on particle stability, two different structured PEI with identical MW and composition were used as surface coating materials: linear polyethylenimine (PEI) and multi branched PEI. Figure 7.7 (a) presents the attachment efficiency of M_xO_y @LPEI under varied ionic salt conditions at pH 7. CCC was 256 mM in NaCl and 139 mM in $CaCl_2$. For the positively charged NPs, divalent cation (Ca^{2+}) did not significantly influence their stability because counter ions are anions (Cl^-) not cations (Na^+ and Ca^{2+}). Theoretically, CCC in NaCl should be 2 times higher than CCC in $CaCl_2$ (the experimental result was 1.8 times). Interestingly, M_xO_y@PEI was extremely stable under 1 M of NaCl or $CaCl_2$ concentration (Figure 7.7 (b)). This fact further highlights the importance of

133

organic coating structure in colloidal stability. For multi branch polymer coated NPs (M_xO_y@PEI), a small portion of interpenetration leads to significant compression because multi branch polymer segments anchored each of carbon chains due inherent structure.
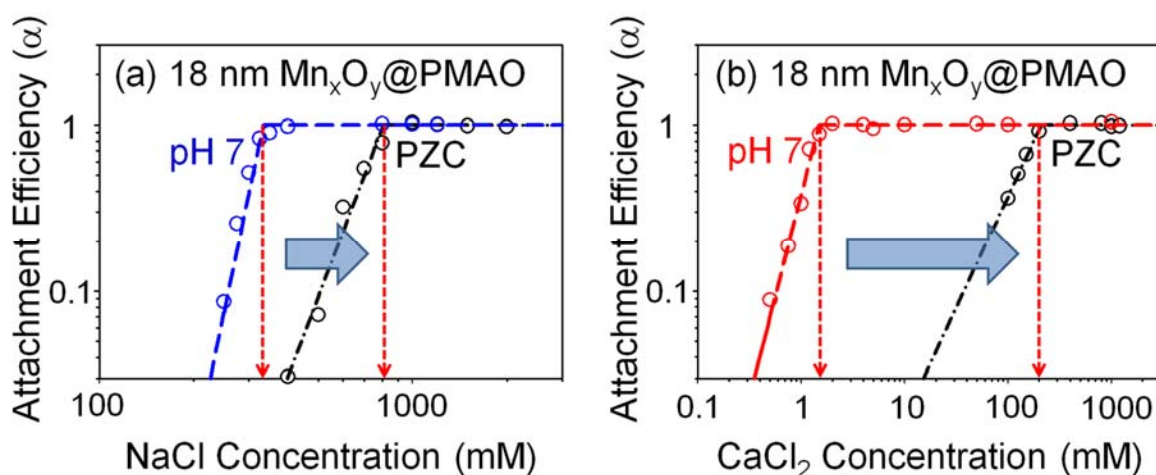
Figure 7.8 Attachment efficiency of poly(maleic anhydride-alt-1-octadecene) coated Mn_xO_y NPs (18 nm Mn_xO_y@PMAO) as a function of (a) NaCl concentration and (b) $CaCl_2$ concentration at pH 7.0 and at PZC.

Polymer coated NPs (M_xO_y@PEI, M_xO_y@LPEI, and M_xO_y@PMAO) maintained their initial hydrodynamic diameters at a point of zero charge (PZC) (Figure 7.S7). Here, we hypothesize that polymer configuration change plays important role in colloidal stability. To further explore this, CCC for M_xO_y@PMAO was measured under two different pH values (pH 7 and pH 2.5 (PZC)) in varied ionic salt concentration (NaCl or $CaCl_2$). As shown in Figure 7.8, CCC for M_xO_y@PMAO was dramatically increased at the PZC, though NPs lost their surface charge (absence of EDL repulsion): 334 mM in NaCl and 1.5 mM in $CaCl_2$ at pH 7 and 807 mM in NaCl and 210 mM in $CaCl_2$ at PZC. Colloidal stability at PZC is attributed to polymer configuration changes. Toward this end, PMAO dynamics were monitored under pH 7 and PZC using QCM-D. Figure 7.9 presents the frequency and dissipation (n=3, 5 and 7) at pH 7 and PZC; the pH was changed every 20 min for six times. As pH increased from PZC to 7.0, the

frequency decreased (increasing dissipation) and then increased (decreasing dissipation) with decreasing pH from 7.0 to PZC. Such PMAO dynamics indicates that polymer was collapses (shrinks) at pH near PZC via releasing adsorbed water molecules due to a charge neutralization.[225-226] Based on these observations, it is likely that the shrink/collapse dynamics of surface polymer chains dramatically increases the colloidal stability of polymer coated NPs.
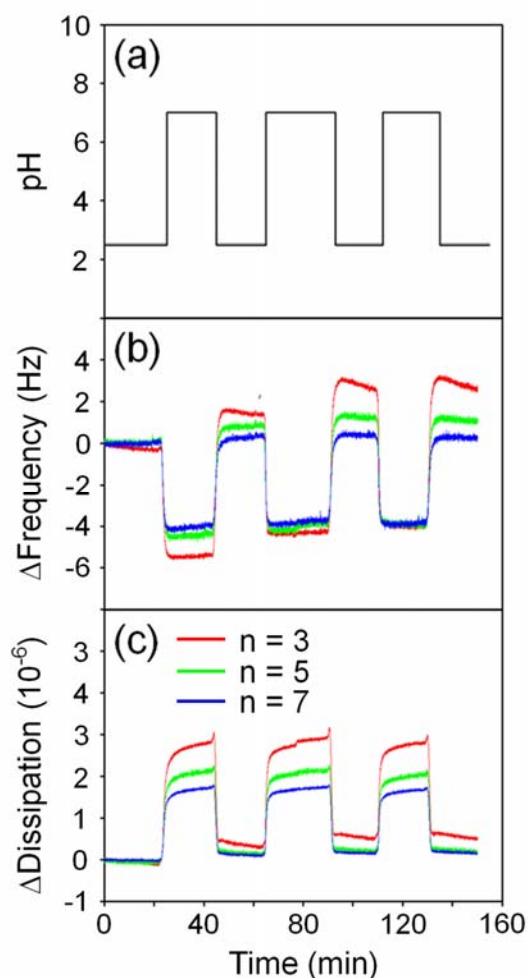
Figure 7.9 Frequency and dissipation shift of poly(maleic anhydride-alt-1-octadecene) (PMAO) at pH 2.5 (PZC) and pH 7.0 with the overtone n = 3 (red), 5 (green), and 7 (blue); time dependent (a) pH, (b) frequency, and (c) dissipation

7.4. Experimental
Chemicals

Manganese (II) chloride tetrahydrate (MnCl$_2$•4H$_2$O, 99.99%), oleic acid (OA, technical grade, 90%), 1-octadecene (ODE, technical grade, 90%), stearic acid (SA, 98.5%), oleic acid (OA, 99%), poly(maleic anhydride-alt-1-octadecene) (PMAO, Mw=40000), linear polyethyleneimine (LPEI, Mw=25000), branched polyethyleneimine (PEI, Mw=25000), Igepal CO-520 ((C$_2$H$_4$O)n·C$_{15}$H$_{24}$O, n≈5), tetraethoxy orthosilcate (TEOS, 99.99%), poly-L-lysine (PLL), cyclohexane (99%), ethanol (99.9%), acetone (99.5%), hexane (98.5%) were purchased from Sigma-Aldrich; sodium oleate (97%) was obtained from TCI America; silica NPs were obtained from NanoComposix.

Synthesis of Manganese Oleate (Mn-oleate)
Mn-oleate was synthesized by the method reported by An et al.[244] The mixtures of manganese chloride tetrahydrate (40 mmol) with oleic acid (80 mmol) in 100 g of ethanol, 50 g of water, and 80 g of hexane were heated at 58 °C for 4 hrs. The resulting Mn-oleate suspension was purified over six times using water and ethanol (1:1 volume ratio) and then extracted the purified Mn-oleate using hexane.

Synthesis of Manganese Oxide Nanoparticles (MnxOy NPs)
Mn$_x$O$_y$ NPs were synthesized by Mn-oleate decomposition at 320 °C under argon gas purging. The size of the M$_x$O$_y$ NPs was controlled by Mn-oleate concentration; for 14, 18, and 25 nm M$_x$O$_y$ NPs, 0.5, 1.0, and 2.0 mmol of precursor were used in the presence of oleic acid (0.5 mmol) in of 1-octadence (5 g), respectively. The resulting NPs were purified using ethanol (20 ml) and acetone (25 ml). The purifying process was repeated over six times. Purified Mn$_x$O$_y$ NPs were stored in nonpolar solvent hexane.

Organic Functionalization
Synthesized Mn$_x$O$_y$ NPs dissolved in non polar solvents were phase transferred from hexane to water by ligands exchange or encapsulation methods.[40, 51] Oleic acid (OA), stearic acid (SA) and

poly (maleic anhydride-alt-1-octadecene) (PMAO) were used as ligands encapsulation agents and linear polyethyleneimine (LPEI) and multi branched polyethyleneimin (PEI) were used for ligand exchange agents. Detailed information for organic functionalization was described in our previous paper and others.[40, 51]

Silica Coating

Silica coating on Mn_xO_y NPs was prepared based on the method reported by Selvan et al.[228-229] For details, 2.0 ml Igepal CO-520 was added in 15 ml cyclohexane containing 40 mg of 18 nm synthesized Mn_xO_y NPs. And then, 0.4ml NH_4OH (29%) and 0.1 ml tetraethoxy orthosilcate (TEOS) were injected rapidly and kept the mixture over night with vigorous mixing. The resulting silica coated NPs were purified using ethanol and DI over six times using centrifugation.

Critical Coagulation Concentration (CCC)

The CCC of NPs was measured by DLS (Malvern, Zetasizer Nano ZS, ZEN3600). Detailed information for measuring CCC has been described in our previous research and by others.[154, 316-317] For the CCC estimated by Schulze-Hardy rule, that was derived from linear superposition Gouy-Chapman expression and unretarded Hamaker expression: $ccc \propto z^{-6}A^{-2}tanh^4(ze\zeta/4kT)$, where z is valence, A is the Hamaker constant, e is the electron charge, ζ is the zeta potential, k is the Boltzmann constant and T is the absolute temperature.[119, 153]

Transmission Electron Microscope (TEM)

The diameters of the synthesized Mn_xO_y NPs were determined using transmission electron microscope (TEM, Tecnai G2 Spirit, FEI) with carbon support film on 300 mesh copper grids (Electron Microscopy Sciences). Average size of Mn_xO_y NPs were analyzed by counting over a thousand of NPs using Image Pro Plus 6.0 (Media Cybernetics, USA).[230]

X-ray Diffraction (XRD)

XRD patterns (from 20º to 80º of 2θ) were measured using a powder diffractometer (Bruker d8 Advance X-ray Diffractometer) with Cu Kα radiation (1.54 Å).

Quartz Crystal Microbalance with Dissipation (QCM-D)

QCM-D (Q-sense E4, Biolin Scientific) with quartz sensor (5MHz silica coated QCM-D crystal, QSX-202, Q-sense) was used to evaluate polymer dynamics at 22.00 ± 0.02 °C. PMAO coating was conducted by the "grafting to" method[224] using PLL as a linker.[16] 2 g/L of PMAO solution was prepared and use its supernatant. Baseline experiments (with PLL linked Q-sensor) were conducted for the compensation of undesired dissipation and the frequency shift caused by ionic strength (viscosity).

7.5. Conclusions

Variable factor of organic coating, such as structure, grafting density, and configuration change have great influence on colloidal stability of NPs. Amount of empty space of organic coating regime is determinant of density of nanoclusters. Situationally, density of aggregates exceeds its primary density. In addition, shrinkage of polymer structure via solution chemistry (i.e. pH, ionic strength) dramatically increases colloidal stability.

7.6. Supporting Information

The van der Waals (vdW) energy interaction was calculated based upon the sphere-sphere geometry. Equations for calculation of vdW energy is as follows.[318]

$$V_{Vdw} = -\frac{A_H}{6}\left[\frac{2a^2}{h^2+4ah} + \frac{2a^2}{h^2+4ah+4a^2} + ln\left(\frac{h^2+4ah}{h^2+4ah+4a^2}\right)\right] \qquad \text{(Equation 7.S1)}$$

Here, h is the separation distance, a is the diameter of Mn_xO_y NPs, and A_H is the Hamaker constant $(7.84 \times 10^{-20}$ J)[308] for Mn_xO_y NPs -water- Mn_xO_y NPs system.
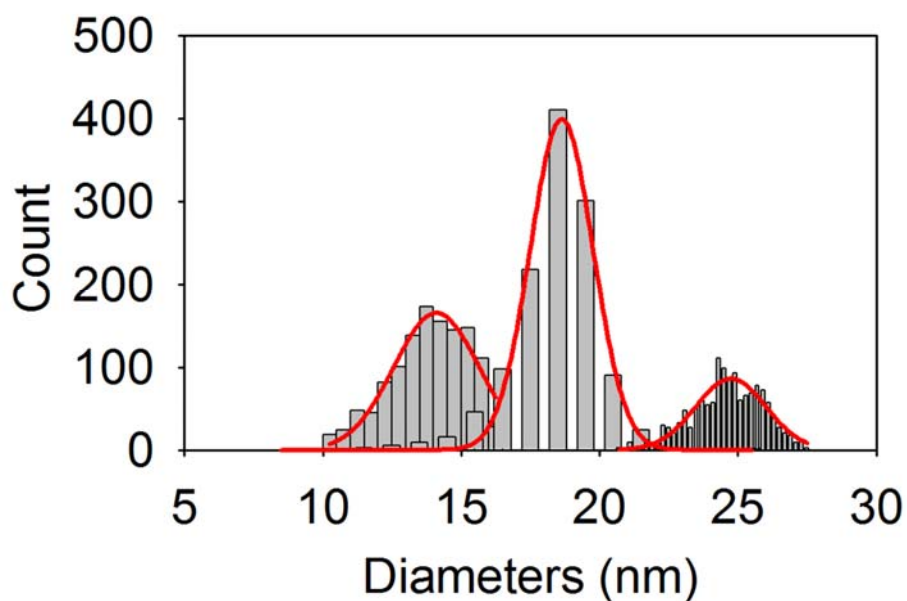
Figure 7.S1 The histograms of the size distribution of synthesized Mn_xO_y NPs. The average diameters and their standard deviation analyzed by Image Pro Plus 6.0 were 13.8 ± 1.4, 18.4 ± 1.5, and 24.6 ± 1.3.
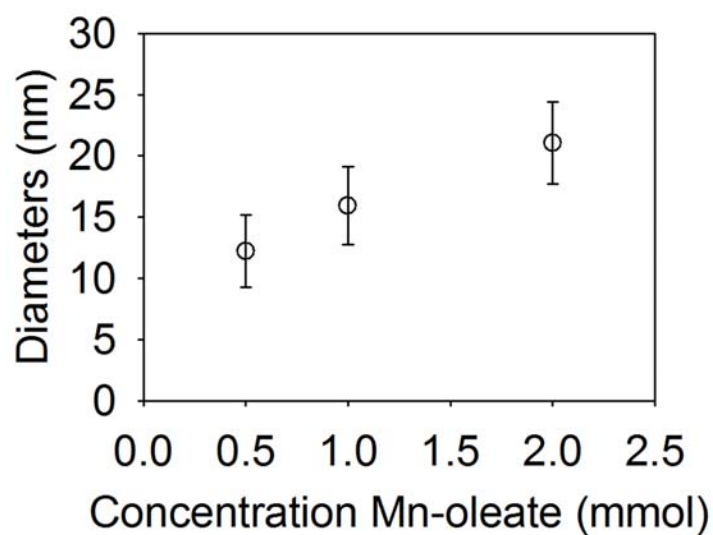
Figure 7.S2 Diameters of synthesized Mn_xO_y NPs as a function of Mn-oleate concentration with 0.5 mmol oleic acid in 5 g of 1-octadecene as a solvent.
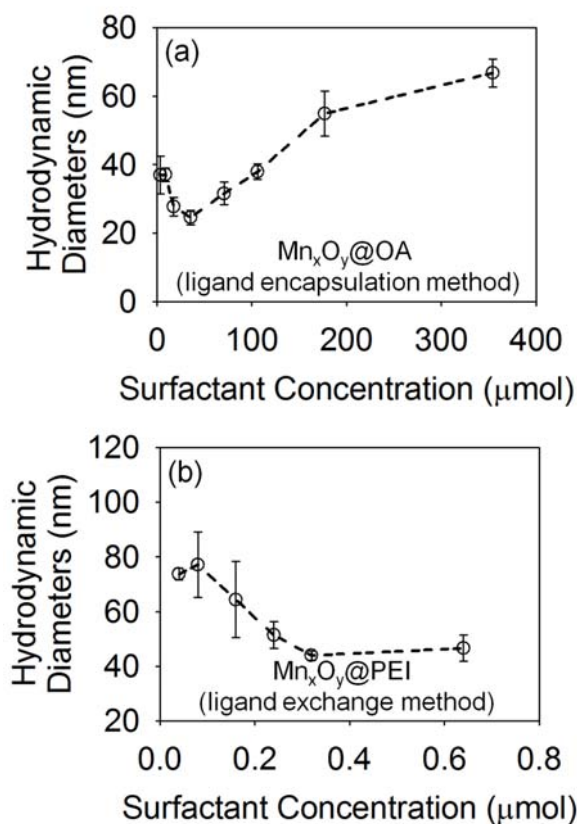
Figure 7.S3 The hydrodynamic diameters of phase transferred Mn_xO_y NPs as a function of surfactant concentration; (a) OA stabilized MnxOy NPs (Mn_xO_y@OA) by ligand encapsulation method; (b) PEI (Mw = 25000) coated MnxOy NPs (Mn_xO_y@PEI) by ligand exchange method.
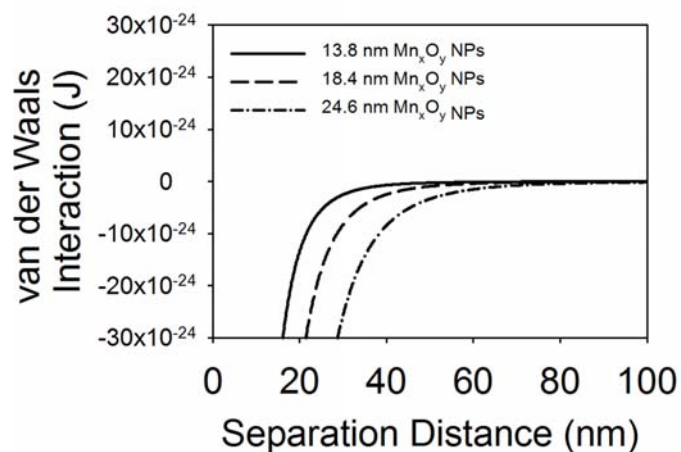
Figure 7.S4 van der Waals energy interaction of three different size (13.8, 18.4, and 24.6 nm) Mn_xO_y NPs as a function of separation distance.
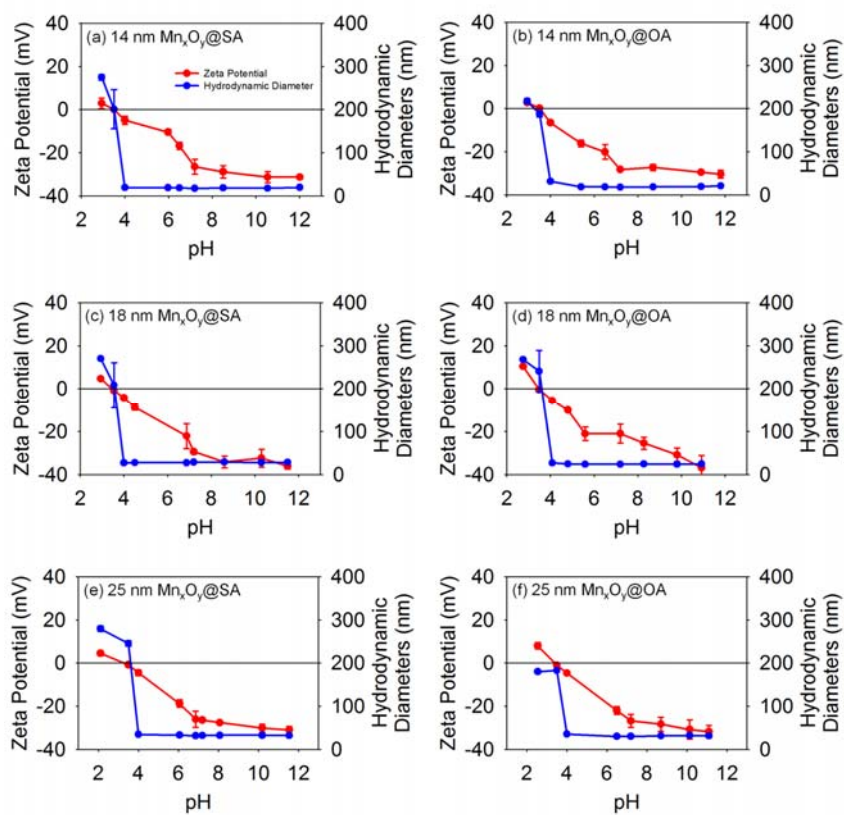
Figure 7.S5 Zeta potential (red) and hydrodynamic diameters (blue) of bilayer structured MnxOy NPs; 14 nm NPs with (a) oleic acid (OA) (14 nm Mn_xO_y@OA); (b) stearic acid (SA) (14 nm Mn_xO_y@OA); 18 nm NPs with (c) OA (18 nm Mn_xO_y@OA); (d) SA (18 nm Mn_xO_y@OA); 25 nm NPs with (e) OA (25 nm Mn_xO_y@OA); (f) SA (25 nm Mn_xO_y@OA)
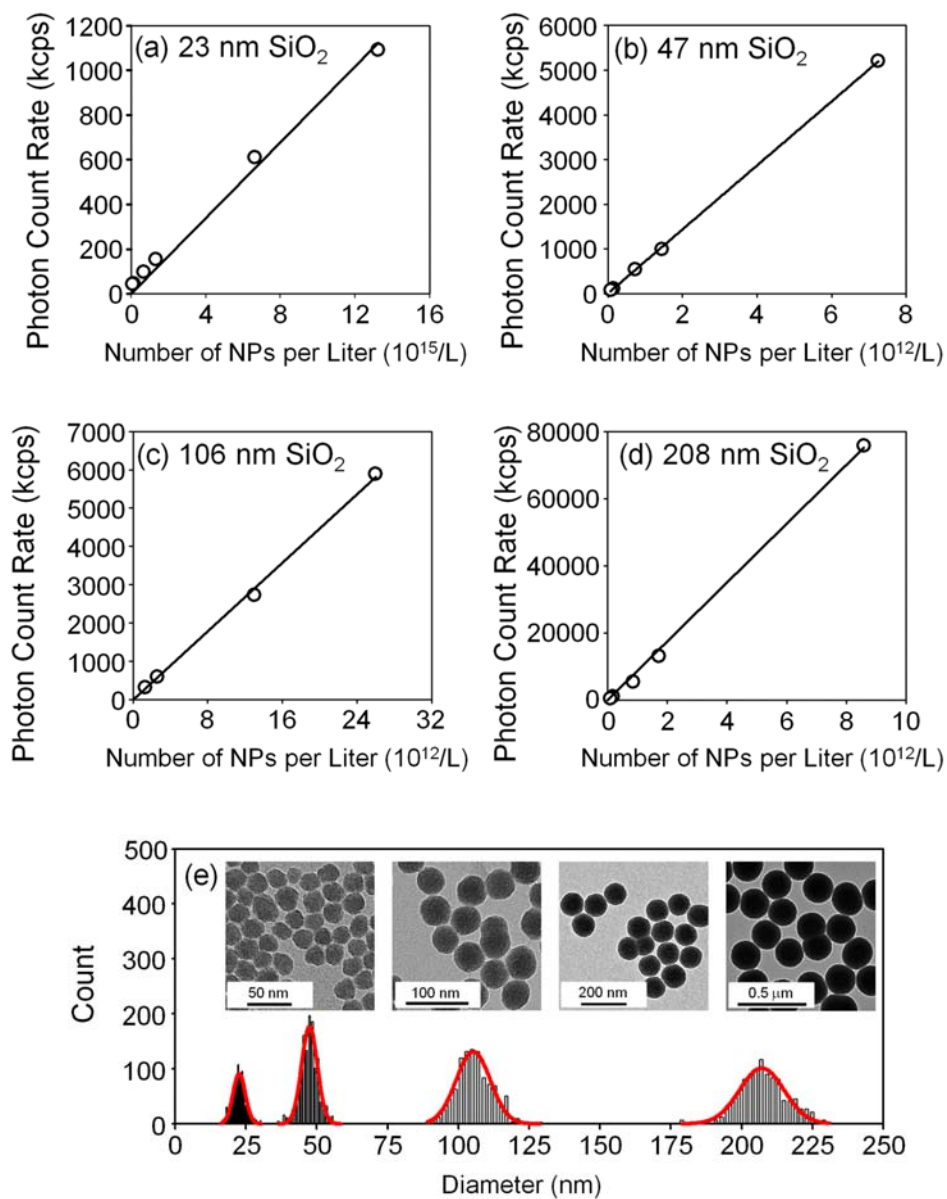
Figure 7.S6 Photon counter rate as a function of the number of silica NPs; (a) 23 nm NPs (23 nm SiO₂); (b) 47 nm NPs (47 nm SiO₂); (c) 106 nm NPs (106 nm SiO₂); (d) 208 nm NPs (208 nm SiO₂); (e) size and size distribution of four different size (23 nm, 47 nm, 106 nm, and 208 nm) silica NPs with TEM images.
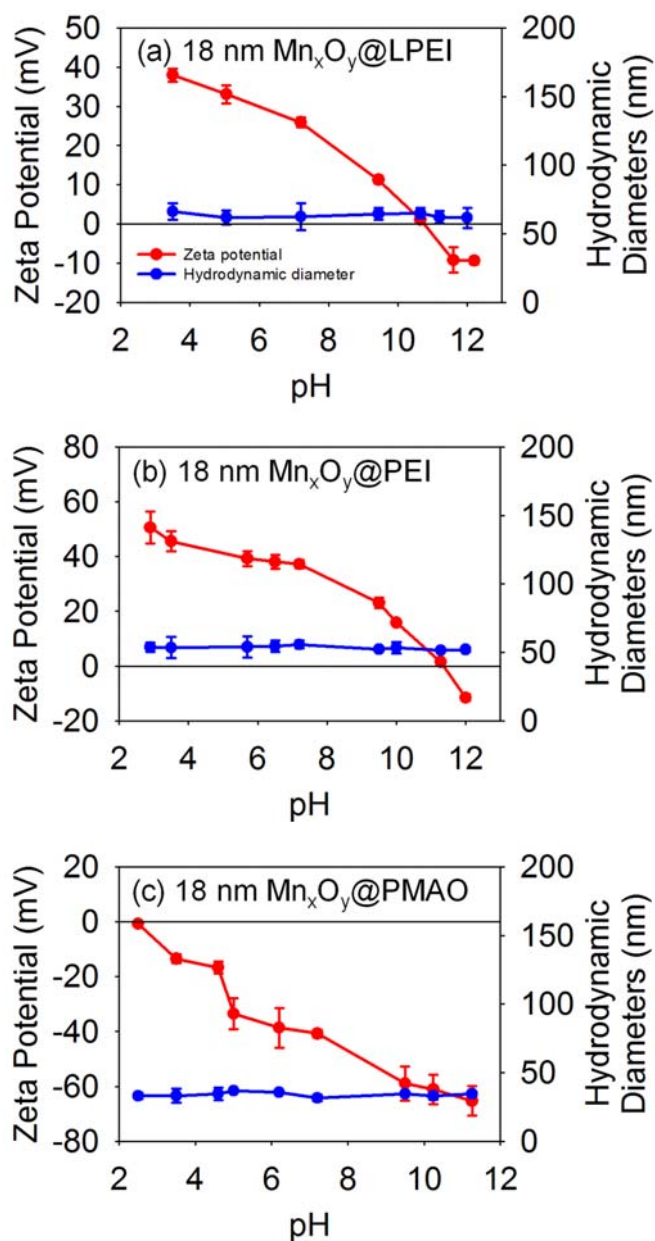
Figure 7.S7 Zeta potential (red) and hydrodynamic diameters (blue) of 18 nm Mn_xO_y NPs with (a) linear polyethyleneimine (Mw = 25000, LPEI)) (18 nm Mn_xO_y@LPEI); (b) Multi branched PEI (Mw = 25000) (18 nm Mn_xO_y@PEI); (c) poly(maleic anhydride-alt-1-octadecene) (Mw = 40000, PMAO) (18 nm Mn_xO_y@PMAO)

Table 7.S1 Total organic carbon (TOC), organic coating volume, and grafting density of organic coated Mn_xO_y NPs.

Nanoparticle	Total Organic Carbon (ppm as carbon) α	Organic coating volume (cubic nm) β	Grafting density(number of carbon per cubic nm) γ	Carbon ratio (carbon mass/total mass
14 nm Mn_xO_y@OA	96.3 ± 1.2	35,616	20.2	0.77
18 nm Mn_xO_y@OA	138.3 ± 1.0	104,699	23.5	0.77
25 nm Mn_xO_y@OA	157.4 ± 3.3	164,217	40.7	0.77
14 nm Mn_xO_y@SA	102.6 ± 0.6	43,221	17.8	0.76
18 nm Mn_xO_y@SA	114.7 ± 1.1	60,728	33.5	0.76
25 nm Mn_xO_y@SA	146.5 ± 0.7	127,725	48.7	0.76
18 nm Mn_xO_y@PEI	276.8 ± 2.2	783,305	6.3	0.56
18 nm Mn_xO_y@LPEI	132.6 ± 1.2	1,115,495	5.0	0.56
18 nm Mn_xO_y@PMAO	179.1 ± 2.1	226,934	14.0	0.75

α. TOC was measured using 50 ppm of Mn_xO_y NPs.

β. Organic coating volume was calculated on the basis of hydrodynamic diameter and size of core Mn_xO_y NPs.

γ. Grafting density was calculated by dividing the number of carbon per NP and organic coating volume.

Chapter 8: Surface Functionalized Superparamagnetic Iron Oxide Nanoparticles as Draw Solutes for Osmotically Driven Water Transport

*To be submitted in peer review journal

8.1. Overview

Here we demonstrate highly stable organic-coated engineered superparamagnetic iron oxide nanoparticles (IONPs), which can create a constant driving force in osmotic pressure driven membrane systems without aggregation, reverse diffusion, or membrane fouling. Organic coatings are compact, thin and have very similar surface charge as the membrane itself, which results in effective osmotic pressure in forward osmosis (FO) mode. To increase the osmotic pressure further, we synthesized and demonstrated hollow IONPs with the same coatings. Finally, water flux can be increased further using an oscillating magnetic field to exploit paramagnetism of the particle cores (for solid particles).

8.2. Introduction

Pressure retarded osmosis (PRO) and forward osmosis (FO) have attracted with regard to energy generation, energy recovery, and water treatment.[319-320] For both PRO and FO processes, developing stable, ideal draw solutes remains a major challenge. Promising draw solutes should have high solubility, be nontoxic, and not physically or chemically react with membrane surface, resulting in sorption or fouling.[161] Further, production and recovery costs of draw solutes should be relatively low for scaled applications. Finally, there should be no reverse diffusion (draw

solute permeation into the feed solution), which causes loss of osmotic pressures and concentration polarization (CP).[162]

Magnetic nanoparticles (MNPs) have been considered as advanced draw solutes as they can be magnetically separated/regenerated, thus controlled in solution.   Among MNPs, superparamagnetic iron oxide nanoparticles (IONPs) are promising candidates because of their relatively low cost[186] and toxicity.[187]   To date, previous studies have reported IONPs as draw solutes with organic surface coatings, including triethylene glycol,[188-189] polyacrylic acid,[321] poly(sodium acrylate),[190] poly(N-isopropylacrylamide),[191] polyglycerol,[192] dextran,[193] citrate,[194] and poly(ethylene glycol)diacid.[195]   For all, IONPs aggregation and deposition on the surface of membrane (fouling) remains a critical challenge that has not been solved.

As draw solutes in membrane systems, MNPs should be colloidally stable.   Colloidal stability of IONPs is depends on the synthesis methods and surface coating strategies. Engineered IONPs can be synthesized by several methods (also discussed above), including thermal decomposition,[42, 48] co-precipitation,[49] and microemulsion.[50]   For producing monodisperse IONPs having high colloidal stability, thermal decomposition with an organic surface surfactants in nonpolar solvent is a highly reproducible method for monodisperse suspensions with precise surface coatings.[51] Here, we prepared highly monodisperse IONPs (12 nm) with a series of surface coatings, including sodium dodecyl sulfate (SDS), cetyltrimethylammonium bromide (CTAB), and polyethylene glycol (PEG).   We evaluated the library of functionalized IONPs as potential draw solutes in osmotic pressure-driven membrane processes.   Draw solutes evaluated are highly colloidally stable due to their steric repulsion, which prevents nanoparticle aggregation and adsorption on the membrane surface.   Additionally, we increased the osmotic pressure of the draw solution by hollowing out the NP core structures,

which enhanced pressure with the same mass of draw solutes. Lastly, we improved the CP profile using an oscillating magnetic field to increase the water flux with superparamagnetic particles.

8.3. Results and discussion

8.3.1. Synthesis of Superparamagnetic IONPs and HNPs

Highly monodisperse 12 nm IONPs were synthesized by thermal decomposition in the presence of OA[42, 260] As measured by TEM (Figure 8.1 (a)), their size was 12.3 ± 1.0 nm and size distribution was presented in Figure 8.2 (a). The crystalline structure of the synthesized IONPs were well known as Fe_3O_4 (JCPDS Card # 190629), which has been previously reported by our group and others. (Figure 8.2 (b))[42, 260] In addition, IONPs were hollowed out via acid etching using technical grade TOPO (Figure 8.1 (b)).[322] The resulting IONPs and HNPs were highly monodisperse in nonpolar solvent because of their hydrophilic functional group of oleic acid coating (hydrophobic head facing into the solvent).[45]
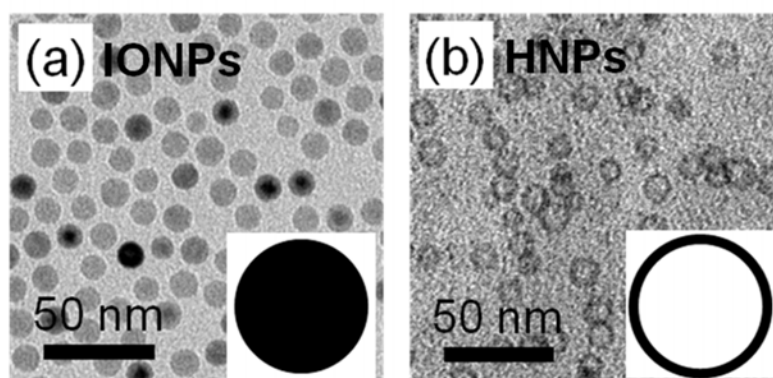
Figure 8.1 TEM images of monodisperse (a) IONPs and (b) HNPs. Average diameter (12.3 ± 1.0 nm) of IONPs and HNPs was measured using Image-Pro 6.0 with over a thousand crystals counted.

Synthesized IONPs were coated by both ligand encapsulation and exchange methods for phase-transfer from into water.[40, 51] SDS, with a negatively charged sulfate terminal group, and

147

CTAB, with a positively charged methyl ammonium terminal group, were used as ligand encapsulation agents. PEG (MW = 5K) with hydroxyl functional groups within the polymer chain was used as a ligand exchange agent. The hydrodynamic diameters (D_H) and zeta potentials of phase transferred IONPs and HNPs were analyzed by DLS at pH 7. As shown in Figure 8.2 (c), D_H values for SDS-coated IONPs (IONP@SDS), CTAB-coated IONPs (IONP@CTAB), PEG-coated IONPs (IONP@PEG), and SDS-coated HNPs (HNP@SDS) were 23.5, 24.6, 37.7, and 26.3 nm, respectively. The zeta potentials for IONP@SDS, IONP@CTAB, IONP@PEG, and HNP@SDS were -25.5, 26.7, -6.3, and -35.1 mV, respectively.
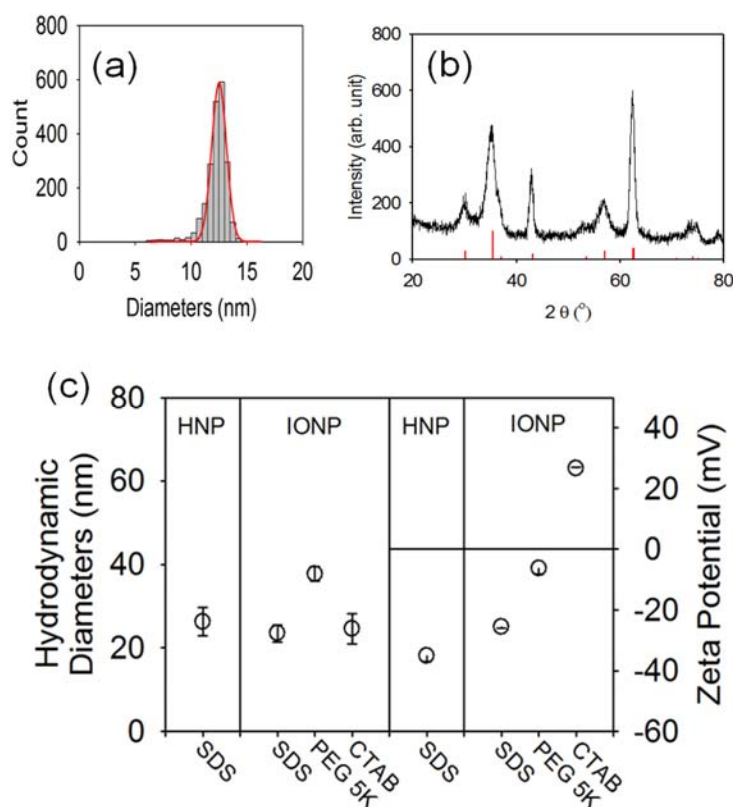
Figure 8.2 (a) Size distribution of synthesized IONPs. The average diameter and the standard deviation were 12.3 ± 1.0 nm. (b) X-ray diffraction (XRD) data of IONPs; diffraction patterns were well matched with magnetite (Fe_3O_4) crystalline structure (JCPDS Card # 190629, lower bars). (c) Hydrodynamic diameters and zeta potentials of IONPs and HNPs coated with various surface stabilizers at pH 7.

8.3.2. Osmotic Pressure Driven Membrane System

An osmotic pressure driven membrane system has two operation modes, depending on the membrane's surface direction. When the active layer of the membrane faces the feed side, the system is in forward osmosis (FO) mode. For FO, significant internal concentration polarization (ICP) occurs in the support layer, leading to a decrease of draw solution concentration at the surface of active layer. External concentration polarization (ECP) is built up near the active layer, increasing the feed solution concentration at the surface of the active layer (Figure 8.3 (a)). On the other hand, as shown in Figure 8.3 (b), ECP and ICP are created on draw side and feed side, respectively, in the PRO mode (active layer facing the draw solution). Both forms of CP are significant problems in osmotic pressure driven membrane processes, due to the reduction of the net driving force.
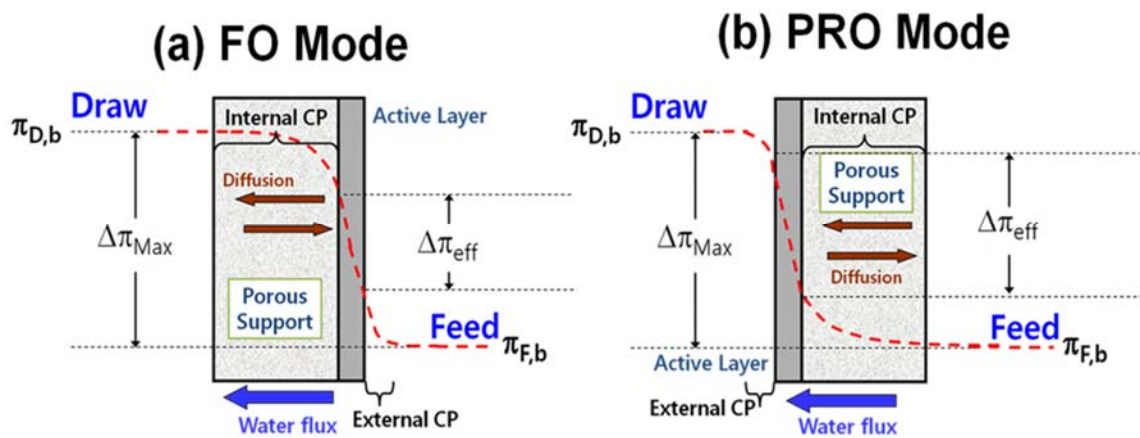
Figure 8.3 Osmotic driving force profile in osmotic pressure driven membrane processes: (a) FO mode (active layer faces feed solution) and (b) PRO mode (active layer faces draw solution). Here, $\pi_{D,b}$ is the osmotic pressure of draw solution at bulk, $\pi_{F,b}$ is the osmotic pressure of feed solution at bulk, $\Delta\pi_{Max}$ is maximum osmotic pressure difference between draw and feed solution (ideal case), and $\Delta\pi_{eff}$ is effective osmotic pressure difference between draw and feed solution (real case).
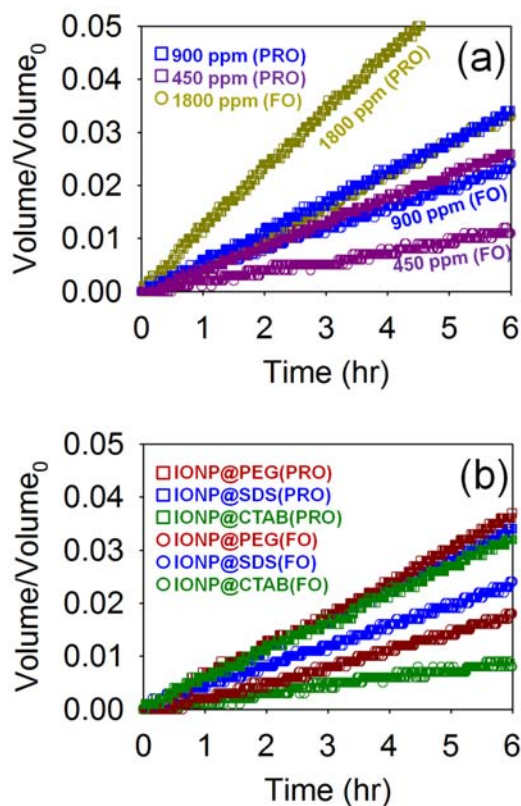
Figure 8.4 Draw solute performances of synthesized NPs in osmotic pressure driven membrane processes (FO and PRO modes). Water fluxes were measured by time dependent total volume increase (V/V_0). (a) Concentration dependence tests using IONP@SDS, (b) organic coating dependence tests using IONP@SDS, IONP@PEG, and IONP@CTAB, (c) inner core particle dependence tests using IONP@SDS and HNP@SDS.

Concentration-dependent (450, 900, and 1800 ppm) draw solute tests were performed using IONP@SDS. The water fluxes were 0.19, 0.42, and 0.58 L/hr·m² for 450, 900, and 1,800 ppm, respectively, in FO mode and 0.42, 0.60, and 1.16 L/hr·m² for 450, 900, and 1,800 ppm, respectively, in PRO mode (Figure 8.4 (a)). As expected, when the particle concentration increased, the water flux increased, because particle concentration and osmotic pressure have a linear relationship (Van't Hoff equation). The increase in draw solution volume was approximately linear as a function of time indicating low fouling. We speculate that the organic coating plays a significant role in NP draw solutes' behavior, as steric repulsion prevents NP

aggregation and membrane adsorption.[36-37] In addition, the synthesized NPs are too large to pass through/into the membrane (via size exclusion). This fact was confirmed by ICP-OES measurements of the feed solution after the experiments. Over the tested concentration ranges, ICP has more influence on osmotic systems than ECP (i.e. flux of PRO mode is higher than that of FO mode). This is due to physical properties of the membrane support layer, such as the thickness, porosity, and tortuosity, as they relate to hindered transport/diffusion of draw solutes.[323]

For optimized organic coated IONPs, the thickness and surface charge of the organic coating need to be considered. Organic coating-dependent tests were performed using an identical IONP concentration (900 ppm) with various organic stabilizers, including SDS, CTAB, and PEG. As shown in Figure 8.4 (b), the water fluxes were respectively 0.42, 0.14, and 0.32 L/hr·m^2 for IONP@SDS, IONP@CTAB, and IONP@PEG, in FO mode, and 0.60, 0.56, and 0.65 L/hr·m^2, respectively for IONP@SDS, IONP@CTAB, and IONP@PEG, in PRO mode. For the tested organic coatings, IONPs performances were similar in PRO mode. On the other hand, their performances varied considerably, depending on the coating type, in FO mode. To create effective osmotic pressure in FO mode, draw solutes in the bulk solution should diffuse to the end of the support layer (toward the active layer). A thin organic coating layer of IONPs (e.g. SDS) is better for diffusion than a thick layer (e.g. PEG). Also, positively charged IONP@CTAB showed a considerably lower water flux than negatively charged IONPs (IONP@SDS and IONP@PEG). The membrane, composed of a polyamide thin film with polysulfone supports, has a negative surface charge.[324] We speculate that oppositely charged IONPs (e.g. CTAB) are more readily transported and associate with negatively charged support layer due to electrostatic attraction, resulting in considerable ICP.
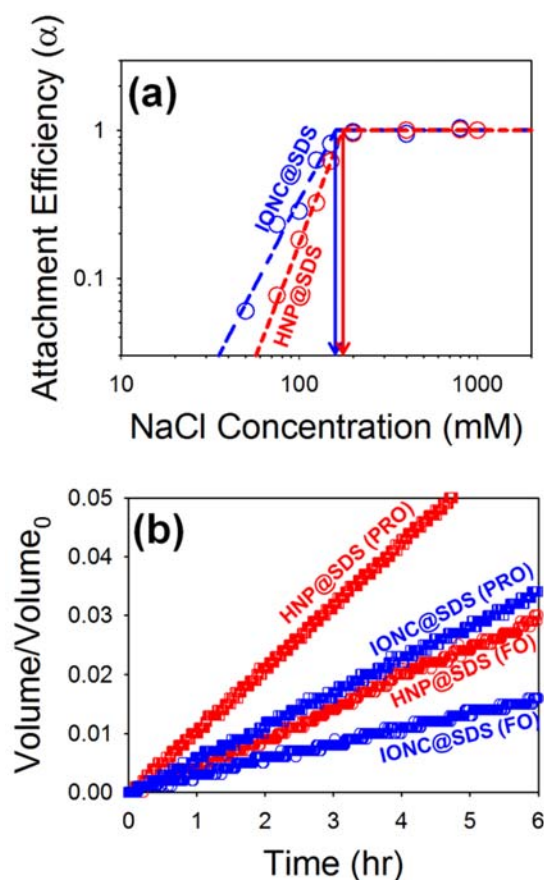
Figure 8.5 (a) Attachment efficiency of IONP@SDS (blue) and HNP@SDS (red) as a function of NaCl concentration (b) Draw solute performances of synthesized IONP@SDS and HNP@SDS in osmotic pressure driven membrane processes (FO and PRO modes). Water fluxes were measured by time dependent total volume increase (V/V_0).

8.3.3. Flux Enhancement

To improve the draw solute performance, we explored the use hollow IONPs (HNPs) as draw solutes and oscillating magnetic field. First, the inners of core IONPs were hollowed to increase the number concentration of NPs (osmotic pressure) for the same mass concentration. High colloidal stability aids draw solute performance by preventing aggregation and membrane fouling. Colloidal stabilities of both IONPs and HNPs were investigated by measuring the critical coagulation concentration (CCC). Both HNP@SDS and IONP@SDS had similar colloidal stabilities; CCC values were 175 mM and 159 mM in NaCl for HNP@SDS and

152

IONP@SDS, respectively (Figure 8.5 (a)). For the same mass concentration (900 ppm), water flux was enhanced using HNPs because they increased the number concentration (Figure 8.5 (b)). The water fluxes were 0.53 and 1.11 L/hr·m^2 for HNP@SDS in FO and PRO modes, respectively.
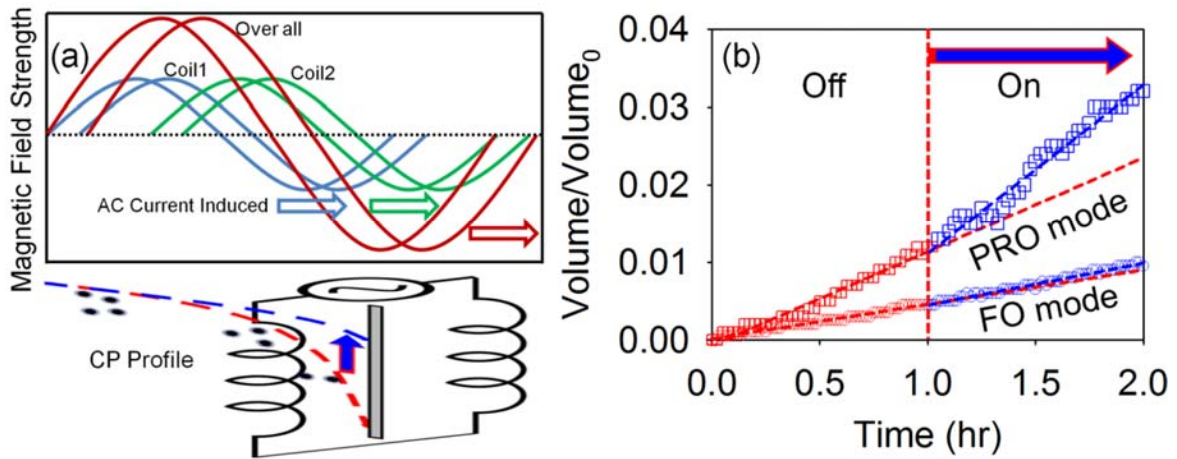
Figure 8.6 (a) Schematic diagrams of oscillating magnetic field for improvement of the concentration polarization (CP) profile of IONPs (b) Total volume increase (V/V_0) as a function of time before and after oscillating magnetic field control in FO and PRO modes.

We next demonstrated the improvement of the CP profile when organic coated IONPs were used as draw solutes. To reduce the CP in osmotic pressure driven membrane systems, we applied a magnetic field using the stator of AC motor, as illustrated in Figure 8.6 (a). This stator is a part of motor (1125 RPM) of tractor (730, John Deere). The stator coils produce an oscillating magnetic field, which have a linear relationship with applied current. We applied 10 times lower current than original current of tractor battery. In this manner, the maximum magnetic field produced by stator is 10 times lower than original magnetic field for operating tractor. Magnetic field-dependence tests were implemented using 1800 ppm of IONP@SDS as a draw solute in both FO and PRO modes. As shown in Figure 8.6 (b), water flux was increased by 23% in FO mode and 80% in PRO mode upon application of the magnetic field. We

153

hypothesize that the magnetic field has a direct effect on ICP because the support layer physically hinders diffusion of the draw solute. Unexpectedly, in a few cases we also observed some case whereby water flux was stopped (no effective osmotic pressure) during the magnetic field applied (data not shown). We hypothesize here that applied magnetic field also boosted the ECP profiles of superparamagnetic IONPs depending on the system location. Oscillating magnetic field control, including direction and strength, is also important factor to be considered as a part of flux optimization, which was beyond the scope of this initial study. To our knowledge this is the first case that stable magnetic particles were demonstrated to increase flux via applied magnetic field for osmotic driven processes.

8.4. Experimental

Materials.

Iron oxy hydroxide (FeOOH), oleic acid (OA, technical grade, 90%), 1-octadecene (ODE, technical grade, 90%), cetyltrimethylammonium bromide (CTAB, 95%), sodium dodecyl sulfate (SDS, 99%), poly (ethylene glycol) (PEG, Mw = 5000), trioctylphosphine oxide (TOPO, technical grade 90%), ethanol (99.9%), acetone (99.5%), and hexane (98.5%) were purchased from Sigma-Aldrich. Membrane material was provided by Porifera (Hayward, CA, USA).

Synthesis of IONPs.

IONPs were synthesized by iron oxyhydroxide decomposition at 320°C.[42, 260] FeOOH (2 mmol) with OA (6 mmol) were used in the ODE (5 g) as a solvent. Detailed information about the synthesis and purification processes for NPs was given in our previous research and other. sources.[42, 260] The purified NPs were dissolved and stored in hexane.

Synthesis of Hollow IONPs (HNPs).

Synthesized IONPs were hollowed out at 300°C using technical grade TOPO as an acid etching agent.[322] IONPs in hexane (particular concentration was 7.8×10^{18} particles) with TOPO (9 g)

154

were used in the 3 g of ODE as a solvent. The resulting HNPs were purified using ethanol (20 mL) and acetone (25 mL), and centrifuged at 8000 rpm for 15 min at 5ºC. The purification processes were repeated six times. The purified NPs were dispersed and stored in hexane.

Organic Coating.
Synthesized IONPs were organically functionalized by ligand exchange using PEG, and by ligand encapsulation using SDS and CTAB.[40, 51]   Detailed information about the organic functionalization protocol and washing processes is given in elsewhere.[65, 213, 260]

Transmission Electron Microscope (TEM).
For over a thousand synthesized NPs, the size and size distributions were measured using a transmission electron microscope (TEM, Tecnai G2 Spirit, FEI) and Image Pro Plus 6.0 software (Media Cybernetics, USA).[230]

Hydrodynamic Diameter and Zeta Potential.
The hydrodynamic diameters and zeta potential of aqueous phase IONPs were determined by a dynamic light scattering (DLS) method (Malvern, Zetasizer Nano ZS, ZEN3600) at pH 7 and 22 ºC.

Colloidal Stability.
The colloidal stability of NPs was evaluated via critical coagulation concentration (CCC) measurement using DLS. The protocol for CCC measurements was given elsewhere.[154, 316-317]

Osmotic Pressure Driven Membrane System.
A diffusion/osmosis apparatus having U-shaped tube (0.95 cm^2 effective surface area) was used as the osmotic pressure driven membrane system. Engineered superparamagnetic NPs were used as draw solutes, with 10 mL of initial draw solution volume. DI water (>18.2 MΩ-cm resistivity, Milli-Q, Millipore Corp) was used as a feed solution and was connected to a digital balance (ML 1502E, Mettler Toledo). Every test was conducted at room temperature.

Magnetic Field System.

The outside stator of an alternating current (AC) motor (Delco, 1103021, 24 volt) were used as a field coil.

X-Ray Diffraction (XRD).
XRD patterns of synthesized NCs were measured using a powder diffractometer (Bruker d8 Advance X-ray Diffractometer) with Cu Kα radiation (1.54 Å).

8.5. Conclusions

Organic coated superparamagnetic IONPs create stable and effective osmotic pressure in osmotic pressure driven membrane system. Their performance can be improved by hollowing out the inner cores or applying oscillating magnetic field.

Chapter 9. Future Directions

9.1 Future Directions

For this doctoral dissertation research, I have focused on the environmental application and implication of organic-coated metal oxide nanocrystals. For the environmental application of organic-inorganic nano systems, I have evaluated particle-optimized sorption processes for the sorption and separation of metals and metalloids. As demonstrated, the specific functional group of organic coating dramatically increased the sorption capacity of engineered nanocrystals. With organically surface coating, however, surface passivation of metal oxide nanocrystals is inevitable. For example, organic coatings may hinder the direct sorption on the surface of metal oxide nanocrystals. Organic surface passivation also can affect the redox reaction of metal oxide nanocrystals. The influence of the organic surface passivation on metal oxide nanocrystals should be considered for the fundamental understanding of environmental sorption and separation processes.

Magnetic nanoparticles have been received attention as inner core particles of organic-inorganic nanocomposites due to their magnetic (thus separation) properties. Among magnetic nanoparticles, superparamagnetic iron oxide nanoparticles are promising candidates due to low cost (i.e. environmental abundance) and low toxicity. Until now, research of magnetic attraction of magnetic nanoparticles, including iron oxide nanoparticles, is unclear. With organic functionalization, magnetic momentum may be blocked by organic surface passivation. Along with the magnetic interaction of organic coated magnetic nanoparticles, their aggregation and redispersion is an attractive research topic.

157

For the environmental implication of organic-inorganic nano systems, their fundamental transport behavior(s), including aggregation and deposition, have been investigated. In this study, I have explored the role of an organic coating in inorganic-organic nano platforms in terms of structure and conformation changes. The organic structures and their configuration changes are significant factors for colloidal stability of organic-inorganic nano systems. With the experimental research, the investigations of nano systems need to be supported/studied by XDLVO computational calculations for complete understanding nano behavior(s). Additionally, the role of organic coating is unclear from classical DLVO perspective; there is no Hamaker constant expression for inorganic-organic nanocomposites. For the fundamental approaches, the combination expressions of geometrically outer surface organic materials and inner metal oxide need to be developed for the interaction energy of organic-inorganic nano matrixes.

While there has been a considerable amount of work focused on both engineered and natural nanomaterial/nanoparticle fate and transport in subsurface environmental systems, fundamental studies for soft (or loose) cluster structures are still being refined. Organic-inorganic nanocomposites have a high probability of taking on properties of soft aggregates. Soft aggregates can be released from deposited site when hydrodynamic drag torques, which overcome resisting adhesive torques. In addition, partial release can occur through solution physico-chemical variations by breaking of soft aggregates. Fundamental aqueous behaviors of loose (or soft) aggregates need to be elucidated for better understanding with improving current theoretical models.

References

1.   Auffan, M.; Rose, J.; Bottero, J.-Y.; Lowry, G. V.; Jolivet, J.-P.; Wiesner, M. R., Towards a definition of inorganic nanoparticles from an environmental, health and safety perspective. *Nature nanotechnology* **2009,** *4* (10), 634-641.

2.   Yadav, B.; Kumar, R., Structure, properties and applications of fullerenes. *International Journal of Nanotechnology and Applications* **2008,** *2* (1), 15-24.

3.   Walter, P.; Welcomme, E.; Hallégot, P.; Zaluzec, N. J.; Deeb, C.; Castaing, J.; Veyssière, P.; Bréniaux, R.; Lévêque, J.-L.; Tsoucaris, G., Early use of PbS nanotechnology for an ancient hair dyeing formula. *Nano letters* **2006,** *6* (10), 2215-2219.

4.   Kolb, A. N., Nanocomposites: From ancient masterpieces to value-adding nanotechnology. *Chemistry in New Zealand* **2014**.

5.   Feynman, R. P., There's plenty of room at the bottom. *Resonance* **2011,** *16* (9), 890.

6.   Echegoyen, L.; Echegoyen, L. E., Electrochemistry of fullerenes and their derivatives. *Accounts of chemical research* **1998,** *31* (9), 593-601.

7.   Yan, Q.-L.; Gozin, M.; Zhao, F.-Q.; Cohen, A.; Pang, S.-P., Highly energetic compositions based on functionalized carbon nanomaterials. *Nanoscale* **2016,** *8* (9), 4799-4851.

8.   Labille, J.; Feng, J.; Botta, C.; Borschneck, D.; Sammut, M.; Cabie, M.; Auffan, M.; Rose, J.; Bottero, J.-Y., Aging of TiO$_2$ nanocomposites used in sunscreen. Dispersion and fate of the degradation products in aqueous environment. *Environmental Pollution* **2010,** *158* (12), 3482-3489.

9.   Monteiro-Riviere, N. A.; Inman, A. O.; Zhang, L., Limitations and relative utility of screening assays to assess engineered nanoparticle toxicity in a human cell line. *Toxicology and applied pharmacology* **2009,** *234* (2), 222-235.

10.   Petosa, A. R.; Jaisi, D. P.; Quevedo, I. R.; Elimelech, M.; Tufenkji, N., Aggregation and deposition of engineered nanomaterials in aquatic environments: role of physicochemical interactions. *Environmental science & technology* **2010,** *44* (17), 6532-6549.

11.   Davarcioglu, B., Nanotechnology Applications in Food Packaging Industry. In *Nanotechnology*, Springer: 2017; pp 87-113.

12.   Piccinno, F.; Gottschalk, F.; Seeger, S.; Nowack, B., Industrial production quantities and uses of ten engineered nanomaterials in Europe and the world. *Journal of Nanoparticle Research* **2012,** *14* (9), 1-11.

13.   Weir, A.; Westerhoff, P.; Fabricius, L.; Hristovski, K.; Von Goetz, N., Titanium dioxide nanoparticles in food and personal care products. *Environmental science & technology* **2012,** *46* (4), 2242-2250.

14.   Kaegi, R.; Sinnet, B.; Zuleeg, S.; Hagendorfer, H.; Mueller, E.; Vonbank, R.; Boller, M.; Burkhardt, M., Release of silver nanoparticles from outdoor facades. *Environmental pollution* **2010,** *158* (9), 2900-2905.

15.   Peters, R. J.; van Bemmel, G.; Herrera-Rivera, Z.; Helsper, H. P.; Marvin, H. J.; Weigel, S.; Tromp, P. C.; Oomen, A. G.; Rietveld, A. G.; Bouwmeester, H., Characterization of titanium dioxide nanoparticles in food products: analytical methods to define nanoparticles. *Journal of agricultural and food chemistry* **2014,** *62* (27), 6285-6293.

16.   Morris, J.; Willis, J., US Environmental Protection Agency nanotechnology white paper. *US Environmental Protection Agency, Washington, DC* **2007**.

17.   Wiesner, M. R.; Lowry, G. V.; Alvarez, P.; Dionysiou, D.; Biswas, P., Assessing the risks of manufactured nanomaterials. *Environmental Science & Technology* **2006,** *40* (14), 4336-4345.

18.   Windler, L.; Lorenz, C.; Von Goetz, N.; Hungerbühler, K.; Amberg, M.; Heuberger, M.; Nowack, B., Release of titanium dioxide from textiles during washing. *Environmental science & technology* **2012,** *46* (15), 8181-8188.

19.   O'Brien, N. J.; Cummins, E. J., A risk assessment framework for assessing metallic nanomaterials of environmental concern: aquatic exposure and behavior. *Risk Analysis* **2011,** *31* (5), 706-726.

20.   Godinez, I. G.; Darnault, C. J., Aggregation and transport of nano-TiO< sub> 2</sub> in saturated porous media: Effects of pH, surfactants and flow velocity. *Water research* **2011,** *45* (2), 839-851.

21.   Solovitch, N.; Labille, J. r. m.; Rose, J. r. m.; Chaurand, P.; Borschneck, D.; Wiesner, M. R.; Bottero, J.-Y., Concurrent aggregation and deposition of TiO2 nanoparticles in a sandy porous media. *Environmental science & technology* **2010,** *44* (13), 4897-4902.

22.   Dunphy Guzman, K. A.; Finnegan, M. P.; Banfield, J. F., Influence of surface potential on aggregation and transport of titania nanoparticles. *Environmental science & technology* **2006,** *40* (24), 7688-7693.

23.   Chowdhury, I.; Hong, Y.; Honda, R. J.; Walker, S. L., Mechanisms of TiO< sub> 2</sub> nanoparticle transport in porous media: Role of solution chemistry, nanoparticle concentration, and flowrate. *Journal of colloid and interface science* **2011,** *360* (2), 548-555.

24.   Lin, D.; Tian, X.; Wu, F.; Xing, B., Fate and transport of engineered nanomaterials in the environment. *Journal of environmental quality* **2010,** *39* (6), 1896-1908.

25.   Levard, C.; Hotze, E. M.; Lowry, G. V.; Brown Jr, G. E., Environmental transformations of silver nanoparticles: impact on stability and toxicity. *Environmental science & technology* **2012,** *46* (13), 6900-6914.

26.   Delay, M.; Dolt, T.; Woellhaf, A.; Sembritzki, R.; Frimmel, F. H., Interactions and stability of silver nanoparticles in the aqueous phase: Influence of natural organic matter (NOM) and ionic strength. *Journal of Chromatography A* **2011,** *1218* (27), 4206-4212.

27.   Keller, A. A.; Wang, H.; Zhou, D.; Lenihan, H. S.; Cherr, G.; Cardinale, B. J.; Miller, R.; Ji, Z., Stability and aggregation of metal oxide nanoparticles in natural aqueous matrices. *Environmental science & technology* **2010,** *44* (6), 1962-1967.

28.   Zhang, Y.; Chen, Y.; Westerhoff, P.; Hristovski, K.; Crittenden, J. C., Stability of commercial metal oxide nanoparticles in water. *Water research* **2008,** *42* (8), 2204-2212.

29.   Spagnoli, D.; Banfield, J. F.; Parker, S. C., Free energy change of aggregation of nanoparticles. *The Journal of Physical Chemistry C* **2008,** *112* (38), 14731-14736.

30.   Åkerman, M. E.; Chan, W. C.; Laakkonen, P.; Bhatia, S. N.; Ruoslahti, E., Nanocrystal targeting in vivo. *Proceedings of the National Academy of Sciences* **2002,** *99* (20), 12617-12621.

31.   Choi, M.; Kleitz, F.; Liu, D.; Lee, H. Y.; Ahn, W.-S.; Ryoo, R., Controlled polymerization in mesoporous silica toward the design of organic− inorganic composite nanoporous materials. *Journal of the American Chemical Society* **2005,** *127* (6), 1924-1932.

32.   Kruk, M.; Jaroniec, M.; Guan, S.; Inagaki, S., Adsorption and Thermogravimetric Characterization of Mesoporous Materials with Uniform Organic− Inorganic Frameworks. *The Journal of Physical Chemistry B* **2001,** *105* (3), 681-689.

33.   Davis, M. E.; Saldarriaga, C.; Montes, C.; Garces, J.; Crowdert, C., A molecular sieve with eighteen-membered rings. *Nature* **1988,** *331*, 698-699.

34.   Moore, P. B.; Shen, J., An X-ray structural study of cacoxenite, a mineral phosphate. **1983**.

35.   Wang, C. M.; Lee, L. W.; Chang, T. Y.; Chen, Y. C.; Lin, H. M.; Lu, K. L.; Lii, K. H., Organic–Inorganic Hybrid Zinc Phosphate with 28-Ring Channels. *Chemistry–A European Journal* **2015,** *21* (5), 1878-1881.

36.   Hotze, E. M.; Phenrat, T.; Lowry, G. V., Nanoparticle aggregation: challenges to understanding transport and reactivity in the environment. *Journal of environmental quality* **2010,** *39* (6), 1909-1924.

37.   Phenrat, T.; Saleh, N.; Sirk, K.; Kim, H.-J.; Tilton, R. D.; Lowry, G. V., Stabilization of aqueous nanoscale zerovalent iron dispersions by anionic polyelectrolytes: adsorbed anionic polyelectrolyte layer properties and their effect on aggregation and sedimentation. *Journal of Nanoparticle Research* **2008,** *10* (5), 795-814.

38.   Ortega-Vinuesa, J.; Martın-Rodrıguez, A.; Hidalgo-Alvarez, R., Colloidal stability of polymer colloids with different interfacial properties: mechanisms. *Journal of colloid and interface science* **1996,** *184* (1), 259-267.

39.   Fritz, G.; Schädler, V.; Willenbacher, N.; Wagner, N. J., Electrosteric stabilization of colloidal dispersions. *Langmuir* **2002,** *18* (16), 6381-6390.

40.   Sperling, R. A.; Parak, W., Surface modification, functionalization and bioconjugation of colloidal inorganic nanoparticles. *Philosophical Transactions of the Royal Society of London A: Mathematical, Physical and Engineering Sciences* **2010,** *368* (1915), 1333-1383.

41.   Laaksonen, T.; Ahonen, P.; Johans, C.; Kontturi, K., Stability and Electrostatics of Mercaptoundecanoic Acid-Capped Gold Nanoparticles with Varying Counterion Size. *ChemPhysChem* **2006,** *7* (10), 2143-2149.

42.   William, W. Y.; Falkner, J. C.; Yavuz, C. T.; Colvin, V. L., Synthesis of monodisperse iron oxide nanocrystals by thermal decomposition of iron carboxylate salts. *Chemical Communications* **2004,** (20), 2306-2307.

43.   LaMer, V. K.; Dinegar, R. H., Theory, production and mechanism of formation of monodispersed hydrosols. *Journal of the American Chemical Society* **1950,** *72* (11), 4847-4854.

44.   Mehranpour, H.; Askari, M.; Ghamsari, M. S.; Farzalibeik, H., Study on the phase transformation kinetics of sol-gel drived TiO 2 nanoparticles. *Journal of Nanomaterials* **2010,** *2010*, 31.

45.   Lee, S. S.; Li, W.; Kim, C.; Cho, M.; Lafferty, B. J.; Fortner, J. D., Surface functionalized manganese ferrite nanocrystals for enhanced uranium sorption and separation in water. *Journal of Materials Chemistry A* **2015,** *3* (43), 21930-21939.

46.   Li, W.; Lee, S. S.; Wu, J.; Hinton, C. H.; Fortner, J. D., Shape and size controlled synthesis of uniform iron oxide nanocrystals through new non-hydrolytic routes. *Nanotechnology* **2016,** *27* (32), 324002.

47.   Chin, S. F.; Pang, S. C.; Tan, C. H., Green synthesis of magnetite nanoparticles (via thermal decomposition method) with controllable size and shape. **2011**.

48.   Park, J.; An, K.; Hwang, Y.; Park, J.-G.; Noh, H.-J.; Kim, J.-Y.; Park, J.-H.; Hwang, N.-M.; Hyeon, T., Ultra-large-scale syntheses of monodisperse nanocrystals. *Nature materials* **2004,** *3* (12), 891-895.

49.   Kang, Y. S.; Risbud, S.; Rabolt, J. F.; Stroeve, P., Synthesis and characterization of nanometer-size Fe3O4 and γ-Fe2O3 particles. *Chemistry of Materials* **1996,** *8* (9), 2209-2211.

50.   Lopez Perez, J.; Lopez Quintela, M.; Mira, J.; Rivas, J.; Charles, S., Advances in the preparation of magnetic nanoparticles by the microemulsion method. *The Journal of Physical Chemistry B* **1997,** *101* (41), 8045-8047.

51.   Prakash, A.; Zhu, H.; Jones, C. J.; Benoit, D. N.; Ellsworth, A. Z.; Bryant, E. L.; Colvin, V. L., Bilayers as phase transfer agents for nanocrystals prepared in nonpolar solvents. *Acs Nano* **2009,** *3* (8), 2139-2146.

52.   Approach, A. N. N. S.-P., to Surfactant-Capped Nanocrystals of Transition Metal Oxides Rockenberger, Joerg; Scher, Erik C.; Alivisatos, A. *Journal of the American Chemical Society* **1999,** *121* (49), 11595-11596.

53.   Hyeon, T.; Lee, S. S.; Park, J.; Chung, Y.; Na, H. B., Synthesis of highly crystalline and monodisperse maghemite nanocrystallites without a size-selection process. *Journal of the American Chemical Society* **2001,** *123* (51), 12798-12801.

54.   Sun, S.; Zeng, H., Size-controlled synthesis of magnetite nanoparticles. *Journal of the American Chemical Society* **2002,** *124* (28), 8204-8205.

55.   Caruntu, D.; Caruntu, G.; Chen, Y.; O'Connor, C. J.; Goloverda, G.; Kolesnichenko, V. L., Synthesis of variable-sized nanocrystals of Fe3O4 with high surface reactivity. *Chemistry of materials* **2004,** *16* (25), 5527-5534.

56.   Lee, G. H.; Huh, S. H.; Jeong, J. W.; Choi, B. J.; Kim, S. H.; Ri, H.-C., Anomalous magnetic properties of MnO nanoclusters. *Journal of the American Chemical Society* **2002,** *124* (41), 12094-12095.

57.   Seo, W. S.; Jo, H. H.; Lee, K.; Kim, B.; Oh, S. J.; Park, J. T., Size-dependent magnetic properties of colloidal Mn3O4 and MnO nanoparticles. *Angewandte Chemie* **2004,** *116* (9), 1135-1137.

58.   Yin, M.; O'Brien, S., Synthesis of monodisperse nanocrystals of manganese oxides. *Journal of the American Chemical Society* **2003,** *125* (34), 10180-10181.

59.   Zhong, X.; Xie, R.; Sun, L.; Lieberwirth, I.; Knoll, W., Synthesis of dumbbell-shaped manganese oxide nanocrystals. *The Journal of Physical Chemistry B* **2006,** *110* (1), 2-4.

60.   Ghosh, M.; Biswas, K.; Sundaresan, A.; Rao, C., MnO and NiO nanoparticles: synthesis and magnetic properties. *Journal of Materials Chemistry* **2006,** *16* (1), 106-111.

61.   Schladt, T. D.; Graf, T.; Tremel, W., Synthesis and characterization of monodisperse manganese oxide nanoparticles− evaluation of the nucleation and growth mechanism. *Chemistry of Materials* **2009,** *21* (14), 3183-3190.

62.   West, A. R., *Basic solid state chemistry*. John Wiley & Sons Inc: 1999; p 415.

63.   Shen, H.; Jiang, X.-D.; Wang, S.; Fu, Y.; Zhou, C.; Li, L. S., Facile preparation of metal telluride nanocrystals using di-n-octylphosphine oxide (DOPO) as an air-stable and less toxic alternative to the common tri-alkylphosphines. *Journal of Materials Chemistry* **2012,** *22* (48), 25050-25056.

64.   Kim, C.; Lee, S. S.; Reinhart, B. J.; Cho, M.; Lafferty, B. J.; Li, W.; Fortner, J. D., Surface-optimized core–shell nanocomposites (Fe 3 O 4@ Mn x Fe y O 4) for ultra-high uranium sorption and low-field separation in water. *Environmental Science: Nano* **2018,** *5* (10), 2252-2256.

65.   Lee, S. S.; Li, W.; Kim, C.; Cho, M.; Catalano, J. G.; Lafferty, B. J.; Decuzzi, P.; Fortner, J. D., Engineered manganese oxide nanocrystals for enhanced uranyl sorption and separation. *Environmental Science: Nano* **2015,** *2* (5), 500-508.

66. Wang, C. M.; Lee, L. W.; Chang, T. Y.; Chen, Y. C.; Lin, H. M.; Lu, K. L.; Lii, K. H., Organic–Inorganic Hybrid Zinc Phosphate with 28-Ring Channels. *Chemistry-A European Journal* **2015,** *21* (5), 1878-1881.

67. Xi, F.; Wu, J.; Lin, X., Novel nylon-supported organic–inorganic hybrid membrane with hierarchical pores as a potential immobilized metal affinity adsorbent. *Journal of Chromatography A* **2006,** *1125* (1), 38-51.

68. Uyeda, H. T.; Medintz, I. L.; Jaiswal, J. K.; Simon, S. M.; Mattoussi, H., Synthesis of compact multidentate ligands to prepare stable hydrophilic quantum dot fluorophores. *Journal of the American Chemical Society* **2005,** *127* (11), 3870-3878.

69. Benoit, D. N.; Zhu, H.; Lilierose, M. H.; Verm, R. A.; Ali, N.; Morrison, A. N.; Fortner, J. D.; Avendano, C.; Colvin, V. L., Measuring the grafting density of nanoparticles in solution by analytical ultracentrifugation and total organic carbon analysis. *Analytical chemistry* **2012,** *84* (21), 9238.

70. Lee, S. S.; Song, W.; Cho, M.; Puppala, H. L.; Nguyen, P.; Zhu, H.; Segatori, L.; Colvin, V. L., Antioxidant properties of cerium oxide nanocrystals as a function of nanocrystal diameter and surface coating. *ACS nano* **2013,** *7* (11), 9693-9703.

71. Theron, J.; Walker, J. A.; Cloete, T. E., Nanotechnology and water treatment: Applications and emerging opportunities. *Crit Rev Microbiol* **2008,** *34* (1), 43-69.

72. Savage, N.; Diallo, M. S., Nanomaterials and water purification: Opportunities and challenges. *Journal of Nanoparticle Research* **2005,** *7* (4-5), 331-342.

73. Šafařík, I.; Šafaříková, M., Magnetic nanoparticles and biosciences. In *Nanostructured materials*, Springer: 2002; pp 1-23.

74. P. Kumar, P. D. J., S.S. Rayalu, S. Devotta, Surface-modified zeolite–A for sequestration of arsenic and chromium anions. *Current science* **2007,** *92* (4), 512.

75. Saifuddin, M.; Kumaran, P., Removal of heavy metal from industrial wastewater using chitosan coated oil palm shell charcoal. *Electronic journal of Biotechnology* **2005,** *8* (1), 43-53.

76. Lagadic, I. L.; Mitchell, M. K.; Payne, B. D., Highly effective adsorption of heavy metal ions by a thiol-functionalized magnesium phyllosilicate clay. *Environmental science & technology* **2001,** *35* (5), 984-990.

77. Celis, R.; Hermosin, M. C.; Cornejo, J., Heavy metal adsorption by functionalized clays. *Environmental science & technology* **2000,** *34* (21), 4593-4599.

78. Järup, L., Hazards of heavy metal contamination. *British medical bulletin* **2003,** *68* (1), 167-182.

79. Mazumder, D. G., Chronic arsenic toxicity & human health. *Indian Journal of Medical Research* **2008,** *128* (4), 436.

80. Zhai, Y.; He, Q.; Yang, X.; Han, Q., Solid phase extraction and preconcentration of trace mercury (II) from aqueous solution using magnetic nanoparticles doped with 1, 5-diphenylcarbazide. *Microchimica Acta* **2010,** *169* (3-4), 353-360.

81. Pang, Y.; Zeng, G.; Tang, L.; Zhang, Y.; Liu, Y.; Lei, X.; Li, Z.; Zhang, J.; Xie, G., PEI-grafted magnetic porous powder for highly effective adsorption of heavy metal ions. *Desalination* **2011,** *281*, 278-284.

82. Mashhadizadeh, M. H.; Karami, Z., Solid phase extraction of trace amounts of Ag, Cd, Cu, and Zn in environmental samples using magnetic nanoparticles coated by 3-(trimethoxysilyl)-1-propantiol and modified with 2-amino-5-mercapto-1, 3, 4-thiadiazole and their determination by ICP-OES. *Journal of hazardous materials* **2011,** *190* (1), 1023-1029.

83.   Suleiman, J. S.; Hu, B.; Peng, H.; Huang, C., Separation/preconcentration of trace amounts of Cr, Cu and Pb in environmental samples by magnetic solid-phase extraction with Bismuthiol-II-immobilized magnetic nanoparticles and their determination by ICP-OES. *Talanta* **2009,** *77* (5), 1579-1583.

84.   Jiang, H.-m.; Yan, Z.-p.; Zhao, Y.; Hu, X.; Lian, H.-z., Zincon-immobilized silica-coated magnetic Fe 3 O 4 nanoparticles for solid-phase extraction and determination of trace lead in natural and drinking waters by graphite furnace atomic absorption spectrometry. *Talanta* **2012,** *94*, 251-256.

85.   Bagheri, H.; Afkhami, A.; Saber-Tehrani, M.; Khoshsafar, H., Preparation and characterization of magnetic nanocomposite of Schiff base/silica/magnetite as a preconcentration phase for the trace determination of heavy metal ions in water, food and biological samples using atomic absorption spectrometry. *Talanta* **2012,** *97*, 87-95.

86.   Cheng, G.; He, M.; Peng, H.; Hu, B., Dithizone modified magnetic nanoparticles for fast and selective solid phase extraction of trace elements in environmental and biological samples prior to their determination by ICP-OES. *Talanta* **2012,** *88*, 507-515.

87.   Huang, C.; Xie, W.; Li, X.; Zhang, J., Speciation of inorganic arsenic in environmental waters using magnetic solid phase extraction and preconcentration followed by ICP-MS. *Microchimica Acta* **2011,** *173* (1-2), 165-172.

88.   Huang, C.; Hu, B., Silica-coated magnetic nanoparticles modified with γ-mercaptopropyltrimethoxysilane for fast and selective solid phase extraction of trace amounts of Cd, Cu, Hg, and Pb in environmental and biological samples prior to their determination by inductively coupled plasma mass spectrometry. *Spectrochimica Acta Part B: Atomic Spectroscopy* **2008,** *63* (3), 437-444.

89.   Mashhadizadeh, M. H.; Amoli-Diva, M., Atomic absorption spectrometric determination of Al 3+ and Cr 3+ after preconcentration and separation on 3-mercaptopropionic acid modified silica coated-Fe 3 O 4 nanoparticles. *Journal of Analytical Atomic Spectrometry* **2013,** *28* (2), 251-258.

90.   Karatapanis, A. E.; Fiamegos, Y.; Stalikas, C. D., Silica-modified magnetic nanoparticles functionalized with cetylpyridinium bromide for the preconcentration of metals after complexation with 8-hydroxyquinoline. *Talanta* **2011,** *84* (3), 834-839.

91.   Faraji, M.; Yamini, Y.; Rezaee, M., Extraction of trace amounts of mercury with sodium dodecyle sulphate-coated magnetite nanoparticles and its determination by flow injection inductively coupled plasma-optical emission spectrometry. *Talanta* **2010,** *81* (3), 831-836.

92.   Faraji, M.; Yamini, Y.; Saleh, A.; Rezaee, M.; Ghambarian, M.; Hassani, R., A nanoparticle-based solid-phase extraction procedure followed by flow injection inductively coupled plasma-optical emission spectrometry to determine some heavy metal ions in water samples. *Analytica chimica acta* **2010,** *659* (1), 172-177.

93.   Pinnavaia, T., Selective adsorption of Hg 2+ by thiol-functionalized nanoporous silica. *Chemical communications* **1999,** (1), 69-70.

94.   Yoshitake, H.; Yokoi, T.; Tatsumi, T., Adsorption behavior of arsenate at transition metal cations captured by amino-functionalized mesoporous silicas. *Chemistry of Materials* **2003,** *15* (8), 1713-1721.

95.   Lu, Y.-K.; Yan, X.-P., An imprinted organic− inorganic hybrid sorbent for selective separation of cadmium from aqueous solution. *Analytical chemistry* **2004,** *76* (2), 453-457.

96.   Warner, C. L.; Addleman, R. S.; Cinson, A. D.; Droubay, T. C.; Engelhard, M. H.; Nash, M. A.; Yantasee, W.; Warner, M. G., High-Performance, Superparamagnetic,

Nanoparticle-Based Heavy Metal Sorbents for Removal of Contaminants from Natural Waters. *ChemSusChem* **2010,** *3* (6), 749-757.

97.   Wang, Z.; Wu, D.; Wu, G.; Yang, N.; Wu, A., Modifying Fe 3 O 4 microspheres with rhodamine hydrazide for selective detection and removal of Hg 2+ ion in water. *Journal of hazardous materials* **2013,** *244*, 621-627.

98.   Takafuji, M.; Ide, S.; Ihara, H.; Xu, Z., Preparation of poly (1-vinylimidazole)-grafted magnetic nanoparticles and their application for removal of metal ions. *Chemistry of materials* **2004,** *16* (10), 1977-1983.

99.   Yantasee, W.; Warner, C. L.; Sangvanich, T.; Addleman, R. S.; Carter, T. G.; Wiacek, R. J.; Fryxell, G. E.; Timchalk, C.; Warner, M. G., Removal of heavy metals from aqueous systems with thiol functionalized superparamagnetic nanoparticles. *Environmental science & technology* **2007,** *41* (14), 5114-5119.

100.   Yavuz, C. T.; Mayo, J.; William, W. Y.; Prakash, A.; Falkner, J. C.; Yean, S.; Cong, L.; Shipley, H. J.; Kan, A.; Tomson, M., Low-field magnetic separation of monodisperse Fe3O4 nanocrystals. *Science* **2006,** *314* (5801), 964-967.

101.   Feng, L.; Cao, M.; Ma, X.; Zhu, Y.; Hu, C., Superparamagnetic high-surface-area Fe 3 O 4 nanoparticles as adsorbents for arsenic removal. *Journal of hazardous materials* **2012,** *217*, 439-446.

102.   Kim, C.; Lee, S., Effect of seepage velocity on the attachment efficiency of TiO 2 nanoparticles in porous media. *Journal of hazardous materials* **2014,** *279*, 163-168.

103.   Liu, J.; Lu, Y., Stimuli-responsive disassembly of nanoparticle aggregates for light-up colorimetric sensing. *Journal of the American Chemical Society* **2005,** *127* (36), 12677-12683.

104.   Li, X.; Lenhart, J. J.; Walker, H. W., Dissolution-accompanied aggregation kinetics of silver nanoparticles. *Langmuir* **2010,** *26* (22), 16690-16698.

105.   Sharma, V. K., Aggregation and toxicity of titanium dioxide nanoparticles in aquatic environment—a review. *Journal of Environmental Science and Health Part A* **2009,** *44* (14), 1485-1495.

106.   Aruoja, V.; Dubourguier, H.-C.; Kasemets, K.; Kahru, A., Toxicity of nanoparticles of CuO, ZnO and TiO 2 to microalgae Pseudokirchneriella subcapitata. *Science of the total environment* **2009,** *407* (4), 1461-1468.

107.   Pelley, A. J.; Tufenkji, N., Effect of particle size and natural organic matter on the migration of nano-and microscale latex particles in saturated porous media. *Journal of Colloid and Interface Science* **2008,** *321* (1), 74-83.

108.   Johnson, R. L.; Johnson, G. O. B.; Nurmi, J. T.; Tratnyek, P. G., Natural organic matter enhanced mobility of nano zerovalent iron. *Environmental Science & Technology* **2009,** *43* (14), 5455-5460.

109.   Xu, Y.; Qin, Y.; Palchoudhury, S.; Bao, Y., Water-soluble iron oxide nanoparticles with high stability and selective surface functionality. *Langmuir* **2011,** *27* (14), 8990-8997.

110.   Hyung, H.; Fortner, J. D.; Hughes, J. B.; Kim, J.-H., Natural organic matter stabilizes carbon nanotubes in the aqueous phase. *Environmental Science & Technology* **2007,** *41* (1), 179-184.

111.   Franchi, A.; O'Melia, C. R., Effects of natural organic matter and solution chemistry on the deposition and reentrainment of colloids in porous media. *Environmental science & technology* **2003,** *37* (6), 1122-1129.

112.   Phenrat, T.; Song, J. E.; Cisneros, C. M.; Schoenfelder, D. P.; Tilton, R. D.; Lowry, G. V., Estimating attachment of nano-and submicrometer-particles coated with organic

macromolecules in porous media: development of an empirical model. *Environmental science & technology* **2010,** *44* (12), 4531-4538.

113.   Elimelech, M., Predicting collision efficiencies of colloidal particles in porous media. *Water Research* **1992,** *26* (1), 1-8.

114.   Bai, R.; Tien, C., A new correlation for the initial filter coefficient under unfavorable surface interactions. *Journal of colloid and interface science* **1996,** *179* (2), 631-634.

115.   Bai, R.; Tien, C., Particle deposition under unfavorable surface interactions. *Journal of colloid and interface science* **1999,** *218* (2), 488-499.

116.   Wu, L.; Liu, L.; Gao, B.; Muñoz-Carpena, R.; Zhang, M.; Chen, H.; Zhou, Z.; Wang, H., Aggregation kinetics of graphene oxides in aqueous solutions: experiments, mechanisms, and modeling. *Langmuir* **2013,** *29* (49), 15174-15181.

117.   Flatt, R. J., Dispersion forces in cement suspensions. *Cement and Concrete Research* **2004,** *34* (3), 399-408.

118.   van Oss, C. J., Long-range and short-range mechanisms of hydrophobic attraction and hydrophilic repulsion in specific and aspecific interactions. *Journal of Molecular Recognition* **2003,** *16* (4), 177-190.

119.   Elimelech, M.; Gregory, J.; Jia, X., *Particle deposition and aggregation: measurement, modelling and simulation*. Butterworth-Heinemann: 2013.

120.   Hamaker, H., The London—van der Waals attraction between spherical particles. *physica* **1937,** *4* (10), 1058-1072.

121.   Israelachvili, J.-N. In *The calculation of van der Waals dispersion forces between macroscopic bodies*, Proceedings of the Royal Society of London A: Mathematical, Physical and Engineering Sciences, The Royal Society: 1972; pp 39-55.

122.   Gregory, J., Approximate expressions for retarded van der Waals interaction. *Journal of Colloid and Interface Science* **1981,** *83* (1), 138-145.

123.   Lifshitz, E., The theory of molecular attractive forces between solids. **1956**.

124.   Sotres, J.; Baró, A., DNA molecules resolved by electrical double layer force spectroscopy imaging. *Applied Physics Letters* **2008,** *93* (10), 103903.

125.   McBride, M. B., A critique of diffuse double layer models applied to colloid and surface chemistry. *Clays and Clay minerals* **1997,** *45* (4), 598-608.

126.   Gebbie, M. A.; Valtiner, M.; Banquy, X.; Fox, E. T.; Henderson, W. A.; Israelachvili, J. N., Ionic liquids behave as dilute electrolyte solutions. *Proceedings of the National Academy of Sciences* **2013,** *110* (24), 9674-9679.

127.   Yates, D. E.; Levine, S.; Healy, T. W., Site-binding model of the electrical double layer at the oxide/water interface. *Journal of the Chemical Society, Faraday Transactions 1: Physical Chemistry in Condensed Phases* **1974,** *70*, 1807-1818.

128.   Torrie, G.; Valleau, J., Electrical double layers. 4. Limitations of the Gouy-Chapman theory. *The Journal of Physical Chemistry* **1982,** *86* (16), 3251-3257.

129.   Sanchez-Sanchez, J.; Lozada-Cassou, M., Exact numerical solution to the integral equation version of the Poisson—Boltzmann equation, for two interacting spherical colloidal particles. *Chemical physics letters* **1992,** *190* (3-4), 202-208.

130.   Stern, O., Zur theorie der elektrolytischen doppelschicht. *Berichte der Bunsengesellschaft für physikalische Chemie* **1924,** *30* (21-22), 508-516.

131.   Chapman, D. L., LI. A contribution to the theory of electrocapillarity. *The London, Edinburgh, and Dublin philosophical magazine and journal of science* **1913,** *25* (148), 475-481.

132. Frens, G.; Overbeek, J. T. G., Repeptization and the theory of electrocratic colloids. *Journal of Colloid and Interface Science* **1972,** *38* (2), 376-387.

133. Dukhin, S.; Lyklema, J., Dynamics of colloid particle interaction. *Langmuir* **1987,** *3* (1), 94-98.

134. Hogg, R.; Healy, T.; Fuerstenau, D., Electrostatic interactions between particles. *Trans. Faraday Soc* **1966,** *62*, 1638-1651.

135. Frens, G., *The reversibility of irreversible colloids*. Drukkerij Hoeijenbos: 1968.

136. Bell, G.; Levine, S.; McCartney, L., Approximate methods of determining the double-layer free energy of interaction between two charged colloidal spheres. *Journal of Colloid and Interface Science* **1970,** *33* (3), 335-359.

137. Tripathy, S.; Kessler, W.; Schanz, T., Determination of interparticle repulsive pressures in clays. In *Unsaturated Soils 2006*, 2006; pp 2198-2209.

138. Sun, W.; Zeng, Q.; Yu, A., Calculation of noncontact forces between silica nanospheres. *Langmuir* **2013,** *29* (7), 2175-2184.

139. Molina-Bolívar, J.; Galisteo-González, F.; Hidalgo-Alvarez, R., Colloidal stability of protein-polymer systems: A possible explanation by hydration forces. *Physical Review E* **1997,** *55* (4), 4522.

140. Wu, W.; Giese, R.; Van Oss, C., Stability versus flocculation of particle suspensions in water—correlation with the extended DLVO approach for aqueous systems, compared with classical DLVO theory. *Colloids and Surfaces B: Biointerfaces* **1999,** *14* (1), 47-55.

141. Cox, P. A., *Transition metal oxides: an introduction to their electronic structure and properties*. Oxford university press: 2010; Vol. 27.

142. Goya, G.; Berquó, T. S.; Fonseca, F. C.; Morales, M., Static and dynamic magnetic properties of spherical magnetite nanoparticles. *Journal of Applied Physics* **2003,** *94* (5), 3520-3528.

143. Kanel, S.; Goswami, R.; Clement, T.; Barnett, M.; Zhao, D., Two dimensional transport characteristics of surface stabilized zero-valent iron nanoparticles in porous media. *Environmental Science & Technology* **2007,** *42* (3), 896-900.

144. Phenrat, T.; Kim, H.-J.; Fagerlund, F.; Illangasekare, T.; Tilton, R. D.; Lowry, G. V., Particle size distribution, concentration, and magnetic attraction affect transport of polymer-modified Fe0 nanoparticles in sand columns. *Environmental science & technology* **2009,** *43* (13), 5079-5085.

145. Romero-Cano, M.; Martin-Rodriguez, A.; De Las Nieves, F., Electrosteric stabilization of polymer colloids with different functionality. *Langmuir* **2001,** *17* (11), 3505-3511.

146. Butt, H.-J.; Kappl, M., *Surface and interfacial forces*. John Wiley & Sons: 2009.

147. Langmuir, I., The role of attractive and repulsive forces in the formation of tactoids, thixotropic gels, protein crystals and coacervates. *The Journal of Chemical Physics* **1938,** *6* (12), 873-896.

148. Babchin, A. J.; Schramm, L. L., Osmotic repulsion force due to adsorbed surfactants. *Colloids and Surfaces B: Biointerfaces* **2012,** *91*, 137-143.

149. Bhattacharjee, S.; Elimelech, M.; Borkovec, M., DLVO interaction between colloidal particles: beyond Derjaguin's approximation. *Croatica Chemica Acta* **1998,** *71* (4), 883-903.

150. Israelachvili, J. N., *Intermolecular and surface forces*. Academic press: 2011.

151. Collins, F. C.; Kimball, G. E., Diffusion-controlled reaction rates. *Journal of colloid science* **1949,** *4* (4), 425-437.

152. O'Brien, C. S., A mathematical model for colloidal aggregation. **2003**.

153. Chen, K. L.; Elimelech, M., Aggregation and deposition kinetics of fullerene (C60) nanoparticles. *Langmuir* **2006,** *22* (26), 10994-11001.

154. Chen, K. L.; Mylon, S. E.; Elimelech, M., Aggregation kinetics of alginate-coated hematite nanoparticles in monovalent and divalent electrolytes. *Environmental science & technology* **2006,** *40* (5), 1516-1523.

155. Yao, K.-M.; Habibian, M. T.; O'Melia, C. R., Water and waste water filtration. Concepts and applications. *Environmental science & technology* **1971,** *5* (11), 1105-1112.

156. Happel, J., Viscous flow in multiparticle systems: slow motion of fluids relative to beds of spherical particles. *AIChE Journal* **1958,** *4* (2), 197-201.

157. Rajagopalan, R.; Tien, C., Trajectory analysis of deep-bed filtration with the sphere-in-cell porous media model. *AIChE Journal* **1976,** *22* (3), 523-533.

158. Tufenkji, N.; Elimelech, M., Correlation equation for predicting single-collector efficiency in physicochemical filtration in saturated porous media. *Environmental science & technology* **2004,** *38* (2), 529-536.

159. Lecoanet, H. F.; Wiesner, M. R., Velocity effects on fullerene and oxide nanoparticle deposition in porous media. *Environmental Science & Technology* **2004,** *38* (16), 4377-4382.

160. Elimelech, M., Predicting collision efficiencies of colloidal particles in porous media. *Water research* **1992,** *26* (1), 1-8.

161. McCutcheon, J. R.; McGinnis, R. L.; Elimelech, M., A novel ammonia-carbon dioxide forward (direct) osmosis desalination process. *Desalination* **2005,** *174* (1), 1-11.

162. Phillip, W. A.; Yong, J. S.; Elimelech, M., Reverse Draw Solute Permeation in Forward Osmosis: Modeling and Experiments. *Environ Sci Technol* **2010,** *44* (13), 5170-5176.

163. Alejo, T.; Arruebo, M.; Carcelen, V.; Monsalvo, V. M.; Sebastian, V., Advances in draw solutes for forward osmosis: Hybrid organic-inorganic nanoparticles and conventional solutes. *Chem Eng J* **2017,** *309*, 738-752.

164. McCutcheon, J. R.; McGinnis, R. L.; Elimelech, M., A novel ammonia—carbon dioxide forward (direct) osmosis desalination process. *Desalination* **2005,** *174* (1), 1-11.

165. Batchelder, G. W., Process for the demineralization of water. Google Patents: 1965.

166. Glew, D. N., Process for liquid recovery and solution concentration. Google Patents: 1965.

167. Chanukya, B.; Patil, S.; Rastogi, N. K., Influence of concentration polarization on flux behavior in forward osmosis during desalination using ammonium bicarbonate. *Desalination* **2013,** *312*, 39-44.

168. Stone, M. L.; Rae, C.; Stewart, F. F.; Wilson, A. D., Switchable polarity solvents as draw solutes for forward osmosis. *Desalination* **2013,** *312*, 124-129.

169. Achilli, A.; Cath, T. Y.; Childress, A. E., Selection of inorganic-based draw solutions for forward osmosis applications. *J Membrane Sci* **2010,** *364* (1), 233-241.

170. Wei, J.; Qiu, C.; Tang, C. Y.; Wang, R.; Fane, A. G., Synthesis and characterization of flat-sheet thin film composite forward osmosis membranes. *J Membrane Sci* **2011,** *372* (1), 292-302.

171. Lee, S.; Boo, C.; Elimelech, M.; Hong, S., Comparison of fouling behavior in forward osmosis (FO) and reverse osmosis (RO). *J Membrane Sci* **2010,** *365* (1), 34-39.

172. Kim, C.; Lee, S.; Shon, H. K.; Elimelech, M.; Hong, S., Boron transport in forward osmosis: Measurements, mechanisms, and comparison with reverse osmosis. *J Membrane Sci* **2012,** *419*, 42-48.

173. Frank, B. S., Desalination of sea water. Google Patents: 1972.

174.   Tan, C.; Ng, H., A novel hybrid forward osmosis-nanofiltration (FO-NF) process for seawater desalination: draw solution selection and system configuration. *Desalination and water treatment* **2010,** *13* (1-3), 356-361.

175.   She, Q.; Jin, X.; Li, Q.; Tang, C. Y., Relating reverse and forward solute diffusion to membrane fouling in osmotically driven membrane processes. *Water research* **2012,** *46* (7), 2478-2486.

176.   Hau, N. T.; Chen, S.-S.; Nguyen, N. C.; Huang, K. Z.; Ngo, H. H.; Guo, W., Exploration of EDTA sodium salt as novel draw solution in forward osmosis process for dewatering of high nutrient sludge. *J Membrane Sci* **2014,** *455*, 305-311.

177.   Rahardianto, A.; Shih, W.-Y.; Lee, R.-W.; Cohen, Y., Diagnostic characterization of gypsum scale formation and control in RO membrane desalination of brackish water. *J Membrane Sci* **2006,** *279* (1), 655-668.

178.   Zhao, D.; Chen, S.; Wang, P.; Zhao, Q.; Lu, X., A dendrimer-based forward osmosis draw solute for seawater desalination. *Ind Eng Chem Res* **2014,** *53* (42), 16170-16175.

179.   Kravath, R. E.; Davis, J. A., Desalination of sea water by direct osmosis. *Desalination* **1975,** *16* (2), 151-155.

180.   Yaeli, J., Method and apparatus for processing liquid solutions of suspensions particularly useful in the desalination of saline water. Google Patents: 1992.

181.   Stache, K., Apparatus for transforming sea water, brackish water, polluted water or the like into a nutrious drink by means of osmosis. Google Patents: 1989.

182.   Cahill, K. M., *Technology for humanitarian action*. Fordham Univ Press: 2005.

183.   Romero, J., Water Recycling Technologies: Forward Osmosis Seminar. **2016**.

184.   Ling, M. M.; Chung, T.-S., Desalination process using super hydrophilic nanoparticles via forward osmosis integrated with ultrafiltration regeneration. *Desalination* **2011,** *278* (1), 194-202.

185.   Guo, C. X.; Zhao, D.; Zhao, Q.; Wang, P.; Lu, X., Na+-functionalized carbon quantum dots: a new draw solute in forward osmosis for seawater desalination. *Chem Commun* **2014,** *50* (55), 7318-7321.

186.   Murad, E.; Cashion, J., Iron oxides. In *Mössbauer Spectroscopy of Environmental Materials and their Industrial Utilization*, 2004.

187.   Arami, H.; Khandhar, A.; Liggitt, D.; Krishnan, K. M., In vivo delivery, pharmacokinetics, biodistribution and toxicity of iron oxide nanoparticles. *Chemical Society Reviews* **2015,** *44* (23), 8576-8607.

188.   Yang, H. M.; Seo, B. K.; Lee, K. W.; Moon, J. K., Hyperbranched Polyglycerol-Coated Magnetic Nanoparticles as Draw Solute in Forward Osmosis. *Asian J Chem* **2014,** *26* (13), 4031-4034.

189.   Ling, M. M.; Chung, T. S., Desalination process using super hydrophilic nanoparticles via forward osmosis integrated with ultrafiltration regeneration. *Desalination* **2011,** *278* (1-3), 194-202.

190.   Dey, P.; Izake, E. L., Magnetic nanoparticles boosting the osmotic efficiency of a polymeric FO draw agent: Effect of polymer conformation. *Desalination* **2015,** *373*, 79-85.

191.   Ling, M. M.; Chung, T. S., Surface-Dissociated Nanoparticle Draw Solutions in Forward Osmosis and the Regeneration in an Integrated Electric Field and Nanofiltration System. *Ind Eng Chem Res* **2012,** *51* (47), 15463-15471.

192.   Yang, H. M.; Choi, H. M.; Jang, S. C.; Han, M. J.; Seo, B. K.; Moon, J. K.; Lee, K. W., Succinate Functionalization of Hyperbranched Polyglycerol-Coated Magnetic Nanoparticles as a Draw Solute During Forward Osmosis. *J Nanosci Nanotechno* **2015,** *15* (10), 8279-8284.

193.   Bai, H. W.; Liu, Z. Y.; Sun, D. D., Highly water soluble and recovered dextran coated Fe3O4 magnetic nanoparticles for brackish water desalination. *Sep Purif Technol* **2011,** *81* (3), 392-399.

194.   Na, Y.; Yang, S.; Le, S., Evaluation of citrate-coated magnetic nanoparticles as draw solute for forward osmosis. *Desalination* **2014,** *347*, 34-42.

195.   Ge, Q. C.; Su, J. C.; Chung, T. S.; Amy, G., Hydrophilic Superparamagnetic Nanoparticles: Synthesis, Characterization, and Performance in Forward Osmosis Processes. *Ind Eng Chem Res* **2011,** *50* (1), 382-388.

196.   Kim, C.; Lee, S. S.; Lafferty, B. J.; Giammar, D. E.; Fortner, J. D., Engineered superparamagnetic nanomaterials for arsenic (V) and chromium (VI) sorption and separation: quantifying the role of organic surface coatings. *Environmental Science: Nano* **2018,** *5* (2), 556-563.

197.   Xu, G.-R.; Wang, J.-N.; Li, C.-J., Preparation of hierarchically nanofibrous membrane and its high adaptability in hexavalent chromium removal from water. *Chemical engineering journal* **2012,** *198*, 310-317.

198.   Dharnaik, A. S.; Ghosh, P. K., Hexavalent chromium [Cr (VI)] removal by the electrochemical ion-exchange process. *Environmental technology* **2014,** *35* (18), 2272-2279.

199.   Arris, S.; Lehocine, M. B.; Meniai, A.-H., Sorption study of chromium sorption from wastewater using cereal by-products. *International journal of hydrogen energy* **2014**.

200.   Shirzad-Siboni, M.; Farrokhi, M.; Darvishi Cheshmeh Soltani, R.; Khataee, A.; Tajassosi, S., Photocatalytic reduction of hexavalent chromium over ZnO nanorods immobilized on kaolin. *Industrial & Engineering Chemistry Research* **2014,** *53* (3), 1079-1087.

201.   Rosales-Landeros, C.; Barrera-Díaz, C. E.; Bilyeu, B.; Guerrero, V. V.; Núñez, F. U., A review on Cr (VI) adsorption using inorganic materials. *American Journal of Analytical Chemistry* **2013,** *4* (07), 8.

202.   Yuan, G. D., Natural and modified nanomaterials as sorbents of environmental contaminants. *J. Environ. Sci. Health Part A-Toxic/Hazard. Subst. Environ. Eng.* **2004,** *39* (10), 2661-2670.

203.   Khin, M. M.; Nair, A. S.; Babu, V. J.; Murugan, R.; Ramakrishna, S., A review on nanomaterials for environmental remediation. *Energ Environ Sci* **2012,** *5* (8), 8075-8109.

204.   Geim, A. K.; Novoselov, K. S., The Rise of Graphene. *Nature Materials* **2007,** *6* (3), 183-191.

205.   Chandra, V.; Park, J.; Chun, Y.; Lee, J. W.; Hwang, I.-C.; Kim, K. S., Water-Dispersible Magnetite-Reduced Graphene Oxide Composites for Arsenic Removal. *ACS Nano* **2010,** *4* (7), 3979-3986.

206.   Mubarak, N. M.; Sahu, J. N.; Abdullah, E. C.; Jayakumar, N. S., Removal of Heavy Metals from Wastewater Using Carbon Nanotubes. *Sep. Purif. Rev.* **2014,** *43* (4), 311-338.

207.   Elliott, D. W.; Zhang, W.-X., Field assessment of nanoscale bimetallic particles for groundwater treatment. *Environmental Science & Technology* **2001,** *35* (24), 4922-4926.

208.   Johnson, R. L.; Pankow, J. F., Dissolution of dense chlorinated solvents into groundwater. 2. Source functions for pools of solvent. *Environmental Science & Technology* **1992,** *26* (5), 896-901.

209.   Johnson, W.; Li, X.; Yal, G., Colloid retention in porous media: Mechanistic confirmation of wedging and retention in zones of flow stagnation. *Environmental science & technology* **2007,** *41* (4), 1279-1287.

210.   Ma, H.; Pedel, J.; Fife, P.; Johnson, W. P., Hemispheres-in-cell geometry to predict colloid deposition in porous media. *Environmental Science & Technology* **2009,** *43* (22), 8573-8579.

211.   Li, W.; Liu, D.; Wu, J.; Kim, C.; Fortner, J. D., Aqueous Aggregation and Surface Deposition Processes of Engineered Superparamagnetic Iron Oxide Nanoparticles for Environmental Applications. *Environmental science & technology* **2014,** *48* (20), 11892-11900.

212.   Woo, K.; Hong, J.; Choi, S.; Lee, H.-W.; Ahn, J.-P.; Kim, C. S.; Lee, S. W., Easy synthesis and magnetic properties of iron oxide nanoparticles. *Chemistry of Materials* **2004,** *16* (14), 2814-2818.

213.   Lee, S. S.; Li, W.; Kim, C.; Cho, M.; Lafferty, B. J.; Fortner, J. D., Surface functionalized manganese ferrite nanocrystals for enhanced uranium sorption and separation in water. *J. Mater. Chem. A* **2015,** *3* (43), 21930-21939.

214.   Lucarini, M.; Franchi, P.; Pedulli, G. F.; Gentilini, C.; Polizzi, S.; Pengo, P.; Scrimin, P.; Pasquato, L., Effect of core size on the partition of organic solutes in the monolayer of water-soluble nanoparticles: An ESR investigation. *J Am Chem Soc* **2005,** *127* (47), 16384-16385.

215.   Cederquist, K. B.; Keating, C. D., Curvature Effects in DNA:Au Nanoparticle Conjugates. *Acs Nano* **2009,** *3* (2), 256-260.

216.   Xie, Q.; Kerrich, R.; Irving, E.; Liber, K.; Abou-Shakra, F., Determination of five arsenic species in aqueous samples by HPLC coupled with a hexapole collision cell ICP-MS. *Journal of Analytical Atomic Spectrometry* **2002,** *17* (9), 1037-1041.

217.   Abdel-Samad, H.; Watson, P. R., An XPS study of the adsorption of chromate on goethite (α-FeOOH). *Applied Surface Science* **1997,** *108* (3), 371-377.

218.   Kartal, S. N.; Imamura, Y., Removal of copper, chromium, and arsenic from CCA-treated wood onto chitin and chitosan. *Bioresource technology* **2005,** *96* (3), 389-392.

219.   Yoshitake, H.; Yokoi, T.; Tatsumi, T., Adsorption of chromate and arsenate by amino-functionalized MCM-41 and SBA-1. *Chemistry of Materials* **2002,** *14* (11), 4603-4610.

220.   Cogswell, C. F.; Jiang, H.; Ramberger, J.; Accetta, D.; Willey, R. J.; Choi, S., Effect of Pore Structure on CO2 Adsorption Characteristics of Aminopolymer Impregnated MCM-36. *Langmuir* **2015,** *31* (15), 4534-4541.

221.   Cogswell, C. F.; Xie, Z.; Wolek, A.; Wang, Y.; Stavola, A.; Finkenaur, M.; Gilmore, E.; Lanzillotti, M.; Choi, S., Pore structure-CO2 adsorption property relations of supported amine materials with multi-pore networks. *J Mater Chem A* **2017,** *5* (18), 8526-8536.

222.   Sahoo, B.; Devi, K. S. P.; Sahu, S. K.; Nayak, S.; Maiti, T. K.; Dhara, D.; Pramanik, P., Facile preparation of multifunctional hollow silica nanoparticles and their cancer specific targeting effect. *Biomaterials Science* **2013,** *1* (6), 647-657.

223.   Dixon, M. C., Quartz crystal microbalance with dissipation monitoring: enabling real-time characterization of biological materials and their interactions. *J Biomol Tech* **2008,** *19* (3), 151-158.

224.   Minko, S., Grafting on solid surfaces:"Grafting to" and "grafting from" methods. In *Polymer surfaces and interfaces*, Springer: 2008; pp 215-234.

225.   Liu, G.; Zhang, G., *QCM-D studies on polymer behavior at interfaces*. Springer: 2013.

226.   Zhang, P.; Qian, J.; An, Q.; Du, B.; Liu, X.; Zhao, Q., Influences of solution property and charge density on the self-assembly behavior of water-insoluble polyelectrolyte sulfonated poly (sulphone) sodium salts. *Langmuir* **2008,** *24* (5), 2110-2117.

227.   Zhang, F.; Ali, Z.; Amin, F.; Feltz, A.; Oheim, M.; Parak, W. J., Ion and pH sensing with colloidal nanoparticles: influence of surface charge on sensing and colloidal properties. *ChemPhysChem* **2010,** *11* (3), 730-735.

228.   Selvan, S.; Patra, P. K.; Ang, C. Y.; Ying, J. Y., Synthesis of silica-coated semiconductor and magnetic quantum dots and their use in the imaging of live cells. *Angewandte Chemie International Edition* **2007,** *46* (14), 2448-2452.

229.   Selvan, S. T.; Tan, T. T.; Ying, J. Y., Robust, Non-Cytotoxic, Silica-Coated CdSe Quantum Dots with Efficient Photoluminescence. *Advanced Materials* **2005,** *17* (13), 1620-1625.

230.   Vigneau, E.; Loisel, C.; Devaux, M.; Cantoni, P., Number of particles for the determination of size distribution from microscopic images. *Powder Technology* **2000,** *107* (3), 243-250.

231.   Gomez-Pastora, J.; Bringas, E.; Ortiz, I., Recent progress and future challenges on the use of high performance magnetic nano-adsorbents in environmental applications. *Chemical Engineering Journal* **2014,** *256*, 187-204.

232.   Tang, S. C. N.; Lo, I. M. C., Magnetic nanoparticles: Essential factors for sustainable environmental applications. *Water Research* **2013,** *47* (8), 2613-2632.

233.   Qu, X. L.; Brame, J.; Li, Q. L.; Alvarez, P. J. J., Nanotechnology for a Safe and Sustainable Water Supply: Enabling Integrated Water Treatment and Reuse. *Accounts of Chemical Research* **2013,** *46* (3), 834-843.

234.   Das, G. K.; Bonifacio, C. S.; De Rojas, J.; Liu, K.; van Benthem, K.; Kennedy, I. M., Ultra-long magnetic nanochains for highly efficient arsenic removal from water. *Journal of Materials Chemistry A* **2014,** *2* (32), 12974-12981.

235.   Jones, C. J.; Chattopadhyay, S.; Gonzalez-Pech, N. I.; Avendano, C.; Hwang, N. N.; Lee, S. S.; Cho, M. J.; Ozarowski, A.; Prakash, A.; Mayo, J. T.; Yavuz, C.; Colvin, V. L., A Novel, Reactive Green Iron Sulfide (Sulfide Green Rust) Formed on Iron Oxide Nanocrystals. *Chemistry of Materials* **2015,** *27* (3), 700-707.

236.   Yeap, S. P.; Leong, S. S.; Ahmad, A. L.; Ooi, B. S.; Lim, J., On Size Fractionation of Iron Oxide Nanoclusters by Low Magnetic Field Gradient. *Journal of Physical Chemistry C* **2014,** *118* (41), 24042-24054.

237.   Crane, R. A.; Dickinson, M.; Popescu, I. C.; Scott, T. B., Magnetite and zero-valent iron nanoparticles for the remediation of uranium contaminated environmental water. *Water Research* **2011,** *45* (9), 2931-2942.

238.   Dui, J. N.; Zhu, G. Y.; Zhou, S. M., Facile and Economical Synthesis of Large Hollow Ferrites and Their Applications in Adsorption for As(V) and Cr(VI). *Acs Applied Materials & Interfaces* **2013,** *5* (20), 10081-10089.

239.   Yavuz, C. T.; Mayo, J. T.; Yu, W. W.; Prakash, A.; Falkner, J. C.; Yean, S.; Cong, L. L.; Shipley, H. J.; Kan, A.; Tomson, M.; Natelson, D.; Colvin, V. L., Low-field magnetic separation of monodisperse Fe3O4 nanocrystals. *Science* **2006,** *314* (5801), 964-967.

240.   Cai, Y.; Wu, C.; Liu, Z.; Zhang, L.; Chen, L.; Wang, J.; Wang, X.; Yang, S.; Wang, S., Fabrication of a phosphorylated graphene oxide–chitosan composite for highly effective and selective capture of U (VI). *Environmental Science: Nano* **2017,** *4* (9), 1876-1886.

241. Chen, L.; Bai, Z.; Zhu, L.; Zhang, L.; Cai, Y.; Li, Y.; Liu, W.; Wang, Y.; Chen, L.; Diwu, J., Ultrafast and Efficient Extraction of Uranium from Seawater Using an Amidoxime Appended Metal–Organic Framework. *ACS applied materials & interfaces* **2017,** *9* (38), 32446-32451.

242. Krycka, K. L.; Borchers, J. A.; Salazar-Alvarez, G.; Lopez-Ortega, A.; Estrader, M.; Estrade, S.; Winkler, E.; Zysler, R. D.; Sort, J.; Peiro, F.; Baro, M. D.; Kao, C. C.; Nogues, J., Resolving Material-Specific Structures within Fe3O4 vertical bar gamma-Mn2O3 Core vertical bar Shell Nanoparticles Using Anomalous Small-Angle X-ray Scattering. *Acs Nano* **2013,** *7* (2), 921-931.

243. Lopez-Ortega, A.; Estrader, M.; Salazar-Alvarez, G.; Estrade, S.; Golosovsky, I. V.; Dumas, R. K.; Keavney, D. J.; Vasilakaki, M.; Trohidou, K. N.; Sort, J.; Peiro, F.; Surinach, S.; Baro, M. D.; Nogues, J., Strongly exchange coupled inverse ferrimagnetic soft/hard, MnxFe3-xO4/FexMn3-xO4, core/shell heterostructured nanoparticles. *Nanoscale* **2012,** *4* (16), 5138-5147.

244. An, K.; Park, M.; Yu, J. H.; Na, H. B.; Lee, N.; Park, J.; Choi, S. H.; Song, I. C.; Moon, W. K.; Hyeon, T., Synthesis of Uniformly Sized Manganese Oxide Nanocrystals with Various Sizes and Shapes and Characterization of Their T1 Magnetic Resonance Relaxivity. *European Journal of Inorganic Chemistry* **2012,** (12), 2148-2155.

245. Prakash, A.; Zhu, H. G.; Jones, C. J.; Benoit, D. N.; Ellsworth, A. Z.; Bryant, E. L.; Colvin, V. L., Bilayers as Phase Transfer Agents for Nanocrystals Prepared in Nonpolar Solvents. *Acs Nano* **2009,** *3* (8), 2139-2146.

246. Sutton, M.; Burastero, S. R., Uranium(VI) solubility and speciation in simulated elemental human biological fluids. *Chemical Research in Toxicology* **2004,** *17* (11), 1468-1480.

247. Langmuir, I., The Adsorption of Gases on Plane Surfaces of Glass, Mica and Platinum. *Journal of the American Chemical Society* **1918,** *40*, 1361-1403.

248. Calì, E.; Qi, J.; Preedy, O.; Chen, S.; Boldrin, D.; Branford, W.; Vandeperre, L.; Ryan, M., Functionalised magnetic nanoparticles for uranium adsorption with ultra-high capacity and selectivity. *Journal of Materials Chemistry A* **2018,** *6* (7), 3063-3073.

249. Li, W.; Troyer, L. D.; Lee, S. S.; Wu, J.; Kim, C.; Lafferty, B. J.; Catalano, J. G.; Fortner, J. D., Engineering Nanoscale Iron Oxides for Uranyl Sorption and Separation: Optimization of Particle Core Size and Bilayer Surface Coatings. *ACS Applied Materials & Interfaces* **2017,** *9* (15), 13163-13172.

250. Wang, Z.; Lee, S.-W.; Catalano, J. G.; Lezama-Pacheco, J. S.; Bargar, J. R.; Tebo, B. M.; Giammar, D. E., Adsorption of Uranium(VI) to Manganese Oxides: X-ray Absorption Spectroscopy and Surface Complexation Modeling. *Environ Sci Technol* **2012,** *47* (2), 850-858.

251. Vigneau, E.; Loisel, C.; Devaux, M. F.; Cantoni, P., Number of particles for the determination of size distribution from microscopic images. *Powder Technol* **2000,** *107* (3), 243-250.

252. Welch, A. H.; Westjohn, D.; Helsel, D. R.; Wanty, R. B., Arsenic in ground water of the United States: occurrence and geochemistry. *Ground water* **2000,** *38* (4), 589-604.

253. Nolan, J.; Weber, K. A., Natural uranium contamination in major US aquifers linked to nitrate. *Environmental Science & Technology Letters* **2015,** *2* (8), 215-220.

254. Guertin, J.; Jacobs, J. A.; Avakian, C. P., *Chromium (VI) handbook*. CRC press: 2016.

255. Hingston, J.; Collins, C.; Murphy, R.; Lester, J., Leaching of chromated copper arsenate wood preservatives: a review. *Environmental Pollution* **2001,** *111* (1), 53-66.

256. Moghaddam, A. H.; Mulligan, C. N., Leaching of heavy metals from chromated copper arsenate (CCA) treated wood after disposal. *Waste Management* **2008,** *28* (3), 628-637.

257. Chini, A.; Buck, R.; Nakajima, S.; Russell, M., Barriers for deconstruction and reuse/recycling of construction materials in USA. *Barriers for Deconstruction and Reuse/Recycling of Construction Materials* **2014**, 115.

258. Troyer, L. D.; Tang, Y.; Borch, T., Simultaneous reduction of arsenic (V) and uranium (VI) by mackinawite: role of uranyl arsenate precipitate formation. *Environmental science & technology* **2014,** *48* (24), 14326-14334.

259. Wiesner, M. R.; Bottero, J.-Y., Environmental nanotechnology. *Applications and Impacts of Nanomaterials* **2007**, 395-517.

260. Kim, C.; Lee, S. S.; Lafferty, B. J.; Giammar, D.; Fortner, J., Engineered Superparamagnetic Nanomaterials for Arsenic (V) and Chromium (VI) Sorption and Separation: Quantifying the Role of Organic Surface Coatings. *Environmental Science: Nano* **2018,** *5* (2), 556-563.

261. Shvareva, T. Y.; Fein, J. B.; Navrotsky, A., Thermodynamic properties of uranyl minerals: constraints from calorimetry and solubility measurements. *Industrial & Engineering Chemistry Research* **2011,** *51* (2), 607-613.

262. An, K.; Park, M.; Yu, J. H.; Na, H. B.; Lee, N.; Park, J.; Choi, S. H.; Song, I. C.; Moon, W. K.; Hyeon, T., Synthesis of uniformly sized manganese oxide nanocrystals with various sizes and shapes and characterization of their T1 magnetic resonance relaxivity. *European Journal of Inorganic Chemistry* **2012,** *2012* (12), 2148-2155.

263. Sun, S.; Zeng, H.; Robinson, D. B.; Raoux, S.; Rice, P. M.; Wang, S. X.; Li, G., Monodisperse mfe2o4 (m= fe, co, mn) nanoparticles. *Journal of the American Chemical Society* **2004,** *126* (1), 273-279.

264. Peltonen, L.; Hirvonen, J., Pharmaceutical nanocrystals by nanomilling: critical process parameters, particle fracturing and stabilization methods. *Journal of Pharmacy and Pharmacology* **2010,** *62* (11), 1569-1579.

265. Kong, S.; Wang, Y.; Zhan, H.; Yuan, S.; Yu, M.; Liu, M., Adsorption/oxidation of arsenic in groundwater by nanoscale Fe-Mn binary oxides loaded on zeolite. *Water Environment Research* **2014,** *86* (2), 147-155.

266. Ahribesh, A. A.; Lazarević, S.; Potkonjak, B.; Bjelajac, A.; Janaćković, D.; Petrović, R., Sorption of cadmium ions from saline waters onto Fe (III)-zeolite. *Chemical Industry/Hemijska Industrija* **2015,** *69* (3).

267. Badawy, A. M. E.; Luxton, T. P.; Silva, R. G.; Scheckel, K. G.; Suidan, M. T.; Tolaymat, T. M., Impact of environmental conditions (pH, ionic strength, and electrolyte type) on the surface charge and aggregation of silver nanoparticles suspensions. *Environmental science & technology* **2010,** *44* (4), 1260-1266.

268. Khaodhiar, S.; Azizian, M. F.; Osathaphan, K.; Nelson, P. O., Copper, chromium, and arsenic adsorption and equilibrium modeling in an iron-oxide-coated sand, background electrolyte system. *Water, air, and soil pollution* **2000,** *119* (1-4), 105-120.

269. Rodahl, M.; Höök, F.; Krozer, A.; Brzezinski, P.; Kasemo, B., Quartz crystal microbalance setup for frequency and Q-factor measurements in gaseous and liquid environments. *Review of Scientific Instruments* **1995,** *66* (7), 3924-3930.

270. Steinem, C.; Janshoff, A., *Piezoelectric sensors*. Springer Science & Business Media: 2007; Vol. 5.

271. Gezahegne, W. A.; Hennig, C.; Tsushima, S.; Planer-Friedrich, B.; Scheinost, A. C.; Merkel, B. J., EXAFS and DFT investigations of uranyl arsenate complexes in aqueous solution. *Environmental science & technology* **2012,** *46* (4), 2228-2233.

272. Gorman-Lewis, D.; Burns, P. C.; Fein, J. B., Review of uranyl mineral solubility measurements. *The Journal of Chemical Thermodynamics* **2008,** *40* (3), 335-352.

273. Baalousha, M.; Manciulea, A.; Cumberland, S.; Kendall, K.; Lead, J. R., Aggregation and surface properties of iron oxide nanoparticles: influence of pH and natural organic matter. *Environmental Toxicology and Chemistry* **2008,** *27* (9), 1875-1882.

274. Dixon, M. C., Quartz crystal microbalance with dissipation monitoring: enabling real-time characterization of biological materials and their interactions. *Journal of biomolecular techniques: JBT* **2008,** *19* (3), 151.

275. Reviakine, I.; Johannsmann, D.; Richter, R. P., Hearing what you cannot see and visualizing what you hear: interpreting quartz crystal microbalance data from solvated interfaces. ACS Publications: 2011.

276. Cosgrove, T., *Colloid science: principles, methods and applications*. John Wiley & Sons: 2010.

277. Tadmor, R.; Klein, J., Additional attraction between surfactant-coated surfaces. *Journal of colloid and interface science* **2002,** *247* (2), 321-326.

278. Das, S. K.; Schechter, R. S.; Sharma, M. M., The role of surface roughness and contact deformation on the hydrodynamic detachment of particles from surfaces. *Journal of colloid and interface science* **1994,** *164* (1), 63-77.

279. Litton, G. M.; Olson, T. M., Particle size effects on colloid deposition kinetics: Evidence of secondary minimum deposition. *Colloids and Surfaces A: Physicochemical and Engineering Aspects* **1996,** *107*, 273-283.

280. Mosley, L. M.; Hunter, K. A.; Ducker, W. A., Forces between colloid particles in natural waters. *Environmental science & technology* **2003,** *37* (15), 3303-3308.

281. Liu, Y.; Janjaroen, D.; Kuhlenschmidt, M. S.; Kuhlenschmidt, T. B.; Nguyen, T. H., Deposition of Cryptosporidium parvum oocysts on natural organic matter surfaces: microscopic evidence for secondary minimum deposition in a radial stagnation point flow cell. *Langmuir* **2009,** *25* (3), 1594-1605.

282. Cho, E. C.; Zhang, Q.; Xia, Y., The effect of sedimentation and diffusion on cellular uptake of gold nanoparticles. *Nature nanotechnology* **2011,** *6* (6), 385-391.

283. Teeguarden, J. G.; Hinderliter, P. M.; Orr, G.; Thrall, B. D.; Pounds, J. G., Particokinetics in vitro: dosimetry considerations for in vitro nanoparticle toxicity assessments. *Toxicological Sciences* **2007,** *95* (2), 300-312.

284. Hiemenz, P. C.; Rajagopalan, R., *Principles of Colloid and Surface Chemistry, revised and expanded*. CRC press: 1997; Vol. 14.

285. Brereton, G., Accuracy in Numerical Solution of the Particle Concentration Field in Laminar Wall-Bounded Flows with Thermophoresis and Diffusion. *Aerosol Science and Technology* **2014,** *48* (9), 957-968.

286. Torkzaban, S.; Bradford, S. A.; Walker, S. L., Resolving the coupled effects of hydrodynamics and DLVO forces on colloid attachment in porous media. *Langmuir* **2007,** *23* (19), 9652-9660.

287. Li, X.; Zhang, P.; Lin, C.; Johnson, W. P., Role of hydrodynamic drag on microsphere deposition and re-entrainment in porous media under unfavorable conditions. *Environmental science & technology* **2005,** *39* (11), 4012-4020.

288. Marieb, E.; Hoehn, K., The Cardiovascular system: blood vessels. Human anatomy & physiology. Pearson Education, Inc. Upper Saddle River, NJ: 2013.

289.   Tortora, G. J.; Grabowski, S. R., The cardiovascular system: blood vessels and hemodynamics. *Principals of anatomy and physiology, 7th edn. Harper Collins College* **1993**, 366-632.

290.   Chen, K. L.; Elimelech, M., Interaction of fullerene (C60) nanoparticles with humic acid and alginate coated silica surfaces: measurements, mechanisms, and environmental implications. *Environmental science & technology* **2008,** *42* (20), 7607-7614.

291.   Ryan, J. N.; Elimelech, M., Colloid mobilization and transport in groundwater. *Colloids and surfaces A: Physicochemical and engineering aspects* **1996,** *107*, 1-56.

292.   Gallego-Urrea, J. A.; Holmberg, J. P.; Hassellöv, M., Influence of different types of natural organic matter on titania nanoparticle stability: effects of counter ion concentration and pH. *Environmental Science: Nano* **2014,** *1* (2), 181-189.

293.   Huynh, K. A.; Chen, K. L., Aggregation kinetics of citrate and polyvinylpyrrolidone coated silver nanoparticles in monovalent and divalent electrolyte solutions. *Environmental science & technology* **2011,** *45* (13), 5564-5571.

294.   Hu, J.-D.; Zevi, Y.; Kou, X.-M.; Xiao, J.; Wang, X.-J.; Jin, Y., Effect of dissolved organic matter on the stability of magnetite nanoparticles under different pH and ionic strength conditions. *Science of the Total Environment* **2010,** *408* (16), 3477-3489.

295.   Elimelech, M.; O'Melia, C. R., Effect of particle size on collision efficiency in the deposition of Brownian particles with electrostatic energy barriers. *Langmuir* **1990,** *6* (6), 1153-1163.

296.   Reerink, H.; Overbeek, J. T. G., The rate of coagulation as a measure of the stability of silver iodide sols. *Discussions of the Faraday Society* **1954,** *18*, 74-84.

297.   Fuchs, v. N., Über die stabilität und aufladung der aerosole. *Zeitschrift für Physik* **1934,** *89* (11-12), 736-743.

298.   Chen, K. L.; Elimelech, M., Influence of humic acid on the aggregation kinetics of fullerene (C 60) nanoparticles in monovalent and divalent electrolyte solutions. *Journal of Colloid and Interface Science* **2007,** *309* (1), 126-134.

299.   Moroi, Y., Stability of Colloidal Particles. In *Micelles*, Springer: 1992; pp 131-148.

300.   de Carvalho, S. J.; Fenley, M. O.; da Silva, F. L. s. B., Protein− Ion Binding Process on Finite Macromolecular Concentration. A Poisson− Boltzmann and Monte Carlo Study. *The Journal of Physical Chemistry B* **2008,** *112* (51), 16766-16776.

301.   Das, P. K.; Bhattacharjee, S.; Moussa, W., Electrostatic double layer force between two spherical particles in a straight cylindrical capillary: finite element analysis. *Langmuir* **2003,** *19* (10), 4162-4172.

302.   Lin, D.; Ma, S.; Zhou, K.; Wu, F.; Yang, K., The effect of water chemistry on homoaggregations of various nanoparticles: Specific role of Cl− ions. *Journal of Colloid and Interface Science* **2015,** *450* (Supplement C), 272-278.

303.   Shih, Y.-h.; Zhuang, C.-m.; Tso, C.-p.; Lin, C.-h., The effect of electrolytes on the aggregation kinetics of titanium dioxide nanoparticle aggregates. *Journal of Nanoparticle Research* **2012,** *14* (8), 924.

304.   Kango, S.; Kalia, S.; Celli, A.; Njuguna, J.; Habibi, Y.; Kumar, R., Surface modification of inorganic nanoparticles for development of organic–inorganic nanocomposites—A review. *Progress in Polymer Science* **2013,** *38* (8), 1232-1261.

305.   Seo, W. S.; Jo, H. H.; Lee, K.; Kim, B.; Oh, S. J.; Park, J. T., Size-dependent magnetic properties of colloidal Mn3O4 and MnO nanoparticles. *Angewandte Chemie International Edition* **2004,** *43* (9), 1115-1117.

306.   Israelachvili, J. N., *Intermolecular and surface forces: revised third edition*. Academic press: 2011.

307.   Butt, H.-J.; Cappella, B.; Kappl, M., Force measurements with the atomic force microscope: Technique, interpretation and applications. *Surface science reports* **2005,** *59* (1), 1-152.

308.   Huangfu, X.; Jiang, J.; Ma, J.; Liu, Y.; Yang, J., Aggregation kinetics of manganese dioxide colloids in aqueous solution: influence of humic substances and biomacromolecules. *Environmental science & technology* **2013,** *47* (18), 10285-10292.

309.   Dobrynin, A. V., Electrostatic persistence length of semiflexible and flexible polyelectrolytes. *Macromolecules* **2005,** *38* (22), 9304-9314.

310.   Boström, M.; Williams, D. R.; Ninham, B. W., The influence of ionic dispersion potentials on counterion condensation on polyelectrolytes. *The Journal of Physical Chemistry B* **2002,** *106* (32), 7908-7912.

311.   Grosberg, A. Y.; Nguyen, T.; Shklovskii, B., Colloquium: the physics of charge inversion in chemical and biological systems. *Reviews of modern physics* **2002,** *74* (2), 329.

312.   Vysotskii, V.; Uryupina, O. Y.; Gusel'nikova, A.; Roldugin, V., On the feasibility of determining nanoparticle concentration by the dynamic light scattering method. *Colloid journal* **2009,** *71* (6), 739-744.

313.   Shang, J.; Gao, X., Nanoparticle counting: towards accurate determination of the molar concentration. *Chemical Society Reviews* **2014,** *43* (21), 7267-7278.

314.   Liu, X.; Dai, Q.; Austin, L.; Coutts, J.; Knowles, G.; Zou, J.; Chen, H.; Huo, Q., A one-step homogeneous immunoassay for cancer biomarker detection using gold nanoparticle probes coupled with dynamic light scattering. *Journal of the American Chemical Society* **2008,** *130* (9), 2780-2782.

315.   Klein, R.; Meakin, P., Universality in colloid aggregation. *Nature* **1989,** *339* (3).

316.   Mylon, S. E.; Chen, K. L.; Elimelech, M., Influence of natural organic matter and ionic composition on the kinetics and structure of hematite colloid aggregation: Implications to iron depletion in estuaries. *Langmuir* **2004,** *20* (21), 9000-9006.

317.   Holthoff, H.; Egelhaaf, S. U.; Borkovec, M.; Schurtenberger, P.; Sticher, H., Coagulation rate measurements of colloidal particles by simultaneous static and dynamic light scattering. *Langmuir* **1996,** *12* (23), 5541-5549.

318.   Elimelech, M.; Gregory, J.; Jia, X.; Williams, R. A., *Particle Deposition and Aggregation: Measurement, Modeling, and Simulation*. 1995.

319.   Lutchmiah, K.; Verliefde, A.; Roest, K.; Rietveld, L. C.; Cornelissen, E. R., Forward osmosis for application in wastewater treatment: a review. *Water research* **2014,** *58*, 179-197.

320.   Altaee, A.; Zaragoza, G.; Drioli, E.; Zhou, J., Evaluation the potential and energy efficiency of dual stage pressure retarded osmosis process. *Applied Energy* **2017,** *199*, 359-369.

321.   Ling, M. M.; Wang, K. Y.; Chung, T. S., Highly Water-Soluble Magnetic Nanoparticles as Novel Draw Solutes in Forward Osmosis for Water Reuse. *Ind Eng Chem Res* **2010,** *49* (12), 5869-5876.

322.   An, K.; Kwon, S. G.; Park, M.; Na, H. B.; Baik, S.-I.; Yu, J. H.; Kim, D.; Son, J. S.; Kim, Y. W.; Song, I. C., Synthesis of uniform hollow oxide nanoparticles through nanoscale acid etching. *Nano letters* **2008,** *8* (12), 4252-4258.

323.   Cath, T. Y.; Childress, A. E.; Elimelech, M., Forward osmosis: principles, applications, and recent developments. *J Membrane Sci* **2006,** *281* (1), 70-87.

324.   Blandin, G.; Vervoort, H.; Le-Clech, P.; Verliefde, A. R., Fouling and cleaning of high permeability forward osmosis membranes. *Journal of Water Process Engineering* **2016,** *9*, 161-169.

Appendices

A.1. Curriculum vitae

Changwoo Kim, Ph.D. candidate

Ph.D.	Tel (work): (314) 650-0061
Department of Energy, Environmental and Chemical Engineering,	Tel (cell): (314) 650-0061
Washington University in St. Louis	Fax: (314) 935-5464
Box 1180 St. Louis, MO 63130-4899	Email: changwookim@wustl.edu

EDUCATION

Washington University in St. Louis, USA	Energy, Environmental and Chemical Eng.	Ph.D.	2013 - present
Korea University, Seoul, Korea	Civil and Environmental Eng.	M.S.	2009 - 2011
Korea University, Seoul, Korea	Civil and Environmental Eng.	B.S.	2003 - 2009

EMPLOYMENT

Center for Water Resource Cycle Research, Korea Institute of Science and Technology, Korea	2011 - 2013
Republic of Korea Army as driver and mechanic	2003 - 2005

RESEARCH EXPERIENCE

***Washington University**, Saint Louis, Missouri, USA*
Ph.D. candidate (advisor: Prof. John D. Fortner) — 2013 - 2018

Synthesis of iron based metal oxides (iron oxide, manganese oxide, cobalt oxide, manganese iron oxide, and cobalt iron oxide) encapsulated in surface coatings (e.g., silica, amino acids, fatty acids, and polymer complex shells) and synthesis of graphene oxide and its functionalization and conjugation with metal oxide nanocrystals, for membrane application, hydrogen energy, environmental remediation, evaluation of fate and transport

- Optimized sorption and separation properties of organic functionalized metal oxide nano composites for single or multi-contaminant water treatment (e.g., arsenic, chromium and uranium)
- Explored amine photo chemistry and its application in environmental remediation
- Designed and developed the organic functionalized graphene oxide and its application in environmental sorption and photo reduction
- Developed catalytic metal oxide nano composites for environmental remediation
- Explored effects of organic stabilizer on organic encapsulated nanocrystals in aggregation kinetic and their deposition behaviors.
- Developed organic-inorganic nano composites for ideal draw solute of forward osmosis system
- Investigated water flux enhanced graphene oxide membrane
- Analysis techniques: STEM-EDS, HR-TEM/SEM, XRD, XPS, FT-IR, UV-Vis, DLS/zeta sizer, ICP-OES/-MS, SQUID, TOC, QCM-D, and Ultra centrifuge

***Korea Institute of Science and Technology**, Seoul, Korea*
Research Scientist (Supervisor: Dr. Seunghak Lee) — 2011 - 2013

Aggregation and deposition of various engineered metal oxides nanoparticles including titanium oxide, zinc oxide, silicon dioxide, cerium oxide in the presence of natural organic matter

- Explored aggregation kinetic of metal oxide nanoparticles and their surface potential variation in terms of pH, ionic strength, and natural organic matter
- Investigated interaction energy between porous media and metal oxide nanoparticle in the absence and presence of natural organic matter by theoretical classical DLVO analysis and AFM measurement
- Elucidated transport of metal oxide nanoparticles in porous media under favorable and unfavorable condition using column system
- Analysis techniques: HR-TEM, DLS/zeta sizer, ICP-OES, XRD, ASTM D422, XRF, and BET

***Korea University**, Seoul, South Korea* — 2009 - 2011

M.S. student (*advisor: Prof.* Seungkwan Hong, *co advisor: Prof.* Menachem Elimelech)

Operation, development, and investigation of membrane systems and membrane modules for reverse osmosis (RO), nanofiltration (NF), ultrafiltration (UF), microfiltration (MF), and forward osmosis (FO)

- System designed FO and RO for comparison rejection and fouling behaviors
- Development for osmotic backwashing technique in FO system, and FO-MBR hybrid process
- Membrane characterization techniques: SEM, AFM, Static & dynamic contact angle, Streaming surface potential, FT-IR, and Silt density index (SDI)
- Standard methods for the examination of drinking water and wastewater for, such as BOD, COD, TN, and TP

TEACHING EXPERIENCE

- Washington University in St. Louis, energy Missouri, USA   2014 - 2016
  Teaching Assistant in Environmental Engineering, Energy Transfer Processes, and Chemical Engineering Laboratory
- *Korea University*, Seoul, Korea   2009- 2010
  Teaching Assistant in Water Chemistry, and Environmental Engineering

HONORS

•	Best Teaching Assistant Award, Washington University in St. Louis, USA	2016
•	Best Paper and Presentation Award, Korean Society of Soil & Groundwater, Korea	2012
•	Research Assistant Scholarships, Korea University, Seoul, Korea	2010
•	General Scholarships, Korea University, Seoul, Korea	2009 - 2010
•	Brain Korea 21 Scholarship, Republic of Korea	2009 - 2010
•	National Science Scholarship, Republic of Korea	2007
•	Science and Engineering Scholarship, Republic of Korea	2006
•	Honors Scholarships, Korea University, Seoul, Korea	2003, 2008
•	Semester High Honors, Korea University, Seoul, Korea	2003, 2006-2007

PUBLICATIONS

21. **Changwoo Kim**, and John D. Fortner "Analysis of Laterally Heterogeneous Films Composited by Nanoparticles using Quartz Crystal Microbalance with Dissipation Monitoring (QCM-D)" *to be submitted*.

20. **Changwoo Kim**, and John D. Fortner "CTAB Encapsulated Superparamagnetic Nanocrystals for Chromium (VI) Sorption and Photoreduction" *to be submitted*.

19. **Changwoo Kim**, Junseok Lee, Daniel Schmucker, and John D. Fortner "Surface Functionalzied Superparamagnetic Iron Oxide Nanoparticles as Draw Solutes for Osmotic Pressure Driven Membrane Processes" *to be submitted*.

18. **Changwoo Kim**, Siyuan An, James Meyer, Marcus B. Foston, and John D. Fortner "Polyethylenimine (PEI) Functionalized Graphene Oxide for Cr(VI) Removal: Quantifying the Role of PEI" *to be submitted*.

17. **Changwoo Kim**, Daniel E. Giammar, and John D. Fortner "The Influence of an Organic Coating on the Deposition of Nanoparticles" *to be submitted*.

16. **Changwoo Kim**, Seung Soo Lee and John D. Fortner "The Role of Organic Coating Structure in Colloidal Stability and Aggregation Density" *to be submitted*.

15. **Changwoo Kim**, Seung Soo Lee, Kit Tan Kwan, Wenlu Li, Brandon J. Lafferty, Daniel E. Giammar and John D. Fortner "Surface Functionalized Manganese Ferrite Nano Sorbent for Single and Multiple Sorption of Arsenic (V), Chromium (VI), and Uranium (VI)" *to be submitted.*

14. **Changwoo Kim**, Seung Soo Lee, Wenlu Li and John D. Fortner "Engineering Cobalt Based Metal Oxide Nanocrystals with Tunable Dimension, Size, Shape, Crystal Structure, and Composition for Hydrogen Generation Applications by $NaBH_4$ Hydrolysis" *to be submitted*.

13. **Changwoo Kim**, Seung Soo Lee, Benjamin J. Reinhart, Minjung Cho, Brandon J. Lafferty, Wenlu Li, and John D. Fortner "Surface Optimized Core-Shell Nanocomposites ($Fe_3O_4@Mn_xFe_yO_4$) for Ultra-High Uranium Sorption and Low-Field Magnetic Separation in Water" *Environmental Science: Nano **2018**, 5 (10), 2252-2256.

12. **Changwoo Kim**, Siyuan An, Junseok Lee, Qingqing Zeng, and John D. Fortner "Engineering Graphene Oxide

Laminate Membranes for Enhanced Flux and Boron Treatment with Polyethylenimine (PEI) Polymers" *Applied Materials & Interfaces*, **2018** accepted.

11. **Changwoo Kim**, Seung Soo Lee, Brandon J Lafferty, Daniel Giammar, and John Fortner " Engineered Superparamagnetic Nanomaterials for Arsenic (V) and Chromium (VI) Sorption and Separation: Quantifying the Role of Organic Surface Coatings" *Environmental Science: Nano* **2018**, 5, 556-563.

10. Wenlu Li, Lyndsay D. Troyer, Seung Soo Lee, Jiewei Wu, **Changwoo Kim**, Brandon J. Lafferty, Jeffrey G. Catalano, John D. Fortner "Engineering Nanoscale Iron Oxides for Uranyl Sorption and Separation: Optimization of Particle Core Size and Bilayer Surface Coatings" *Applied Materials & Interfaces* **2017**, 9, 13163-13172.

9. Seung Soo Lee, Wenlu Li, **Changwoo Kim**, Minjung Cho, Jeffrey G. Catalano, Brandon J. Lafferty, Paolo Decuzzi, and John D. Fortner "Engineered Manganese Oxide Nanocrystals for Enhanced Uranyl Sorption and Separation" *Environmental Science Nano* **2015**, 2, 500-508.

8. **Changwoo Kim**, Jaesang Lee, and Seunghak Lee "TiO$_2$ Nanoparticle Sorption in the presence of Natural Organic Matter" *Environmental Earth Sciences* **2015**, 73, 5585-5591.

7. Seung Soo Lee, Wenlu Li, **Changwoo Kim**, Minjung Cho, Brandon J. Lafferty, and John D. Fortner "Surface Functionalized Manganese Ferrite Nanocrystals for Enhanced Uranium Sorption and Separation in Water" *J. Mater. Chem. A* **2015**, *3*, 21930-21939.

6. Wenlu Li, Di Liu, Jiewei Wu, **Changwoo Kim**, and John D Fortner "Aqueous Aggregation and Surface Deposition Processes of Engineered Superparamagnetic Iron Oxide Nanoparticles for Environmental Applications" *Environmental Science & Technology* **2014**, 48, 11892-11900.

5. **Changwoo Kim**, and Seunghak Lee "Effect of Seepage Velocity on the Attachment Efficiency of TiO$_2$ nanoparticles in porous media" *J. Hazardous Materials* **2014**, 279, 163-168.

4. **Changwoo Kim**, and Sangyoup Lee, Ho Kyong Shon, Menachem Elimelech, Seungkwan Hong "Boron Transport in Forward Osmosis: Measurements, Mechanisms, and Comparison with Reverse Osmosis" *J. membrane science* **2012**, 419, 42-48.

3. **Changwoo Kim**, Sangyoup Lee, and Seungkwan Hong "Application of Osmotic Backwashing in Forward Osmosis: Mechanisms and Factors Involved" *Desalination and Water Treatment* **2012**, 43, 314-322.

2. Eunhyea Chung, Sotira Yiacoumi, Candice Halbert, John Ankner, Wei Wang, **Changwoo Kim**, and Costas Tsouris "Interaction of Silica Nanoparticles with a Flat Silica Surface through Neutron Reflectometry" *Environmental Science & Technology* **2012**, 46, 4532-4538.

1. Keewoong Hong, Sangyounp Lee, **Changwoo Kim**, Cha hee Boo, Myunggyun Park, Hochul An, and Seungkwan Hong "Evaluation of RO process feasibility and membrane fouling for wastewater reuse" *J. Korean Society on Water Quality* **2010**, 26, 289-296.

CONFERENCE PRESENTATIONS

11. **Changwoo Kim**, Siyuan An, and John D. Fortner "PEI Functionalized Graphene Oxide for Enhanced Sorption and Rapid Photoreduction of Chromium (VI)" 255th American Chemical Society National Meeting and Exposition Press Conference, March 18–22, **2018**, New Orleans, LA, USA

10. **Changwoo Kim**, Junseok Lee, Daniel Schmucker, and John D. Fortner **"**Engineered Superparamagnetic Nanomaterials as Draw solutes for Osmotic Pressure Driven Membrane Process" 2017 Mid-American Environmental Engineering Conference October 7, **2017**, Saint Louis, MO, USA.

9. **Changwoo Kim**, Seung Soo Lee, John Fortner "Quantifying nanoparticle stability and aggregation dynamics as a function of organic coating structure and density" 254th American Chemical Society National Meeting and Exposition Press Conference, August 20–24, **2017**, Washington, DC, USA.

8. **Changwoo Kim**, Seung Soo Lee, Wenlu Li, John Fortner "Engineering Superparamagnetic Metal Oxide Nanocrystals for Chromium and Arsenic Sorption, and Separation" 250th American Chemical Society National Meeting and Exposition Press Conference, August 16–20, **2015**, Boston, USA.

7. Wenlu Li, Seung Soo Lee, Jiewei Wu, Yi Jiang, **Changwoo Kim**, Carl Hinton, John Fortner "Engineering Superparamagnetic Iron Oxide Nanocrystals for Environmental Applications" *250th American Chemical Society National Meeting and Exposition Press Conference*, August 16–20, **2015**, Boston, USA.

6. Yoontaek Oh, Sangyoup Lee, Seungkwan Hong, **Changwoo Kim**, Youngbeom Yu, Seockheon Lee "Relationship between Reverse Salt Diffusion and Rejection Rate in Forward Osmosis (FO)" *International*

Water Association Specialist Conference on Membrane Technology for Water & Wastewater Treatment, October 4-7, **2011**, Aachen, Germany.

5. **Changwoo Kim**, Sangyoup Lee, Chanhee Boo, Yoontaek Oh, Hyunchul Hur, Menachem Elimelech, Seungkwan Hong "Osmotic backwashing for forward osmosis" *Membrane in Drinking and Industrial Water Treatment*, November 22-24, **2010**, Singapore.

4. Chanhee Boo, Sangyoup Lee, **Changwoo Kim**, Menachem Elimelech, Seungkwan Hong "Colloidal fouling in forward osmosis: Role of reverse diffusion in colloidal fouling" *Membrane in Drinking and Industrial Water Treatment*, November 4-5, **2010**, Jeju, Korea.

3. **Changwoo Kim**, Sangyoup Lee, Chanhee Boo, Menachem Elimelech, Seungkwan Hong "Comparison of boron rejection behaviors in forward and reverse osmosis systems" *International Water Association regional conference (membrane technology and water reuse)*, October 18-22, **2010**, Istanbul, Turkey.

2. **Changwoo Kim**, Sangyoup Lee, Chanhee Boo, Menachem Elimelech, Seungkwan Hong "Comparison of solute rejection behaviors in forward and reverse osmosis systems" *Membrane in Drinking and Industrial Water Treatment*, June 27-30, **2010**, Trondheim, Norway.

1. Chanhee Boo, Sangyoup Lee, **Changwoo Kim**, Suingil Choi, Menachem Elimelech, Seungkwan Hong "Investigation of fouling layer characteristics in forward and reverse osmosis systems", Membrane in Drinking and Industrial Water Treatment, June 27-30, **2010**, Trondheim, Norway.

EXTRACURRICULAR ACTIVITY
- Manager of the Club of Central Square, Korea University   2008-2013

LICENCE
- License of Civil Engineering, Republic of Korea.   2007-prsent

PROFESSIONAL MEMBERSHIPS
- American Chemical Society
- Korean Society of Water Environment
- Korean Society of Water and Wastewater
- Korean Society of Hazard Mitigation
- Korean Society of Environmental Engineers

SKILLS
- *Organic-Inorganic Nano Composite Synthesis*: Iron/cobalt/manganese based metal oxides with commercial or synthetic polymers (PEG, PEI, PAA, PMAO, and amidoxime), organic acid (CTAB, SDS, OA, and OP) and silica synthesized by wet chemical synthesis
- *Organometallic Compound Synthesis*: Transition metal carboxylates and chalcogenides containing iron, manganese, cobalt, nickel, copper, zinc, indium, gallium, sulfur, and selenium using a Schlenk line technique
- *Graphene Oxide Synthesis*: Control the oxidation of graphene and its functionalization
- *Computation of Theoretical DLVO Energy Interaction and Collision Efficiency of Nanomaterials*
- *Instruments:* SEM, TEM, HR-TEM, EDS, AFM, XRD, XPS, XRF, TOC, QCM-D, UV-Vis, FTIR, , TGA, DLS/zeta sizer, SQUID, ICP-OES/-MS, Column system, Glove Box, Schlenk Technique, and High pressure/ thermal reactor.
- Computer: Microsoft office, Origin Lab, Sigma plot, Endnote, MultiPak, Image Pro, and Matlab

REFERENCES
- **Dr. John D. Fortner**, InCEES Career Development Associate Professor of Energy, Environmental, & Chemical Engineering, Washington University, St. Louis, Missouri, USA. email: jfortner@wustl.edu; phone: 1-314-935-5548
- **Dr. Seunghak Lee**, Principal Researcher, Center for Water Resource Cycle Research, Korea Institute of Science and Technology, Seoul, Korea. email: seunglee@kist.re.kr; phone: 82-2-02-958-5817
- **Dr. Seungkwan Hong**, Professor of Civil and Environmental Engineering, Korea University, Seoul, Korea. email: skhong21@korea.ac.kr; phone: 82-02-3290-3322
- **Dr. Menachem Elimelech**, Roberto C. Goizueta Professor of Chemical & Environmental Engineering, Yale

University, New Haven, Connecticut, USA. email: menachem.elimelech@yale.edu; phone: 1-203-432-2789